Svend Tollak Munkejord

Analysis of the two-fluid model and the drift-flux model for numerical calculation of two-phase flow

Doctoral thesis
for the degree of philosophiae doctor

Trondheim, January 2006

Norwegian University of
Science and Technology
Faculty of Engineering Science and Technology
Department of Energy and Process Engineering

NTNU
Norwegian University of
Science and Technology

Doctoral thesis
for the degree of philosophiae doctor

Faculty of Engineering Science and Technology
Department of Energy and Process Engineering

ISBN 82-471-7338-7 (printed ver.)
ISBN 82-471-7337-9 (electronic ver.)
ISSN 1503-8181

Doctoral Theses at NTNU, 2005:219

Printed by Tapir Uttrykk

Abstract

THIS THESIS analyses models for two-phase flows and methods for the numerical resolution of these models. It is therefore one contribution to the development of reliable design tools for multiphase applications. Such tools are needed and expected by engineers in a range of fields, including in the oil and gas industry.

The approximate Riemann solver of Roe has been studied. Roe schemes for three different two-phase flow models have been implemented in the framework of a standard numerical algorithm for the solution of hyperbolic conservation laws. The schemes have been analysed by calculation of benchmark tests from the literature, and by comparison with each other.

A Roe scheme for the four-equation one-pressure two-fluid model has been implemented, and a second-order extension based on wave decomposition and flux-difference splitting was shown to work well and to give improved results compared to the first-order scheme. The convergence properties of the scheme were tested on smooth and discontinuous solutions.

A Roe scheme has been proposed for a five-equation two-pressure two-fluid model with pressure relaxation. The use of analogous numerical methods for the five-equation and four-equation models allowed for a direct comparison of a method with and without pressure relaxation. Numerical experiments demonstrated that the two approaches converged to the same results, but that the five-equation pressure-relaxation method was significantly more dissipative, particularly for contact discontinuities. Furthermore, even though the five-equation model with instantaneous pressure relaxation has real eigenvalues, the calculations showed that it produced oscillations for cases where the four-equation model had complex eigenvalues.

A Roe scheme has been constructed for the drift-flux model with general closure laws. For the case of the Zuber–Findlay slip law describing bubbly flows, the Roe matrix is completely analytical. Hence the present Roe scheme is more efficient than previous fully numerical Roe schemes for the drift-flux model.

An isentropic discrete-equation multiphase model has been presented. The incorporation of different interfacial-pressure models was discussed, and examples were given. With the adequate models for the interfacial pressure and velocity, the agreement was very good between the discrete-equation model and the five-equation Roe scheme.

The flux-limiter centred (FLIC) scheme was tested for the four-equation two-fluid model. Only the first-order version (FORCE) of the scheme was found to work well, but it was rather diffusive.

The purpose of the multi-stage (MUSTA) method is to come close to the accuracy of upwind schemes while retaining the simplicity of centred schemes. Here it has been applied to the drift-flux model. As the number of stages was increased, the results of the MUSTA scheme approached those of the Roe method. The good results of the MUSTA scheme were dependent on the use of a large-enough local grid. Hence, the main advantage of the MUSTA scheme is its simplicity.

A multiphase characteristic-based boundary-condition method has been tested, and it was shown to be workable for transient problems.

Sammendrag

FLERFASESTRØMNING er av betydning i en lang rekke anvendelser, blant annet i olje- og gassindustrien, i den kjemiske og i prosessindustrien, inkludert i varmepumpende systemer, samt i sikkerhetsanalyse av kjernekraftverk. Denne avhandlingen analyserer modeller for tofasestrømning, og metoder for numerisk løsning av disse modellene. Den er derfor ett bidrag til å utvikle pålitelige ingeniørverktøy for flerfase-anvendelser. Slike verktøy trengs og forventes av ingeniører i industrien.

Den tilnærmede Riemann-løseren framsatt av Roe har blitt studert. Roe-skjema for tre ulike modeller for tofasestrømning har blitt implementert i rammen av en standard numerisk algoritme for løsning av hyperbolske bevaringslover. Disse skjemaene har blitt analysert ved hjelp av referanse-regnestykker fra litteraturen, og ved sammenlikning med hverandre.

Et Roe-skjema for den fire-liknings ett-trykks tofluid-modellen har blitt implementert, og det har blitt vist at en andreordens utvidelse basert på bølge-dekomponering og fluksdifferanse-splitting virker godt, og gir forbedrede resultater sammenliknet med det førsteordens skjemaet.

Det har blitt foreslått et Roe-skjema for en fem-liknings totrykks tofluid-modell med trykkrelaksering. Bruken av analoge numeriske metoder for fire-liknings- og fem-likningsmodellene gjorde det mulig med en direkte sammenlikning av en metode med og uten trykkrelaksering. Numeriske eksperiment demonstrerte at de to framgangsmåtene konvergerte til samme resultat, men at den fem-likningsmodellens trykkrelakserings-metoden var betydelig mer dissipativ, særlig for kontaktdiskontinuiteter. Videre viste beregninger at selv om fem-likningsmodellen har reelle egenverdier, så produserte den oscillasjoner for tilfeller der fire-likningsmodellen hadde komplekse egenverdier.

Et Roe-skjema har blitt konstruert for driftfluksmodellen med generelle lukningslover. Roe-matrisen er helt analytisk for det tilfellet at man kan anvende Zuber–Findlay-slipploven som beskriver boblestrømning. Dermed er dette Roe-skjemaet mer effektivt enn tidligere fullt numeriske Roe-skjema for driftfluksmodellen.

En isentropisk diskret-nivå-flerfasemodell har blitt presentert. En diskusjon av hvordan man kan ta hensyn til ulike interfasetrykkmodeller har blitt gitt. Med de passende modellene for interfase-trykk og -fart, var samsvaret svært godt mellom diskret-nivåmodellen og det fem-likningsmodellens Roe-skjemaet.

Multi-steg- (MUSTA) metoden har som siktemål å komme nær oppstrøms-metodene i nøyaktighet, samtidig som den bevarer enkelheten til sentrerte skjema. Her har metoden blitt brukt på driftfluks-modellen. Når antallet steg økes, nærmer resultatene fra MUSTA-metoden seg det man får med Roe-metoden. De gode resultatene til MUSTA-metoden er avhengige av at man bruker et stort nok lokalt grid. Derfor er hovedfordelen med MUSTA-metoden at den er enkel, snarere enn at man sparer regnetid.

En karakteristikk-basert metode for å spesifisere grensebetinglser for flerfase-modeller har blitt testet, og funnet å virke godt for transiente problem.

Mon rêve serait de faire un travail de longue haleine qui se corrige au cours de sa progression, qui soit également ouvert tant aux réactions qu'il provoque qu'aux conjonctures qu'il croise en chemin et, peut-être aussi, ouvert à de nouvelles hypothèses. Ce que je souhaite, c'est un travail dispersé et changeant.

La volonté de savoir
Michel Foucault

Preface

The present work was initiated in connection with a research project on electrocoalescence carried out at Sintef Energy Research and NTNU. It bears some relation to the work of the PhD candidates Erik B. Hansen and Jens A. Melheim.

The financial support received from the Science and Technology division of the Research Council of Norway is gratefully acknowledged. I was allocated a three-year personal PhD grant as well as a half-year overseas fellowship.

I am pleased to thank my supervisor, Professor Inge R. Gran, for his insightful guidance, which helped me keep a realistic time schedule, and which enhanced the quality of the work. Furthermore, he gave me the freedom to pursue the topics I found interesting. Thanks are also due to my co-supervisor, Professor Morten Chr. Melaaen, for valuable discussions.

I am indebted to Professor Rémi Abgrall for inviting me to spend one semester at Mathématiques Appliquées de Bordeaux in the spring of 2004. Dr Mikael Papin deserves thanks for explaining the implementation of the method studied in Chapter 5. The time in Bordeaux was a most rewarding period regarding the topic of this thesis, but perhaps not less significantly, regarding the learning of French, and encountering important persons.

I would like to give my sincere thanks to my colleague, Dr Robert Olsen, for providing me with his numerical code, which gave a good starting point for implementing the methods tested in the present work. The discussions we have had were stimulating, and I am grateful for his comments on the manuscript.

My fellow PhD candidate Erik B. Hansen has read the manuscript, and contributed constructive suggestions. I have also much appreciated the discussions with my colleague Jens A. Melheim.

Towards the end of this work, I have had the pleasure of carrying out an interesting and fruitful cooperation with Dr Tore Flåtten of IRIS. I hereby express my gratitude for that. In addition to the obvious effect shown in Chapters 7–8, Tore provided several helpful suggestions regarding Chapter 3. He also introduced me to his colleague, Dr Steinar Evje, to whom I am thankful for the rewarding collaboration on Chapter 8.

Finally, I would like to thank all my colleagues at the Department of Energy and Process Engineering at NTNU, and at Sintef Energy Research, for an enjoyable time.

Svend Tollak Munkejord

Trondheim, November 2005

Contents

Nomenclature

> There arises from a bad and unapt formation of words a wonderful obstruction to the mind.
>
> Francis Bacon

Latin letters

a	Acoustic impedance (ρc)	$\mathrm{kg}/(\mathrm{m}^2\,\mathrm{s})$
a	Interfacial area density, Sec. 2.4.1	$\mathrm{m}^2/\mathrm{m}^3$
A	Area	m^2
$\boldsymbol{A}$	Coefficient matrix for composite variables, see (3.2), (3.34), (3.43)	–
$\mathcal{A}$	Control surface	m^2
$\mathcal{A}^{\pm}\Delta\boldsymbol{Q}_{i-1/2}$	Fluctuations defined by (3.54)	–
$\boldsymbol{b}$	Body-force field vector	$\mathrm{m/s}^2$
B	Displacement factor, see (2.107)	–
$\boldsymbol{B}$	Coefficient matrix for primitive variables, see (3.3)	–
c	Speed of sound, see (2.88)	m/s
C	Courant–Friedrichs–Lewy (CFL) number. $C = \|\lambda\|_\infty \Delta t/\Delta x$	–
C	Constant in interphasic friction model, see (4.19)	–
$\boldsymbol{C}$	Matrix, see (3.10)	–
C_i	Control 'volume' number i	m
c_v	Specific heat at constant volume	J/kg
$\boldsymbol{D}$	Matrix, see (3.10)	–
$\boldsymbol{e}$	Vector for source terms, see (3.13)	–
E	Ensemble, Section 2.4.1	–
E	Error, see (3.99)	–
$\boldsymbol{f}$	Flux function	–
F	Momentum source, see (4.18), (7.162)	$\mathrm{N/m}^3$
$\boldsymbol{F}$	Numerical approximation to $\boldsymbol{f}$	–
$\tilde{\boldsymbol{F}}$	High-resolution correction flux vector, see (3.57)	–
$\boldsymbol{F}$	Matrix containing the fluxes, see (5.5)	–
$\boldsymbol{F}^{\mathrm{lag}}$	Matrix of Lagrangian fluxes, see (5.31)	–
g	Gravitational acceleration	$\mathrm{m/s}^2$
H_s	Mean curvature	1/m
$\mathcal{H}$	Right-hand side of semi-discrete formulation, Chap. 8	–

I	Volumetric momentum, $I_k = \alpha_k \rho_k u_k$, Chap. 7	$\mathrm{kg/(m^2\,s)}$
$\boldsymbol{I}$	Unitary tensor	–
$\boldsymbol{J}$	Transformation matrix, see (3.4)	–
k	Constant in interphasic friction model, see (4.19)	–
k_D	Differential constant, see (6.14)	–
k_I	Integral constant, see (6.14)	–
k_P	Proportional constant, see (6.14)	–
K	Distribution parameter in the Zuber–Findlay relation, see (7.11)	–
$\boldsymbol{l}^T$	Left eigenvector (row vector)	–
L	Length	m
$\mathcal{L}$	Vector in boundary procedure, see (6.3)	–
m	Mass, Sec. 3.4.1	kg
m	Measure, Sec. 2.4.1	–
m	Volumetric mass, $m_k = \alpha_k \rho_k$, Chap. 7	$\mathrm{kg/m^3}$
$m_{\mathrm{i}k}$	Interfacial momentum source, Chap. 2	$\mathrm{N/m^3}$
M	Number of sub-cells, Sec. 5.3.3	–
M	Number of stages in the MUSTA scheme, Chap. 8	–
n	Order of convergence, see (3.104)	–
$\boldsymbol{n}$	Unit normal vector	m
N	Half the number of cells on the local MUSTA grid, Chap. 8	–
$N_{\mathrm{int},i}$	Number of internal interfaces in C_i	–
$\mathcal{O}$	Order of magnitude	–
p	Pressure	Pa
δp	Local pressure variation, see (2.22)	Pa
$\mathcal{P}$	Probability, see (5.44)	–
$\boldsymbol{q}$	Vector containing the composite variables, see (3.1), (3.32), (3.41), (5.4), (7.3)	–
$\boldsymbol{Q}_i^n$	Numerical approximation to the cell average of $\boldsymbol{q}(x(i), t_n)$	–
r_p	Pressure-relaxation parameter, see (2.96)	$\mathrm{1/(Pa\,s)}$
r_u	Velocity-relaxation parameter, see (2.98)	$\mathrm{Pa\,s/m^2}$
$\boldsymbol{r}$	Right eigenvector	–
$\boldsymbol{R}$	Matrix containing right eigenvectors as its columns	–
s	Source term in momentum equation	$\mathrm{(N/m^3)}$
s	Specific entropy	$\mathrm{J/(kg\,K)}$
s	Wave speed	m/s
$\boldsymbol{s}$	Source-term vector for composite variables, see (3.1), (3.35), (3.44)	–
S	Drift velocity in the Zuber–Findlay relation, see (7.11)	–
$\boldsymbol{S}$	Matrix of non-conservative source terms, see (5.27)	–
t	Time	s
T	Temperature	K

T	Time scale or period, see (6.14)	s
$\boldsymbol{T}$	Stress tensor, $\boldsymbol{T} = -p\boldsymbol{I} + \boldsymbol{\tau}$	Pa
u	Velocity	m/s
$\boldsymbol{u}$	Velocity vector	m/s
v	Specific volume	m^3/kg
$\boldsymbol{v}$	Vector containing the primitive variables, see (3.3), (3.11), (3.36)	–
V	Volume	m^3
V_m	Variable defined in (5.56)	–
$\mathcal{V}$	Control volume	m^3
$\boldsymbol{w}$	Characteristic-variable vector, see (6.6)	–
$\boldsymbol{w}$	Parameter vector, Chap. 7	–
$\mathcal{W}$	Wave, see (3.68)	–
$\widetilde{\mathcal{W}}$	Limited wave, see (3.83)	–
x	Length coordinate	m

Greek letters

α	Volume fraction	–
β	Quantity in hyperbolicity analysis, see (3.48)	Pa
β	Wave strength, see (3.66)	–
$(\beta^{(k,l)}_{m-1/2})^+$	Variable defined in (5.57)	–
$(\beta^{(k,l)}_{m+1/2})^-$	Variable defined in (5.58)	–
γ	Constant in (3.103)	–
γ	Factor in the CATHARE model, see (2.109)	–
γ	Quantity in hyperbolicity analysis, see (3.49)	m^2/s^2
δ	Parameter in the smoothed absolute-value function, see (3.80)	–
ζ	Velocity derivative, see (7.18)	–
η	Dynamic (molecular) viscosity, Chap. 7	Pa s
η	Sub-cell spatial coordinate, Sec. 5.3.3	–
θ	Smoothness measure, see (3.84)	–
κ	Quantity in pressure differential, see (7.31)	$m^5/(kg\,s)$
λ	Eigenvalue	m/s
$\boldsymbol{\lambda}$	Vector containing eigenvalues	m/s
$\boldsymbol{\Lambda}$	Diagonal matrix containing eigenvalues	m/s
μ	Realization, Sec. 2.4.1	–
μ_g	Slip derivative, see (7.15)	$m^4/(kg\,s)$
μ_ℓ	Slip derivative, see (7.16)	$m^4/(kg\,s)$
μ_v	Slip derivative, see (7.17)	–
ξ	Path	–
ξ_l	Interface number l, see Figure 5.1	–
ρ	(Mass) density	kg/m^3

ϱ	Pseudo mass, see (7.19)	kg/m^3
σ	Constant related to surface tension etc., see (2.89)	Pa
σ	Surface-tension coefficient	N/m
$\boldsymbol{\varsigma}$	Source-term vector for primitive variables	–
$\boldsymbol{\tau}$	Viscous stress tensor	Pa
ϕ	Flux-limiter function, see (3.83)	–
ϕ	Test function, Sec. 2.4.1	–
ϕ_δ	Smoothed absolute-value function, see (3.80)	–
Φ	Interphase friction parameter, see (4.19)	–
Φ	Slip relation, see (2.114)	m/s
χ	Phase-indicator function	–
ψ	General function	–
Ω	Calculation domain	–

Subscripts

$\circ$	Reference, see (5.22)
0	Initial / Reference
c	Critical
f	Pertaining to phase f
g	Gas
i	Interface
int	Interface, Chap. 5
i	Spatial index
j	Sub-cell spatial index, Sec. 5.3.3
j	Time-step index, Chap. 8
k	Pertaining to phase k
l	Left-hand side
l	Pertaining to phase l
ℓ	Liquid
L	Left-hand side
m	Mixture
n	Local spatial index, Chap. 8
n	Time-step index
r	Right-hand side
R	Right-hand side
s	A known state, see (5.77)
w	Wall

Superscripts

$\circ$	Initial
$\circ$	Reference, see (2.88)

$*$	Value in Riemann-problem solution, see Figure 5.2
d	Drag
(g)	Pertaining to the gas phase
h	High-order, see (4.10)
j	Time-step index, Chap. 8
(k)	Pertaining to phase k
(l)	Pertaining to phase l
(ℓ)	Pertaining to the liquid phase
l	Low-order, see (4.6)
l	Low-order, see (8.3)
L	Left-hand side
LF	Lax–Friedrichs, see (4.7)
m	Local time-step index, Chap. 8
$-$	Corresponding to negative eigenvalues, Sec. 6.2
$-$	Left-hand side value, Chap. 5
$-$	Negative part
n	Time-step index
p	Related to the pth eigenvalue
$+$	Corresponding to positive eigenvalues, Sec. 6.2
$+$	Positive part
$+$	Right-hand side value, Chap. 5
R	Richtmyer, see (4.9)
R	Right-hand side
Ru	Rusanov, see (4.17)

Other symbols

$\overline{\psi}$	Average (context dependent)
$\overline{\psi}$	Ensemble average of ψ, see Sec. 2.4.3
$\breve{\psi}$	'Conventional' equation system, see (5.66)
$\hat{\psi}$	Roe average of ψ
$[\psi]$	$\psi^+ - \psi^-$
$\tilde{\psi}$	Augmented equation system, see (5.39)
$\tilde{\psi}$	Quantities in Section 4.1
$\tilde{\psi}$	Various averages, Chap. 7

Abbreviations

AUSMD	Advection upstream splitting method
CFL	Courant–Friedrichs–Lewy
CPU	Central processing unit
EOS	Equation of state
FLIC	Flux-limiter centred

FORCE	First-order centred
HLL	Harten, Lax and van Leer
LLF	Local Lax–Friedrichs
LRV	Large relative velocity
MC	Monotonized central difference
MPCBC	Multiphase characteristic-based boundary conditions
MUSCL	Monotonic upwind-centred scheme for conservation laws
MUSTA	Multi-stage
ODE	Ordinary differential equation
PID	Proportional-integral-derivative
PVRS	Primitive-variables Riemann solver
TVD	Total variation diminishing

1 Introduction

> Upon those who step into the same rivers different and ever different waters flow down.
>
> Heracleitus, c. 540–c. 480 BC

1.1 Motivation for the thesis

Multiphase flows are important in a large range of industrial applications, such as in the oil and gas industry, in the chemical and process industry, including in heat-pumping systems, as well as in the safety analysis of nuclear power plants.

In Norway, the oil and gas industry is of particular importance. A growing number of oil and gas fields are situated far from the shore, and at great depths. This increases the drive towards field developments based on sub-sea processing and multiphase flow transportation. Therefore, it is of significance to be able to predict the flows in greater detail, not only in pipelines, but also inside process equipment with complex geometries. To do that, one needs good and rigorous mathematical models, and accurate numerical methods to solve them. This is the topic of the present thesis.

1.2 Multiphase modelling

Depending on the problem at hand, the desired level of detail, and the computational resources available, a range of techniques are employed for the numerical simulation of multiphase flows. These may be divided into the following categories:

Interface-tracking methods The interfaces between the phases are fully resolved.

Particle-tracking methods The bubbles, droplets or solid particles are treated as point particles, and their individual trajectories are calculated.

Multifluid methods The various phases are treated as fluids, and no explicit information of the interface is retained.

The interface-tracking methods are generally the most CPU-intensive for a given physical domain. The multifluid methods are less so, whereas the particle-tracking methods reside somewhere in between.

The *interface-tracking methods* can be classified as Lagrangian, Eulerian, or combined Lagrangian–Eulerian methods (see e.g. Hansen, 2005; Singh *et al.*, 2005, for an overview). Lagrangian methods use a body-fitted grid that deforms with the interface. The grid is modified after each time step. The Eulerian methods, such as the volume-of-fluid (VOF) (see Scardovelli and Zaleski, 1999) and level-set methods (see Osher and Fedkiw, 2001; Sethian, 2001), solve the governing equations on a fixed grid. They are often referred to as *front-capturing* methods. In the VOF method, the interface is reconstructed based on the calculated mass fraction. The level-set method employs a scalar function advected with the interface velocity. From this function, the interface and its geometric properties are calculated. The combined Lagrangian–Eulerian methods are often called *front-tracking* methods (see Tryggvason *et al.*, 2001). They solve the fluid-flow equations on an Eulerian grid, but use a set of massless markers to track the interface. As the interface evolves, some markers must be added and others deleted to maintain a reasonable marker spacing. The algorithms needed to reconstruct a moving and deforming interface are complex. Among the combined Lagrangian–Eulerian methods one finds the continuous interface methods, such as the immersed boundary methods (see Peskin, 2002), and sharp interface methods.

The *particle-tracking methods* are usually Eulerian–Lagrangian methods, where the fluid flow is calculated on a fixed grid, whereas the point particles, being smaller than the grid size, are tracked in a Lagrangian manner. This is often called the *discrete-particle* model (DPM) or *discrete-element* model (DEM). Particle-particle, particle-wall, particle-fluid and fluid-particle interactions can be accounted for (see e.g. Loth, 2000; van der Hoef *et al.*, 2005, for an overview). A range of techniques are employed to reduce the computational cost (Melheim, 2005). It is possible to increase the system size by considering each numerical particle to be a group of physical particles. To do this, however, closure relations must be added.

At the other end of the scale, lattice Boltzmann models or standard computational fluid dynamics models may be employed to fully resolve the flow field around the particles, which are then larger than the grid size. This can be used for instance for finding drag laws.

Smooth particle hydrodynamics (SPH) (see Cleary *et al.*, 2005) is a Lagrangian continuum method. The fluid (or solid) is discretized and the properties of each of these elements are attributed to their centres, which are then interpreted as particles. The method has been applied for solving incompressible, partially

enclosed free-surface flow problems.

In *multifluid methods*, or continuum methods, all the involved phases, such as particles, droplets, bubbles or liquids, are considered to be fluids. Hence, in principle, quite large systems can be calculated, but this comes at the cost of modelling challenges. These include formulating a well-understood and well-posed basic mathematical model, finding closure relations for the involved phenomena, and devising robust and accurate numerical methods for solving the models.

Not every method is suited for calculating every kind of flow. One example is the assumption of point particles in the particle-tracking methods. On the other hand, it is possible to combine elements from the above-mentioned methods, if desired.

Different applications involve diverse flow topologies. At the same time, the various modelling methods have their strong points for different flow topologies. The existence of a range of modelling approaches may therefore be regarded as an advantage.

In this thesis, we study multifluid methods, but restrict the number of phases to two.

Even in one spatial dimension, two-phase flows are often highly complicated, and display topological changes as a function of the thermodynamical and flow parameters. The observed patterns can be divided into *flow regimes*. The terms and classifications used vary with the author. Taitel (1990) employs four main classes;

1. Stratified flow,
2. Intermittent flow,
3. Annular flow,
4. Bubble flow.

For example, the intermittent flow is in the form of liquid slugs which fill the pipe and are separated by gas zones in a form of elongated bubbles which contain a stratified liquid layer flowing along the bottom of the pipe. This is perhaps the most challenging flow regime to model.

In the present work, the emphasis is on numerical methods and basic models, and constitutive relations are not analysed in depth. Incidentally, in some instances, even simple models may provide reasonable results (Munkejord *et al.*, 2005).

Simulation codes Much of the early development of numerical two-phase models was conducted by the nuclear industry for the purpose of reactor safety analysis. Among the codes are TRAC, RELAP (see Trapp and Riemke, 1986; Mahaffy, 1993, for an overview) and CATHARE (Barre and Bernard, 1990; Bestion, 1990).

Modelling work has also been performed in the petroleum industry, leading to codes such as OLGA (Bendiksen *et al.*, 1991), employing the two-fluid model, and the slug-tracking model PeTra (Larsen *et al.*, 1997). These are employed for the design of pipelines and top-side facilities. There also exist codes based on the drift-flux model. Examples are TACITE (Pauchon *et al.*, 1994) and RF-Kick (Vefring *et al.*, 1995).

Several commercial computational fluid dynamics (CFD) codes are equipped with multiphase flow models. One example is described in Brown (2002).

1.3 Previous work

This section provides a brief literature review regarding the models and methods analysed here. Further details may be found in Chapters 3, 7–8 and 5.

1.3.1 Two-fluid models

For the numerical solution of flow models, the approximate Riemann solver of Roe (1981) is an attractive candidate, since it provides an *upwind* resolution of all wave phenomena inherent in the models, and as it requires only the solution of a *linear* Riemann problem at each cell interface. Among the problems encountered for the two-fluid model, is the complicated eigenstructure, as well as the appearance of non-conservative terms (Toumi, 1996).

Sainsaulieu (1995) introduced a Roe-type Riemann solver for the case of incompressible liquid droplets suspended in a gas, that is, for small liquid volume fractions. More general configurations were considered by Toumi (1996), and a Roe-type method for the isentropic two-fluid model was presented by Toumi and Kumbaro (1996). However, also in the latter works, the liquid density was assumed to be constant. That assumption was not used in the method by Evje and Flåtten (2003).

A different approach has been to consider two-pressure models, whose mathematical properties have been found preferable (Ransom and Hicks, 1984). On the other hand, for many cases, the latter kind of methods needs a *pressure-relaxation* procedure.

Saurel and Abgrall (1999) presented a two-velocity two-pressure two-phase model of seven equations, where pressure and / or velocity relaxation could be

performed after the hyperbolic time step. The model can be thought of as an extension of that of Baer and Nunziato (1986). It was expanded to several space dimensions by Saurel and LeMetayer (2001), and it was stated to be suitable for compressible multiphase flows with interfaces, shocks, detonation waves and cavitation. Murrone and Guillard (2005) discussed a five-equation diffuse interface model where the two phases had common pressures and velocities. Different pressure-relaxation procedures were tested by Lallemand *et al.* (2005).

The approximate Riemann solver employed by Saurel and Abgrall (1999) was a modified Harten, Lax and van Leer (HLL) scheme. Other authors have later presented similar methods using other solvers. Niu (2001) applied a modified advection upstream splitting method (AUSMD) and solved the seven-equation model in one and two dimensions, also adding a k–ε turbulence model. A Roe-type scheme for the seven-equation model was presented by Karni *et al.* (2004).

1.3.2 Drift-flux model

For several flow regimes, it is possible to correlate the relative velocity between the phases, the *slip velocity,* as a function of the flow variables (see e.g. Zuber and Findlay, 1965; Ishii, 1977; Hibiki and Ishii, 2002). This a priori knowledge of the flow can be employed to reduce the number of transport equations to be solved, and the result is called the *drift-flux model.*

The closure law for the slip velocity is often a complicated function of the state variables and flow parameters. As has been pointed out by several researchers (Baudin *et al.*, 2005a,b; Evje and Fjelde, 2002, 2003; Faille and Heintzé, 1999; Romate, 1998), the complexity of these laws severely restricts the possibilities for constructing a Roe solver by purely algebraic manipulations. Nevertheless, Roe-type schemes have been proposed for this model. Romate (1998) presented a method for constructing a Roe matrix using a fully numerical approach. This method was used as the conservative part of the hybrid primitive-conservative method of Fjelde and Karlsen (2002). Faille and Heintzé (1999) proposed a linearized Riemann solver which may be interpreted as a simplified version of the approach of Romate. However, their suggested scheme does not satisfy the Roe conditions, with the consequence that the numerical fluxes are generally discontinuous if there is a change of sign in an eigenvalue between neighbouring cells.

A more formal approach was undertaken by Toumi and Caruge (1998) for a related model involving a mixture mass equation and a mixture energy equation. Based on a splitting of the flux into a ‘mixture’ and ‘drift’ part, they described how a Roe matrix could be obtained using the parameter-vector approach of

Roe (1981).

Baudin *et al.* (2005a,b) suggested a *relaxation* scheme of the type proposed by Jin and Xin (1995). This is somewhat related to the Roe scheme in that one needs only to solve a linear Riemann problem at each cell interface.

Upwind schemes are known to be accurate, but they are relatively complicated. Centred schemes, on the other hand, are simpler, but more dissipative (Chen and Toro, 2004). The multi-stage (MUSTA) method proposed by Toro (2003); Titarev and Toro (2005) is aimed at coming close to the accuracy of upwind schemes while retaining the simplicity of centred schemes. In this approach, the solution of the Riemann problem at the cell interface is approximated numerically by employing a first-order centred scheme on a local grid.

1.4 Present contribution

This thesis analyses models for two-phase flows and methods for the numerical resolution of these models.

Roe schemes for three different two-phase flow models have been implemented in the framework of a standard numerical algorithm for the solution of hyperbolic conservation laws (LeVeque, 2002, Chapter 15).

The Roe scheme of Evje and Flåtten (2003) for the four-equation one-pressure two-fluid model has been implemented, and a second-order extension based on wave decomposition and flux-difference splitting was shown to work well and to give improved results compared to the first-order scheme.

A Roe scheme has been proposed for a five-equation two-pressure two-fluid model with pressure relaxation. The use of analogous numerical methods for the five-equation and four-equation models allowed for a direct comparison of a method with and without pressure relaxation. The hypothesis was put forth that the five-equation model with instantaneous pressure relaxation can be regarded as providing an alternative numerical method for solving the four-equation model. Numerical experiments showed that the two approaches converged to the same results, but that the five-equation pressure-relaxation method was significantly more dissipative, particularly for contact discontinuities. Furthermore, even though the five-equation model has real eigenvalues, numerical evidence showed that the five-equation method with instantaneous pressure relaxation produced oscillations for cases where the four-equation model had complex eigenvalues.

A Roe scheme has been constructed for the drift-flux model with general closure laws. For the case of the Zuber–Findlay slip law describing bubbly flows,

the Roe matrix is fully analytical, thus addressing computational efficiency issues associated with previous Roe schemes for the drift-flux model.

An isentropic version of the discrete-equation multiphase model of Abgrall and Saurel (2003) has been presented. The incorporation of different interfacial-pressure models was discussed, and examples were given. With the adequate models for the interfacial pressure and velocity, the agreement was very good between the discrete-equation model and the five-equation Roe scheme.

The multi-stage (MUSTA) centred-scheme approach has been applied to the drift-flux model. It has been shown that the good results of the MUSTA scheme are dependent on the use of a large-enough local grid. Hence, the main benefit of the MUSTA scheme is its simplicity, rather than a speed-up of the calculations. A second-order extension based on a semi-discrete MUSCL scheme was shown to provide enhanced results.

The multiphase characteristic-based boundary-condition method of Olsen (2004) was shown to be workable for transient problems, and the faucet case was employed as an example.

1.5 Structure of the thesis

Even though this thesis appears as a monograph, some of the chapters are self-contained. In particular, this is true for Chapter 5, co-authored by Mikael Papin (Munkejord and Papin, 2005), and Chapter 7, co-authored by Tore Flåtten (Flåtten and Munkejord, 2006), and partly for Chapter 8, co-authored by Tore Flåtten and Steinar Evje (Munkejord *et al.*, 2006). The interested reader may read them first, if desired.

Chapter 2 treats basic multiphase flow models. The volume-averaging and ensemble-averaging approaches are reviewed in some detail. Thereafter, the employed model formulations are presented. Chapters 3–6 concern the two-fluid model, while Chapters 7–8 are about the drift-flux model.

In Chapter 3, two numerical methods for solving the two-fluid model are discussed. Both are Roe-type methods, but one method employs pressure relaxation, and the other does not. Basic testing of the general numerical algorithm is performed.

Chapter 4 provides some tests and discussion of the flux-limiter centred (FLIC) scheme.

The discrete-equation multiphase model is presented in Chapter 5. Different models for the interfacial pressure are discussed, and a comparison with the Roe-type method is provided.

Some results regarding the use of characteristic-based boundary conditions using PID controllers for transient problems are given in Chapter 6.

In Chapter 7, a Roe solver for the drift-flux model is derived and discussed.

Chapter 8 explores the multi-stage (MUSTA) centred-scheme approach for the drift-flux model, discusses the involved parameters describing the local grid, and compares the scheme to the Roe and FORCE schemes.

Chapter 9 draws the main conclusions of this thesis and gives suggestions for further work.

2 Basic multiphase flow models

> **Exception,** *n.* A thing which takes the liberty to differ from other things of its class, as an honest man, a truthful woman, etc. 'The exception proves the rule' is an expression constantly upon the lips of the ignorant, who parrot it from one another with never a thought of its absurdity. In the Latin, *'Exceptio probat regulam'* means that the exception *tests* the rule, puts it to the proof, not *confirms* it. The malefactor who drew the meaning from this excellent dictum and substituted a contrary one of his own exerted an evil power which appears to be immortal.
>
> *The Devil's Dictionary*
> Ambrose Bierce

This chapter reviews the derivation of the multifluid model, which is achieved by averaging the single-phase equations. Several averaging procedures can be employed, most notably time, volume and ensemble averaging. The two former techniques are convenient in that time and volume-averaged quantities may easily be observed in the laboratory. However, the latter technique seems to be more general. Here we review the volume-averaging and the ensemble-averaging approaches in some detail. As will be seen, the resulting model has the same form in both cases.

Several authors have proposed to repeatedly apply one or more of the averaging processes on the governing equations, particularly for the purpose of turbulence modelling. This approach leads to correlations whose interpretation is less than straightforward, and it will not be considered here.

In the following, we do not attempt to provide a full literature review regarding the various developments of multiphase models, but rather to cite expositions that were found useful or instructive in the present work.

At the end of the chapter, the simplifying assumptions employed in the present work will be outlined, and some comments regarding well-posedness will be given.

2.1 Basic equations

This section briefly reviews the balance equations for single-phase flow, and for a phase interface.

2.1.1 Equations for a pure phase

The balance equations for a pure phase are well known, and are therefore stated here without derivation. The continuity equation[1] is

$$\frac{\partial}{\partial t}\rho_k + \boldsymbol{\nabla}\cdot(\rho_k \boldsymbol{u}_k) = 0, \tag{2.1}$$

and the momentum equation is

$$\frac{\partial}{\partial t}(\rho_k \boldsymbol{u}_k) + \boldsymbol{\nabla}\cdot(\rho_k \boldsymbol{u}_k \otimes \boldsymbol{u}_k) = -\boldsymbol{\nabla} p_k + \boldsymbol{\nabla}\cdot\boldsymbol{\tau}_k + \rho_k \boldsymbol{b}, \tag{2.2}$$

where $\boldsymbol{u}_k \otimes \boldsymbol{u}_k = u_{i,k}u_{j,k}\boldsymbol{e}_i \otimes \boldsymbol{e}_j$ is the tensor product between the velocities. Henceforth, we drop the tensor multiplication sign, that is, the tensor product will be denoted as for instance $\boldsymbol{u}_k\boldsymbol{u}_k$. For simplicity, the energy equation has not been considered in this work (see also Section 2.5.2 on page 29).

2.1.2 Interface relations

To derive interface relations for multiphase flow, it is necessary to consider a control volume with more than one phase inside. Such a control volume and the interacting phases are shown in Figure 2.1 on the next page. V_k is the volume of phase k inside the control volume $\mathcal{V}$, and V is the total volume of $\mathcal{V}$. The control surface $\mathcal{A}_k$ has an area A_k and is the interface between phases k and f inside $\mathcal{V}$. Generally, other phases l might also be present, but they are not considered when discussing the interaction between the phases k and f.

The mass and momentum balances at the interface between phases k and f are represented by

$$\rho_k(\boldsymbol{u}_k - \boldsymbol{u}_\mathrm{i})\cdot\boldsymbol{n}_k + \rho_f(\boldsymbol{u}_f - \boldsymbol{u}_\mathrm{i})\cdot\boldsymbol{n}_f = 0, \tag{2.3}$$

[1] In the following, Einstein's summation rule is not to be applied to the indices k and f, which are being used to denote phases.

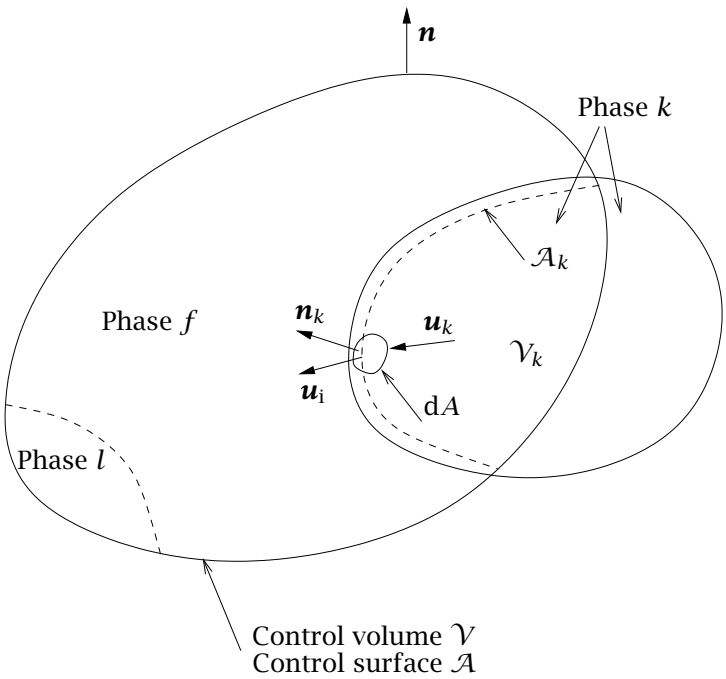

Figure 2.1: Control volume and interacting phases.

and

$$\underbrace{-\nabla_s\sigma}_{\text{(i)}} + \underbrace{2\sigma H_s \boldsymbol{n}}_{\text{(ii)}} - \underbrace{\rho_k \boldsymbol{u}_k(\boldsymbol{u}_k - \boldsymbol{u}_i)\cdot\boldsymbol{n}_k}_{\text{(iii)}} - \underbrace{\rho_f \boldsymbol{u}_f(\boldsymbol{u}_f - \boldsymbol{u}_i)\cdot\boldsymbol{n}_f}_{\text{(iv)}} + \underbrace{(-\boldsymbol{I}p_k + \boldsymbol{\tau}_k)\cdot\boldsymbol{n}_k}_{\text{(v)}} + \underbrace{(-\boldsymbol{I}p_f + \boldsymbol{\tau}_f)\cdot\boldsymbol{n}_f}_{\text{(vi)}} = 0, \quad (2.4)$$

where $\boldsymbol{n}_k$ is the outward unit normal vector from phase k, H_s^{-1} is the mean radius of curvature along $\boldsymbol{n}_k$, σ is the coefficient of surface tension, ∇_s is the surface gradient operator, and $\boldsymbol{I}$ is the unitary tensor. The interfacial velocity is given by $\boldsymbol{u}_i$ and H_s is positive when the associated radius of curvature is pointing outward. The effect of change in the mean curvature is ignored.

The equation (2.3) plainly states that the mass transfer from phase k to phase f must be equal in size and opposite to the mass transfer from phase f to phase k. If $\boldsymbol{u}_k = \boldsymbol{u}_i = \boldsymbol{u}_f$, or if $(\boldsymbol{u}_k - \boldsymbol{u}_i)\cdot\boldsymbol{n}_k = 0$ at the interface, then no mass transfer takes place.

The momentum balance (2.4) is written in force per length (N/m) units, where

term (i) is due to changes in the surface tension along the interface, for example due to temperature or composition gradients[2],

term (ii) is because the radius of curvature will cause the surface tension to yield a resultant force normal to the interface,

term (iii) is due to mass transfer from phase k to phase f,

term (iv) is due to mass transfer from phase f to phase k,

term (v) is due to pressure and stresses in phase k, and

term (vi) is due to pressure and stresses in phase f.

When no mass transfer takes place, the terms (iii) and (iv) will disappear from the interface momentum equation (2.4), because $(\boldsymbol{u}_k - \boldsymbol{u}_\mathrm{i}) \cdot \boldsymbol{n}_k = 0$ at the interface. That is, for a flow without mass transfer, the surface-tension forces are balanced by pressure and stress forces. If furthermore the surface tension is negligible, then the pressure and stress of each phase are equal at the interface.

The computational domain has been divided into small control volumes $\mathcal{V}$ according to Figure 2.1 on the preceding page. The finest level of detail of the computation is the control-volume level. The basic equations, however, are written on a microscopical level. Therefore it is necessary to introduce a proper averaging technique, something which will be done in the following section.

2.2 Averaging approaches

The fluid flow in engineering applications varies over so many orders of magnitude in both length and time scales, that it is computationally intractable to directly solve the full balance equations (2.1)–(2.2), except in detail studies. An additional problem in multiphase flow is that in the general case, the configuration and location of the interfaces cannot be rigorously defined even initially. Therefore, a proper averaging procedure is needed.

Averaging may be seen as a sort of low-pass filtering which is employed to reduce the amount of computational power required to solve the equations. It is necessary to introduce models to account for the physics behind what happens on the scales which are 'filtered away'. A model can be defined as a simplified view of a physical phenomenon (physical model) *and* mathematical expressions describing this view (mathematical model) (see Ertesvåg, 2000, pages 31–33 or Aris, 1962, page 1 ff.). In this respect, no model is also a model.

[2] That is, $\sigma = \sigma(p, T, n_i)$, where n_i indicates the material components involved.

The multifluid model can be deduced from the basic equations of single-phase flow. Several approaches have been used, for instance temporal averaging, volume averaging, and ensemble averaging (see e.g. Ishii, 1975; Soo, 1989; Drew and Passman, 1999). It is also possible to derive the multifluid model without averaging, but by introducing distributions, i.e., generalized functions (Kataoka, 1986). The different deductions lead to equations having the same form. However, the form of the unclosed terms and the interpretation of the variables in the equations may differ.

2.2.1 Time versus volume averaging

In his two-fluid model, Ishii (1975, page 61) applied time averaging to the basic balance equations. He argued that since time averaging has proven useful in single-phase turbulent flow analysis, it is natural and logical also to apply time averaging to two-phase flow. Ishii identified two main consequences of time averaging, namely

1. to smooth out turbulent fluctuations in the same sense as in single-phase flow, and

2. to bring two phases, which are alternately occupying a volume element, into two continua simultaneously existing at the same point with a properly defined expectation for each phase.

Soo (1989, page 49), on the other hand, maintained that volume averaging is convenient in expressing dynamic phases in terms of volume fractions, while an a priori time averaging yields fraction residence times of phases. He further stated that dynamic and thermodynamic properties of a mixture are not cumulative with fraction residence time, but with volume fractions, and that the fraction residence time is equal to the volume fraction only in the instance of one-dimensional uniform motion in a mixture. Therefore, the time and volume averaging operations are not commutative. Soo recommended to carry out time averaging after volume averaging to account for the high frequency fluctuations retained by instantaneous volume averaging.

The above-cited authors do not seem to have thoroughly discussed whether different averaging techniques may or may not express the same thing.

2.2.2 Ensemble averaging

The ensemble averaging is defined and discussed by Drew and Passman (1999, Chapter 9). The ensemble average allows for the interpretation of the phe-

nomena in terms of the repeatability of the multiphase[3] flows. The ensemble corresponding to a given motion can be thought of as a very large set of realizations, with observable variations. The initial conditions and calculated fields are interpreted as expected values. Drew and Passman point out several implications of using the ensemble average as the basis for the theory of multiphase flows:

1. In situations where time and / or volume averaging are appropriate, these averages can be used as 'samples' of the ensemble.

2. Ensemble averaging does not require that a control volume contain a large number of particles in any given realization. (See (2.15).)

3. An elementary concept of averaging involves adding the observed values and dividing by the number of observations. From the point of view of ensemble averaging, this represents sampling the distribution implicit in the description of the ensemble a finite number of times. The difficulty is in describing the set of observations, for instance; if the initial position of the bubbles is changed, they may coalesce, something which may be a fundamental variation.

4. The ensemble-average view of a physical event allows for an interpretation that all realizations are only approximations of the ideal. Consider for instance a system where the variability is contained in the locations of the particles or bubbles at the initial instant. If the observer were able to control the initial locations more precisely, the ensemble could be viewed as smaller. For the flow of a single particle, whose initial position was exactly determined, in a fluid flow without fluctuations, the ensemble would contain only one realization, and the 'averaging' would lead to the exact equations and jump conditions.

2.3 Volume-averaged equations

In this section, we review the volume-averaging approach as presented by Soo (1989, 1990). Much of the material presented here is from Munkejord *et al.* (2000).

[3] Drew and Passman prefer the term 'multicomponent'.

2.3.1 Volume averaging of a phase in a mixture

The volume averaging, when applied to any scalar, vector or tensor, ψ_k, associated with phase k, is defined by

$$\langle \psi_k \rangle = \frac{1}{V} \int_{\mathcal{V}_k} \psi_k \, \mathrm{d}V, \tag{2.5}$$

when averaged over the volume V, and when averaged over V_k, the result is the intrinsic average:

$$^{\mathrm{i}}\langle \psi_k \rangle = \frac{1}{V_k} \int_{\mathcal{V}_k} \psi_k \, \mathrm{d}V. \tag{2.6}$$

That is, $\langle \psi_k \rangle$ is averaged over the whole control volume $\mathcal{V}$, whereas $^{\mathrm{i}}\langle \psi_k \rangle$ is averaged only over the part of the control volume where phase k is present, $\mathcal{V}_k$.

To achieve a mathematically more rigorous fundament, the definition of volume averaging in equation (2.5) may instead be written as

$$\langle \psi_k \rangle = \frac{1}{V} \int_{\mathcal{V}} \psi_k \chi_k \, \mathrm{d}V. \tag{2.7}$$

Now the integration is performed over the whole control volume $\mathcal{V}$. The factor χ_k is defined as 1 inside $\mathcal{V}_k$ and as 0 outside $\mathcal{V}_k$. Analogously we get for the intrinsic average in equation (2.6):

$$^{\mathrm{i}}\langle \psi_k \rangle = \frac{1}{V_k} \int_{\mathcal{V}} \psi_k \chi_k \, \mathrm{d}V. \tag{2.8}$$

When the averaging relations (2.5) and (2.6) are applied to a specific quantity such as density, we have:

$$\langle \rho_k \rangle = \frac{1}{V} \int_{\mathcal{V}_k} \rho_k \, \mathrm{d}V = \alpha_k \overline{\rho}_k, \tag{2.9}$$

and

$$^{\mathrm{i}}\langle \rho_k \rangle = \frac{1}{V_k} \int_{\mathcal{V}_k} \rho_k \, \mathrm{d}V = \overline{\rho}_k. \tag{2.10}$$

Herein the volume fraction of phase k is defined as $\alpha_k = V_k/V$. The latter equalities are for uniform material density $\overline{\rho}_k$ of phase k.

Some points are worth noting (Soo, 1989, page 51):

1. Intrinsic averaging gives rise to quantities inside $\mathcal{V}_k$.

2. Volume averaging will spread phase k over the whole volume $\mathcal{V}$, superposing on phase f, which is correspondingly averaged in the same manner. So, for instance, the density $\langle \rho_k \rangle$ is averaged over $\mathcal{V}$ and is equal to ${\alpha_k}^{\mathrm{i}}\langle \rho_k \rangle$.

3. Volume averaging can only be applied to quantities per volume or area. These include density, momentum per unit volume, energy per unit volume, and gradients of stresses and fluxes for ψ_k in the equations (2.5) and (2.6). Therefore, for instance, the intrinsic average of the phase velocity is given by

$$ {}^{\mathrm{i}}\langle \boldsymbol{u}_k \rangle = \frac{1}{{}^{\mathrm{i}}\langle \rho_k \rangle V_k} \int_{\mathcal{V}_k} \rho_k \boldsymbol{u}_k \, \mathrm{d}V = \frac{1}{\langle \rho_k \rangle V} \int_{\mathcal{V}_k} \rho_k \boldsymbol{u}_k \, \mathrm{d}V. \tag{2.11} $$

   One sees that only ${}^{\mathrm{i}}\langle \boldsymbol{u}_k \rangle$ and $\boldsymbol{\nabla} \cdot {}^{\mathrm{i}}\langle \boldsymbol{u}_k \rangle$ are meaningful.

4. Stresses and fluxes in a formulation can be expressed as $\langle \psi_k \rangle = {\alpha_k}^{\mathrm{i}}\langle \psi_k \rangle$; the physical meaning is represented in the 'volume average' where all interactions are represented.

$\langle \boldsymbol{\tau}_k \rangle$, the viscous stress, is not necessarily contributed by the viscous stress inside phase k. It may represent the resistance to transfer of momentum by bodily displacement of one phase through another. That is, $\langle \boldsymbol{\tau}_k \rangle$ has two contributions; one from within the phase and one from its surface. The same applies to $\langle p_k \rangle$.

In the derivation of the multifluid model, relations are needed for the volume average of derivatives. The volume average of the divergence and gradient terms are rewritten using the Slattery averaging theorem (Slattery, 1967; Whitaker, 1969):

$$ \langle \boldsymbol{\nabla} \psi_k \rangle \equiv \frac{1}{V} \int_{\mathcal{V}_k} \boldsymbol{\nabla} \psi_k \, \mathrm{d}V = \boldsymbol{\nabla} \langle \psi_k \rangle + \frac{1}{V} \int_{\mathcal{A}_k} \psi_k \boldsymbol{n}_k \, \mathrm{d}A, \tag{2.12} $$

or

$$ \langle \boldsymbol{\nabla} \cdot \boldsymbol{\psi}_k \rangle = \boldsymbol{\nabla} \cdot \langle \boldsymbol{\psi}_k \rangle + \frac{1}{V} \int_{\mathcal{A}_k} \boldsymbol{\psi}_k \cdot \boldsymbol{n}_k \, \mathrm{d}A, \tag{2.13} $$

while an expression for the volume average of time derivatives is found by employing the Reynolds transport theorem:

$$ \left\langle \frac{\partial}{\partial t} \psi_k \right\rangle = \frac{\partial}{\partial t} \langle \psi_k \rangle - \frac{1}{V} \int_{\mathcal{A}_k} \psi_k \boldsymbol{u}_{\mathrm{i}} \cdot \boldsymbol{n}_k \, \mathrm{d}A. \tag{2.14} $$

Herein, $\boldsymbol{u}_{\mathrm{i}} \cdot \boldsymbol{n}_k$ is the speed of displacement of the interface.

The volume-averaging approach is subject to the restriction that

$$\begin{aligned}\{&\text{characteristic lengths of phases or pores}\}\\ &\ll \{\text{characteristic length of averaging volume } \mathcal{V}\}\\ &\ll \{\text{characteristic length of physical system}\}.\end{aligned} \tag{2.15}$$

Therefore, the control volume $\mathcal{V}$ under consideration cannot be arbitrarily small or become infinitesimal. Furthermore, the control volume $\mathcal{V}$ needs to be much larger than the size of the phases or pores, so that a small translation of the control volume will not influence the magnitude of the averaged variables $\langle\psi_k\rangle$. Yet in order that the average be representative of the local variations, the control volume must be small, such that its characteristic dimension is smaller than that of the physical system under consideration.

Inserting $\psi_k = 1$ in (2.5) yields

$$\langle 1\rangle = \frac{1}{V}V_k = \alpha_k. \tag{2.16}$$

Using (2.16) in (2.14) then gives

$$\frac{\partial}{\partial t}\alpha_k = \frac{1}{V}\int_{\mathcal{A}_k} \boldsymbol{u}_\mathrm{i}\cdot\boldsymbol{n}_k\,\mathrm{d}A, \tag{2.17}$$

and analogously for the equation (2.12):

$$\boldsymbol{\nabla}\alpha_k = -\frac{1}{V}\int_{\mathcal{A}_k} \boldsymbol{n}_k\,\mathrm{d}A. \tag{2.18}$$

2.3.2 Volume-averaged balance equations

Continuity

As the average of a sum equals the sum of averages, the averaging relations (2.12)–(2.14) can be applied term-wise to the continuity equation (2.1):

$$\frac{\partial}{\partial t}\langle\rho_k\rangle - \frac{1}{V}\int_{\mathcal{A}_k}\rho_k\boldsymbol{u}_\mathrm{i}\cdot\boldsymbol{n}_k\,\mathrm{d}A + \boldsymbol{\nabla}\cdot\langle\rho_k\boldsymbol{u}_k\rangle + \frac{1}{V}\int_{\mathcal{A}_k}\rho_k\boldsymbol{u}_k\cdot\boldsymbol{n}_k\,\mathrm{d}A = 0, \tag{2.19}$$

so that

$$\frac{\partial}{\partial t}\langle\rho_k\rangle + \boldsymbol{\nabla}\cdot\langle\rho_k\boldsymbol{u}_k\rangle = -\frac{1}{V}\int_{\mathcal{A}_k}\rho_k(\boldsymbol{u}_k-\boldsymbol{u}_\mathrm{i})\cdot\boldsymbol{n}_k\,\mathrm{d}A = \Gamma_k, \tag{2.20}$$

where Γ_k is the rate of generation of phase k per unit volume of $\mathcal{V}$ as the interface displaces outward relatively to phase k.

Momentum

Similarly to what was done in the preceding subsection, applying the averaging relations to the momentum equation (2.2) yields:

$$\frac{\partial}{\partial t}\langle \rho_k \boldsymbol{u}_k \rangle + \boldsymbol{\nabla} \cdot \langle \rho_k \boldsymbol{u}_k \boldsymbol{u}_k \rangle = -\boldsymbol{\nabla} \langle p_k \rangle + \boldsymbol{\nabla} \cdot \langle \boldsymbol{\tau}_k \rangle + \langle \rho_k \rangle \boldsymbol{b} + \frac{1}{V}\int_{\mathcal{A}_k} (-p_k \boldsymbol{n}_k + \boldsymbol{\tau}_k \cdot \boldsymbol{n}_k)\,\mathrm{d}A - \frac{1}{V}\int_{\mathcal{A}_k} \rho_k \boldsymbol{u}_k (\boldsymbol{u}_k - \boldsymbol{u}_\mathrm{i}) \cdot \boldsymbol{n}_k \,\mathrm{d}A, \quad (2.21)$$

where the force field per unit mass, $\boldsymbol{b}$, is assumed to be constant in $\mathcal{V}$. The last two terms are transfer integrals, and it is necessary to give them a careful physical interpretation. They account for the transfer of pressure, viscous stresses and inertia forces across the interface per unit volume.

In principle, the equations (2.20) and (2.21) (together with the energy equation) are the basic integro-differential equations of multiphase flow.

The transfer integral due to pressure and viscous stresses needs to be modelled. However, the pressure p_k on the interface is generally unknown. It is therefore convenient to assume that it may be written as the sum of the mean pressure in the control volume, and a local variation:

$$p_k = {}^\mathrm{i}\langle p_k \rangle + \delta p_k. \quad (2.22)$$

A similar splitting was made by Drew and Passman (1999, Section 11.3.2), see also Section 2.4.5 on page 27.

Insert (2.22) and (2.18) into the pressure-part of the transfer integral of the equation (2.21):

$$\frac{1}{V}\int_{\mathcal{A}_k} -p_k \boldsymbol{I} \cdot \boldsymbol{n}_k \,\mathrm{d}A = {}^\mathrm{i}\langle p_k \rangle \boldsymbol{\nabla} \alpha_k - \frac{1}{V}\int_{\mathcal{A}_k} \delta p_k \boldsymbol{n}_k \,\mathrm{d}A. \quad (2.23)$$

For the pressure-gradient term of the equation (2.21), we have:

$$-\boldsymbol{\nabla} \langle p_k \rangle = -\alpha_k \boldsymbol{\nabla}^\mathrm{i}\langle p_k \rangle - {}^\mathrm{i}\langle p_k \rangle \boldsymbol{\nabla} \alpha_k, \quad (2.24)$$

and the ${}^\mathrm{i}\langle p_k \rangle \boldsymbol{\nabla} \alpha_k$ term from the pressure-gradient term and from the transfer integral are seen to cancel. Therefore, the volume-averaged momentum equation may be written as

$$\frac{\partial}{\partial t}\langle \rho_k \boldsymbol{u}_k \rangle + \boldsymbol{\nabla} \cdot \langle \rho_k \boldsymbol{u}_k \boldsymbol{u}_k \rangle = -\alpha_k \boldsymbol{\nabla}^\mathrm{i}\langle p_k \rangle + \boldsymbol{\nabla} \cdot \langle \boldsymbol{\tau}_k \rangle + \langle \rho_k \rangle \boldsymbol{b} + \frac{1}{V}\int_{\mathcal{A}_k} (-\delta p_k \boldsymbol{I} + \boldsymbol{\tau}_k) \cdot \boldsymbol{n}_k \,\mathrm{d}A - \frac{1}{V}\int_{\mathcal{A}_k} \rho_k \boldsymbol{u}_k (\boldsymbol{u}_k - \boldsymbol{u}_\mathrm{i}) \cdot \boldsymbol{n}_k \,\mathrm{d}A. \quad (2.25)$$

Interface balances

The volume-averaged interface balance equations are arrived at by integrating equations (2.3) and (2.4) over the interface $\mathcal{A}_k$ and dividing by the control volume. The mass balance is given by:

$$\Gamma_k = -\frac{1}{V}\int_{\mathcal{A}_k} \rho_k(\boldsymbol{u}_k - \boldsymbol{u}_\mathrm{i})\cdot\boldsymbol{n}_k \,\mathrm{d}A = \frac{1}{V}\int_{\mathcal{A}_k} \rho_f(\boldsymbol{u}_f - \boldsymbol{u}_\mathrm{i})\cdot\boldsymbol{n}_f \,\mathrm{d}A = -\Gamma_f. \quad (2.26)$$

Note that the first and second equalities constitute two independent relations because Γ_k is given by the physical and phenomenological relations at the interface.

The (linear) momentum balance is given by:

$$\begin{aligned}\frac{1}{V}\int_{\mathcal{A}_k} &(-\boldsymbol{\nabla}_s\sigma + 2\sigma H_s\boldsymbol{n})\,\mathrm{d}A \\ &- \frac{1}{V}\int_{\mathcal{A}_k} \rho_k\boldsymbol{u}_k(\boldsymbol{u}_k - \boldsymbol{u}_\mathrm{i})\cdot\boldsymbol{n}_k \,\mathrm{d}A - \frac{1}{V}\int_{\mathcal{A}_k} \rho_f\boldsymbol{u}_f(\boldsymbol{u}_f - \boldsymbol{u}_\mathrm{i})\cdot\boldsymbol{n}_f \,\mathrm{d}A \\ &+ \frac{1}{V}\int_{\mathcal{A}_k} (-\boldsymbol{I}p_k + \boldsymbol{\tau}_k)\cdot\boldsymbol{n}_k \,\mathrm{d}A + \frac{1}{V}\int_{\mathcal{A}_k} (-\boldsymbol{I}p_f + \boldsymbol{\tau}_f)\cdot\boldsymbol{n}_f \,\mathrm{d}A = 0. \quad (2.27)\end{aligned}$$

For bubbles and droplets, the first integral gives the capillary pressure (denoted by subscript c) difference:

$$\frac{1}{V}\int_{\mathcal{A}_k} (-\boldsymbol{\nabla}_s\sigma + 2\sigma H_s\boldsymbol{n})\,\mathrm{d}A = \frac{1}{V}\int_{\mathcal{A}_k} (p_{\mathrm{c},k} - p_{\mathrm{c},f})\,\mathrm{d}A. \quad (2.28)$$

The equations in the present section include averages of products as well as local values in the interface transfer integrals. The configurations of the interface and its motion are given by $\boldsymbol{u}_\mathrm{i}$, $\boldsymbol{n}_k$, and $\mathcal{A}_k$. A solution of equations (2.20) and (2.21) calls for expressing averages of products in terms of products of averages and to express the integrals in terms of averaged dependent variables by introducing proper constitutive relations.

Recall the expression for the intrinsic average of the phase velocity from equation (2.11) on page 16. Analogously, we may now write for the volume averaged rate of change of momentum flux of phase k per unit area:

$$\begin{aligned}\langle\rho_k\boldsymbol{u}_k\boldsymbol{u}_k\rangle \equiv \frac{1}{V}\int_{V_k} \rho_k\boldsymbol{u}_k\boldsymbol{u}_k \,\mathrm{d}V &= \langle\rho_k\rangle \frac{1}{{}^\mathrm{i}\langle\rho_k\rangle\, V_k}\int_{V_k} \rho_k\boldsymbol{u}_k\boldsymbol{u}_k \,\mathrm{d}V \\ &= \langle\rho_k\rangle\, {}^\mathrm{i}\langle\boldsymbol{u}_k\boldsymbol{u}_k\rangle = \alpha_k{}^\mathrm{i}\langle\rho_k\rangle\, {}^\mathrm{i}\langle\boldsymbol{u}_k\boldsymbol{u}_k\rangle\,. \quad (2.29)\end{aligned}$$

In the second and in the last equality, we have used that

$$\alpha_k = \frac{V_k}{V} = \frac{\langle\rho_k\rangle}{{}^\mathrm{i}\langle\rho_k\rangle}. \quad (2.30)$$

To express the average of the velocity product, ${}^{\mathrm{i}}\langle \boldsymbol{u}_k \boldsymbol{u}_k \rangle$, as a product of averages, it is necessary to introduce modelling assumptions.

2.4 Ensemble-averaged equations

In this section, we briefly review the ensemble-averaging approach as presented by Drew and Passman (1999).

The starting point for the derivation of the ensemble-averaged equations is, of course, the same single-phase balance equations (2.1)–(2.2) and jump conditions (2.3)–(2.4) as before (see also Drew, 1983).

2.4.1 Ensemble-average basics

Definition

Drew and Passman (1999, Chapter 9) define an *ensemble* as a set of motions 'possible' in the system. A realization of the system is denoted by μ, and the set of all realizations μ is the ensemble, E.

The ensemble average of ψ is defined by

$$\mathcal{E}\left(\psi(\boldsymbol{x},t)\right) = \int_E \psi(\boldsymbol{x},t;\mu)\,\mathrm{d}m(\mu), \tag{2.31}$$

where $\mathrm{d}m$ is the density for the measure (probability) on the set of all processes E. Further details and definitions can be found in Drew and Passman (1999).

Reynolds rules

Let c_1 and c_2 be constants, and ψ_1 and ψ_2 be fields. Drew and Passman (1999) show that the linearity property

$$\mathcal{E}\left(c_1\psi_1 + c_2\psi_2\right) = c_1\mathcal{E}\left(\psi_1\right) + c_2\mathcal{E}\left(\psi_2\right), \tag{2.32}$$

hold if ψ_1 and ψ_2 are realizations in the same ensemble E, or if ψ_1 and ψ_2 are realizations in different ensembles E_1 and E_2, respectively. Furthermore,

$$\mathcal{E}\left(\mathcal{E}\left(\psi_1\right)\psi_2\right) = \mathcal{E}\left(\psi_1\right)\mathcal{E}\left(\psi_2\right), \tag{2.33}$$

if ψ_1 and ψ_2 are realizations in the same ensemble E. Hence the usual 'Reynolds rules' of averaging apply to the ensemble averaging as well.

Derivatives of generalized functions

In multiphase flows, the fields may be discontinuous. Therefore, $\partial\psi/\partial t$ and $\nabla\psi$ are generalized functions, and they are defined by

$$\int_\Omega \phi(\boldsymbol{x},t)\frac{\partial\psi(\boldsymbol{x},t)}{\partial t}\,\mathrm{d}V\,\mathrm{d}t = -\int_\Omega \frac{\partial\phi(\boldsymbol{x},t)}{\partial t}\psi(\boldsymbol{x},t)\,\mathrm{d}V\,\mathrm{d}t, \tag{2.34}$$

and

$$\int_\Omega \phi(\boldsymbol{x},t)\nabla\psi(\boldsymbol{x},t)\,\mathrm{d}V\,\mathrm{d}t = -\int_\Omega \nabla\phi(\boldsymbol{x},t)\psi(\boldsymbol{x},t)\,\mathrm{d}V\,\mathrm{d}t, \tag{2.35}$$

where ϕ is a test function, that is, it has compact support[4] and derivatives to all orders. Ω is the space-time integration domain.

Characteristic function

Each phase k is separated theoretically by the phase-indicator function, or characteristic function, χ_k. It is defined by

$$\chi_k(\boldsymbol{x},t;\mu) = \begin{cases} 1 & \text{if } \boldsymbol{x}\in k \text{ in realization } \mu, \\ 0 & \text{otherwise.} \end{cases} \tag{2.36}$$

Interface delta function

The quantity $\nabla\chi_k$ will appear in the description of the multiphase flow, and it needs an interpretation. Let ϕ be a test function. Then we have

$$\int_\Omega \phi(\boldsymbol{x},t)\nabla\chi_k(\boldsymbol{x},t)\,\mathrm{d}V\,\mathrm{d}t = -\int_\Omega \nabla\phi(\boldsymbol{x},t)\chi_k(\boldsymbol{x},t)\,\mathrm{d}V\,\mathrm{d}t \tag{2.37}$$

$$= -\int_{\Omega_k} \nabla\phi(\boldsymbol{x},t)\,\mathrm{d}V\,\mathrm{d}t \tag{2.38}$$

and by using the divergence theorem, we get

$$= -\int_{\partial\Omega_k} \boldsymbol{n}_k\phi(\boldsymbol{x},t)\,\mathrm{d}A\,\mathrm{d}t \tag{2.39}$$

$$= -\int_\Omega \boldsymbol{n}_k\delta(\boldsymbol{x}-\boldsymbol{x}_\mathrm{i},t)\phi(\boldsymbol{x},t)\,\mathrm{d}V\,\mathrm{d}t. \tag{2.40}$$

[4] $\phi(\boldsymbol{x},t)$ has compact support if it is identically zero outside some bounded region in space and time, as well as on the boundary.

Herein, Ω_k is the intersection of Ω with k, and $\partial\Omega_k$ denotes the phase interface, $\boldsymbol{n}_k$ is the unit normal to it in the direction exterior to phase k, $\boldsymbol{x}_\mathrm{i}$ is the position of the interface, and δ is the Dirac delta function. The last equation shows that

$$\boldsymbol{\nabla}\chi_k = -\boldsymbol{n}_k\delta(\boldsymbol{x}-\boldsymbol{x}_\mathrm{i},t). \tag{2.41}$$

Topological equation

In the averaging process, the result

$$\frac{\partial\chi_k}{\partial t} + \boldsymbol{u}_\mathrm{i}\cdot\boldsymbol{\nabla}\chi_k = 0 \tag{2.42}$$

will be used. It can be derived in two ways. The first and less rigorous way is simply to claim that it is logical that the phase-indicator function be advected with the interface velocity. The second way is to use results for generalized functions: Let ϕ be a test function. Then

$$\begin{aligned}\int_\Omega \phi\frac{\partial\chi_k}{\partial t}\,\mathrm{d}V\,\mathrm{d}t &= -\int_\Omega \frac{\partial\phi}{\partial t}\chi_k\,\mathrm{d}V\,\mathrm{d}t,\\ \int_\Omega \phi\boldsymbol{\nabla}\chi_k\,\mathrm{d}V\,\mathrm{d}t &= -\int_\Omega \boldsymbol{\nabla}\phi\chi_k\,\mathrm{d}V\,\mathrm{d}t.\end{aligned} \tag{2.43}$$

Thus

$$\begin{aligned}\int_\Omega \phi\Big(\frac{\partial\chi_k}{\partial t} + \boldsymbol{u}_\mathrm{i}\cdot\boldsymbol{\nabla}\chi_k\Big)\,\mathrm{d}V\,\mathrm{d}t &= \int_\Omega\Big(\phi\frac{\partial\chi_k}{\partial t} + \phi\boldsymbol{\nabla}(\boldsymbol{u}_\mathrm{i}\boldsymbol{\nabla}\chi_k) - \phi\chi_k\boldsymbol{\nabla}\cdot\boldsymbol{u}_\mathrm{i}\Big)\,\mathrm{d}V\,\mathrm{d}t\\ &\overset{(2.43)}{=} \int_\Omega\Big(-\chi_k\frac{\partial\phi}{\partial t} - \boldsymbol{u}_\mathrm{i}\chi_k\boldsymbol{\nabla}\phi - \phi\chi_k\boldsymbol{\nabla}\cdot\boldsymbol{u}_\mathrm{i}\Big)\,\mathrm{d}V\,\mathrm{d}t\\ &= -\int_\Omega\Big(\frac{\partial\phi}{\partial t} + \boldsymbol{\nabla}\cdot(\phi\boldsymbol{u}_\mathrm{i})\Big)\chi_k\,\mathrm{d}V\,\mathrm{d}t.\end{aligned} \tag{2.44}$$

Consider the Reynolds transport theorem (see e.g. Wesseling, 2001, page 10)

$$\frac{\mathrm{d}}{\mathrm{d}t}\int_{\mathcal{V}(t)}\phi\,\mathrm{d}V = \int_{\mathcal{V}(t)}\Big(\frac{\partial\phi}{\partial t} + \boldsymbol{\nabla}\cdot(\phi\boldsymbol{u})\Big)\,\mathrm{d}V, \tag{2.45}$$

where $\mathcal{V}(t)$ is a material volume. This gives

$$\begin{aligned}-\int_\Omega\Big(\frac{\partial\phi}{\partial t} + \boldsymbol{\nabla}\cdot(\phi\boldsymbol{u}_\mathrm{i})\Big)\chi_k\,\mathrm{d}V\,\mathrm{d}t &= -\int_0^\infty\int_{\mathcal{V}_k(t)}\Big(\frac{\partial\phi}{\partial t} + \boldsymbol{\nabla}\cdot(\phi\boldsymbol{u}_\mathrm{i})\Big)\,\mathrm{d}V\,\mathrm{d}t\\ &= -\int_0^\infty\frac{\mathrm{d}}{\mathrm{d}t}\int_{\mathcal{V}_k(t)}\phi\,\mathrm{d}V\,\mathrm{d}t\\ &= -\Big[\int_{\mathcal{V}_k(t)}\phi\,\mathrm{d}V\Big]_{t=0}^{t=\infty} = 0,\end{aligned} \tag{2.46}$$

since ϕ has compact support. Hence the integrand in (2.46) and in (2.44) is zero, and (2.42), referred to as the *topological equation*, is valid. The left-hand side is the material derivative of χ_k following the interface. For a point that is not on the interface, either $\chi_k = 1$ or $\chi_k = 0$, and the partial derivatives both vanish, so that the left-hand side of the topological equation vanishes. For a point on the interface, moving at the interface velocity, the jump in χ_k is constant, so that its material derivative following the interface vanishes.

Gauss and Leibniz rules

If ψ is sufficiently well behaved so that the limiting process of integration and differentiation can be interchanged, then the definition of the ensemble average gives that

$$\mathcal{E}\left(\frac{\partial \psi}{\partial t}\right) = \frac{\partial \mathcal{E}(\psi)}{\partial t}, \tag{2.47}$$

and

$$\mathcal{E}(\nabla \psi) = \nabla \mathcal{E}(\psi). \tag{2.48}$$

Further, we have, for example

$$\mathcal{E}\left(\int \psi \, \mathrm{d}V \, \mathrm{d}t\right) = \int \mathcal{E}(\psi) \, \mathrm{d}V \, \mathrm{d}t. \tag{2.49}$$

Now we will derive an expression for $\nabla(\chi_k \psi)$. By the definition of derivatives for generalized functions, we have

$$\int_\Omega \phi \nabla(\chi_k \psi) \, \mathrm{d}V \, \mathrm{d}t = -\int_\Omega \chi_k \nabla \phi \, \mathrm{d}V \, \mathrm{d}t = -\int_{\Omega_k} \nabla \phi \, \mathrm{d}V \, \mathrm{d}t. \tag{2.50}$$

Assuming that ψ is well behaved in Ω_k, and applying the divergence theorem, we get

$$\begin{aligned} -\int_{\Omega_k} \nabla \phi \, \mathrm{d}V \, \mathrm{d}t &= -\int_{\Omega_k} \nabla(\phi \psi) \, \mathrm{d}V \, \mathrm{d}t + \int_{\Omega_k} \phi \nabla \psi \, \mathrm{d}V \, \mathrm{d}t \\ &= -\oint_{\partial \Omega_k} \boldsymbol{n} \phi \psi_{\mathrm{i}k} \, \mathrm{d}A \, \mathrm{d}t + \int_\Omega \phi \chi_k \nabla \psi \, \mathrm{d}V \, \mathrm{d}t, \end{aligned} \tag{2.51}$$

where $\psi_{\mathrm{i}k}$ is the value of the function ψ evaluated on the phase k-side of the interface. Using the equation (2.39), we see that

$$\int_\Omega \phi \nabla(\chi_k \psi) \, \mathrm{d}V \, \mathrm{d}t = \int_\Omega \phi \psi_{\mathrm{i}k} \nabla \chi_k \, \mathrm{d}V \, \mathrm{d}t + \int_\Omega \phi \chi_k \nabla \psi \, \mathrm{d}V \, \mathrm{d}t, \tag{2.52}$$

and hence

$$\nabla(\chi_k \psi) = \chi_k \nabla \psi + \psi_{\mathrm{i}k} \nabla \chi_k. \tag{2.53}$$

Ensemble-averaging and applying (2.48) gives

$$\mathcal{E}\left(\chi_k \nabla \psi\right) = \nabla \mathcal{E}\left(\chi_k \psi\right) - \mathcal{E}\left(\psi_{ik} \nabla \chi_k\right), \tag{2.54}$$

which is called the *Gauss rule*. A similar sequence of calculation leads to

$$\mathcal{E}\left(\chi_k \frac{\partial \psi}{\partial t}\right) = \frac{\partial}{\partial t}\mathcal{E}\left(\chi_k \psi\right) - \mathcal{E}\left(\psi_{ik} \frac{\partial \chi_k}{\partial t}\right), \tag{2.55}$$

which is termed the *Leibniz rule*[5]. These equations are similar to (2.12)–(2.14) for volume averaging.

2.4.2 Ensemble-averaged balance equations

Armed with the ensemble-averaging arsenal from the previous subsection, we are ready to find the averaged balance equations. The single-phase balance equations can be written in the form

$$\frac{\partial}{\partial t}(\rho \boldsymbol{\psi}) + \nabla \cdot (\rho \boldsymbol{\psi} \boldsymbol{u}) = \nabla \cdot \boldsymbol{J} + \rho \boldsymbol{s}. \tag{2.56}$$

The continuity equation is recovered by setting $\boldsymbol{\psi} = 1$, $\boldsymbol{J} = \boldsymbol{0}$ and $\boldsymbol{s} = 0$, and the momentum equation is given by $\boldsymbol{\psi} = \boldsymbol{u}$, $\boldsymbol{J} = \boldsymbol{T} = -p\boldsymbol{I} + \boldsymbol{\tau}$ and $\boldsymbol{s} = \boldsymbol{b}$.

By using the product rule for derivatives, and by applying the topological equation (2.42) to $\partial \chi_k / \partial t$, we get

$$\chi_k \frac{\partial}{\partial t}(\rho \boldsymbol{\psi}) = \frac{\partial}{\partial t}(\chi_k \rho \boldsymbol{\psi}) - \rho \boldsymbol{\psi} \frac{\partial \chi_k}{\partial t} = \frac{\partial}{\partial t}(\chi_k \rho \boldsymbol{\psi}) + \rho \boldsymbol{\psi} \boldsymbol{u}_i \cdot \nabla \chi_k. \tag{2.57}$$

Multiply the equation (2.56) by χ_k. Using the above equation and the product rule for derivatives, we obtain

$$\frac{\partial}{\partial t}(\chi_k \rho \boldsymbol{\psi}) + \rho \boldsymbol{\psi} \boldsymbol{u}_i \cdot \nabla \chi_k + \nabla \cdot (\chi_k \rho \boldsymbol{\psi} \boldsymbol{u}) - \rho \boldsymbol{\psi} \boldsymbol{u} \cdot \nabla \chi_k - \nabla \cdot (\chi_k \boldsymbol{J}) + \boldsymbol{J} \nabla \cdot \chi_k - \chi_k \rho \boldsymbol{s} = \boldsymbol{0}. \tag{2.58}$$

Ensemble averaging and applying (2.47)–(2.48) gives

$$\frac{\partial}{\partial t}\mathcal{E}\left(\chi_k \rho \boldsymbol{\psi}\right) + \nabla \cdot \mathcal{E}\left(\chi_k \rho \boldsymbol{\psi} \boldsymbol{u}\right) - \nabla \cdot \mathcal{E}\left(\chi_k \boldsymbol{J}\right) - \mathcal{E}\left(\chi_k \rho \boldsymbol{s}\right) = \mathcal{E}\left(\left[\rho \boldsymbol{\psi}(\boldsymbol{u} - \boldsymbol{u}_i) - \boldsymbol{J}\right] \cdot \nabla \chi_k\right). \tag{2.59}$$

[5] The Leibniz rule in Drew and Passman is not the same as the Leibniz rule for differentiation of a definite integral which can found in calculus books.

Thus we obtain the ensemble-averaged continuity equation

$$\frac{\partial}{\partial t}\mathcal{E}\left(\chi_k\rho\right) + \boldsymbol{\nabla}\cdot\mathcal{E}\left(\chi_k\rho\boldsymbol{u}\right) = \mathcal{E}\left(\left[\rho(\boldsymbol{u}-\boldsymbol{u}_\mathrm{i})\right]\cdot\boldsymbol{\nabla}\chi_k\right), \tag{2.60}$$

and the ensemble-averaged momentum equation

$$\begin{aligned}\frac{\partial}{\partial t}\mathcal{E}\left(\chi_k\rho\boldsymbol{u}\right) + \boldsymbol{\nabla}\cdot\mathcal{E}\left(\chi_k\rho\boldsymbol{u}\boldsymbol{u}\right)\\ = \boldsymbol{\nabla}\cdot\mathcal{E}\left(\chi_k\boldsymbol{T}\right) + \mathcal{E}\left(\chi_k\rho\boldsymbol{b}\right) + \mathcal{E}\left(\left[\rho\boldsymbol{u}(\boldsymbol{u}-\boldsymbol{u}_\mathrm{i}) - \boldsymbol{T}\right]\cdot\boldsymbol{\nabla}\chi_k\right)\end{aligned} \tag{2.61}$$

which are comparable to the volume-averaged equations (2.20) and (2.21). The equations contain averages of products which need to be 'dissolved' before they can be employed for calculations.

2.4.3 Definition of average variables

As for the volume-average, some care has to be taken when defining the average variables. The average of the phase-indicator function is

$$\alpha_k = \mathcal{E}\left(\chi_k\right). \tag{2.62}$$

It is customarily called the volume-fraction, even for the ensemble-averaged equations. The correct interpretation is that α_k is the expected value of the ratio of the volume of phase k to the total volume, in the limit as the volume approaches zero. Following Drew and Passman (1999, Section 11.2), we employ weighted averages for the remaining variables: The average density is

$$\overline{\rho}_k = \frac{\mathcal{E}\left(\chi_k\rho\right)}{\alpha_k}, \tag{2.63}$$

the average velocity is

$$\overline{\boldsymbol{u}}_k = \frac{\mathcal{E}\left(\chi_k\rho\boldsymbol{u}\right)}{\alpha_k\overline{\rho}_k}, \tag{2.64}$$

the average stress tensor is

$$\overline{\boldsymbol{T}}_k = \frac{\mathcal{E}\left(\chi_k\boldsymbol{T}\right)}{\alpha_k}, \tag{2.65}$$

and the average body force is

$$\overline{\boldsymbol{b}}_k = \frac{\mathcal{E}\left(\chi_k\rho\boldsymbol{b}\right)}{\alpha_k\overline{\rho}_k}. \tag{2.66}$$

The transfer integrals appearing in the volume-averaged formulation have their ensemble-averaged analogue in the $\nabla\chi_k$ terms. In particular, the interfacial stress momentum source is

$$\boldsymbol{m}_k = -\mathcal{I}\left(\boldsymbol{T}\cdot\nabla\chi_k\right). \tag{2.67}$$

The mass source is

$$\Gamma_k = \mathcal{I}\left(\rho(\boldsymbol{u}-\boldsymbol{u}_\mathrm{i})\cdot\nabla\chi_k\right), \tag{2.68}$$

and the corresponding momentum source due to mass transfer is

$$\boldsymbol{u}_{\mathrm{i}k}^{\mathrm{m}}\Gamma_k = \mathcal{I}\left(\rho\boldsymbol{u}(\boldsymbol{u}-\boldsymbol{u}_\mathrm{i})\cdot\nabla\chi_k\right), \tag{2.69}$$

where the mean mass-transfer velocity $\boldsymbol{u}_{\mathrm{i}k}^{\mathrm{m}}$ is defined by the above equation.

2.4.4 Fluctuations

The instantaneous field value at a point may vary from the average value due to

- turbulence,
- the distribution of the phases.

This fluctuation has implications on the $\nabla\cdot\mathcal{I}\left(\chi_k\rho\boldsymbol{u}\boldsymbol{u}\right)$ term. The velocity fluctuation is expressed by

$$\boldsymbol{u}_k' = \boldsymbol{u}_k - \overline{\boldsymbol{u}}_k. \tag{2.70}$$

Other variables may also fluctuate, but pressure and density fluctuations were not considered by Drew and Passman (1999).

We have:

$$\mathcal{I}\left(\chi_k\rho\overline{\boldsymbol{u}}_k\right) = \mathcal{I}\left(\chi_k\rho\frac{\mathcal{I}\left(\chi_k\rho\boldsymbol{u}\right)}{\mathcal{I}\left(\chi_k\rho\right)}\right) = \mathcal{I}\left(\chi_k\rho\right)\frac{\mathcal{I}\left(\chi_k\rho\boldsymbol{u}\right)}{\alpha_k\overline{\rho}_k} = \mathcal{I}\left(\chi_k\rho\right)\overline{\boldsymbol{u}}_k. \tag{2.71}$$

Further, the equations (2.63) and (2.64) imply that

$$\mathcal{I}\left(\chi_k\rho\right)\overline{\boldsymbol{u}}_k = \mathcal{I}\left(\chi_k\rho\right)\frac{\mathcal{I}\left(\chi_k\rho\boldsymbol{u}\right)}{\alpha_k\overline{\rho}_k} = \mathcal{I}\left(\chi_k\rho\boldsymbol{u}\right). \tag{2.72}$$

At the same time, we get from (2.70):

$$\mathcal{I}\left(\chi_k\rho\boldsymbol{u}\right) = \mathcal{I}\left(\chi_k\rho\overline{\boldsymbol{u}}_k\right) + \mathcal{I}\left(\chi_k\rho\boldsymbol{u}_k'\right), \tag{2.73}$$

whence

$$\mathcal{I}\left(\chi_k\rho\boldsymbol{u}_k'\right) = 0. \tag{2.74}$$

Therefore, we get for the momentum flux:

$$\begin{aligned}\mathcal{E}\left(\chi_k\rho\boldsymbol{u}\boldsymbol{u}\right) &= \mathcal{E}\left(\chi_k\rho(\overline{\boldsymbol{u}}_k+\boldsymbol{u}'_k)(\overline{\boldsymbol{u}}_k+\boldsymbol{u}'_k)\right)\\ &= \mathcal{E}\left(\chi_k\rho\right)\overline{\boldsymbol{u}}_k\overline{\boldsymbol{u}}_k+\mathcal{E}\left(\chi_k\rho\boldsymbol{u}'_k\boldsymbol{u}'_k\right)\\ &= \alpha_k\overline{\rho}_k\overline{\boldsymbol{u}}_k\overline{\boldsymbol{u}}_k-\alpha_k\boldsymbol{T}_k^{\mathrm{t}},\end{aligned} \tag{2.75}$$

where

$$\boldsymbol{T}_k^{\mathrm{t}} = -\frac{\mathcal{E}\left(\chi_k\rho\boldsymbol{u}'_k\boldsymbol{u}'_k\right)}{\alpha_k} \tag{2.76}$$

is often called the Reynolds-stress tensor. It should be noted, however, that it is not the same as the Reynolds-stress tensor of single-phase flow, since the latter comes from time averaging, and, in addition, does not contain the effect of the phase distribution. That is, $\boldsymbol{T}_k^{\mathrm{t}}$ may be non-zero for a laminar flow.

2.4.5 Manipulations

It is convenient to write the pressure terms as one ∇p_k term and one $\nabla\alpha_k$ term. This is done by adding the contributions from the 'usual' pressure term and from the interfacial term. The interfacial pressure is defined by

$$p_{\mathrm{i}k} = \frac{\mathcal{E}\left(p\boldsymbol{n}_k\cdot\nabla\chi_k\right)}{a_k} = \frac{\mathcal{E}\left(p\delta(\boldsymbol{x}-\boldsymbol{x}_{\mathrm{i}})\right)}{\mathcal{E}\left(\delta(\boldsymbol{x}-\boldsymbol{x}_{\mathrm{i}})\right)}. \tag{2.77}$$

Herein, a_k is the interfacial area density of phase k:

$$a_k = -\mathcal{E}\left(\boldsymbol{n}_k\cdot\nabla\chi_k\right) = \mathcal{E}\left(\delta(\boldsymbol{x}-\boldsymbol{x}_{\mathrm{i}})\right). \tag{2.78}$$

Similarly, the interfacial shear stress is

$$\boldsymbol{\tau}_{\mathrm{i}k} = \frac{\mathcal{E}\left(\boldsymbol{\tau}\boldsymbol{n}_k\cdot\nabla\chi_k\right)}{a_k} = \frac{\mathcal{E}\left(\boldsymbol{\tau}\delta(\boldsymbol{x}-\boldsymbol{x}_{\mathrm{i}})\right)}{\mathcal{E}\left(\delta(\boldsymbol{x}-\boldsymbol{x}_{\mathrm{i}})\right)}. \tag{2.79}$$

The interfacial force density $\boldsymbol{m}_k$ may be split as

$$\boldsymbol{m}_k = \mathcal{E}\left(p\nabla\chi_k\right)-\mathcal{E}\left(\boldsymbol{\tau}\cdot\nabla\chi_k\right) = p_{\mathrm{i}k}\nabla\alpha_k+\boldsymbol{m}_{\mathrm{i}k}, \tag{2.80}$$

where the term $\boldsymbol{m}_{\mathrm{i}k}$ contains the remainder:

$$\boldsymbol{m}_{\mathrm{i}k} = \mathcal{E}\left((p-p_{\mathrm{i}k})\nabla\chi_k\right)-\mathcal{E}\left(\boldsymbol{\tau}\cdot\nabla\chi_k\right). \tag{2.81}$$

2.4.6 Ensemble-averaged balance equations revisited

Using the results from Sections 2.4.3–2.4.5, we can write the ensemble-averaged continuity equation (2.60) as

$$\frac{\partial t}{\partial t}(\alpha_k \overline{\rho}_k) + \boldsymbol{\nabla} \cdot (\alpha_k \overline{\rho}_k \overline{\boldsymbol{u}}_k) = \Gamma_k, \tag{2.82}$$

and the ensemble-averaged momentum equation (2.61) as

$$\begin{aligned}\frac{\partial}{\partial t}(\alpha_k \overline{\rho}_k \overline{\boldsymbol{u}}_k) + \boldsymbol{\nabla} \cdot (\alpha_k \overline{\rho}_k \overline{\boldsymbol{u}}_k \overline{\boldsymbol{u}}_k) \\ = -\alpha_k \boldsymbol{\nabla} \overline{p}_k - (\overline{p}_k - p_{\mathrm{i}k}) \boldsymbol{\nabla} \alpha_k + \boldsymbol{\nabla} \cdot \alpha_k (\overline{\boldsymbol{\tau}}_k + \boldsymbol{T}_k^{\mathrm{t}}) + \alpha_k \overline{\rho}_k \overline{\boldsymbol{b}}_k + \boldsymbol{m}_{\mathrm{i}k} + \boldsymbol{u}_{\mathrm{i}k}^{\mathrm{m}} \Gamma_k.\end{aligned} \tag{2.83}$$

The above equations are exact, that is, no modelling assumptions have been introduced. To close the equation system, several such assumptions will have to be made. This is addressed in the next section.

2.5 Model formulation

This section presents the employed model formulations. First, the exact equations from the preceding section are simplified so as to render the problem tractable. Next, the two-fluid model and the drift-flux model are described.

2.5.1 Simplifying assumptions

Even though the energy equation has been neglected, the equations (2.82)–(2.83) still pose serious challenges regarding the modelling of the interfacial terms and turbulence, and regarding the numerical solution algorithm. In the present case, several simplifying assumptions are appropriate:

- One-dimensional flow.
- Inviscid flow: $\overline{\boldsymbol{\tau}}_k \equiv \boldsymbol{0}$.
- No turbulence or phase-distribution effects on the average: $\boldsymbol{T}_k^{\mathrm{t}} \equiv \boldsymbol{0}$.
- No mass transfer: $\Gamma_k \equiv 0$.
- Most often, no interfacial forces are considered: $\boldsymbol{m}_{\mathrm{i}k} \equiv \boldsymbol{0}$. An interfacial drag term is employed in some instances, where specified.

Furthermore, we consider only two phases. In practical applications, one or more of the mentioned effects can be important. In the present work, on the other hand, we wish to focus on the mathematically essential parts of the two-phase flow model, keeping the number of parameters low.

Real fluids have a non-zero viscosity. Nevertheless, the assumption of inviscid flow is beneficial for several reasons:

- It makes the equations simpler.
- The inclusion of a viscosity would make it less straightforward to assess the artificial viscosity introduced by the numerical schemes.
- A numerical scheme for a two-phase flow model should be sufficiently robust so as to not be dependent upon a certain viscosity to yield stable results.

2.5.2 Four-equation system

Following the discussion of the preceding subsection, and dropping the explicit average notation for simplicity, we write the continuity equation as

$$\frac{\partial}{\partial t}(\alpha_k \rho_k) + \frac{\partial}{\partial x}(\alpha_k \rho_k u_k) = 0, \tag{2.84}$$

and the momentum equation as

$$\frac{\partial}{\partial t}(\alpha_k \rho_k u_k) + \frac{\partial}{\partial x}(\alpha_k \rho_k u_k^2) + \alpha_k \frac{\partial p_k}{\partial x} + (p_k - p_{\mathrm{i}k})\frac{\partial \alpha_k}{\partial x} = s_k, \tag{2.85}$$

where s_k is a momentum-source term. It can be written as $s_k = b_k + m_{\mathrm{i}k}$, where b_k is a body force and $m_{\mathrm{i}k}$ is the interfacial momentum exchange. The body force that will be considered here is gravity:

$$b_k = \alpha_k \rho_k g_x, \tag{2.86}$$

where g_x is the acceleration of gravity in the x direction. $m_{\mathrm{i}k}$ might contain interfacial friction. Most often one would like the interfacial exchange term to obey Newton's third law, that is,

$$m_{\mathrm{i}k} = -m_{\mathrm{i}f} \tag{2.87}$$

for the two phases k and f.

Due to the term $p_{\mathrm{i}k}\partial\alpha_k/\partial x$, the equation system cannot be written on conservation form in terms of the variables $\alpha_k\rho_k$ and $\alpha_k\rho_k u_k$. Therefore, special care is needed for the spatial discretization of the system.

In addition to the above equations, an equation of state is needed. Here we take the linear model

$$p_k = c_k^2(\rho_k - \rho_k^\circ), \tag{2.88}$$

where the speed of sound, c_k, and the 'reference density', ρ_k°, are constants for each phase. In this work we consider two phases, air (gas, denoted by the subscript g) and water (liquid, denoted by the subscript ℓ), with the properties given in Table 2.1 (unless otherwise stated). These values correspond to the ones used by Evje and Flåtten (2003). A constant speed of sound in the equation of state (EOS) is an implicit assumption of isentropic flow. This is shown in Section 2.5.5 on page 34. As can be seen from Toumi (1996), the entropy waves are advected with the fluid velocities, that is, they are uncoupled from the remaining wave structure, which can therefore be studied by considering an isentropic model.

Moreover, an expression is needed for the relation between the pressures in the phases, for example

$$p_k = p_f + \sigma_{kf} \quad \forall k \neq f, \tag{2.89}$$

where σ_{kf} is a constant pertaining to the relation between the phases k and f. In this work we shall take $\sigma_{kf} = 0$. Finally, of course, a relation for the interfacial pressure p_{ik} must be specified.

The equation system described in this subsection will be called the *four-equation system*.

2.5.3 Five-equation system

The ensemble-average of the topological equation (2.42) on page 22 is

$$\frac{\partial \alpha_k}{\partial t} + \mathcal{E}\left(\boldsymbol{u}_i \cdot \boldsymbol{\nabla}\chi_k\right) = 0. \tag{2.90}$$

Assume that

$$\mathcal{E}\left(\boldsymbol{u}_i \cdot \boldsymbol{\nabla}\chi_k\right) = \overline{\boldsymbol{u}}_{ik} \cdot \mathcal{E}\left(\boldsymbol{\nabla}\chi_k\right) = \overline{\boldsymbol{u}}_{ik} \cdot \boldsymbol{\nabla}\alpha_k, \tag{2.91}$$

Table 2.1: Constants in the equation of state

	c_k (m/s)	ρ_k° (kg/m^3)
air (g)	$\sqrt{10^5}$	0
water (ℓ)	1000	999.9

where $\overline{\boldsymbol{u}}_{ik}$ is an adequately averaged interfacial velocity. In the one-dimensional case we get:

$$\overline{u}_{ik} = \frac{\mathcal{E}\left(u_i \boldsymbol{n}_x \cdot \boldsymbol{\nabla}\chi_k\right)}{\partial \alpha_k / \partial x}, \tag{2.92}$$

that is, the mean interfacial velocity is the 'grad α-weighted' average of the local interfacial velocity. Dropping the overbar for notational convenience, we write

$$\frac{\partial \alpha_k}{\partial t} + u_{ik}\frac{\partial \alpha_k}{\partial x} = 0, \tag{2.93}$$

which expresses that the volume fraction is advected with the mean interfacial velocity. This equation can be added to the basic-equations system (2.84)–(2.85), as was similarly done by Saurel and Abgrall (1999); Baer and Nunziato (1986).

Interfacial-velocity models

Some model has to be specified for the average interface velocity, since the numerator in (2.92) cannot be calculated in a straightforward way. Saurel and Abgrall (1999) took the average interface velocity to be the mass-weighted velocity:

$$u_{ik} = u_i = \frac{\sum_{\forall k} \alpha_k \rho_k u_k}{\sum_{\forall k} \alpha_k \rho_k}. \tag{2.94}$$

This will be the default model in the present work.

Another model can be found by considering the continuous limit of the discrete-equation model of Abgrall and Saurel (2003) (Papin, 2005, Chapter 6) (see also Chapter 5):

$$u_{ik} = u_i = \frac{a_g u_g + a_\ell u_\ell + (p_\ell - p_g)\,\mathrm{sgn}(\partial \alpha_g / \partial x)}{a_g + a_\ell}, \tag{2.95}$$

where $a = \rho c$ is the acoustic impedance.

Pressure relaxation

When the energy equation is disregarded, the Saurel and Abgrall model can be written as

$$\frac{\partial \alpha_g}{\partial t} + u_i \frac{\partial \alpha_g}{\partial x} = r_p(p_g - p_\ell), \tag{2.96}$$

$$\frac{\partial}{\partial t}(\alpha_k \rho_k) + \frac{\partial}{\partial x}(\alpha_k \rho_k u_k) = 0, \tag{2.97}$$

$$\frac{\partial}{\partial t}(\alpha_k \rho_k u_k) + \frac{\partial}{\partial x}(\alpha_k \rho_k u_k^2) + \alpha_k \frac{\partial p_k}{\partial x} + (p_k - p_{ik})\frac{\partial \alpha_k}{\partial x} = s_k + r_u(u_f - u_k). \tag{2.98}$$

Herein, s_k is a momentum-source term. The parameters r_u and r_p deserve some attention. r_u is a velocity-relaxation parameter, and a large value of r_u will force equality of the two phasic velocities. In this work we shall not consider velocity relaxation, and henceforth

$$r_u \equiv 0. \tag{2.99}$$

In the cases where interphasic friction is accounted for, that phenomenon will be put into the source term s_k. See for instance (4.18) on page 111.

r_p is a pressure-relaxation parameter. It is the inverse of the compaction viscosity discussed by Baer and Nunziato (1986), something which can be confirmed by checking that the unit of r_p is the inverse of that of the molecular viscosity. For $r_p = 0$, the two phasic pressures are linearly independent, and when $r_p \to \infty$, they are equal.

The system (2.96)–(2.98) with (2.99) will be referred to as the *five-equation system*.

With the addition of the equation (2.96) to the system, the condition (2.89) is no longer needed. However, for many two-phase flows, including the ones considered here, the phasic pressures are not independent. This dependence is accounted for by the *pressure-relaxation procedure*. That procedure was discussed by Saurel and Abgrall (1999) for the full seven-equation system. Here the situation is somewhat simpler, since the energy equation is not considered.

Finite pressure relaxation Since the source term in the equation (2.96) may be large, it is necessary to solve the five-equation system using a suitable numerical method. Here, we employ a fractional-step method: First, the 'hyperbolic part' of the system (2.96)–(2.98) (that is, with $r_p \equiv 0$) is advanced one step, Δt, in time using a method to be described in Chapter 3. Next, the 'relaxation part' is considered:

$$\frac{\mathrm{d}\alpha_\mathrm{g}}{\mathrm{d}t} = r_p(p_\mathrm{g} - p_\ell), \tag{2.100}$$

$$\frac{\mathrm{d}}{\mathrm{d}t}(\alpha_k \rho_k) = 0, \tag{2.101}$$

$$\frac{\mathrm{d}}{\mathrm{d}t}(\alpha_k \rho_k u_k) = 0. \tag{2.102}$$

With the solution from the hyperbolic step as initial condition, the above system can be also be advanced one step Δt in time, using an ODE solver. The resulting solution is then passed to the hyperbolic solver for the next time step, etc.

Instantaneous pressure relaxation Specific values for the pressure-relaxation parameter r_p are most often unknown. However, the assumption of equal phasic pressures is widespread. Such situations can be catered for by setting r_p to a large value. However, instead of solving the system (2.100)–(2.102) of ordinary differential equations, it is numerically more efficient to solve the problem directly. After the hyperbolic operator has been applied, the volume fraction is modified so as to render the two pressures equal, keeping $\alpha_k\rho_k$ and $\alpha_k\rho_k u_k$ constant. This leads to a second-degree equation with positive solution

$$\alpha_\ell = \frac{-\psi_2 - \sqrt{\psi_2^2 - 4\psi_1\psi_3}}{2\psi_1}, \tag{2.103}$$

where

$$\psi_1 = c_\ell^2\rho_\ell^\circ - c_\mathrm{g}^2\rho_\mathrm{g}^\circ, \tag{2.104}$$

$$\psi_2 = -c_\ell^2(\alpha_\ell\rho_\ell + \rho_\ell^\circ) + c_\mathrm{g}^2(-\alpha_\mathrm{g}\rho_\mathrm{g} + \rho_\mathrm{g}^\circ), \tag{2.105}$$

and

$$\psi_3 = c_\ell^2\alpha_\ell\rho_\ell. \tag{2.106}$$

When solving the five-equation system, we will be employing instantaneous pressure relaxation, unless otherwise stated. For the case of instantaneous pressure relaxation, the volume-fraction equation (2.96) becomes singular. A difference between the phasic pressures would then cause an immediate change in the volume fraction so as to render the pressures equal. Since the rest of the five-equation system is equal to the four-equation system, the solution of the former should approach that of the latter. Indeed, it is hypothesized that the five-equation system with instantaneous pressure relaxation can be regarded as providing an alternative *numerical method* for solving the four-equation two-fluid model. This hypothesis will be tested in Chapter 3.

2.5.4 Interfacial-pressure models

Several models for the interfacial pressure have been proposed in the literature. However, their physical content is often debatable.

The model of Soo (1990, pages 319–321) reads

$$p_k - p_{\mathrm{i}k} = (1 - B_k)p_k, \tag{2.107}$$

where B_k is a 'displacement factor' close to unity, and it can be regarded as a simplified model for forces causing dispersion of the volume-fraction profile, e.g. in intermittent flow.

Saurel and Abgrall (1999) suggested taking

$$p_k - p_{ik} = p_k - \sum_{\forall k} \alpha_k p_k \tag{2.108}$$

in conjunction with their seven-equation model (that is, basically the five-equation model with an energy equation for each phase in addition). This seems like a reasonable first approximation. Unfortunately, it yields complex eigenvalues in the four-equation model.

In the CATHARE code, the following expression was employed for non-stratified flows (Bestion, 1990):

$$p_k - p_{ik} = \Delta p_{ik} = \gamma \frac{\alpha_g \alpha_\ell \rho_g \rho_\ell}{\alpha_g \rho_\ell + \alpha_\ell \rho_g} (u_g - u_\ell)^2, \tag{2.109}$$

where γ is a factor not appearing explicitly in Bestion (1990). It is remarkable that the above expression was employed without physical argumentation, but rather 'simply to provide the hyperbolicity of the system', which, indeed, it normally does, at least when there is slip between the phases, that is, $(u_g - u_\ell)^2 \neq 0$. On the other hand, the CATHARE expression has the redeeming feature that it approaches zero in the case of stagnant fluids, which seems reasonable when no surface-tension effects are accounted for. Because of this, and because it is commonly cited, the CATHARE model will be our default expression for the interfacial pressure difference, and we will take $\gamma = 1.2$, following Evje and Flåtten (2003), unless otherwise stated.

2.5.5 Thermodynamics

In the present work, the energy equation is not considered, and the equation of state (2.88) with constant coefficients is employed. We will now show that this implies the assumption of both an isentropic and an isothermal flow.

First, (2.88) is derived assuming constant entropy. Consider the general equation of state $p = p(\rho, s)$, which means that

$$\mathrm{d}p = \left(\frac{\partial p}{\partial \rho}\right)_s \mathrm{d}\rho + \left(\frac{\partial p}{\partial s}\right)_\rho \mathrm{d}s. \tag{2.110}$$

For constant entropy, $\mathrm{d}s = 0$, we obtain

$$\mathrm{d}p = \left(\frac{\partial p}{\partial \rho}\right)_s \mathrm{d}\rho = c^2 \, \mathrm{d}\rho, \tag{2.111}$$

which can be integrated between the states $(p_{\text{ref}}, \rho_{\text{ref}})$ and (p, ρ). If we assume a constant speed of sound, this gives

$$p = c^2[\rho - (\rho_{\text{ref}} - p_{\text{ref}}/c^2)], \tag{2.112}$$

yielding the equation (2.88) if we define $\rho^\circ = \rho_{\text{ref}} - p_{\text{ref}}/c^2$.

The fact that the equation (2.88) with constant c and ρ° also implies an isothermal flow, can be seen by considering the relation

$$\mathrm{d}s = \frac{c_v}{T}\,\mathrm{d}T + \left(\frac{\partial p}{\partial T}\right)_v \mathrm{d}v, \tag{2.113}$$

which can be found in a thermodynamics textbook (e.g. Moran and Shapiro, 1993, Section 11.4). Herein, v is the specific volume, $v = 1/\rho$. Differentiating (2.88) with respect to T while keeping ρ constant, yields 0. At the same time, (2.88) has been derived under the assumption of constant entropy, or $\mathrm{d}s = 0$. Therefore, the equation (2.113) dictates $\mathrm{d}T = 0$, or isothermal flow.

2.5.6 Drift-flux model

For several flow regimes, it is possible to correlate the relative velocity between the phases, the *slip velocity,* as a function of the flow variables (see e.g. Zuber and Findlay, 1965; Ishii, 1977; Hibiki and Ishii, 2002). This can be written as

$$u_{\text{g}} - u_\ell = \Phi(\alpha_{\text{g}}, p, u_{\text{g}}) \tag{2.114}$$

where the function Φ is referred to as the *slip relation*, and $p = \alpha_{\text{g}} p_{\text{g}} + \alpha_\ell p_\ell$ is the mixture pressure. This a priori knowledge of the flow can be employed to reduce the complexity of the model, and the result is called the *drift-flux model*. It is most easily derived by considering the two-fluid model (2.84)–(2.85), where, in the momentum equation, the interfacial pressure is assumed to be the same for both phases, $p_{\text{ig}} = p_{\text{i}\ell} = p_{\text{i}}$. Then the momentum equation for the gas is added to that of the liquid, to yield an equation for the mixture momentum. Thus the drift-flux model consists of two continuity equations and one momentum equation:

$$\frac{\partial}{\partial t}(\alpha_{\text{g}}\rho_{\text{g}}) + \frac{\partial}{\partial x}(\alpha_{\text{g}}\rho_{\text{g}}u_{\text{g}}) = 0, \tag{2.115}$$

$$\frac{\partial}{\partial t}(\alpha_\ell\rho_\ell) + \frac{\partial}{\partial x}(\alpha_\ell\rho_\ell u_\ell) = 0, \tag{2.116}$$

$$\frac{\partial}{\partial t}(\alpha_{\text{g}}\rho_{\text{g}}u_{\text{g}} + \alpha_\ell\rho_\ell u_\ell) + \frac{\partial}{\partial x}(\alpha_{\text{g}}\rho_{\text{g}}u_{\text{g}}^2 + \alpha_\ell\rho_\ell u_\ell^2 + p) = b_{\text{g}} + b_\ell. \tag{2.117}$$

It is also possible to formulate the drift-flux model in other ways. Ishii (1977), for example, employed a mixture continuity equation, a continuity equation for the dispersed phase, a mixture momentum equation, and a mixture enthalpy equation.

Since the gradient of the volume fraction is equal and opposite for the two phases, the $p_i \nabla \alpha$ terms do not appear in the drift-flux model. Hence the model can be written on conservation form, and the difficulties associated with the discretization of the 'non-conservative' terms are avoided. Another simplification occurs due to the cancellation of the interfacial momentum-source terms m_{ik}. With a slight abuse of terms, we will in some instances add a wall-friction source to the right-hand side of (2.117).

2.6 Well-posedness

2.6.1 Two-fluid model

The one-pressure 'plain' two-fluid model (with $p_k = p_{ik}$ in the equation (2.85)) has complex eigenvalues, resulting in an ill-posed initial-value problem, where there is an unphysical and unbounded growth of small-wavelength disturbances. Nevertheless, Stewart (1979) showed that numerical calculations can be well-behaved provided there is sufficient momentum transfer between the phases, and that the spatial grid is not too fine. However, the determination of which grid is 'not too fine' is not necessarily obvious in complex calculations. The ill-posedness will produce instabilities if not balanced by exchange terms (which damp low frequencies) and by numerical diffusion (at high frequencies) (see also Stewart and Wendroff, 1984).

The eigenvalues can be rendered real by adding differential terms to the model. Several effects have been considered, such as surface tension (Ramshaw and Trapp, 1978), interfacial pressure forces (Stuhmiller, 1977), virtual mass (Lahey *et al.*, 1980) and viscous stresses (Travis *et al.*, 1976; Arai, 1980).

While forcing real characteristics by including differential terms seems more satisfactory mathematically and numerically than relying on having a sufficient amount of numerical diffusion, it is not automatically more physical. Drew and Passman (1999, Chapter 20) noted that while it is true that a viscous system (with other effects neglected) has real characteristics, in the limit of vanishing viscosity, the complex characteristics of the inviscid system give rise to small-scale instabilities which are artefacts of the model, and not physically real. In this respect, Drew and Passman believed that the systematic inclusion of all terms arising in the averaged momentum equations, each soundly based on physics, will yield an appropriate working model, and that hope appears

still to be the state of the art.

2.6.2 Drift-flux model

The drift-flux model (2.115)–(2.117) is less 'problematic' than the two-fluid model with respect to well-posedness, and normally, no modification of the model is necessary. Even if the Jacobian matrix (see Chapter 7) has complicated expressions for its eigenvalues and eigenvectors, and cannot be shown to be diagonalizable in general, practical calculations indicate that it is diagonalizable for many relevant flow conditions.

2.7 Summary

In this section, we have reviewed the derivation of the multifluid model. Both the volume-averaging and the ensemble-averaging approaches were employed, and the resulting equations were seen to have the same form, even though the interpretation differ. The ensemble-averaging approach seems to be preferable, since it is more general. Among other things, it permits taking limits as the volume approaches zero.

In this work, three two-phase flow models will be considered; the four-equation model (Section 2.5.2 on page 29), the five-equation model (Section 2.5.3 on page 30), and the drift-flux model (Section 2.5.6 on page 35).

3 Roe-type methods for two-fluid models

> Like a malign version of the Cheshire cat, the rogue eigenvector might seem to have disappeared, but its hideous grin stays and is bound to thwart our endeavours.
>
> *A First Course in the Numerical Analysis of Differential Equations*
> Arieh Iserles

Two strategies for the numerical resolution of a two-fluid model have been investigated. Both methods employ a Roe-type scheme. The first method (Roe4) solves the four-equation, one-pressure, isentropic two-fluid model directly.

The second strategy (Roe5) is to add an evolution equation for the volume fraction. In the present case, that results in a five-equation two-pressure model, where it is necessary to employ pressure relaxation to calculate the typical two-phase problems that have been tested: The water faucet and three benchmark shock tube problems known from the literature.

The numerical calculations showed that the Roe4 and Roe5 schemes converge to the same solution when instantaneous pressure relaxation is employed in the Roe5 scheme. This is true both with and without the use of high-resolution flux-limiter functions. However, the Roe5 scheme was found to be significantly more diffusive than the Roe4 scheme. The diffusion is a strong function of the chosen time-step length, the grid size, whether a limiter function is employed or not, and also the liquid speed of sound.

As the pressure-relaxation parameter in the Roe5 scheme was increased, the solution gradually approached that obtained using instantaneous pressure relaxation.

Furthermore, the results indicate that the approach of two pressures and instantaneous pressure relaxation does not provide an easy way to overcome the problem of complex eigenvalues in the one-pressure two-fluid model.

A shortened version of this chapter has been submitted for publication as an article (Munkejord, 2005a).

3.1 Introduction

For the numerical solution of flow models, the approximate Riemann solver of Roe (1981) is an attractive candidate, since it provides an upwind resolution of all wave phenomena inherent in the models, and as it requires only the solution of a linear Riemann problem at each cell interface. Among the problems encountered for the two-fluid model, is the complicated eigenstructure, as well as the appearance of non-conservative terms (Toumi, 1996).

Sainsaulieu (1995) introduced a Roe-type Riemann solver for the case of incompressible liquid droplets suspended in a gas, that is, for small liquid volume fractions. More general configurations were considered by Toumi (1996), and a Roe-type method for the isentropic two-fluid model was presented by Toumi and Kumbaro (1996). However, also in the latter works, the liquid density was assumed to be constant. That assumption was not used in the method by Evje and Flåtten (2003).

A different approach has been to consider two-pressure models, whose mathematical properties have been found preferable (Ransom and Hicks, 1984). On the other hand, for many cases, the latter kind of methods needs a *pressure-relaxation* procedure.

Saurel and Abgrall (1999) presented a two-velocity two-pressure two-phase model of seven equations, where pressure and / or velocity relaxation could be performed after the hyperbolic time step. The model can be thought of as an extension of that of Baer and Nunziato (1986). It was expanded to several space dimensions by Saurel and LeMetayer (2001), and it was stated to be suitable for compressible multiphase flows with interfaces, shocks, detonation waves and cavitation. Murrone and Guillard (2005) discussed a five-equation diffuse interface model where the two phases had common pressures and velocities. Different pressure-relaxation procedures were tested by Lallemand *et al.* (2005).

The approximate Riemann solver employed by Saurel and Abgrall (1999) was a modified Harten, Lax and van Leer (HLL) scheme. Other authors have later presented similar methods using other solvers. Niu (2001) applied a modified advection upstream splitting method (AUSMD) and solved the seven-equation model in one and two dimensions, also adding a k–ε turbulence model. A Roe-type scheme for the seven-equation model was presented by Karni *et al.* (2004).

In this work, we perform a direct comparison between a one-pressure four-equation approach, and a two-pressure five-equation approach, employing a Roe-type method in each case. A priori, both strategies have advantages. For the five-equation system, simple, analytical expressions for the eigenvalues and eigenvectors are available. On the other hand, the four-equation system has

one less equation to be solved. Only the five-equation system can be used if the physical system to be modelled has two independent pressures. Here we explore the effect of varying pressure-relaxation parameter in the five-equation system.

In Section 3.2, the equation systems are written in characteristic form, and the Roe matrices are detailed. The Roe method is described in Section 3.3. In Section 3.4, numerical tests are performed. Finally, in Section 3.5, the main conclusions are drawn.

3.2 Characteristic form of the basic equations

To be able to solve the system of transport equations using well-established numerical methods, we would prefer to write it on conservation form:

$$\frac{\partial \boldsymbol{q}}{\partial t} + \frac{\partial \boldsymbol{f}(\boldsymbol{q})}{\partial x} = \boldsymbol{s}(\boldsymbol{q}), \tag{3.1}$$

where $\boldsymbol{q}$ is the vector of composite variables (see the equation (3.32)), $\boldsymbol{f}(\boldsymbol{q})$ is the corresponding flux function, and $\boldsymbol{s}(\boldsymbol{q})$ is the vector of source terms. Unfortunately, this cannot be done, because of the $\nabla\alpha_k$ terms appearing in the momentum equation (2.85). One way around this would be to discretize the $\nabla\alpha_k$ terms using central differences. Another way is to use a Roe solver, to be described later.

First, it is necessary to devote some attention to the characteristic form of the equation system. We seek to write this system on the following quasi-linear form:

$$\frac{\partial \boldsymbol{q}}{\partial t} + \boldsymbol{A}(\boldsymbol{q})\frac{\partial \boldsymbol{q}}{\partial x} = \boldsymbol{s}(\boldsymbol{q}). \tag{3.2}$$

However, for the multifluid equations, it is tricky to derive the matrix $\boldsymbol{A}$ from the governing equations presented in Section 2.5 on page 28. On the other hand, it is straightforward to write the equation system (2.84)–(2.85) on quasi-linear form using the vector of primitive variables $\boldsymbol{v}$ (see the equation (3.11)):

$$\frac{\partial \boldsymbol{v}}{\partial t} + \boldsymbol{B}(\boldsymbol{v})\frac{\partial \boldsymbol{v}}{\partial x} = \boldsymbol{\varsigma}(\boldsymbol{v}). \tag{3.3}$$

From the form (3.3), we can calculate the matrix $\boldsymbol{A}$ in the following manner: Define the transformation matrix $\boldsymbol{J}$ as

$$\boldsymbol{J} = \frac{\partial \boldsymbol{q}}{\partial \boldsymbol{v}}, \tag{3.4}$$

whence

$$\boldsymbol{J}^{-1} = \frac{\partial \boldsymbol{v}}{\partial \boldsymbol{q}}. \tag{3.5}$$

Using the chain rule on the equation (3.3), we get

$$\frac{\partial \boldsymbol{v}}{\partial \boldsymbol{q}} \frac{\partial \boldsymbol{q}}{\partial t} + \boldsymbol{B} \frac{\partial \boldsymbol{v}}{\partial \boldsymbol{q}} \frac{\partial \boldsymbol{q}}{\partial x} = \boldsymbol{\varsigma}, \tag{3.6}$$

or

$$\boldsymbol{J}^{-1} \frac{\partial \boldsymbol{q}}{\partial t} + \boldsymbol{B}\boldsymbol{J}^{-1} \frac{\partial \boldsymbol{q}}{\partial x} = \boldsymbol{\varsigma}, \tag{3.7}$$

which implies that

$$\boldsymbol{A} = \boldsymbol{J}\boldsymbol{B}\boldsymbol{J}^{-1}, \tag{3.8}$$

and

$$\boldsymbol{s} = \boldsymbol{J}\boldsymbol{\varsigma}. \tag{3.9}$$

In the following subsections, the matrices $\boldsymbol{A}$ and $\boldsymbol{B}$ will be derived for the four- and the five-equation systems.

3.2.1 Characteristic form of the four-equation system

To obtain the coefficient matrix $\boldsymbol{B}(\boldsymbol{v})$, we first seek to write the four-equation system (see Section 2.5.2 on page 29) on the form

$$\boldsymbol{C} \frac{\partial \boldsymbol{v}}{\partial t} + \boldsymbol{D} \frac{\partial \boldsymbol{v}}{\partial x} = \boldsymbol{e}, \tag{3.10}$$

where $\boldsymbol{v}$ is the vector containing the chosen linearly independent primitive variables:

$$\boldsymbol{v} = \begin{bmatrix} \alpha_{\mathrm{g}} & p_{\mathrm{g}} & u_{\mathrm{g}} & u_{\ell} \end{bmatrix}^T, \tag{3.11}$$

This enables us to calculate

$$\boldsymbol{B} = \boldsymbol{C}^{-1}\boldsymbol{D}, \tag{3.12}$$

and

$$\boldsymbol{\varsigma} = \boldsymbol{C}^{-1}\boldsymbol{e}. \tag{3.13}$$

In the following subsections, we will find expressions for $\boldsymbol{C}$, $\boldsymbol{D}$ and $\boldsymbol{e}$, and hence for $\boldsymbol{B}$ and $\boldsymbol{\varsigma}$.

Continuity equation

By using the product rule of differentiation, we can write the continuity equation (2.84) as

$$\alpha_k \frac{\partial \rho_k}{\partial t} + \rho_k \frac{\partial \alpha_k}{\partial t} + \alpha_k \rho_k \frac{\partial u_k}{\partial x} + \alpha_k u_k \frac{\partial \rho_k}{\partial x} + \rho_k u_k \frac{\partial \alpha_k}{\partial x} = 0. \tag{3.14}$$

The equation of state (2.88) implies that

$$\frac{\partial \rho_k}{\partial p_k} = \frac{1}{c_k^2}. \tag{3.15}$$

This gives:

$$\alpha_k \frac{1}{c_k^2} \frac{\partial p_k}{\partial t} + \rho_k \frac{\partial \alpha_k}{\partial t} + \alpha_k \rho_k \frac{\partial u_k}{\partial x} + \alpha_k u_k \frac{1}{c_k^2} \frac{\partial p_k}{\partial x} + \rho_k u_k \frac{\partial \alpha_k}{\partial x} = 0. \tag{3.16}$$

Substituting k with g, we get the desired continuity equation for the gas:

$$\rho_g \frac{\partial \alpha_g}{\partial t} + \alpha_g \frac{1}{c_g^2} \frac{\partial p_g}{\partial t} + \rho_g u_g \frac{\partial \alpha_g}{\partial x} + \alpha_g u_g \frac{1}{c_g^2} \frac{\partial p_g}{\partial x} + \alpha_g \rho_g \frac{\partial u_g}{\partial x} = 0, \tag{3.17}$$

and since the equation (2.89) implies that

$$\frac{\partial p_g}{\partial x} = \frac{\partial p_\ell}{\partial x}, \tag{3.18}$$

where ℓ denotes the liquid phase, and, since

$$\frac{\partial \alpha_g}{\partial x} = -\frac{\partial \alpha_\ell}{\partial x}, \tag{3.19}$$

we can write down the following continuity equation for the liquid:

$$-\rho_\ell \frac{\partial \alpha_g}{\partial t} + \alpha_\ell \frac{1}{c_\ell^2} \frac{\partial p_g}{\partial t} - \rho_\ell u_\ell \frac{\partial \alpha_g}{\partial x} + \alpha_\ell u_\ell \frac{1}{c_\ell^2} \frac{\partial p_g}{\partial x} + \alpha_\ell \rho_\ell \frac{\partial u_\ell}{\partial x} = 0. \tag{3.20}$$

Momentum equation

The momentum equation (2.85) is manipulated in a similar manner as the continuity equation. By using the product rule of differentiation, the relations between the gradients of the gas and liquid volume fractions and ditto for the pressures, as well as by employing the continuity equation to cancel the terms

$$u_k \frac{\partial}{\partial t}(\alpha_k \rho_k) + u_k \frac{\partial}{\partial x}(\alpha_k \rho_k u_k) = 0, \tag{3.21}$$

we get for the gas:

$$\alpha_g\rho_g\frac{\partial u_g}{\partial t} + (p_g - p_{ig})\frac{\partial \alpha_g}{\partial x} + \alpha_g\frac{\partial p_g}{\partial x} + \alpha_g\rho_g u_g\frac{\partial u_g}{\partial x} = \alpha_g\rho_g g_x, \tag{3.22}$$

and for the liquid:

$$\alpha_\ell\rho_\ell\frac{\partial u_\ell}{\partial t} - (p_\ell - p_{i\ell})\frac{\partial \alpha_g}{\partial x} + \alpha_\ell\frac{\partial p_g}{\partial x} + \alpha_\ell\rho_\ell u_\ell\frac{\partial u_\ell}{\partial x} = \alpha_\ell\rho_\ell g_x. \tag{3.23}$$

Results

The results from the preceding subsections imply that

$$\boldsymbol{C} = \begin{bmatrix} \rho_g & \alpha_g/c_g^2 & 0 & 0 \\ -\rho_\ell & \alpha_\ell/c_\ell^2 & 0 & 0 \\ 0 & 0 & \alpha_g\rho_g & 0 \\ 0 & 0 & 0 & \alpha_\ell\rho_\ell \end{bmatrix}, \tag{3.24}$$

and

$$\boldsymbol{D} = \begin{bmatrix} \rho_g u_g & \alpha_g u_g/c_g^2 & \alpha_g\rho_g & 0 \\ -\rho_\ell u_\ell & \alpha_\ell u_\ell/c_\ell^2 & 0 & \alpha_\ell\rho_\ell \\ (p_g - p_i) & \alpha_g & \alpha_g\rho_g u_g & 0 \\ -(p_\ell - p_i) & \alpha_\ell & 0 & \alpha_\ell\rho_\ell u_\ell \end{bmatrix}. \tag{3.25}$$

Calculating $\boldsymbol{C}^{-1}$, we obtain the coefficient matrix

$$\boldsymbol{B}(\boldsymbol{v}) = \begin{bmatrix} \dfrac{\psi}{\varkappa} & \dfrac{\alpha_\ell\alpha_g(u_g - u_\ell)}{c_g^2c_\ell^2\varkappa} & \dfrac{\alpha_\ell\alpha_g\rho_g}{c_\ell^2\varkappa} & -\dfrac{\alpha_g\alpha_\ell\rho_\ell}{c_g^2\varkappa} \\ \dfrac{\rho_\ell\rho_g(u_g - u_\ell)}{\varkappa} & \dfrac{\zeta}{\varkappa} & \dfrac{\rho_\ell\alpha_g\rho_g}{\varkappa} & \dfrac{\rho_g\alpha_\ell\rho_\ell}{\varkappa} \\ \dfrac{\Delta p_{ig}}{\alpha_g\rho_g} & \dfrac{1}{\rho_g} & u_g & 0 \\ \dfrac{-\Delta p_{i\ell}}{\alpha_\ell\rho_\ell} & \dfrac{1}{\rho_\ell} & 0 & u_\ell \end{bmatrix}, \tag{3.26}$$

with

$$\psi = \alpha_\ell\rho_g u_g/c_\ell^2 + \alpha_g\rho_\ell u_\ell/c_g^2, \tag{3.27}$$

$$\zeta = \alpha_g\rho_\ell u_g/c_g^2 + \alpha_\ell\rho_g u_\ell/c_\ell^2, \tag{3.28}$$

$$\varkappa = \alpha_\ell\rho_g/c_\ell^2 + \rho_\ell\alpha_g/c_g^2, \tag{3.29}$$

$$\Delta p_{ik} = p_k - p_{ik}, \tag{3.30}$$

and the source-term vector

$$\boldsymbol{\varsigma} = \begin{bmatrix} 0 & 0 & g_x & g_x \end{bmatrix}^T. \tag{3.31}$$

The vector of composite variables is

$$\boldsymbol{q} = \begin{bmatrix} \alpha_g\rho_g & \alpha_\ell\rho_\ell & \alpha_g\rho_g u_g & \alpha_\ell\rho_\ell u_\ell \end{bmatrix}^T. \tag{3.32}$$

Therefore, the transformation matrix $\boldsymbol{J}$ becomes

$$\boldsymbol{J} = \begin{bmatrix} \rho_g & \alpha_g/c_g^2 & 0 & 0 \\ -\rho_\ell & \alpha_\ell/c_\ell^2 & 0 & 0 \\ \rho_g u_g & \alpha_g u_g/c_g^2 & \alpha_g\rho_g & 0 \\ -\rho_\ell u_\ell & \alpha_\ell u_\ell/c_\ell^2 & 0 & \alpha_\ell\rho_\ell \end{bmatrix}, \tag{3.33}$$

and hence one can calculate the coefficient matrix:

$$\boldsymbol{A}(\boldsymbol{q}) = \begin{bmatrix} 0 & 0 & 1 & 0 \\ 0 & 0 & 0 & 1 \\ \dfrac{\alpha_g\rho_\ell + \Delta p_{ig}\alpha_\ell/c_\ell^2}{\varkappa} - u_g^2 & \dfrac{\alpha_g\rho_g - \Delta p_{ig}\alpha_g/c_g^2}{\varkappa} & 2u_g & 0 \\ \dfrac{\alpha_\ell\rho_\ell + \Delta p_{i\ell}\alpha_\ell/c_\ell^2}{\varkappa} & \dfrac{\alpha_\ell\rho_g + \Delta p_{i\ell}\alpha_g/c_g^2}{\varkappa} - u_\ell^2 & 0 & 2u_\ell \end{bmatrix}. \tag{3.34}$$

This could not be shown to be the Jacobian such that $\boldsymbol{A} = \partial \boldsymbol{f}/\partial \boldsymbol{q}$, since the flux function $\boldsymbol{f}$ has not been found. Hence, the standard numerical methods for conservation laws cannot necessarily be straightforwardly applied for solving the present equation system.

The vector of source terms becomes

$$\boldsymbol{s} = \begin{bmatrix} 0 & 0 & \alpha_g\rho_g g_x & \alpha_\ell\rho_\ell g_x \end{bmatrix}^T. \tag{3.35}$$

The matrices $\boldsymbol{A}$ and $\boldsymbol{B}$ have the same characteristic polynomial and hence the same eigenvalues. However, it is unfeasible to derive exact closed-form expressions for them. The approximate expressions of Evje and Flåtten (2003) are given in Appendix A on page 251.

3.2.2 Characteristic form of the five-equation system

In the present subsection, we repeat the analysis of subsection 3.2.1 on page 42 for the five-equation system (see Section 2.5.3 on page 30). Note that we re-use the notation of that section, in order not to introduce too many symbols.

The five-equation system can be written directly in the form (3.3), using the following vector of linearly independent variables:

$$\boldsymbol{v} = \begin{bmatrix} \alpha_\mathrm{g} & \rho_\mathrm{g} & u_\mathrm{g} & \rho_\ell & u_\ell \end{bmatrix}^T, \tag{3.36}$$

The volume-fraction equation (2.93) is already on the desired form. The continuity equation (2.84) can be rewritten by using the product rule of differentiation and inserting the equation (2.93), and the result is:

$$\frac{\partial \rho_k}{\partial t} + \frac{\rho_k}{\alpha_k}(u_k - u_\mathrm{i})\frac{\partial \alpha_k}{\partial x} + u_k \frac{\partial \rho_k}{\partial x} + \rho_k \frac{\partial u_k}{\partial x} = 0. \tag{3.37}$$

The momentum equation (2.85) can then be written in the characteristic form by inserting c_k^2 from equation (3.15), using the product rule of differentiation and by using the equation (2.84):

$$\frac{\partial u_k}{\partial t} + \frac{\Delta p_{\mathrm{i}k}}{\alpha_k \rho_k}\frac{\partial \alpha_k}{\partial x} + u_k \frac{\partial u_k}{\partial x} + \frac{c_k^2}{\rho_k}\frac{\partial \rho_k}{\partial x} = 0. \tag{3.38}$$

System matrix

Noting that $\partial \alpha_\mathrm{g}/\partial x = -\partial \alpha_\ell / \partial x$, we can write down the coefficient matrix:

$$\boldsymbol{B}(\boldsymbol{v}) = \begin{bmatrix} u_\mathrm{i} & 0 & 0 & 0 & 0 \\ \dfrac{\rho_\mathrm{g}}{\alpha_\mathrm{g}}(u_\mathrm{g} - u_\mathrm{i}) & u_\mathrm{g} & \rho_\mathrm{g} & 0 & 0 \\ \dfrac{\Delta p_{\mathrm{i}\mathrm{g}}}{\alpha_\mathrm{g}\rho_\mathrm{g}} & \dfrac{c_\mathrm{g}^2}{\rho_\mathrm{g}} & u_\mathrm{g} & 0 & 0 \\ -\dfrac{\rho_\ell}{\alpha_\ell}(u_\ell - u_\mathrm{i}) & 0 & 0 & u_\ell & \rho_\ell \\ -\dfrac{\Delta p_{\mathrm{i}\ell}}{\alpha_\ell \rho_\ell} & 0 & 0 & \dfrac{c_\ell^2}{\rho_\ell} & u_\ell \end{bmatrix}, \tag{3.39}$$

and the vector of source terms

$$\boldsymbol{\varsigma} = \begin{bmatrix} 0 & 0 & g_x & 0 & g_x \end{bmatrix}^T. \tag{3.40}$$

The vector of composite variables is

$$\boldsymbol{q} = \begin{bmatrix} \alpha_\mathrm{g} & \alpha_\mathrm{g}\rho_\mathrm{g} & \alpha_\mathrm{g}\rho_\mathrm{g}u_\mathrm{g} & \alpha_\ell \rho_\ell & \alpha_\ell \rho_\ell u_\ell \end{bmatrix}^T, \tag{3.41}$$

and hence the transformation matrix $\boldsymbol{J} = \partial \boldsymbol{q}/\partial \boldsymbol{v}$ for the five-equation system is

$$\boldsymbol{J} = \begin{bmatrix} 1 & 0 & 0 & 0 & 0 \\ \rho_{\mathrm{g}} & \alpha_{\mathrm{g}} & 0 & 0 & 0 \\ \rho_{\mathrm{g}} u_{\mathrm{g}} & \alpha_{\mathrm{g}} u_{\mathrm{g}} & \alpha_{\mathrm{g}} \rho_{\mathrm{g}} & 0 & 0 \\ -\rho_{\ell} & 0 & 0 & \alpha_{\ell} & 0 \\ -\rho_{\ell} u_{\ell} & 0 & 0 & \alpha_{\ell} u_{\ell} & \alpha_{\ell} \rho_{\ell} \end{bmatrix}, \tag{3.42}$$

whence the coefficient matrix for the composite-variable system is found to be

$$\boldsymbol{A}(\boldsymbol{q}) = \begin{bmatrix} u_{\mathrm{i}} & 0 & 0 & 0 & 0 \\ 0 & 0 & 1 & 0 & 0 \\ \Delta p_{\mathrm{ig}} - \rho_{\mathrm{g}} c_{\mathrm{g}}^2 & c_{\mathrm{g}}^2 - u_{\mathrm{g}}^2 & 2u_{\mathrm{g}} & 0 & 0 \\ 0 & 0 & 0 & 0 & 1 \\ -\Delta p_{\mathrm{i}\ell} + \rho_{\ell} c_{\ell}^2 & 0 & 0 & c_{\ell}^2 - u_{\ell}^2 & 2u_{\ell} \end{bmatrix}, \tag{3.43}$$

with the source-term vector

$$\boldsymbol{s}(\boldsymbol{q}) = \begin{bmatrix} 0 & 0 & \alpha_{\mathrm{g}} \rho_{\mathrm{g}} g_x & 0 & \alpha_{\ell} \rho_{\ell} g_x \end{bmatrix}^T. \tag{3.44}$$

Eigenstructure and hyperbolicity

The matrices $\boldsymbol{A}$ and $\boldsymbol{B}$ have one advantage over their counterparts in Section 3.2.1 on page 44 in that their eigenvalues are available as simple analytical expressions:

$$\boldsymbol{\lambda} = \begin{bmatrix} u_{\mathrm{i}} & u_{\mathrm{g}} - c_{\mathrm{g}} & u_{\mathrm{g}} + c_{\mathrm{g}} & u_{\ell} - c_{\ell} & u_{\ell} + c_{\ell} \end{bmatrix}^T. \tag{3.45}$$

These eigenvalues are always real, and moreover, they are mostly distinct, except for the 'transonic difficulty' when one of the phasic velocities passes through its phasic speed of sound. The eigenvector matrix, $\boldsymbol{R}$, with the right eigenvectors $\boldsymbol{r}_i$ of $\boldsymbol{A}$ as its columns, was found as

$$\boldsymbol{R} = \begin{bmatrix} 1 & 0 & 0 & 0 & 0 \\ -\dfrac{(-\Delta p_{\mathrm{ig}} + \rho_{\mathrm{g}} c_{\mathrm{g}}^2)}{(u_{\mathrm{g}} - u_{\mathrm{i}})^2 - c_{\mathrm{g}}^2} & 1 & 1 & 0 & 0 \\ -\dfrac{(-\Delta p_{\mathrm{ig}} + \rho_{\mathrm{g}} c_{\mathrm{g}}^2) u_{\mathrm{i}}}{(u_{\mathrm{g}} - u_{\mathrm{i}})^2 - c_{\mathrm{g}}^2} & \lambda_2 & \lambda_3 & 0 & 0 \\ \dfrac{(-\Delta p_{\mathrm{i}\ell} + \rho_{\ell} c_{\ell}^2)}{(u_{\ell} - u_{\mathrm{i}})^2 - c_{\ell}^2} & 0 & 0 & 1 & 1 \\ \dfrac{(-\Delta p_{\mathrm{i}\ell} + \rho_{\ell} c_{\ell}^2) u_{\mathrm{i}}}{(u_{\ell} - u_{\mathrm{i}})^2 - c_{\ell}^2} & 0 & 0 & \lambda_4 & \lambda_5 \end{bmatrix}, \tag{3.46}$$

where λ_i is element i of the vector $\boldsymbol{\lambda}$ in equation (3.45). Further, the eigenvector $\boldsymbol{r}_i$ corresponds to the eigenvalue λ_i.

The matrix $\boldsymbol{R}^{-1}$, with the left eigenvectors $\boldsymbol{l}_j^T$ of $\boldsymbol{A}$ as its rows, is given by:

$$\boldsymbol{R}^{-1} = \begin{bmatrix} 1 & 0 & 0 & 0 & 0 \\ \frac{1}{2}\frac{(-\Delta p_{\mathrm{ig}} + \rho_{\mathrm{g}} c_{\mathrm{g}}^2)}{(\lambda_2 - u_{\mathrm{i}})c_{\mathrm{g}}} & \frac{1}{2}\frac{\lambda_3}{c_{\mathrm{g}}} & -\frac{1}{2c_{\mathrm{g}}} & 0 & 0 \\ -\frac{1}{2}\frac{(-\Delta p_{\mathrm{ig}} + \rho_{\mathrm{g}} c_{\mathrm{g}}^2)}{(\lambda_3 - u_{\mathrm{i}})c_{\mathrm{g}}} & -\frac{1}{2}\frac{\lambda_2}{c_{\mathrm{g}}} & \frac{1}{2c_{\mathrm{g}}} & 0 & 0 \\ -\frac{1}{2}\frac{(-\Delta p_{\mathrm{i}\ell} + \rho_{\ell} c_{\ell}^2)}{(\lambda_4 - u_{\mathrm{i}})c_{\ell}} & 0 & 0 & \frac{1}{2}\frac{\lambda_5}{c_{\ell}} & -\frac{1}{2c_{\ell}} \\ \frac{1}{2}\frac{(-\Delta p_{\mathrm{i}\ell} + \rho_{\ell} c_{\ell}^2)}{(\lambda_5 - u_{\mathrm{i}})c_{\ell}} & 0 & 0 & -\frac{1}{2}\frac{\lambda_4}{c_{\ell}} & \frac{1}{2c_{\ell}} \end{bmatrix}. \tag{3.47}$$

Since here the left eigenvectors are taken from from $\boldsymbol{R}^{-1}$, the left and the right eigenvectors are orthonormal: $\boldsymbol{l}_i^T \boldsymbol{r}_j = \delta_{ij}$.

For the five-equation system to be hyperbolic, the matrix $\boldsymbol{A}$ must be diagonalizable with real eigenvalues. Therefore, the right eigenvectors $\boldsymbol{r}_i$ must be linearly independent, and it is easy to show that $\boldsymbol{r}_2$, $\boldsymbol{r}_3$, $\boldsymbol{r}_4$ and $\boldsymbol{r}_5$ are so. $\boldsymbol{r}_1$, on the other hand, needs special attention. Ransom and Hicks (1984) studied a five-equation two-pressure two-fluid model whose coefficient matrix was mathematically analogous to the one considered here. They showed that the hyperbolicity depends on the quantities

$$\beta_k = -\Delta p_{\mathrm{i}k} + \rho_k c_k^2, \tag{3.48}$$

and

$$\gamma_k = (u_k - u_{\mathrm{i}})^2 - c_k^2. \tag{3.49}$$

There are four cases, concerning the eigenvector $\boldsymbol{r}_1$ associated with $\lambda_1 = u_{\mathrm{i}}$:

1. When $\gamma_{\mathrm{g}} \neq 0$ and $\gamma_{\ell} \neq 0$, then $\boldsymbol{r}_1$ as given by the equation (3.46) is linearly independent of the other eigenvectors for all values of β_{g} and β_{ℓ}.

2. When $\gamma_{\mathrm{g}} = 0$ and $\gamma_{\ell} \neq 0$, then there exists a linearly independent $\boldsymbol{r}_1$ if and only if $\beta_{\mathrm{g}} = 0$. It is given by

$$\boldsymbol{r}_1 = \begin{bmatrix} 1 & 0 & 0 & \frac{(-\Delta p_{\mathrm{i}\ell} + \rho_{\ell} c_{\ell}^2)}{(u_{\ell} - u_{\mathrm{i}})^2 - c_{\ell}^2} & \frac{(-\Delta p_{\mathrm{i}\ell} + \rho_{\ell} c_{\ell}^2) u_{\mathrm{i}}}{(u_{\ell} - u_{\mathrm{i}})^2 - c_{\ell}^2} \end{bmatrix}^T. \tag{3.50}$$

3. When $\gamma_g \neq 0$ and $\gamma_\ell = 0$, then there exists a linearly independent $\boldsymbol{r}_1$ if and only if $\beta_\ell = 0$. It is given by

$$\boldsymbol{r}_1 = \begin{bmatrix} 1 & -\dfrac{(-\Delta p_{ig} + \rho_g c_g^2)}{(u_g - u_i)^2 - c_g^2} & -\dfrac{(-\Delta p_{ig} + \rho_g c_g^2)u_i}{(u_g - u_i)^2 - c_g^2} & 0 & 0 \end{bmatrix}^T. \tag{3.51}$$

4. When $\gamma_g = 0$ and $\gamma_\ell = 0$, then there exists a linearly independent $\boldsymbol{r}_1$ if and only if $\beta_g = 0$ and $\beta_\ell = 0$. It is given by

$$\boldsymbol{r}_1 = \begin{bmatrix} 1 & 0 & 0 & 0 & 0 \end{bmatrix}^T. \tag{3.52}$$

Here we mainly consider low-speed flows, and the restriction $u_k \pm c_k \neq u_i$ is not thought to be of very much concern. Thus we find that the five-equation system is not quite unconditionally hyperbolic, but it is much more so than the four-equation system.

It is interesting to note that for the five-equation system, the interfacial pressure difference Δp_{ik} may very well be equal to zero. For the four-equation system, on the other hand, this quantity must not be too small. This can be shown by numerical experiments or analytical considerations (see e.g. Ramshaw and Trapp, 1978). As a result of this, several researchers have dedicated their efforts to inventing large-enough expressions for the interfacial pressure difference, leading, conveniently, to a diagonalizable $\boldsymbol{A}$. One example is Chung *et al.* (2002).

Since the relaxation terms in (2.96)–(2.98) do not contain derivatives of $\boldsymbol{q}$, the hyperbolicity of the five-equation system is not influenced by them. However, the case of instantaneous pressure relaxation might be interesting to study mathematically in more detail, but that is outside the scope of the present work.

3.3 Numerical algorithm and Roe solver

In this section, a Roe-type method for the multiphase equations will be described. For basic notions about hyperbolic conservation laws and numerical methods to solve them using Riemann solvers, reference is made to the books of LeVeque (2002) and Toro (1999).

3.3.1 Framework

A high-resolution extension of Godunov's method can be written as (LeVeque, 2002, Section 15.4)

$$\boldsymbol{Q}_i^{n+1} = \boldsymbol{Q}_i^n - \frac{\Delta t}{\Delta x}\left(\mathcal{A}^-\Delta\boldsymbol{Q}_{i+1/2} + \mathcal{A}^+\Delta\boldsymbol{Q}_{i-1/2}\right) - \frac{\Delta t}{\Delta x}\left(\tilde{\boldsymbol{F}}_{i+1/2} - \tilde{\boldsymbol{F}}_{i-1/2}\right), \quad (3.53)$$

where $\boldsymbol{Q}_i^n$ denotes the numerical approximation to the cell average of the vector of unknowns $\boldsymbol{q}(x(i), t_n)$, that is, in control volume i at time step n. Quantities without a time index are evaluated at time step n. The symbol $\mathcal{A}^-\Delta\boldsymbol{Q}_{i+1/2}$ denotes the net effect of all left-going waves at $x_{i+1/2}$, that is, at the control-volume boundary midway between x_i and x_{i+1}, while $\mathcal{A}^+\Delta\boldsymbol{Q}_{i-1/2}$ measures the net effect of all right-going waves at $x_{i-1/2}$. The waves and wave speeds from the approximate Riemann solution are used to define

$$\begin{aligned}\mathcal{A}^-\Delta\boldsymbol{Q}_{i-1/2} &= \sum_{p=1}^{m} (s_{i-1/2}^p)^- \mathcal{W}_{i-1/2}^p,\\ \mathcal{A}^+\Delta\boldsymbol{Q}_{i-1/2} &= \sum_{p=1}^{m} (s_{i-1/2}^p)^+ \mathcal{W}_{i-1/2}^p,\end{aligned} \quad (3.54)$$

where $\mathcal{W}_{i-1/2}^p$ is the pth wave arising in the solution to the Riemann problem at $x_{i-1/2}$, that is, it is a vector with one component for each equation. m is the number of waves, and since we will be using a linearized Riemann solver, it is equal to the number of equations. $s_{i-1/2}^p$ is the wave speed of the pth wave, and

$$(s_{i-1/2}^p)^+ = \max(s_{i-1/2}^p, 0), \qquad (s_{i-1/2}^p)^- = \min(s_{i-1/2}^p, 0), \quad (3.55)$$

which can also be written as

$$(s_{i-1/2}^p)^\pm = \frac{1}{2}(s_{i-1/2}^p \pm |s_{i-1/2}^p|). \quad (3.56)$$

The flux vector $\tilde{\boldsymbol{F}}_{i-1/2}$ is what LeVeque calls the high-resolution correction. It is given by

$$\tilde{\boldsymbol{F}}_{i-1/2} = \frac{1}{2}\sum_{p=1}^{m} |s_{i-1/2}^p|\left(1 - \frac{\Delta t}{\Delta x}|s_{i-1/2}^p|\right)\widetilde{\mathcal{W}}_{i-1/2}^p, \quad (3.57)$$

where $\widetilde{\mathcal{W}}_{i-1/2}^p$ is a limited version of the wave $\mathcal{W}_{i-1/2}^p$ (see Section 3.3.4 on page 56).

It should be noted that (3.54) leads to a conservative method only if the condition

$$\boldsymbol{f}(\boldsymbol{Q}_i) - \boldsymbol{f}(\boldsymbol{Q}_{i-1}) = \sum_{p=1}^{m} s_{i-1/2}^{p} \mathcal{W}_{i-1/2}^{p} \tag{3.58}$$

is satisfied (LeVeque, 2002, Section 15.3). This is precisely what the Roe method does.

3.3.2 Roe linearization

The Roe (1981) linearization of conservation laws is well explained by LeVeque (2002, Section 15.3). Here some of the key points are repeated, after which the multifluid extension is presented.

Conservation law basics

To define an approximate Riemann solution, the nonlinear problem

$$\frac{\partial \boldsymbol{q}}{\partial t} + \frac{\partial}{\partial x}\boldsymbol{f}(\boldsymbol{q}) = \boldsymbol{0} \tag{3.59}$$

is replaced by a linearized problem defined locally at each cell interface;

$$\frac{\partial \hat{\boldsymbol{q}}}{\partial t} + \hat{\boldsymbol{A}}_{i-1/2}\frac{\partial \hat{\boldsymbol{q}}}{\partial x} = \boldsymbol{0}. \tag{3.60}$$

The matrix $\hat{\boldsymbol{A}}_{i-1/2}$ is an approximation to $\boldsymbol{f}'(\boldsymbol{q})$, valid in a neighbourhood of the data $\boldsymbol{Q}_{i-1}$ and $\boldsymbol{Q}_i$, and it is called the Roe matrix. It should satisfy the following conditions:

1. $\hat{\boldsymbol{A}}_{i-1/2}$ is diagonalizable with real eigenvalues,
2. $\hat{\boldsymbol{A}}_{i-1/2} \to \boldsymbol{f}'(\bar{\boldsymbol{q}})$ as $\boldsymbol{Q}_{i-1}, \boldsymbol{Q}_i \to \bar{\boldsymbol{q}}$,
3. $\hat{\boldsymbol{A}}_{i-1/2}(\boldsymbol{Q}_i - \boldsymbol{Q}_{i-1}) = \boldsymbol{f}(\boldsymbol{Q}_i) - \boldsymbol{f}(\boldsymbol{Q}_{i-1})$.

Condition 1 ensures that (3.60) is hyperbolic, condition 2 makes it consistent with the original conservation law (3.59), and condition 3 guarantees that (3.54) yields a conservative method. Hence the Lax–Wendroff theorem (given in LeVeque, 2002, Section 12.10) states that the method, if it converges, will converge to a weak solution of the conservation law (3.59).

Moreover, the latter condition is derived from imposing the property on $\hat{\boldsymbol{A}}_{i-1/2}$ that if $\boldsymbol{Q}_{i-1}$ and $\boldsymbol{Q}_i$ are connected by a single wave $\mathcal{W}^p = \boldsymbol{Q}_i - \boldsymbol{Q}_{i-1}$ in the true Riemann solution, then $\mathcal{W}^p$ should also be an eigenvector of $\hat{\boldsymbol{A}}_{i-1/2}$:

If $\boldsymbol{Q}_{i-1}$ and $\boldsymbol{Q}_i$ are connected by a single wave, then the Rankine-Hugoniot condition (that is, conservation across a discontinuity) gives:

$$\boldsymbol{f}(\boldsymbol{Q}_i) - \boldsymbol{f}(\boldsymbol{Q}_{i-1}) = s(\boldsymbol{Q}_i - \boldsymbol{Q}_{i-1}), \tag{3.61}$$

where s is the wave speed. If this is also to be a solution to the linearized Riemann problem, then we must have

$$\hat{\boldsymbol{A}}_{i-1/2}(\boldsymbol{Q}_i - \boldsymbol{Q}_{i-1}) = s(\boldsymbol{Q}_i - \boldsymbol{Q}_{i-1}), \tag{3.62}$$

which shows that the wave $\mathcal{W}^p$ should be an eigenvector of $\hat{\boldsymbol{A}}_{i-1/2}$. Combining the two above equations gives condition 3.

For the Roe solver, we have the interpretation that

$$\mathcal{A}^{\pm}\Delta\boldsymbol{Q}_{i-1/2} = \hat{\boldsymbol{A}}^{\pm}_{i-1/2}(\boldsymbol{Q}_i - \boldsymbol{Q}_{i-1}). \tag{3.63}$$

Herein,

$$\hat{\boldsymbol{A}}^{\pm}_{i-1/2} = \hat{\boldsymbol{R}}_{i-1/2}\hat{\boldsymbol{\Lambda}}^{\pm}_{i-1/2}\hat{\boldsymbol{R}}^{-1}_{i-1/2}, \tag{3.64}$$

where $\hat{\boldsymbol{R}}_{i-1/2}$ is the matrix having the right eigenvectors $\hat{\boldsymbol{r}}_{i-1/2}$ of $\hat{\boldsymbol{A}}_{i-1/2}$ as its columns, and $\hat{\Lambda}^{+}_{i-1/2}$ and $\hat{\Lambda}^{-}_{i-1/2}$ are the diagonal matrices containing the positive and negative eigenvalues, respectively, of $\hat{\boldsymbol{A}}_{i-1/2}$.

The approximate Riemann solution consists of m waves proportional to the eigenvectors $\hat{\boldsymbol{r}}_{i-1/2}$ of $\hat{\boldsymbol{A}}_{i-1/2}$, propagating with speeds

$$s^p_{i-1/2} = \hat{\lambda}^p_{i-1/2} \tag{3.65}$$

given by the eigenvalues. The proportionality coefficients $\beta^p_{i-1/2}$ can be found by solving the linear system

$$\boldsymbol{Q}_i - \boldsymbol{Q}_{i-1} = \sum_{p=1}^{m} \beta^p_{i-1/2}\hat{\boldsymbol{r}}^p_{i-1/2}, \tag{3.66}$$

and $\beta^p_{i-1/2}$ can be interpreted as wave strengths (Toro, 1999, Section 2.3.3). The solution of the equation (3.66) is

$$\boldsymbol{\beta}_{i-1/2} = \hat{\boldsymbol{R}}^{-1}_{i-1/2}(\boldsymbol{Q}_i - \boldsymbol{Q}_{i-1}), \tag{3.67}$$

whence the waves can be found as

$$\mathcal{W}^p_{i-1/2} = \beta^p_{i-1/2}\hat{\boldsymbol{r}}^p_{i-1/2}. \tag{3.68}$$

One disadvantage of using a linearized Riemann solver is that the approximate Riemann solution consists only of discontinuities, with no rarefaction waves (LeVeque, 2002, Section 15.3.5). This may require the use of an entropy fix, see Section 3.3.3 on page 55. For the result presented here, no entropy fix is employed unless otherwise stated.

Multifluid extension

Given the definitions of the previous subsection, the remaining chief difficulty is actually finding the Roe matrix $\hat{\boldsymbol{A}}_{i-1/2}$. It is done by finding a special average $\hat{\boldsymbol{Q}}_{i-1/2}$ of $\boldsymbol{Q}_{i-1}$ and $\boldsymbol{Q}_i$ such that

$$\hat{\boldsymbol{A}}_{i-1/2} = \boldsymbol{f}'(\hat{\boldsymbol{Q}}_{i-1/2}) \tag{3.69}$$

has the desired properties. Roe (1981) devised a method for hyperbolic conservation laws (3.59), which is explained by LeVeque (2002, Section 15.3).

The multifluid equations pose a problem, since they cannot be written in the conservation form (3.59). Nevertheless, a Roe-type method was derived by Toumi (1996) for the multifluid equations (including the energy equation), and a version for the isentropic multifluid equations was presented by Toumi and Kumbaro (1996). In those articles, the liquid density was assumed to be constant. Under the additional assumption of smooth solutions, the equation system could be written in conservation form, and a Roe matrix was derived, using some manipulations.

In the present work, we do not wish to make the above-mentioned assumptions. Hence we follow the approach of Evje and Flåtten (2003), who simply opted at showing that their candidate for a Roe matrix fulfilled the 'weak' conditions of Toumi and Kumbaro (1996). Here these conditions are given as stated by Evje and Flåtten (2003):

1. $\hat{\boldsymbol{A}}_{i-1/2}$ is diagonalizable with real eigenvalues,
2. $\hat{\boldsymbol{A}}_{i-1/2} \to \boldsymbol{A}(\bar{\boldsymbol{q}})$ smoothly as $\boldsymbol{Q}_{i-1}, \boldsymbol{Q}_i \to \bar{\boldsymbol{q}}$,
3. $\hat{\boldsymbol{A}}_{i-1/2}(\boldsymbol{Q}_i - \boldsymbol{Q}_{i-1}) = \Delta\boldsymbol{F}(\boldsymbol{Q}_{i-1}, \boldsymbol{Q}_i)$.

The two first conditions are relatively straightforward. The last one involves some trickery. Herein,

$$\Delta\boldsymbol{F}(\boldsymbol{Q}_{i-1}, \boldsymbol{Q}_i) = \begin{bmatrix} \{\alpha_\mathrm{g}\rho_\mathrm{g}u_\mathrm{g}\} \\ \{\alpha_\ell\rho_\ell u_\ell\} \\ \{\alpha_\mathrm{g}\rho_\mathrm{g}u_\mathrm{g}^2\} + \{\alpha_\mathrm{g}\Delta p_\mathrm{ig}\} + \overline{\alpha}_\mathrm{g}\{p_\mathrm{g} - \Delta p_\mathrm{ig}\} \\ \{\alpha_\ell\rho_\ell u_\ell^2\} + \{\alpha_\ell\Delta p_{\mathrm{i}\ell}\} + \overline{\alpha}_\ell\{p_\ell - \Delta p_{\mathrm{i}\ell}\} \end{bmatrix}, \tag{3.70}$$

where

$$\{x\} = x_i - x_{i-1}. \tag{3.71}$$

The definition of $\Delta\boldsymbol{F}(\boldsymbol{Q}_{i-1}, \boldsymbol{Q}_i)$ is motivated by regrouping terms in the momentum equation (2.85) on page 29, to get

$$\frac{\partial}{\partial t}(\alpha_k\rho_k u_k) + \frac{\partial}{\partial x}\Big(\alpha_k\rho_k u_k^2 + (p_k - p_{\mathrm{i}k})\alpha_k\Big) + \alpha_k\frac{\partial p_{\mathrm{i}k}}{\partial x} = \alpha_k\rho_k g_x. \tag{3.72}$$

In the presence of discontinuities, the equations must be put in integral form in order for a solution to exist. In the momentum equation cast as above, the $\alpha_k \partial p_{ik}/\partial x$ term poses problems, for the integral

$$\int_{\boldsymbol{q}_1}^{\boldsymbol{q}_2} \alpha_k \frac{\partial p_{ik}}{\partial \xi} \, \mathrm{d}\xi \tag{3.73}$$

is dependent on the path $\xi(\boldsymbol{q})$ between the two states $\boldsymbol{q}_1$ and $\boldsymbol{q}_2$. Toumi and Kumbaro (1996) suggested writing such integrals as

$$\int_{\boldsymbol{q}_1}^{\boldsymbol{q}_2} \alpha_k \frac{\partial p_{ik}}{\partial \xi} \, \mathrm{d}\xi = \overline{\alpha}_k(\alpha_{k,1}, \alpha_{k,2})(p_{ik,2} - p_{ik,1}), \tag{3.74}$$

defining the path ξ implicitly through the choice of an averaging function $\overline{\alpha}_k(\alpha_{k,1}, \alpha_{k,2})$. The expression derived by Toumi and Kumbaro (1996) was, somewhat inconveniently, not symmetric with respect to phasic indices. Evje and Flåtten (2003) proposed

$$\overline{\alpha}_k((\alpha_{k,1}, \alpha_{k,2}) = \frac{1}{2}((\alpha_{k,1} + \alpha_{k,2}) \tag{3.75}$$

instead, which is adopted here. Evje and Flåtten (2003) used an average state $\hat{\boldsymbol{Q}}_{i-1/2}$ given by the following expressions, where the phasic indices have been dropped:

$$\begin{aligned}
\hat{u} &= \frac{u_{i-1}\sqrt{(\alpha\rho)_{i-1}} + u_i\sqrt{(\alpha\rho)_i}}{\sqrt{(\alpha\rho)_{i-1}} + \sqrt{(\alpha\rho)_i}}, \\
\hat{\alpha} &= \frac{1}{2}(\alpha_{i-1} + \alpha_i), \\
\hat{\rho} &= \frac{1}{2}(\rho_{i-1} + \rho_i), \\
\widehat{\Delta p} &= \frac{1}{2}(\Delta p_{i-1} + \Delta p_i),
\end{aligned} \tag{3.76}$$

where Δp is the interfacial pressure difference (3.30) on page 44. Putting all this into the coefficient matrix (3.34), $\boldsymbol{A}(\hat{\boldsymbol{Q}}) = \hat{\boldsymbol{A}}(\boldsymbol{Q}_{i-1}, \boldsymbol{Q}_i)$, using the equation of state (2.88) to remove the densities, and assuming that the phasic pressures are different only by a constant, one can confirm that condition 3 on the previous page is satisfied.

Considerations for the five-equation system

The verification of condition 3 on the preceding page was performed for the four-equation system. However, the same exercise can be performed for the

five-equation system, that is, the coefficient matrix (3.43). In doing that, it is necessary to define the average interfacial velocity. Here, similarly to what was done in the equation (3.75), we took

$$\overline{u}_{\mathrm{i}k} = \frac{1}{2}(u_{\mathrm{i}k,1} + u_{\mathrm{i}k,2}), \tag{3.77}$$

and, in addition to equation (3.76), we set

$$\hat{u}_{\mathrm{i}} = \frac{1}{2}(u_{\mathrm{i},i-1} + u_{\mathrm{i},i}). \tag{3.78}$$

Contrary to the case for the four-equation system, here the phasic pressures can be linearly independent.

Karni *et al.* (2004) presented results for a Roe-type scheme for a seven-equation system, that is, without assuming isentropic flow, contrary to what is done the present work. Karni *et al.* (2004) did not use quite the same Roe average as the one employed here (equations (3.76) and (3.78)). In particular, they used the average $\widehat{\alpha\rho}_i = \sqrt{(\alpha\rho)_{i-1}(\alpha\rho)_i}$.

3.3.3 Sonic entropy fix

For transonic rarefactions, that is, when an eigenvalue λ^p is negative to the left of the p-wave, $\mathcal{W}^p$, and positive to the right, a scheme using a linearized Riemann solver may converge to an unphysical solution, violating the entropy condition (LeVeque, 2002, Section 15.3.5).

Several remedies are conceivable. Here we will outline two entropy fixes, as presented by LeVeque.

In the Roe scheme, the numerical viscosity is proportional to the eigenvalues. Hence, when an eigenvalue is close to zero, the amount of numerical viscosity might be too small to prevent an entropy-condition violation.

Harten's entropy fix

Harten's entropy fix (Harten, 1983) can be regarded as an addition of numerical viscosity to the pth field if the eigenvalue $\hat{\lambda}^p_{i-1/2}$ is too close to zero. In the present framework, this is achieved by redefining the functions $(\cdot)^+$ and $(\cdot)^-$ employed for the wave speeds in the equation (3.53) (but not those in (3.57)):

$$\begin{aligned} (\lambda)^- &\equiv \frac{1}{2}[\lambda - \phi_\delta(\lambda)], \\ (\lambda)^+ &\equiv \frac{1}{2}[\lambda + \phi_\delta(\lambda)]. \end{aligned} \tag{3.79}$$

Herein, $\phi_\delta(\lambda)$ is a smoothed version of the absolute-value function that is always positive, staying above some value $\delta/2$:

$$\phi_\delta(\lambda) = \begin{cases} |\lambda| & \text{if } |\lambda| \geq \delta, \\ (\lambda^2 + \delta^2)/(2\delta) & \text{if } |\lambda| < \delta. \end{cases} \tag{3.80}$$

An advantage of this approach is its easy implementation. A disadvantage, on the other hand, is that the parameter δ must typically be tuned to the problem.

Note that the definition (3.79) agrees with the usual one (3.56) when $\phi_\delta(\lambda) = |\lambda|$.

The LLF entropy fix

The local Lax–Friedrichs method (LLF) can also be used as an approach for adding more numerical viscosity. As for Harten's entropy fix, it can be viewed as a redefinition of $(\lambda)^\pm$ to be employed in the equation (3.53):

$$(\hat{\lambda}^p_{i-1/2})^\pm \equiv \frac{1}{2}\Big[\hat{\lambda}^p_{i-1/2} \pm \max\Big(|\lambda^p_{i-1}|, |\lambda^p_i|\Big)\Big]. \tag{3.81}$$

Here, λ^p_{i-1} and λ^p_i are the pth eigenvalues evaluated at the states $\boldsymbol{Q}_{i-1}$ and $\boldsymbol{Q}_i$, respectively.

An advantage of the LLF approach is that it contains no parameters to be tuned. However, it has the disadvantage of adding numerical viscosity to all fields, whether or not there is a transonic rarefaction. Nevertheless, whenever the solution is smooth, we have $\hat{\lambda}^p_{i-1/2} \approx \lambda^p_{i-1} \approx \lambda^p_i$, and so (3.81) is not far from the standard definition (3.56).

From a numerical point of view, the LLF entropy fix has another disadvantage: It involves additional evaluations of the eigenvalues of the coefficient matrix, something which may be computationally expensive.

3.3.4 High-resolution terms

The high-resolution correction terms defined by the equation (3.57) is a way of obtaining good accuracy while avoiding to introduce spurious oscillations: The spatial discretization approaches second order when the solution is smooth, but it becomes first order at steep gradients.

As stated in Section 3.3.2, the wave speeds $s^p_{i-1/2}$ are taken to be the eigenvalues of the Roe matrix. The limited waves $\widetilde{\mathcal{W}}^p_{i-1/2}$ are found by comparing the wave $\mathcal{W}^p_{i-1/2}$ with the upwind wave $\mathcal{W}^p_{I-1/2}$ (see LeVeque, 2002, Section 9.13),

where

$$I = \begin{cases} i-1 & \text{if } s^p_{i-1/2} \geq 0, \\ i+1 & \text{if } s^p_{i-1/2} < 0. \end{cases} \tag{3.82}$$

We write

$$\widetilde{\mathcal{W}}^p_{i-1/2} = \phi(\theta^p_{i-1/2})\mathcal{W}^p_{i-1/2}, \tag{3.83}$$

where ϕ is a flux-limiter function, and $\theta^p_{i-1/2}$ is a measure of the smoothness of the pth characteristic component of the solution:

$$\theta^p_{i-1/2} = \frac{\mathcal{W}^p_{I-1/2} \cdot \mathcal{W}^p_{i-1/2}}{\mathcal{W}^p_{i-1/2} \cdot \mathcal{W}^p_{i-1/2}}, \tag{3.84}$$

where $\cdot$ denotes the scalar product in $\mathbb{R}^m$. LeVeque (2002, Section 6.11) presents various flux-limiter functions that can be used together with the above-defined smoothness measure $\theta^p_{i-1/2}$:

Linear methods

The upwind method is first-order, while the Lax–Wendroff, Beam–Warming, and Fromm methods are second-order.

$$\begin{aligned} \text{First-order upwind}: &\quad \phi(\theta) = 0, \\ \text{Lax–Wendroff}: &\quad \phi(\theta) = 1, \\ \text{Beam–Warming}: &\quad \phi(\theta) = \theta, \\ \text{Fromm}: &\quad \phi(\theta) = \frac{1}{2}(1+\theta). \end{aligned} \tag{3.85a}$$

High-resolution limiters

The high-resolution limiters produce methods that are formally first-order, but they approach second-order methods for smooth solutions.

$$\begin{aligned} \text{minmod}: &\quad \phi(\theta) = \text{minmod}(1,\theta), \\ \text{van Leer}: &\quad \phi(\theta) = \frac{\theta + |\theta|}{1+|\theta|}. \\ \text{MC}: &\quad \phi(\theta) = \max(0, \min((1+\theta)/2, 2, 2\theta)), \\ \text{superbee}: &\quad \phi(\theta) = \max(0, \min(1, 2\theta), \min(2, \theta)), \end{aligned} \tag{3.85b}$$

The minmod function is defined by

$$\text{minmod}(a,b) = \begin{cases} 0 & \text{if } ab \leq 0, \\ a & \text{if } |a| < |b| \text{ and } ab > 0, \\ b & \text{if } |a| \geq |b| \text{ and } ab > 0. \end{cases} \tag{3.86}$$

The MC (monotonized central-difference) limiter appears to be a good default choice for a wide class of problems (LeVeque, 2002, Section 6.10). One might choose a different limiter function for each of the m waves. Some experiments were made in this respect, without obtaining better results.

3.4 Numerical tests

In this section, we analyse the Roe-type scheme for the four-equation system (Roe4), and for the five-equation system (Roe5) by performing numerical simulations.

For the numerical results presented in this chapter, simple boundary conditions were used. The variables not being set as boundary conditions, were extrapolated to the boundaries from the inner domain.

3.4.1 Water faucet test case

The water faucet case is described in Ransom (1987), and it has become a common test case for one-dimensional two-fluid models.

Problem description

The problem consists of a vertical tube 12 m in length and 1 m in diameter. Here, of course, it is represented one-dimensionally. A schematic is shown in Figure 3.1 on the next page. The top has a fixed volumetric inflow rate of water at a velocity of $u_\ell^\circ = 10\,\mathrm{m/s}$, a liquid volume fraction of $\alpha_\ell^\circ = 0.8$ and a temperature of $T = 50\,^\circ\mathrm{C}$. The bottom of the tube is open to the ambient pressure, $p = 1.0 \cdot 10^5\,\mathrm{Pa}$, and the top of the tube is closed to vapour flow.

Initially, the flow is uniform throughout the computational domain, and the initial conditions are equal to the inlet conditions. A thinning of the liquid jet will take place due to the effect of gravity.

Analytical expressions for volume fraction and velocity

Ransom (1987) stated that when pressure variation in the vapour phase is ignored, the transient problem has a simple analytical solution. Nevertheless, this solution was not provided. Coquel *et al.* (1997) provided the solution for

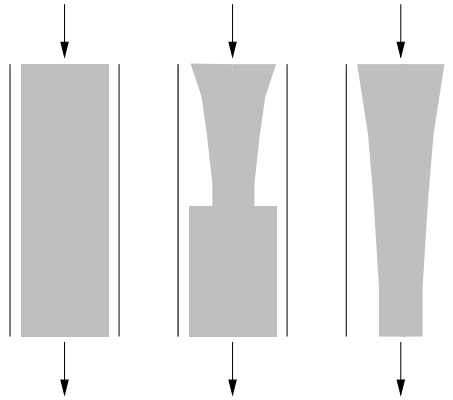

Figure 3.1: Sketch of the water faucet test case. In the transient phase, a volume-fraction discontinuity propagates towards the exit.

the gas volume-fraction profile:

$$\alpha_{\mathrm{g}}(x,t) = \begin{cases} 1 - \dfrac{\alpha_\ell^\circ u_\ell^\circ}{\sqrt{2gx + (u_\ell^\circ)^2}} & \text{if } x \le u_\ell^\circ t + \frac{1}{2} g t^2, \\ 1 - \alpha_\ell^\circ & \text{otherwise,} \end{cases} \tag{3.87}$$

and the expression for the liquid velocity is given by Evje and Flåtten (2003):

$$u_\ell(x,t) = \begin{cases} \sqrt{(u_\ell^\circ)^2 + 2gx} & \text{if } x \le u_\ell^\circ t + \frac{1}{2} g t^2, \\ u_\ell^\circ + gt & \text{otherwise.} \end{cases} \tag{3.88}$$

Trapp and Riemke (1986) partially described the solution procedure, which we give here for completeness.

One can arrive at the above expressions by a simplified analysis considering the liquid alone.[1] That is, the analytical solution is not a solution of the full multifluid equations, but it is assumed that it is very close in this case.

Any pressure variation in the gas, and consequently in the liquid, is ignored. Hence, the density is constant. We first consider the stationary part of the solution. When the transient terms are deleted, the continuity and momentum equations reduce to

$$\frac{\partial}{\partial x}(\rho u) = 0, \tag{3.89}$$

[1] Therefore, phasic indices are dropped henceforth in this subsection.

and

$$\frac{\partial}{\partial x}(\rho u^2) = \rho g, \tag{3.90}$$

respectively. Straightforward integration of the momentum equation yields

$$u(x) = \sqrt{2gx + (u^\circ)^2} \tag{3.91}$$

for the velocity. The expression for the liquid volume fraction then follows from continuity:

$$\alpha^\circ \rho u^\circ = \alpha(x)\rho u(x) \tag{3.92}$$

or

$$\alpha(x) = \frac{\alpha^\circ u^\circ}{u(x)}. \tag{3.93}$$

A liquid particle leaving the faucet at $t = 0$ will mark the border between the initial condition and the following transient solution. Since the pressure is constant, the speed of this particle will be that of a particle falling under the influence of gravity. Newton's second law gives

$$mg = m\frac{\mathrm{d}u}{\mathrm{d}t} \tag{3.94}$$

and integrated,

$$u(t) = gt + u^\circ. \tag{3.95}$$

The position of the article is, of course, given by

$$\frac{\mathrm{d}x}{\mathrm{d}t} = u(t), \tag{3.96}$$

inserting (3.95) and integrating gives

$$x(t) = gt^2 + u^\circ t + x^\circ, \tag{3.97}$$

and since $x^\circ = 0$,

$$x(t) = u^\circ t + gt^2. \tag{3.98}$$

The above considerations lead to the equations (3.87) and (3.88).

Grid convergence and limiter functions

The grid convergence of the Roe4 method was tested on numerical grids ranging from 51 to 1601 grid points, using the different limiter functions described in Section 3.3.4 on page 56. The time step was set to $\Delta t = 1.97 \cdot 10^{-5}$ s, which corresponds to a Courant–Friedrichs–Lewy CFL number of $C = 0.9$ for the finest grid. For all the calculations presented in the present section, the CATHARE model (2.109) was used for the interfacial pressure difference.

No limiter First, liquid volume-fraction profiles are presented at time $t = 0.6$ s in Figure 3.2 on the next page. In Figure 3.2(a), no limiter function was employed; this is called the first-order (upwind) method[2]. It is seen that the convergence was steady, but slow. In fact, the convergence was less than first order, even if the scheme is formally first-order accurate in space. This is due to the discontinuity in the solution. For discontinuous solutions, the smooth-solution order of the scheme can normally not be attained (see LeVeque, 2002, Section 8.7). In Figure 3.2(a), a data set is added for 3201 grid points to further illustrate the convergence. For this calculation, a CFL number of $C = 0.9$ was used, that is, the time step was shorter than for the other grids.

High-resolution limiters Figure 3.2(b) shows the results for the minmod limiter. It is known as the most diffusive of the limiter functions, and it is perhaps surprising that it gave overshoots in front of the discontinuity in this case. The magnitude of the overshoots diminished by grid refinement, however. All the high-resolution methods gave overshoots for the coarsest grid of 51 points, but this is only shown for the monotonized central-difference (MC) limiter in Figure 3.2(d). The results for the van Leer limiter are given in Figure 3.2(c). Both the van Leer and the MC limiter performed well in this case, and can be regarded as good all-round limiters.

Volume-fraction profiles calculated using the superbee limiter can be seen in Figure 3.2(e). The superbee limiter performed similarly to the van Leer and the MC limiter on the very finest grid, but on the 201-point grid it gave a somewhat distorted top of the volume-fraction profile, and on the 101-point grid it gave overshoots.

Second-order limiters The linear limiter functions corresponding to the Lax–Wendroff, the Beam–Warming and the Fromm methods have been tested, and

[2] Sometimes it is only referred to as the upwind method. This is slightly confusing, as the methods arising from the use of limiter functions are also upwind methods.

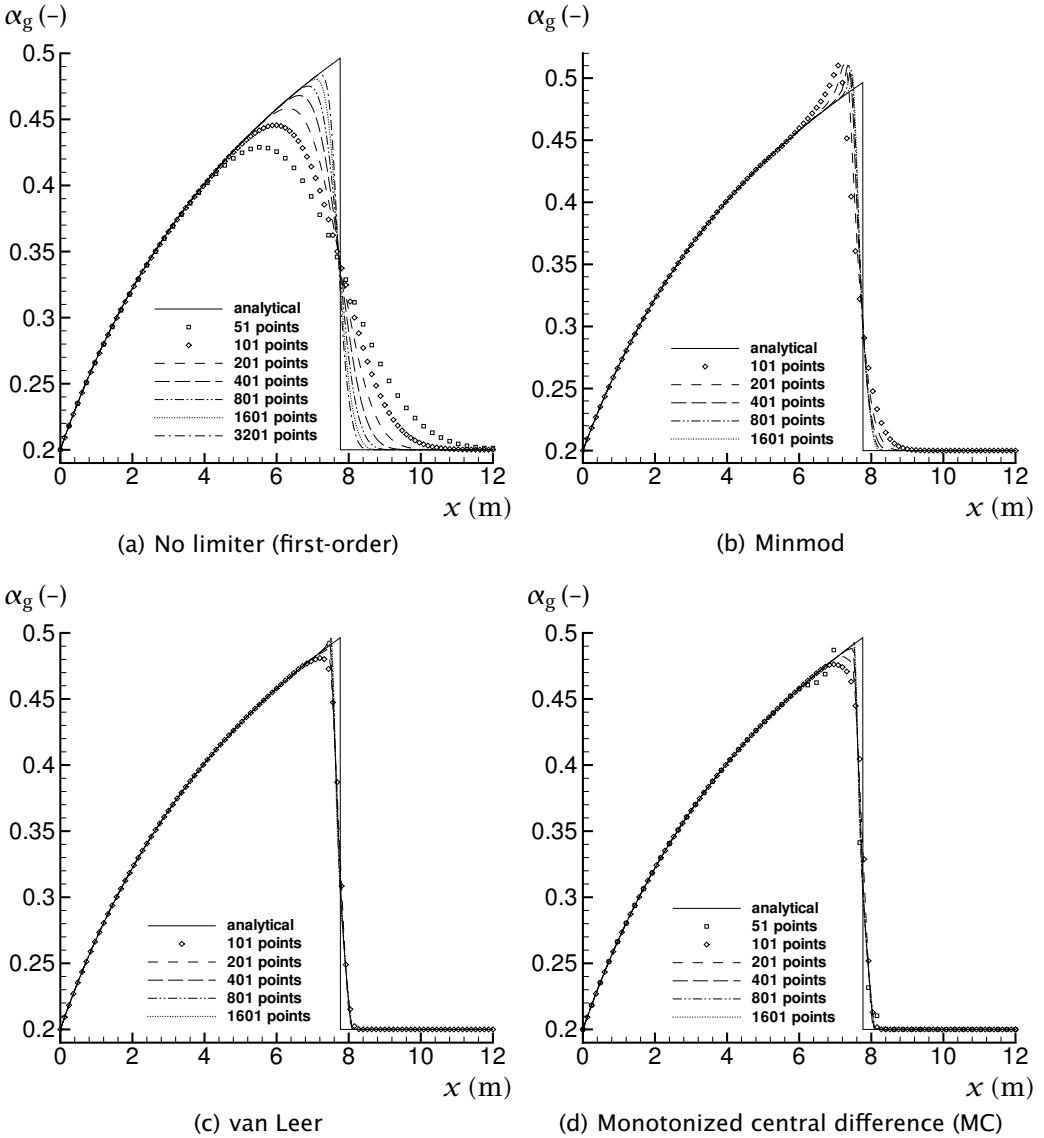

(a) No limiter (first-order)

(b) Minmod

(c) van Leer

(d) Monotonized central difference (MC)

Figure 3.2: Gas volume fraction for the water faucet. Grid convergence of the Roe4 method for different limiter functions.

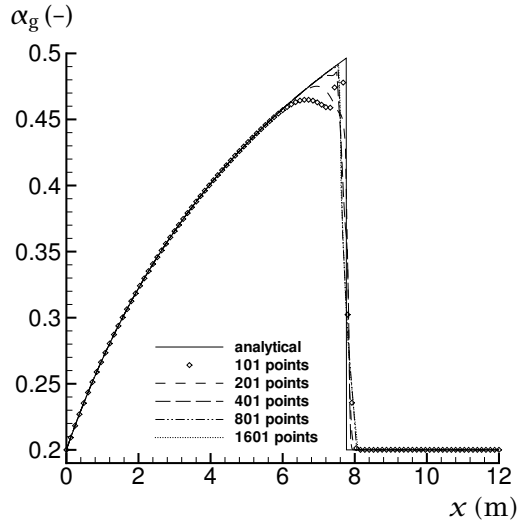

(e) Superbee

Figure 3.2: (Continued) Gas volume fraction for the water faucet. Grid convergence of the Roe4 method for different limiter functions.

the resulting volume-fraction profiles are shown in Figure 3.3 on the following page for a 101-point grid and $C = 1$. These methods are second-order in space, yet, as the figure shows, that is no guarantee for a good solution. The Lax–Wendroff method produces oscillations travelling slower than the discontinuity, whereas the Beam–Warming method creates oscillations which are faster. This behaviour is discussed by LeVeque (1990, Chapter11) for the scalar case, by showing that the methods, while being second-order approximations to the advection equation, are third-order accurate approximations to a dispersive equation. That discussion is somewhat shorter in the new edition (LeVeque, 2002, Section 8.6).

In the present case, the Fromm method gives the best results among the linear methods. The oscillations seem to occur ahead of the discontinuity, but they are weaker than the ones produced by the Beam–Warming method.

Pressure The pressure is by far the most sensitive variable in the faucet case. It is shown in Figure 3.4 on the next page for the MC limiter and for the first-order scheme. It can be observed that the first-order and the MC schemes seem to converge to the same value, and that the latter converges much faster. The pressure profile is also sensitive to the boundary treatment. See Section 6.4.1 on page 160.

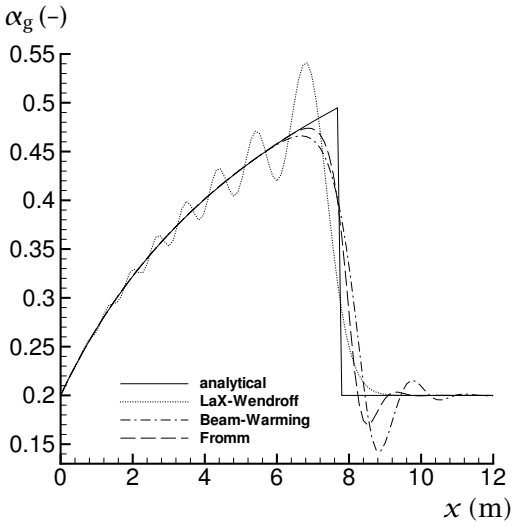

Figure 3.3: Gas volume fraction for the water faucet. Roe4 method and linear limiter functions on a 101-point grid.

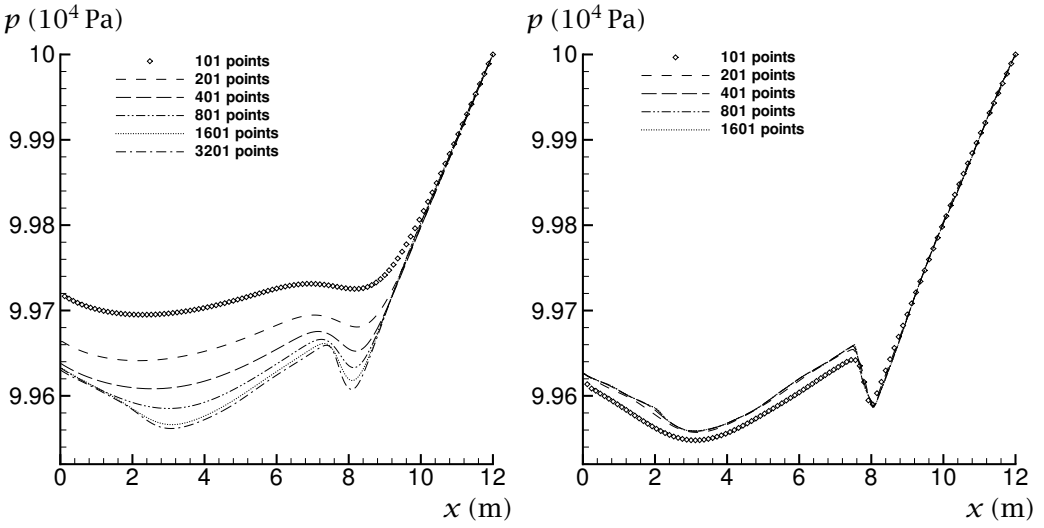

(a) First-order (no limiter)

(b) MC limiter

Figure 3.4: Pressure for the water faucet. Grid convergence of the Roe4 method with and without a limiter function.

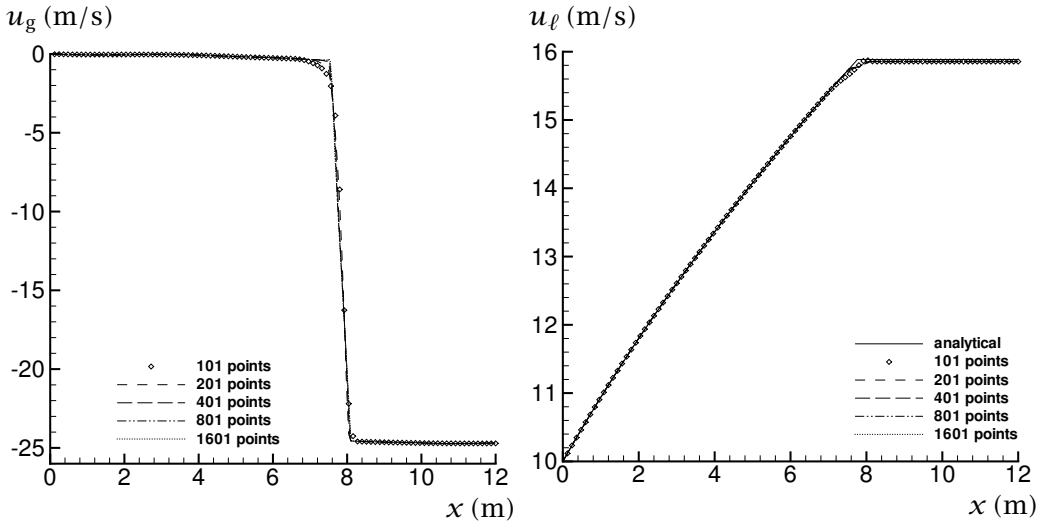

(a) Gas velocity (b) Liquid velocity

Figure 3.5: Velocities for the water faucet. Grid convergence of the Roe4 method.

The remaining physical variables, namely the gas and liquid velocities, are displayed in Figure 3.5. As shown in Figure 3.5(b), the Roe4 method reproduced the analytical solution for the liquid velocity accurately, except just at the location of the volume-fraction discontinuity.

A comparison between the first-order scheme and the high-resolution method using the MC limiter function is given in Figure 3.6 on the following page. It is clear that the first-order method needs over ten times more grid points than the high-resolution method to produce a comparable volume-fraction profile.

Results for the Roe5 scheme Figure 3.7 on page 67 displays the results of computations performed using the Roe5 method with the MC limiter and numerical grids from 26 to 10001 points. The time-step length was the one corresponding to $C = 0.9$ for the finest grid, in this case $\Delta t = 1.06 \cdot 10^{-6}$ s. What is most striking about the figure, is that the results for the grids between 101 and 10001 points are virtually identical. This was not expected, and an explanation has yet to be found. Further, it can be seen that the Roe5 method is much more diffusive than the Roe4 method for the intermediate and fine grids. For the very coarse grid of 26 points, on the other hand, the Roe5 results are surprisingly good, and better than those of Roe4.

The same exercise has been performed without using any limiter function,

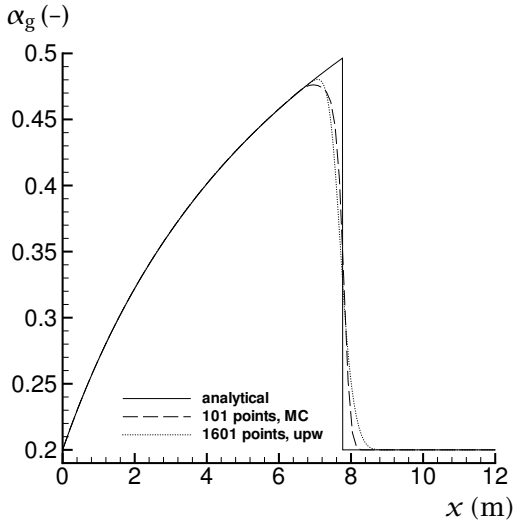

Figure 3.6: Gas volume fraction for the water faucet. Comparison of the first-order and the MC-limiter methods with the Roe4 scheme.

that is, with the first-order Roe5 method. The results are given in Figure 3.8 on page 68. The results for the fine grid of 10001 points are equal to those of the MC-limited Roe5 method. However, for the coarser grids, the first-order method shows the expected behaviour of producing more diffusive results.

Reference is made to Chapter 5, where results obtained with the Roe5 scheme are shown to agree very well with those from a five-equation version of the discrete-equation method of Abgrall and Saurel (2003).

Convergence order The error of the numerical approximation Q to a physical variable q at any time step is given by

$$E = Q - q. \tag{3.99}$$

To quantify the error in the calculation domain Ω, we measure it using the p-norms

$$\|E\|_p = \left(\Delta x \sum_{\forall i \in \Omega} |E_i|^p \right)^{1/p}, \tag{3.100}$$

which are discrete analogues of the function-space norms

$$\|E\|_p = \left(\int_\Omega |E(x)|^p \, \mathrm{d}x \right)^{1/p}. \tag{3.101}$$

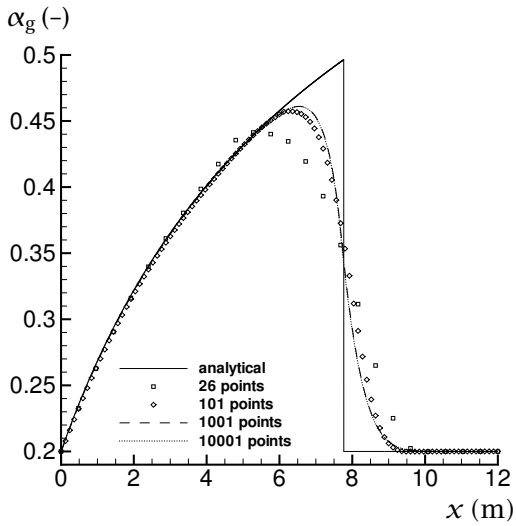

(a) Gas volume fraction

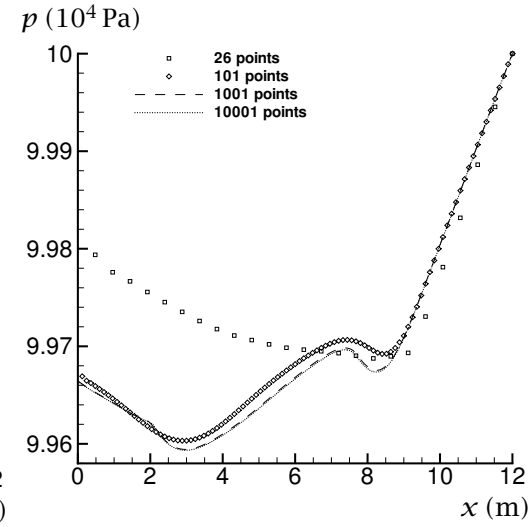

(b) Pressure

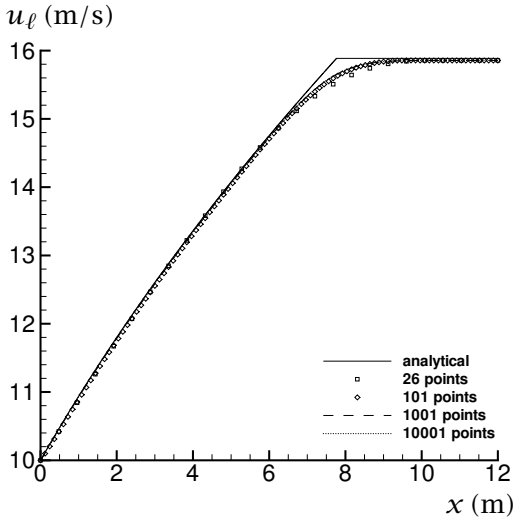

(c) Liquid velocity

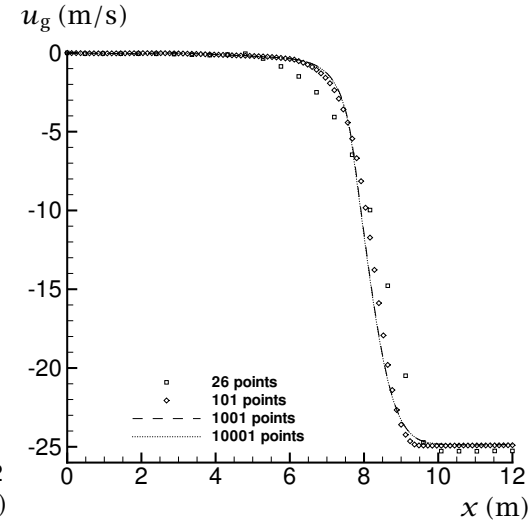

(d) Gas velocity

Figure 3.7: Water faucet. Grid refinement for the MC-limited Roe5 scheme.

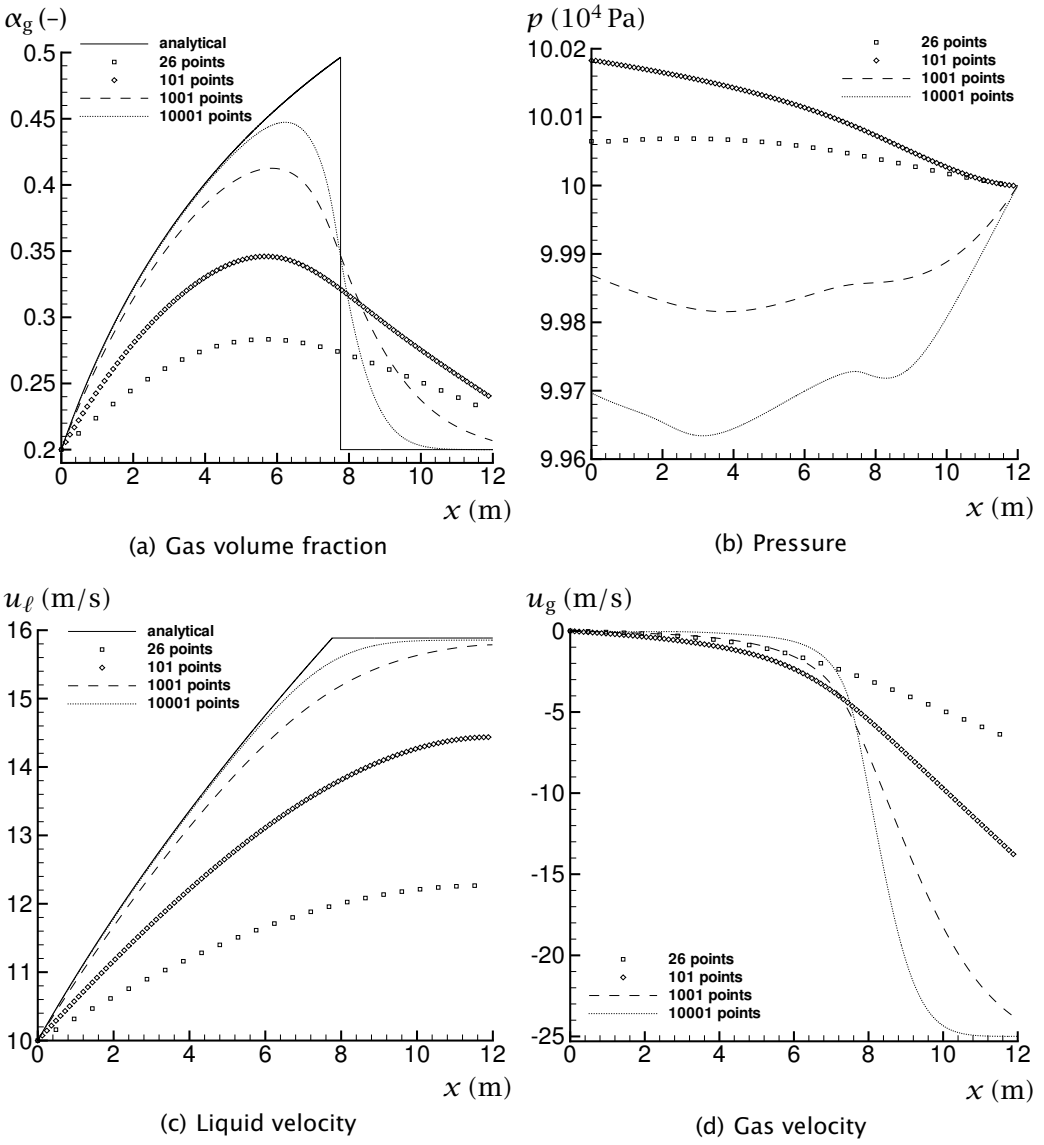

(a) Gas volume fraction

(b) Pressure

(c) Liquid velocity

(d) Gas velocity

Figure 3.8: Water faucet. Grid refinement for the first-order Roe5 scheme.

The 1-norm (with $p = 1$) is commonly used for conservation laws, since integrals of the solution itself are of particular importance (LeVeque, 2002, Section 8.1.1).

A numerical method is said to be accurate of order n in space if

$$\|E\| = \mathcal{O}(\Delta x^n) \text{ as } \Delta x \to 0. \tag{3.102}$$

If we assume that the norm can be written as

$$\|E\| = \gamma(\Delta x)^n, \tag{3.103}$$

where γ is a constant, then the order of convergence between two grids with regular spacings Δx_1 and Δx_2 is given by

$$n = \frac{\ln[\|E(\Delta x_2)\|/\|E(\Delta x_1)\|]}{\ln[\Delta x_2/\Delta x_1]}. \tag{3.104}$$

The convergence of the Roe4 method by grid refinement has been assessed using the 1-norm. It was calculated for the faucet case with the error in the gas volume fraction as error measure, that is, setting

$$E = \alpha_g - \alpha_{g,\text{ref}} \tag{3.105}$$

in (3.100). The reference volume fraction was calculated using the MC limiter on a very fine grid of 10001 points with a CFL number of $C = 0.9$. For the test grids, the time-step length was $\Delta t = 3.17 \cdot 10^{-6}$ s, corresponding to $C = 0.9$ on the reference grid.

The results are given in Table 3.1 on the next page for three different limiter functions: The first-order method (no limiter), the MC limiter, and the Fromm method. The latter method is second-order in space. The grid spacings Δx of 0.48, 0.24, 0.12, 0.06, 0.03 and 0.012 m correspond to grids of 26, 51, 101, 201, 401 and 1001 points, respectively. Hence, the fine grid of 10001 points has a control volume whose centre position corresponds exactly to that of the control-volume centres in each of the employed test grids.

The data under the label 'all domain' have been calculated for all inner control volumes, whereas the other data have been calculated for inner control volumes positioned to the left of $x = 4$ m, that is, where the volume-fraction profiles of Figure 3.2 seemed to be smooth.

The convergence rate n is for the line it stands on, compared to the previous line. For instance, the convergence rate for the first-order method as Δx was refined from 0.48 to 0.24 m, was 0.54.

The table shows that

Table 3.1: Water faucet. Roe4 method. 1-norm of the error in gas volume fraction by grid refinement and for different limiter functions.

		All domain		For $x < 4\,\mathrm{m}$	
Limiter	$\Delta x\,(\mathrm{m})$	$\|E(\alpha_g)\|_1$	n	$\|E(\alpha_g)\|_1$	n
First-Order	0.48	$4.276 \cdot 10^{-1}$	–	$7.162 \cdot 10^{-3}$	–
	0.24	$3.041 \cdot 10^{-1}$	0.49	$3.408 \cdot 10^{-3}$	1.07
	0.12	$2.111 \cdot 10^{-1}$	0.53	$1.584 \cdot 10^{-3}$	1.11
	0.06	$1.389 \cdot 10^{-1}$	0.62	$8.219 \cdot 10^{-4}$	0.95
	0.03	$8.945 \cdot 10^{-2}$	0.63	$4.099 \cdot 10^{-4}$	1.00
	0.012	$4.755 \cdot 10^{-2}$	0.58	$1.655 \cdot 10^{-4}$	0.99
MC	0.48	$1.208 \cdot 10^{-1}$	–	$5.292 \cdot 10^{-4}$	–
	0.24	$2.413 \cdot 10^{-2}$	2.32	$1.734 \cdot 10^{-4}$	1.61
	0.12	$2.618 \cdot 10^{-2}$	−0.12	$7.169 \cdot 10^{-5}$	1.27
	0.06	$1.467 \cdot 10^{-2}$	0.84	$2.783 \cdot 10^{-5}$	1.37
	0.03	$6.157 \cdot 10^{-3}$	1.25	$1.478 \cdot 10^{-5}$	0.92
	0.012	$2.164 \cdot 10^{-3}$	1.14	$5.700 \cdot 10^{-6}$	1.04
Fromm	0.48	$2.188 \cdot 10^{-1}$	–	$3.815 \cdot 10^{-4}$	–
	0.24	$1.342 \cdot 10^{-1}$	0.71	$1.735 \cdot 10^{-4}$	1.14
	0.12	$7.281 \cdot 10^{-2}$	0.88	$7.182 \cdot 10^{-5}$	1.27
	0.06	$3.045 \cdot 10^{-2}$	1.26	$2.792 \cdot 10^{-5}$	1.36
	0.03	$1.276 \cdot 10^{-2}$	1.25	$1.474 \cdot 10^{-5}$	0.92
	0.012	$4.362 \cdot 10^{-3}$	1.17	$5.694 \cdot 10^{-6}$	1.04

– None of the methods attain a convergence rate corresponding to their formal order when the whole domain is considered.

– For the smooth part of the solution, all the methods have a first-order convergence rate.

– The MC-limited scheme has the lowest error for the whole domain.

For the smooth part of the solution, the MC limiter and the Fromm method perform equally, except at the very coarse grid of 26 points. Both have a significantly lower error than the first-order method. However, second-order convergence is not attained. The convergence rate is higher than one for all but one point (from 201 to 401 grid points), but it is never higher than 1.6. It is conceivable that this is due the effect of the discontinuity spreading, even to the 'smooth portion' of the solution. This is certainly possible, regarding the wave-propagation speeds. Some support of this hypothesis is also offered in Section 3.4.2 on page 76, where a nice and smooth solution is studied, and the expected convergence rates are found.

Time-step convergence

Roe4 The effect of time-step refinement, using a 101-point grid and the MC limiter, is shown in Figure 3.9 on the next page. For CFL numbers below 0.5, the effect of time-step refinement is very slight.

Roe5 Results for the Roe5 scheme regarding the effect of time-step refinement is shown in Figure 3.10 on the following page for a grid of 101 points. The difference between the first-order scheme in Figure 3.10(a) and the MC-limiter scheme in Figure 3.10(b) is very large. In the latter figure, the differences between the curves are striking compared to the miniscule ones for the Roe4 method in Figure 3.9. Furthermore, the difference between the first-order scheme and the MC-limiter scheme is very large. For the latter one, as can be seen in Figure 3.10(b), for $C = 0.9$, the volume-fraction profile is very smeared indeed. For $C = 0.01$, on the other hand, it lies between the profiles calculated using the MC-limited and first-order (no-limiter) Roe4 method (Figure 3.2 on page 62). As the CFL number is reduced to miniscule values ($C = 0.0001$), the curves seem to converge. Unfortunately, there is a slight overshoot to the left of the discontinuity.

Figure 3.10 shows that the method resulting from combining the method (3.53) for (the hyperbolic part of) the equation system and an instantaneous pressure-relaxation procedure, is not of high order in time.

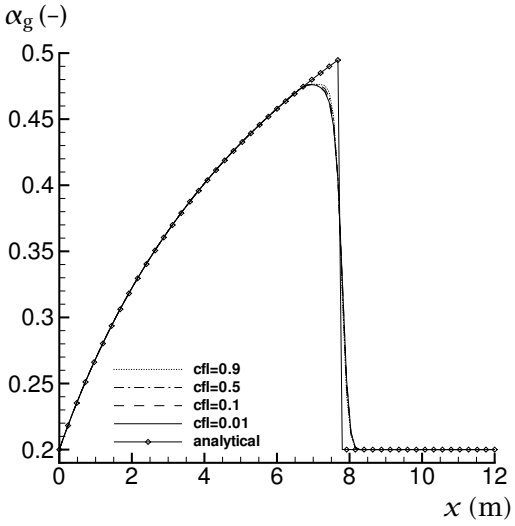

Figure 3.9: Gas volume fractions for the water faucet. Time-step refinement for the Roe4 method using the MC limiter.

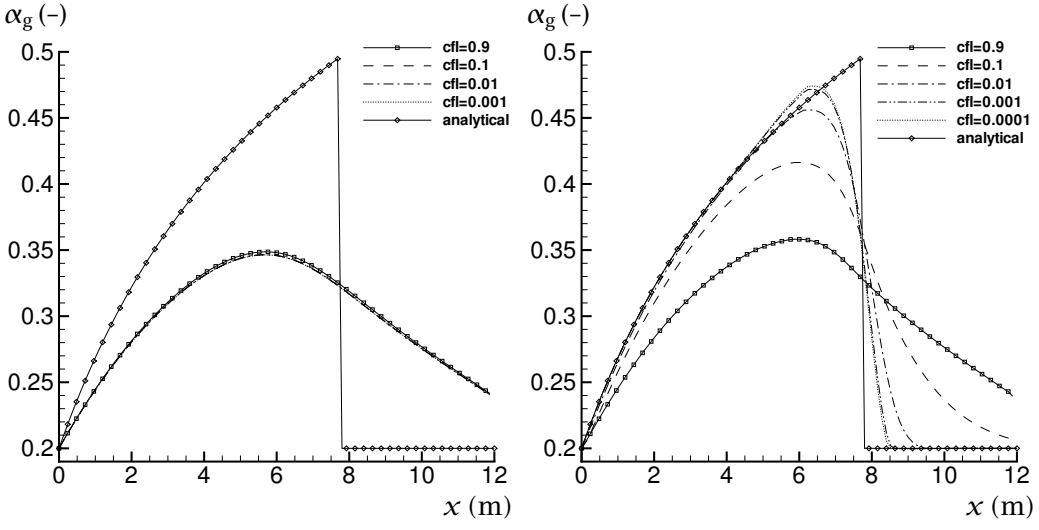

(a) No limiter (first-order)

(b) MC-limiter

Figure 3.10: Gas volume fraction for the water faucet. Effect of time-step length on the Roe5 scheme with and without MC-limiter.

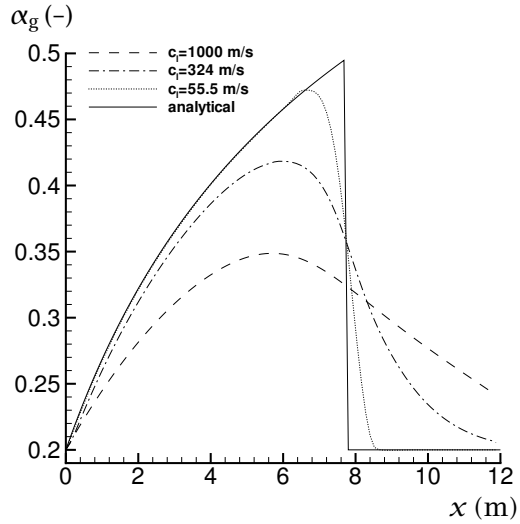

Figure 3.11: Gas volume fraction for the water faucet. Effect of liquid speed of sound on the Roe5 scheme.

Effect of liquid speed of sound

The Roe5 scheme is rather diffusive, and it is tempting to try to remove some of the diffusion. One way of doing that, is by reducing the liquid speed of sound. While this changes the problem under consideration, it illustrates the behaviour of the scheme. An investigation of the effect of the speed of sound is shown in Figure 3.11. The calculations have been performed on a grid of 101 points, using the MC limiter and the same time-step length of $\Delta t = 1.06 \cdot 10^{-4}$ s, corresponding to $C = 0.9$ for the case of the highest (that is, closest-to-physical) liquid speed of sound. The only thing being varied, is the liquid speed of sound, c_ℓ, together with a corresponding variation of ρ_ℓ° to maintain the same initial liquid density, $\rho_\ell = 1000\,\mathrm{kg/m^3}$.

First, we tried to obtain the same maximum eigenvalue as for the four-equation system. At $t = 0.6$ s, the four-equation system has $\lambda_{\max} \approx 340\,\mathrm{m/s}$, and the maximum liquid speed is about 16 m/s. Hence the liquid speed of sound was set to $c_\ell = 324\,\mathrm{m/s}$. The figure shows that this gave less diffusion, but it is still far from what one obtains using the Roe4 scheme.

Next, as an educated guess, $c_\ell = 55.5\,\mathrm{m/s}$ was tried. This helped considerably on the volume-fraction profile, which is now better than the one produced with the first-order Roe4 method on the same grid (see Figure 3.2(a) on page 62). Still, it does not reach the volume-fraction profile from the MC-limited Roe4 method (Figure 3.2(d)).

We remark that the phasic speeds of sound have an effect on the Roe4 scheme as well, but to a much lesser extent than on the Roe5 scheme. This is thought to be due to the pressure-relaxation being performed in the latter scheme. Indeed, in the pressure-relaxation procedure, the densities (and hence pressures) are tightly linked to the volume fraction. Hence fast-moving pressure waves are transferred to the volume fraction, and this may be an explanation of the smeared volume-fraction profiles of the Roe5 scheme.

Wave propagation speed

The different eigenvalues for the four-equation system and the five-equation system might lead one into thinking that sonic waves in the two systems would propagate at different speeds (for instance Flåtten, 2003, Section 3.3.1); for the faucet case at $t = 0.6\,\mathrm{s}$, the maximum eigenvalue in the four-equation system is about $340\,\mathrm{m/s}$, while it is $1013\,\mathrm{m/s}$ in the five-equation system.

However, the above simple consideration does not take the instantaneous pressure-relaxation procedure into account. To illustrate this, we study the following example calculation: In the faucet case, a wave forms at the inlet at $t = 0$, and it travels towards the outlet. This is shown in Figure 3.12 on the facing page. Calculations have been performed using the Roe4 and Roe5 schemes, and both schemes were run using about $C = 0.2$ (that is, a shorter time-step for the Roe5 scheme) and the MC limiter. Figure 3.12(a) shows snapshots of $(\alpha\rho u)_\mathrm{g}$ at $\Delta t = 0.005\,\mathrm{s}$ intervals, while the time history of the same variable at $x = 12\,\mathrm{m}$ is shown in Figure 3.12(b).

Figure 3.12(a) clearly shows that the disturbance propagates with the same velocity in the two schemes. Moreover, no faster-moving disturbances could be observed in any of the variables in the Roe5 scheme.

As can be seen from Figure 3.12(b), the wave reached the boundary at about $t = 0.037\,\mathrm{s}$. At this time, there was virtually no difference between the Roe4 and the Roe5 schemes.

The wave propagation speed was found to be $12\,\mathrm{m}/0.037\,\mathrm{s} \approx 324\,\mathrm{m/s}$, whereas the maximum eigenvalue of the coefficient matrix of the four-equation system was $317\,\mathrm{m/s}$ at $t = 0.005\,\mathrm{m/s}$, increasing to $324\,\mathrm{m/s}$ at $t = 0.2\,\mathrm{m/s}$. The correspondence is clear.

As can be seen for instance in Figure 3.12(b), $(\alpha\rho u)_\mathrm{g}$ immediately starts to increase. The reason for this, is the action of gravity.

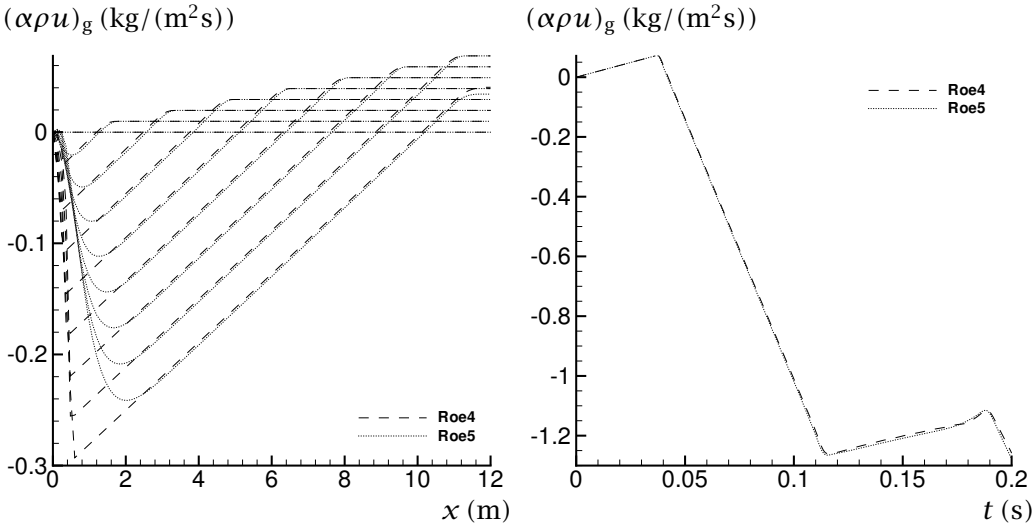

(a) Snapshots at $\Delta t = 0.005$ s intervals

(b) Time history at the outlet

Figure 3.12: Gas volumetric momentum for the water faucet. Comparison of wave propagation in the Roe4 and the Roe5 schemes.

Non-hyperbolic underlying model

One of the advantages of the Roe5 method perceived in Section 3.2.2 on page 45, is that the coefficient matrix remains hyperbolic, even when the '0 model'

$$\Delta p_{ik} = 0 \tag{3.106}$$

is taken for the interfacial pressure difference. For such cases, the 'underlying' four-equation model is non-hyperbolic with complex eigenvalues.

Figure 3.13 on the following page shows the water-faucet gas volume-fraction profile calculated on a grid of 101 points using the MC limiter and a quite short time-step length of $\Delta t = 1.06 \cdot 10^{-6}$ s. Two models have been employed for the interfacial pressure difference; the CATHARE model (2.109) and the 0 model (3.106). Further, two different liquid speeds of sound were tried; $c_\ell = 1000$ m/s and $c_\ell = 55.5$ m/s, as commented upon on page 73.

As can be observed, the use of the 0 model for the interfacial pressure difference together with the low liquid speed of sound results in a severe undershoot in front of the discontinuity, whereas the curve for the CATHARE model and the low liquid speed of sound is quite well-behaved. This may indicate that the use of the Roe5 scheme and similar methods provides no easy way to avoid the problem of complex eigenvalues in the four-equation model.

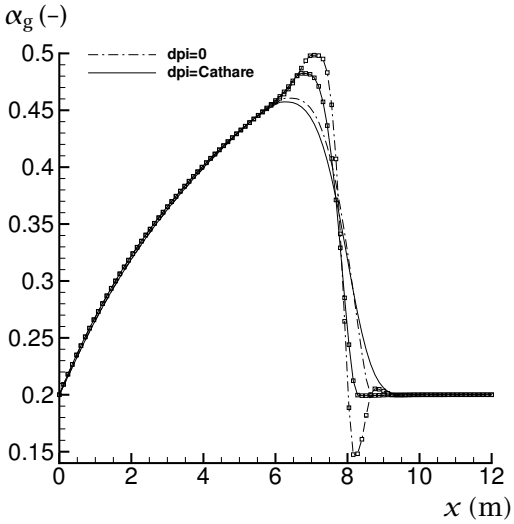

Figure 3.13: Gas volume fraction for the water faucet. Roe5 scheme. Results for the 0 model and the CATHARE model for the interfacial pressure difference, for two liquid speeds of sound, $c_\ell = 1000\,\mathrm{m/s}$ (lines) and $c_\ell = 55.5\,\mathrm{m/s}$ (with □).

For the high liquid speed of sound, no anomalies were incurred by the 0 model. This might be a result of the high liquid speed of sound providing 'enough' diffusion in the Roe5 scheme. Indeed, this was the case even on a fine grid of 20001 points.

Karni *et al.* (2004) reported undershoots for their Roe-type solver with pressure relaxation and the 0 model for the interfacial pressure difference, even for equation-of-state parameters giving a high liquid speed of sound, speculating that this might be due to the ill-posedness of the underlying one-pressure two-phase model.

3.4.2 Advection of a 'hat'

This test case has been designed to test the convergence properties of the Roe4 scheme employing the MC limiter in a case where the solution is smooth. A smooth 'hat' in the volume fraction is advected along a computational domain of length $L = 12\,\mathrm{m}$. The initial volume-fraction profile is given by

$$\alpha_g(x) = \begin{cases} \{1 + 0.49[1 + \tanh(2x - L/3)]\} - 0.99 & \text{if } x < L/2, \\ \{1 + 0.49[1 + \tanh(-2x - 2L/3)]\} - 0.99 & \text{otherwise .} \end{cases} \tag{3.107}$$

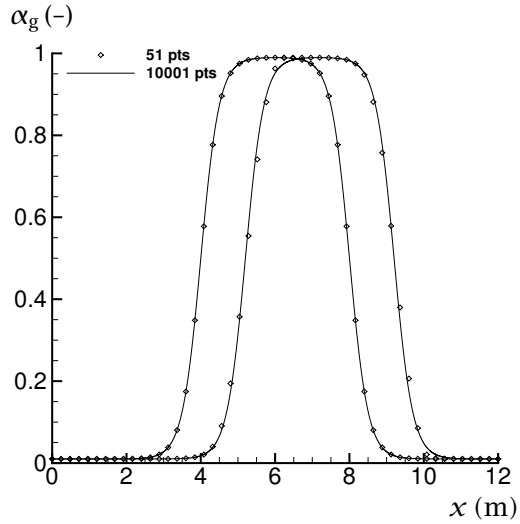

Figure 3.14: Advection of a smooth volume-fraction profile. Initial condition and solution after $t = 0.12\,\mathrm{s}$ for the MC limiter.

The other variables are initially uniform: The initial pressure is $p = 10 \cdot 10^5\,\mathrm{Pa}$, and the initial velocities are $u_g = u_\ell = 10\,\mathrm{m/s}$. The equation-of-state parameters are, as usual, given by Table 2.1 on page 30.

For equal phasic velocities, the coefficient matrix (3.34) has complex eigenvalues when the interfacial pressure-difference is zero. Hence the Soo model (2.107) was employed, with the displacement factor $B_k = 0.999999$.

Grid refinement with constant time-step length

Solutions for different grid sizes were compared at $t = 0.12\,\mathrm{s}$. The tested grids had 51, 101, 201, 401 and 1001 points, corresponding to a grid spacing, Δx, of 0.24, 0.12, 0.06, 0.03 and 0.012, respectively. The reference solution was calculated on a 10001-point grid. The time-step length for all the calculations was $\Delta t = 3.18 \cdot 10^{-6}\,\mathrm{s}$, corresponding to a CFL number of $C = 0.9$ for the reference grid.

Figure 3.14 shows the initial condition for the volume fraction, as well as the solution after $t = 0.12\,\mathrm{s}$. Since the solution is smooth, even the coarse-grid solution is not far away from the reference solution.

Table 3.2 on the next page shows the 1-norm of the volume-fraction error by grid refinement. The norm and the convergence order n were calculated in the same way as for Table 3.1 on page 70, as described in Section 3.4.1. The data

Table 3.2: Smooth volume-fraction advection test case. 1-norm of the error in gas volume fraction by grid refinement with a constant time-step length of $\Delta t = 3.18 \cdot 10^{-6}$ s.

Δx(m)	$\|E(\alpha_g)\|_1$	n
0.24	$6.886 \cdot 10^{-2}$	–
0.12	$1.811 \cdot 10^{-2}$	1.93
0.06	$4.448 \cdot 10^{-3}$	2.03
0.03	$1.092 \cdot 10^{-3}$	2.03
0.012	$1.725 \cdot 10^{-4}$	2.01

Table 3.3: Smooth volume-fraction advection test case. 1-norm of the error in gas volume fraction by grid refinement with a constant CFL number of 0.9.

Δx(m)	$\|E(\alpha_g)\|_1$	n
0.24	$6.595 \cdot 10^{-2}$	–
0.12	$1.695 \cdot 10^{-2}$	1.96
0.06	$4.126 \cdot 10^{-3}$	2.04
0.03	$1.012 \cdot 10^{-3}$	2.03
0.012	$1.603 \cdot 10^{-4}$	2.01

shows that the method (3.53) using the MC limiter is second-order in space.

Grid refinement with constant CFL number

The exercise in the preceding subsection has been repeated, but with a constant CFL number of 0.9. The 1-norm of the volume-fraction error is shown in Table 3.3. As one can see, the MC-limited Roe4 method may be called second-order.

Time-step refinement with a given grid

The convergence-rate by time-step refinement has also been tested for a grid of 101 points. The reference solution was calculated using a time-step length of $\Delta t = 1.0 \cdot 10^{-6}$ s, and the 1-norm of the error in the volume fraction can be seen in Table 3.4 on the facing page. It is clear that the convergence rate in this case is first-order.

Table 3.4: Smooth volume-fraction advection test case. 1-norm of the error in gas volume fraction by time-step refinement with a 101-point grid.

Δt (s)	$\|E(\alpha_g)\|_1$	n
$1.2 \cdot 10^{-4}$	$4.543 \cdot 10^{-4}$	–
$6.0 \cdot 10^{-5}$	$2.259 \cdot 10^{-4}$	1.00
$3.0 \cdot 10^{-5}$	$1.112 \cdot 10^{-4}$	1.02
$1.5 \cdot 10^{-5}$	$5.373 \cdot 10^{-5}$	1.05

Table 3.5: Initial conditions in the large relative velocity (LRV) shock tube

Quantity	symbol (unit)	left	right
Gas volume fraction	α_g (–)	0.29	0.30
Pressure	p (kPa)	265	265
Gas velocity	u_g (m/s)	65	1
Liquid velocity	u_ℓ (m/s)	1	1

Discussion

The grid-refinement results show that the method (3.53) employing a limiter function is second-order for smooth solutions. However, the 'smooth hat' test case did not include source terms. In the present work, source terms are accounted for by adding a term, $\Delta t \boldsymbol{S}_i$, on the right-hand side of (3.53). This corresponds to a Forward Euler time integration. Therefore, the second-order convergence rate may well not be attained for cases with source terms.

The first-order convergence obtained by time-step refinement is a result of the $\Delta t / \Delta x$ term appearing in the flux-correction term (3.57). Therefore, the method cannot be written in semi-discrete form, unless first-order spatial accuracy is found to be sufficient, such that $\tilde{\boldsymbol{F}} \equiv \boldsymbol{0}$. A semi-discrete formulation would have been an advantage, as that would have allowed for employing accurate and stable ODE solvers, such as suitable Runge–Kutta methods (Kraaijevanger, 1991; Carpenter and Kennedy, 1994; Spiteri and Ruuth, 2002; Ketcheson and Robinson, 2005). One semi-discrete method is discussed in Chapter 8 for the drift-flux model.

3.4.3 Large relative velocity shock tube

The large relative velocity (LRV) shock was investigated by Cortes *et al.* (1998); Evje and Flåtten (2003). The initial left and right states are given in Table 3.5.

Roe4 The result of grid refinement for the Roe4 method is shown in Figure 3.15 on the facing page for the primitive variables at $t = 0.1$ s. The calculations were run with a time-step length of $\Delta t = 2.35 \cdot 10^{-5}$ s, corresponding to $C = 0.9$ for the finest grid, and the MC limiter was used.

As Evje and Flåtten (2003) pointed out, the wedge that can be seen in the volume fraction, and also in the gas velocity, at $x = 50$ m, is two volume-fraction waves. This detail is shown for the volume fraction in Figure 3.16. In the figure, data have been added for a grid of 40001 points and $C = 0.9$, something which clearly shows the convergence.

The resolution of sonic waves is dependent on the CFL number. Time-step refinement is shown in Figure 3.17 on page 83 for a grid of 101 points. As can bee seen, the resolution of the sonic waves (at about $x = 25$ m and $x = 85$ m) improves with increasing CFL number, whereas the resolution of volume-fraction waves (at $x = 50$ m) is largely unaffected. The latter effect was also seen for the faucet case in Section 3.4.1.

An improving sonic-wave resolution with increasing CFL number is in accordance with what is known about upwind methods. For instance, an upwind method can solve the advection equation exactly for $C = 1$.

The effect of the limiter function is displayed in Figure 3.18 on page 84. It can be observed that employing the MC limiter function gives a significantly improved resolution of both the sonic waves (Figure 3.18(a)) and the volume-fraction waves (Figure 3.18(b)). Still, the effect in the present case is perhaps less striking that what was observed for the faucet case in Figure 3.2 on page 62. The calculation of Figure 3.18(b) has been performed on a finer grid, since the volume-fraction wedge is confined to a small area.

Roe5 Figure 3.19 on page 85 shows the result of grid refinement for the Roe5 scheme using the MC limiter. The time-step length was $\Delta t = 8.99 \cdot 10^{-6}$ s, corresponding to $C = 0.9$ on the finest grid of 10001 points. The results obtained with the Roe4 method on the fine grid are drawn as a reference. The figure shows that the results of the Roe5 scheme converge towards those of the Roe4 scheme. However, for the volume fraction wave at $x = 50$ m, the convergence is very slow. This is thought to be mainly due to the high diffusivity of the Roe5 scheme, and it can be seen in Figure 3.19(a) for the liquid volume fraction, where the focus is on the middle of the shock tube. In that figure, results from the Roe5 method on a very fine grid of 40001 points, using $C = 0.05$, have been added to illustrate the effect of further grid and time-step refinement. In addition to slow convergence, the Roe5 method suffers from instabilities at the left-hand-side of the volume-fraction wedge.

Time-step refinement is displayed in Figure 3.20 on page 86 for a grid of

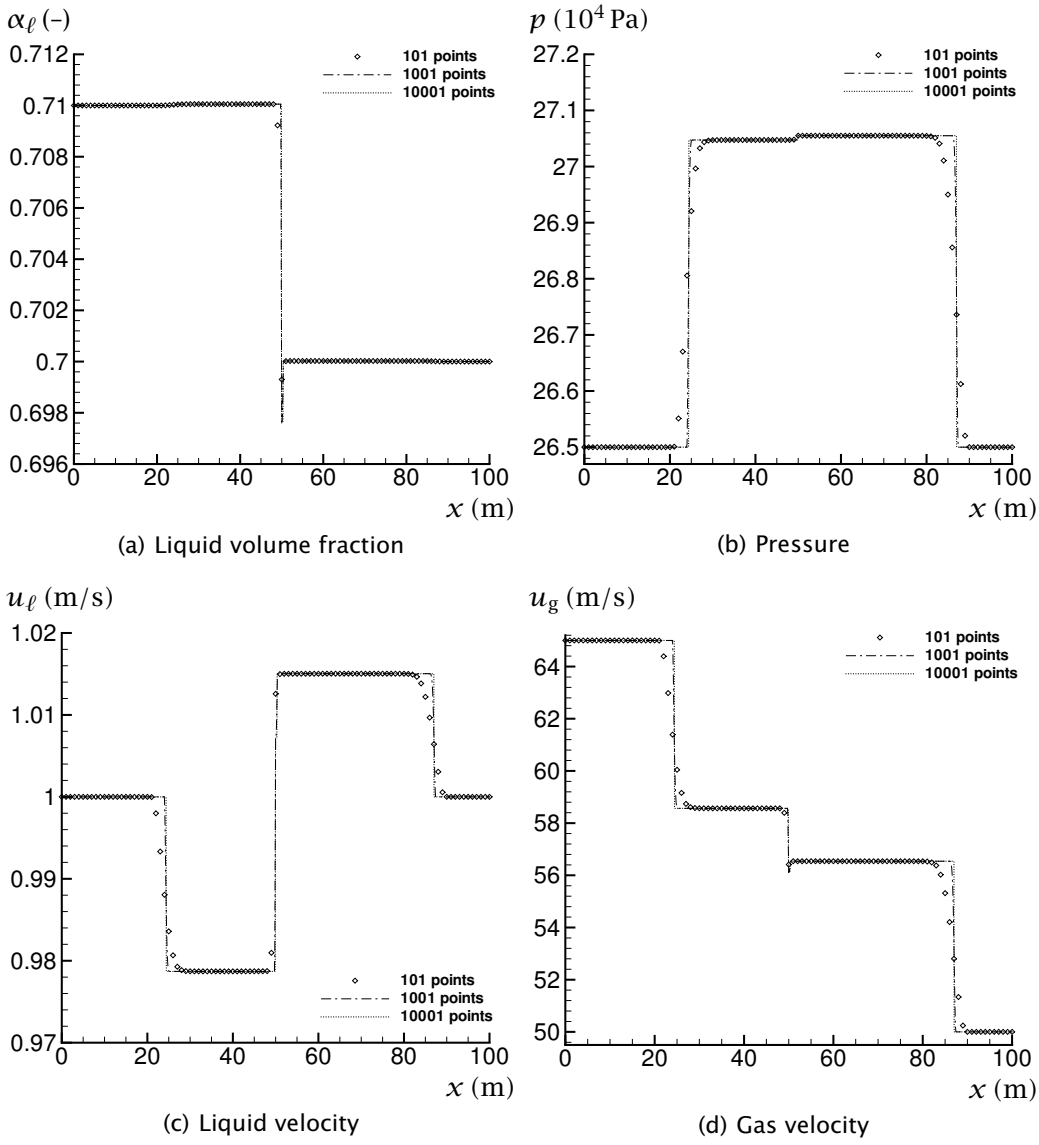

(a) Liquid volume fraction

(b) Pressure

(c) Liquid velocity

(d) Gas velocity

Figure 3.15: LRV shock tube. Grid refinement for the Roe4 (MC) scheme.

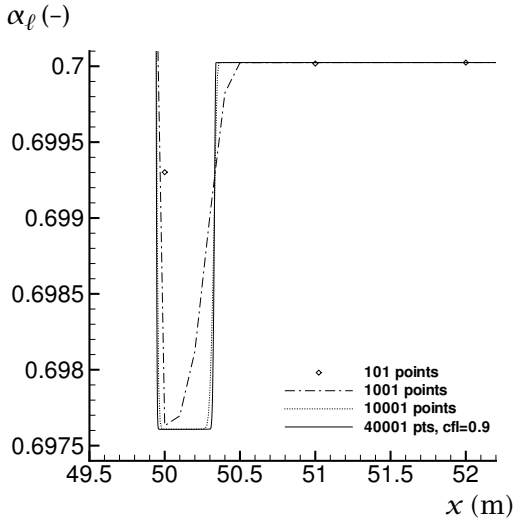

Figure 3.16: LRV shock tube. Close-up of volume-fraction waves.

Table 3.6: Initial conditions in the modified large relative velocity (modified LRV) shock tube

Quantity	symbol (unit)	left	right
Gas volume fraction	α_g (–)	0.30	0.90
Pressure	p (kPa)	265	265
Gas velocity	u_g (m/s)	65	50
Liquid velocity	u_ℓ (m/s)	10	15

101 points. Similarly to the Roe4 method, the sonic waves are slightly better resolved for the highest CFL number. Contrary to the Roe4 method, however, the resolution of the liquid velocity at the discontinuity at $x = 50\,\text{m}$ is strongly time-step dependent. This is shown in Figure 3.20(c). Here, the resolution is increasingly poor for increasing CFL numbers.

3.4.4 Modified large relative velocity shock tube

The modified large relative velocity shock tube is based on the LRV shock tube presented in the previous subsection, and was introduced by Evje and Flåtten (2003). As shown in Table 3.6, a jump in the liquid velocity has been imposed, and the volume-fraction jump has been increased.

The liquid volume fraction, the pressure, and the velocities calculated using the Roe4 method are shown in Figure 3.21 on page 87 at $t = 0.1\,\text{s}$, for numerical

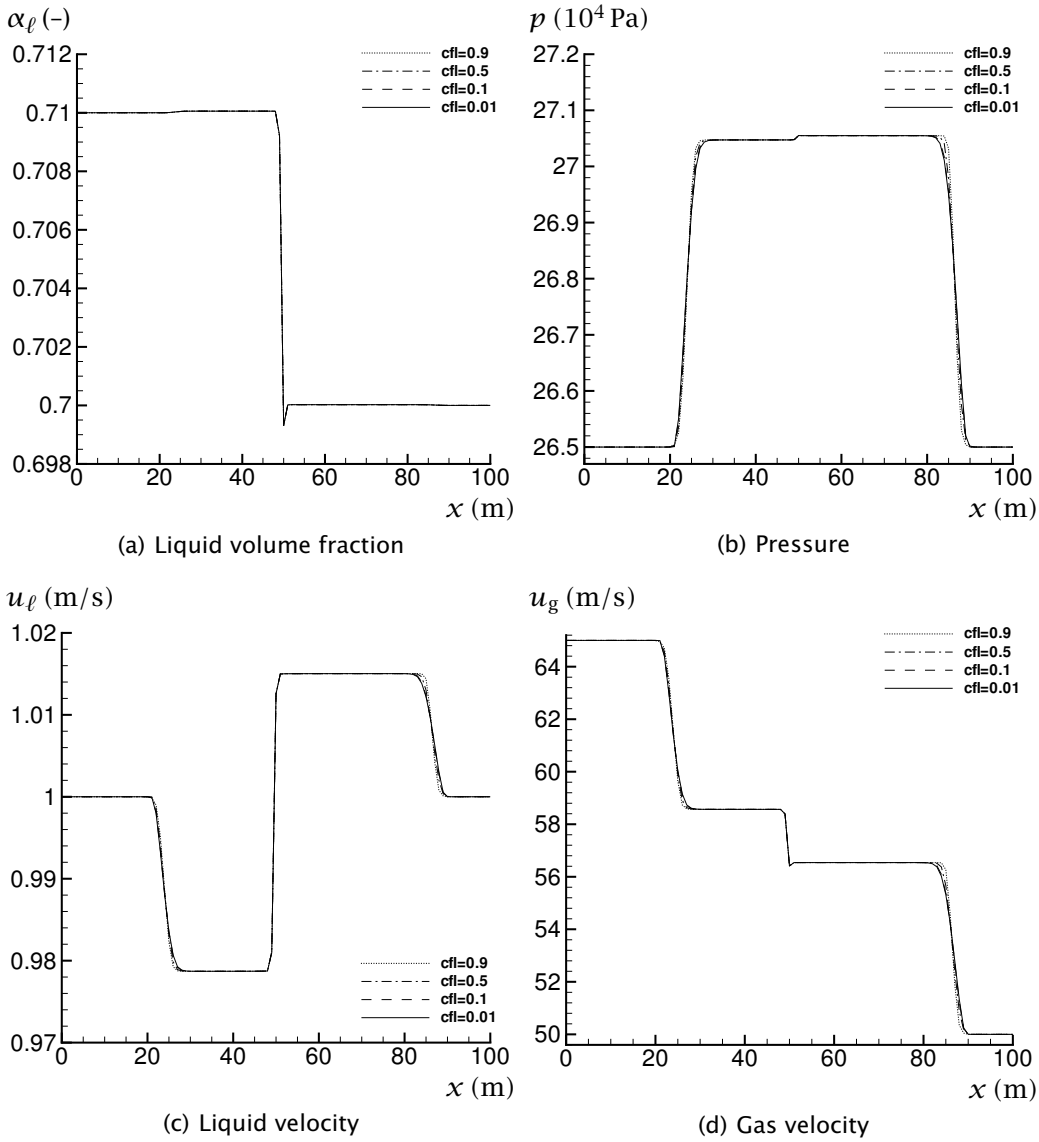

(a) Liquid volume fraction

(b) Pressure

(c) Liquid velocity

(d) Gas velocity

Figure 3.17: LRV shock tube. Time-step refinement for the Roe4 (MC) scheme on a grid of 101 points.

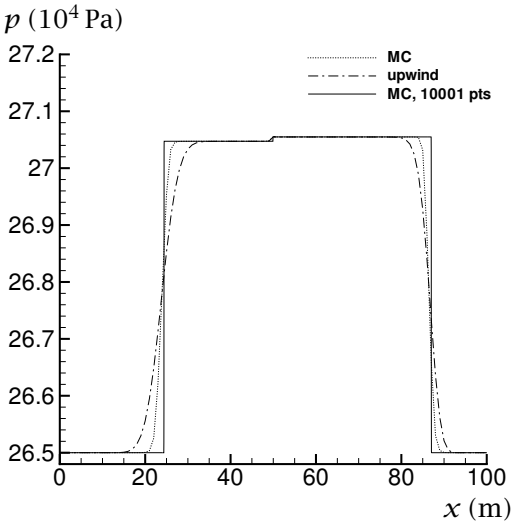

(a) Pressure. 101 grid points.

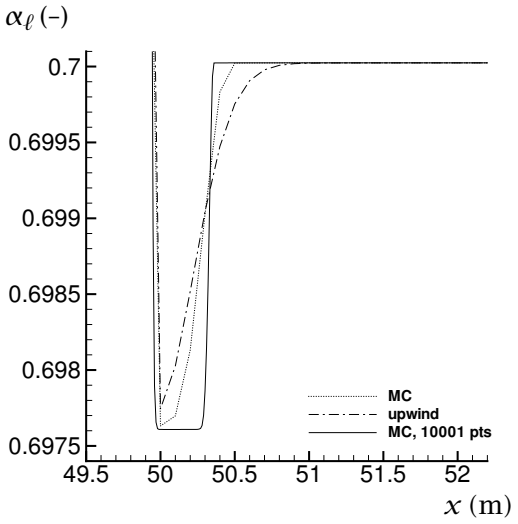

(b) Liquid volume fraction. 1001 grid points.

Figure 3.18: LRV shock tube. Effect of limiter function for the Roe4 scheme, with fine-grid data as reference. $C = 0.9$.

grids between 101 and 10001 points. As usual, the time-step length, $\Delta t = 2.35 \cdot 10^{-5}$ s, was chosen to correspond to $C = 0.9$ for the finest grid. This time, however, the minmod limiter was applied, as the MC limiter produced instabilities at the middle of the tube.

The small wedges that can be seen at $x = 50$ m in the pressure and the gas velocity, form part of the volume-fraction wave. In Figure 3.21(a), the convergence at the volume-fraction wedge has been further illustrated by the addition of data calculated on a 40001-point grid with $C = 0.9$.

The results of grid refinement of the Roe5 scheme employing the minmod limiter are given in Figure 3.22 on page 88. The employed time-step length was the one corresponding to $C = 0.9$ for the finest grid, in this case $\Delta t = 8.86 \cdot 10^{-6}$ s. Similarly to the non-modified LRV shock tube, the results of the Roe5 scheme seem to converge towards those of the Roe4 scheme, but very slowly at the discontinuity at $x = 50$ m. This can be seen in Figure 3.22(a) for the liquid volume fraction, where an extra plot for a grid of 10001 points and $C = 0.05$ has been added. Further, the convergence is slow for the plateau between about $x = 25$ m and 50 m seen for the pressure in Figure 3.22(b). The Roe5 scheme also produces a curious roller-coaster pattern with a local maximum and a local minimum in the liquid velocity at $x = 50$ m. It is visible for the finest grid in Figure 3.22(c), at about (50 m, 11 m/s). This behaviour is

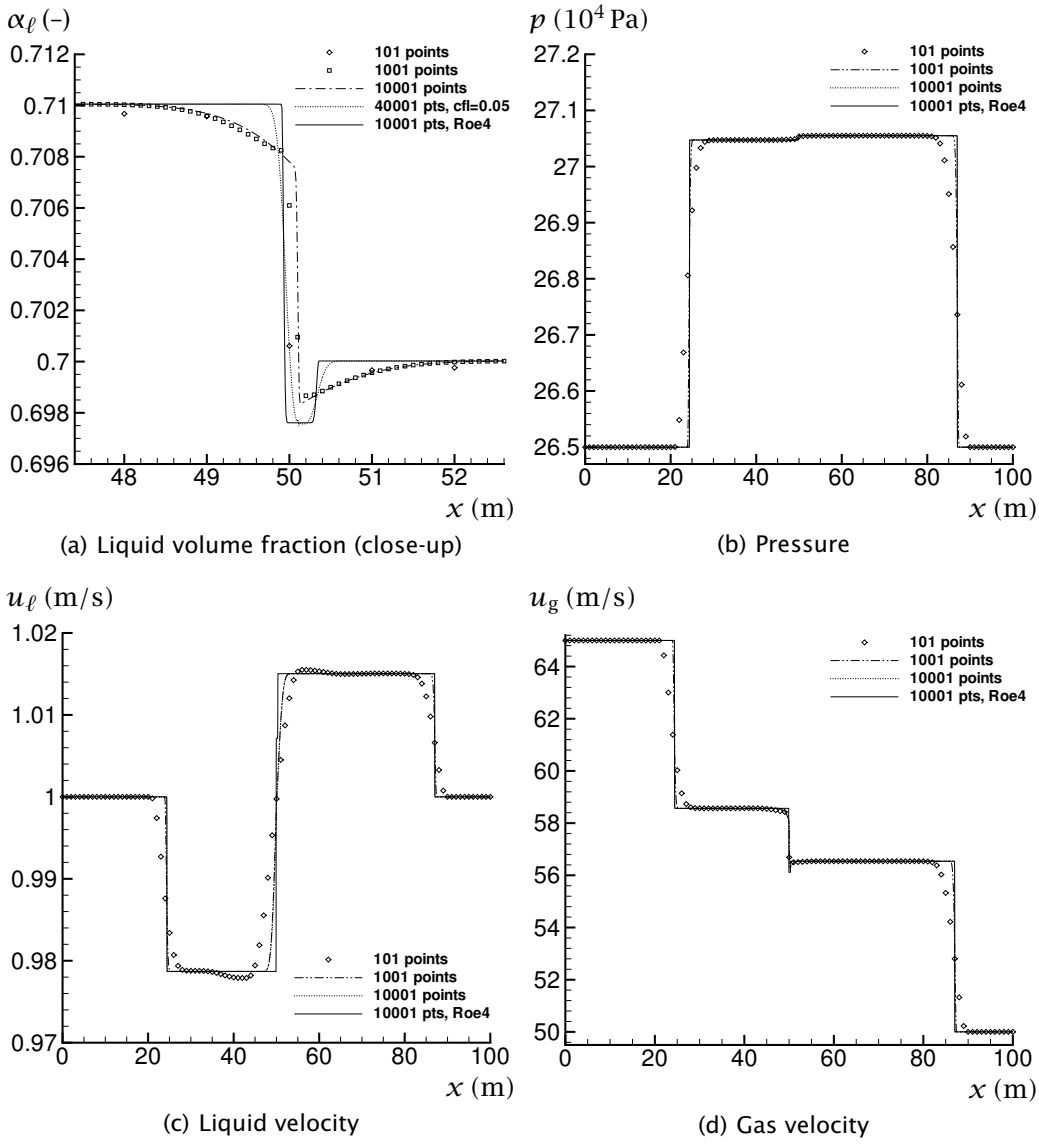

(a) Liquid volume fraction (close-up)

(b) Pressure

(c) Liquid velocity

(d) Gas velocity

Figure 3.19: LRV shock tube. Grid refinement for the Roe5 (MC) scheme.

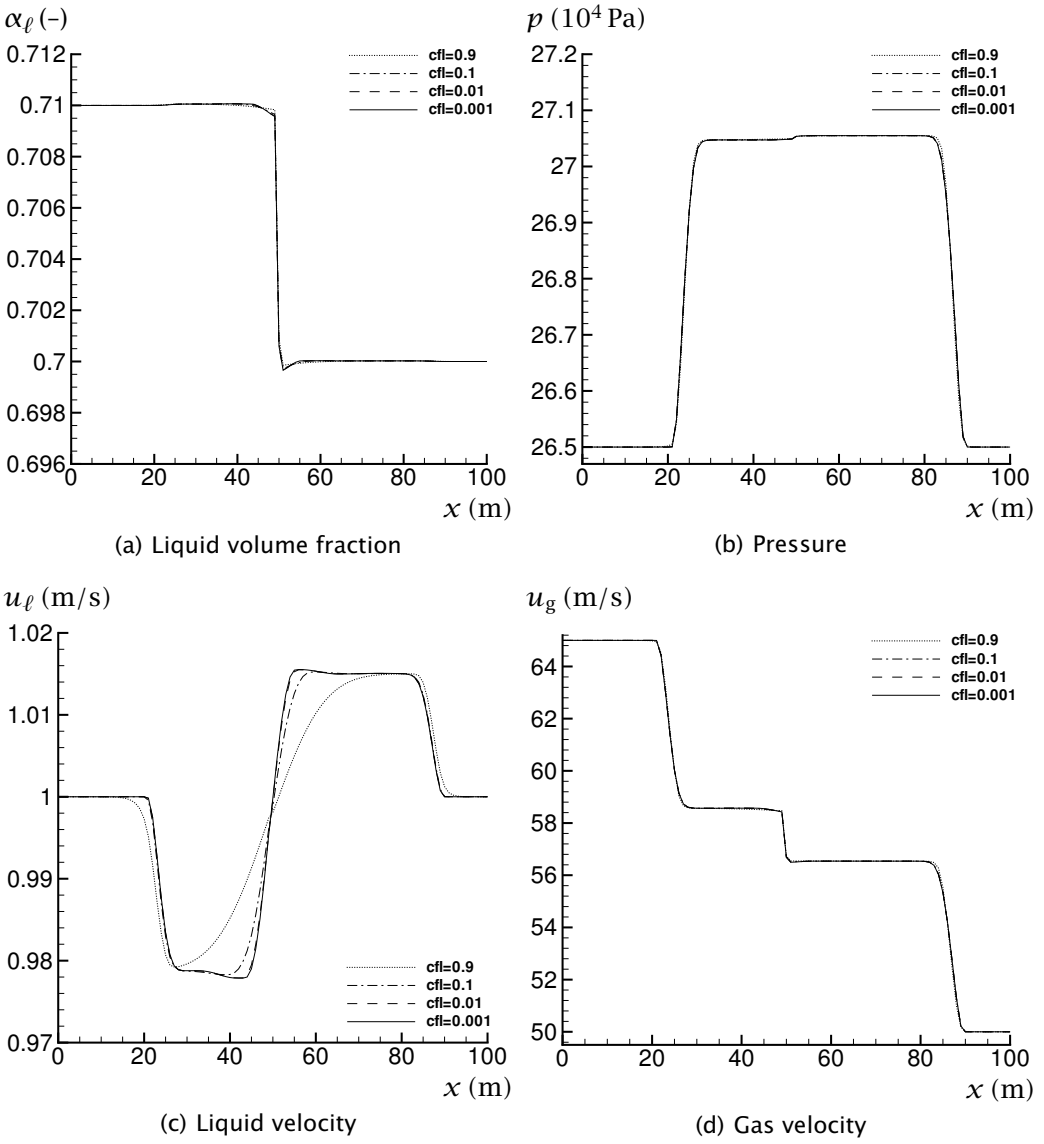

(a) Liquid volume fraction

(b) Pressure

(c) Liquid velocity

(d) Gas velocity

Figure 3.20: LRV shock tube. Time-step refinement for the Roe5 (MC) scheme on a grid of 101 points.

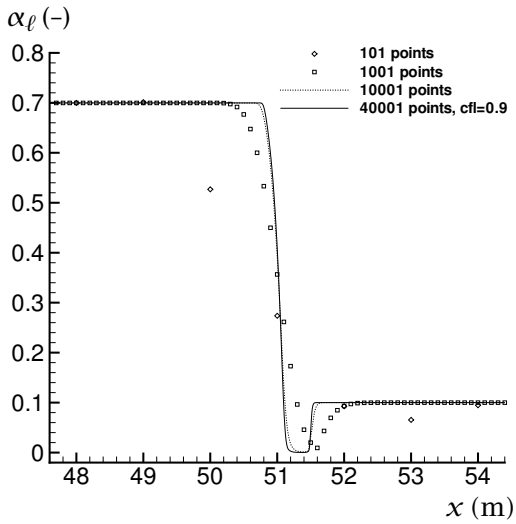

(a) Liquid volume fraction (close-up)

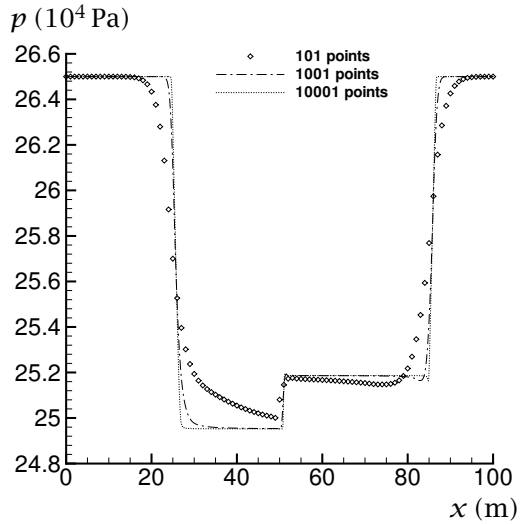

(b) Pressure

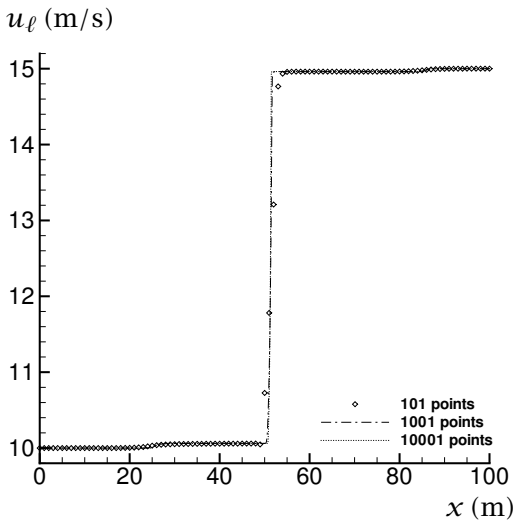

(c) Liquid velocity

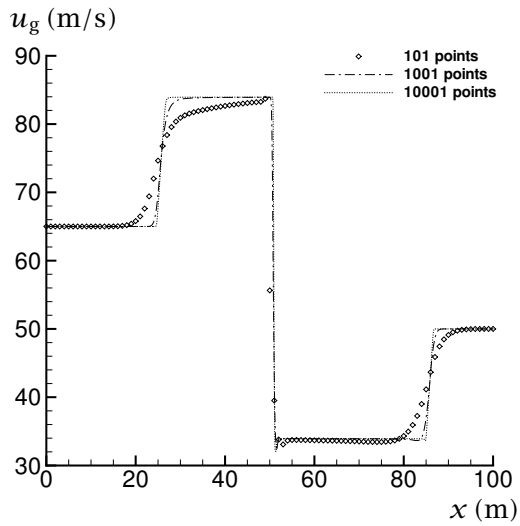

(d) Gas velocity

Figure 3.21: Modified LRV shock tube. Grid refinement for the Roe4 (minmod) scheme.

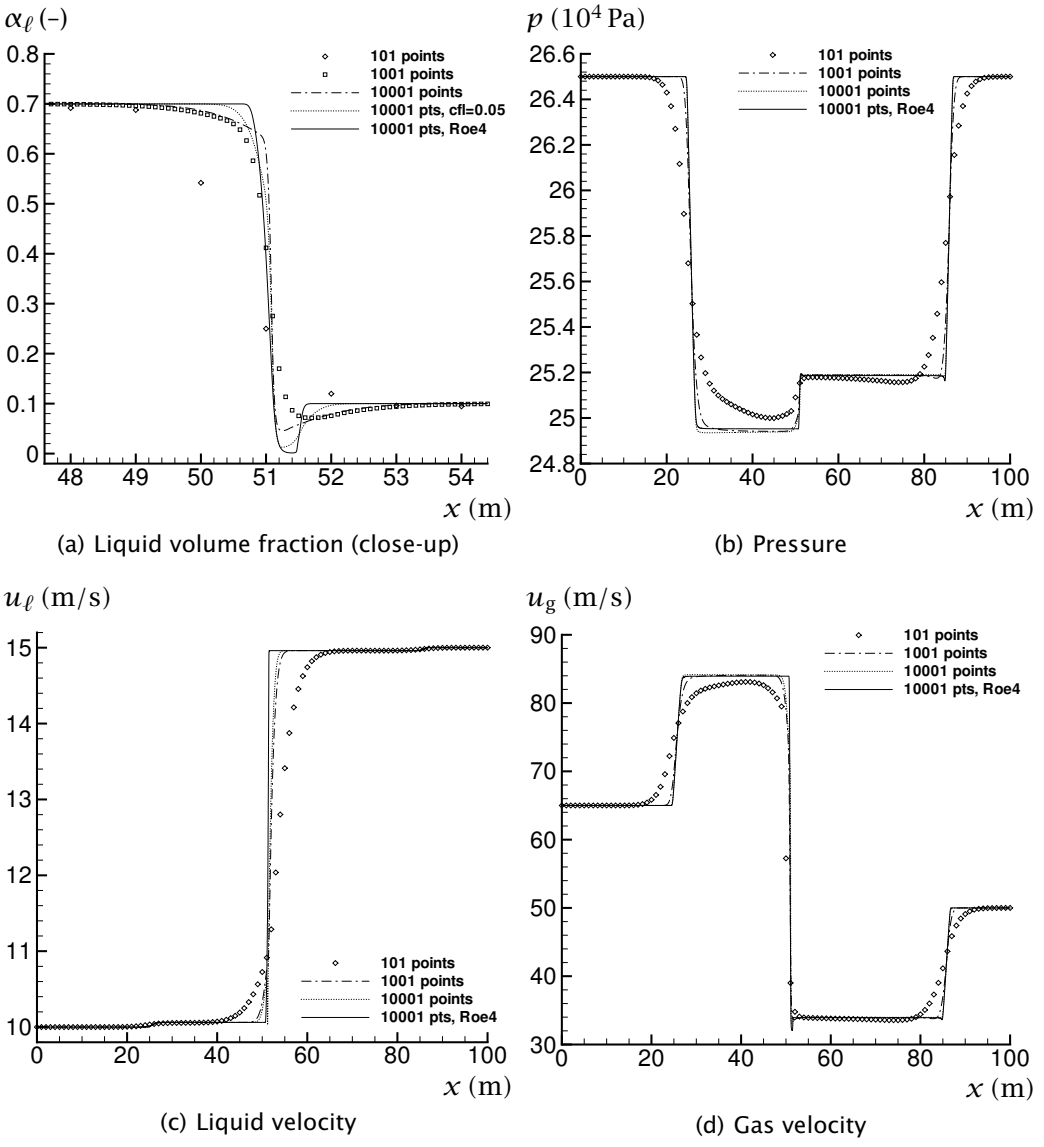

(a) Liquid volume fraction (close-up)

(b) Pressure

(c) Liquid velocity

(d) Gas velocity

Figure 3.22: Modified LRV shock tube. Grid refinement for the Roe5 (minmod) scheme.

Table 3.7: Initial conditions in Toumi's shock tube

Quantity	symbol (unit)	left	right
Gas volume fraction	α_g (–)	0.25	0.10
Pressure	p (MPa)	20	10
Gas velocity	u_g (m/s)	0	0
Liquid velocity	u_ℓ (m/s)	0	0

thought to be unphysical. In fact, it can be removed by the use of the acoustic-solver model (2.95) for the interfacial velocity. It also disappears if Harten's entropy fix is employed with $\delta = 80$, but that introduces some additional numerical diffusion.

3.4.5 Toumi's shock tube

Problem description

The present problem was introduced as a test case by Toumi (1996) for his Roe-type solver for a six-equation model. It has also been studied by Tiselj and Petelin (1997); Paillère *et al.* (2003) and Evje and Flåtten (2005a), the latter researchers using a four-equation model. The initial values are given in Table 3.7, and no source terms are considered.

First we consider the Roe4 method. Unfortunately, with the CATHARE expression (2.109) for the interfacial pressure difference, the coefficient matrix (3.34) is not diagonalizable for the initial condition $u_g = u_\ell$. Hence, an ad hoc approach was taken, combining the CATHARE and the Soo models:

$$p_k - p_{ik} = \Delta p_{ik} = \gamma \frac{\alpha_g \alpha_\ell \rho_g \rho_\ell}{\alpha_g \rho_\ell + \alpha_\ell \rho_g} (u_g - u_\ell)^2 + (1 - B_k) p_k, \tag{3.108}$$

where the displacement factor was set to a high value; $B_k = 0.999999$, that is, giving negligible additional diffusion, but making the coefficient matrix diagonalizable. Furthermore, following Paillère *et al.* (2003); Evje and Flåtten (2005a), $\gamma = 2$ was employed for this problem.

No source terms were considered.

Naïve approach

The result of grid refinement is shown in Figure 3.23 on page 91 for $t = 0.08$ s. The first-order scheme was used, that is, no limiter function was applied. The time-step length was $\Delta t = 9.13 \cdot 10^{-6}$ s, which corresponds to $C = 0.5$ for the

finest grid. The calculations were also performed with $B_k = 0.9999$, that is, more additional diffusion. This gave identical results to plotting accuracy.

The scheme seems to converge and all is fine – at first sight. However, in Figures 3.23(a) and 3.23(d) for the gas volume fraction and the gas velocity, respectively, six plateaux are visible. This is not at all expected for a four-equation model with four waves. Four waves should give five plateaux. Indeed, Toumi (1996) observed seven plateaux for his six-equation model, and Evje and Flåtten (2005a) produced five plateaux with their four-equation model. It is therefore unlikely that the results displayed in Figure 3.23 are physically obtainable.

Entropy fix

An inspection of the eigenvalues calculated in the case shown in Figure 3.23 revealed that one of them became negative, and then rapidly turned positive, immediately before $x = 50\,\text{m}$. This, together with the fact that the results seemed physically implausible, motivated the recalculation of the case employing an entropy fix. The results for various values of the parameter δ in Harten's entropy fix (3.80) are shown in Figure 3.24 on page 92. The grid had 1001 points, and the MC limiter was used. Figure 3.24(a) shows the volume fraction for the whole shock tube, while Figure 3.24(b) displays a close-up of the middle section of the tube.

First, it is interesting to note that for 'no' entropy fix ($\delta = 1$), the MC-limited Roe4 scheme displayed more problems than what was seen in Figure 3.23 for the first-order Roe4 scheme. The spurious wave in the middle of the tube is more pronounced, there is a peak at $x = 60\,\text{m}$, and also an overshoot at $x = 25\,\text{m}$.

As the parameter δ was increased, the spurious wave at $x = 50\,\text{m}$ gradually weakened, and for $\delta = 20$ it more or less disappeared. As δ was further increased, the solution between about 52 and 60 m started resembling a plateau, while the edges in the solution got more rounded. In the present case, the solution for $\delta = 50$ seemed reasonable.

The volume-fraction profile obtained using the LLF entropy fix is also shown for comparison. It can be observed that the LLF entropy fix introduced perhaps too little smoothing in the middle part of the tube, leaving a local maximum in the volume fraction at about 59 m.

Figure 3.25 on page 93 shows the case of Figure 3.23 recalculated employing the MC limiter and Harten's entropy fix with $\delta = 50$. As can be seen, the strange behaviour at the middle of the tube has disappeared.

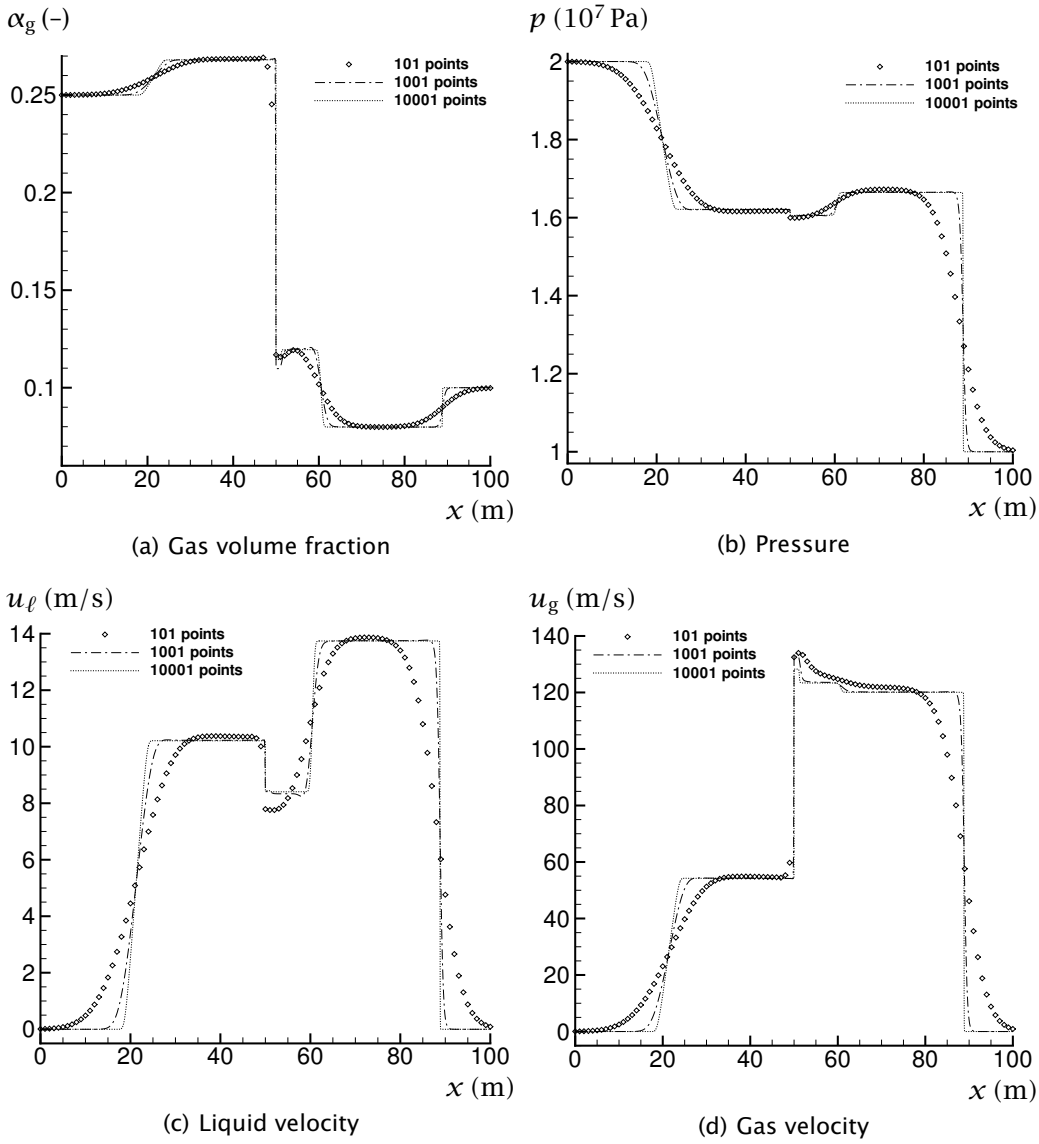

(a) Gas volume fraction

(b) Pressure

(c) Liquid velocity

(d) Gas velocity

Figure 3.23: Toumi's shock tube. Grid refinement for the Roe4 (first-order) scheme without entropy fix.

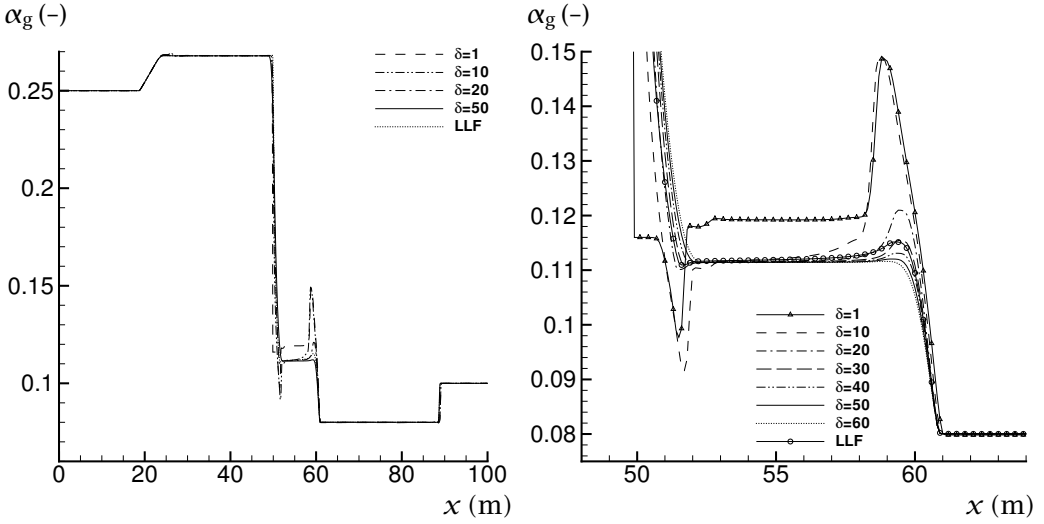

(a) Gas volume fraction (b) Gas volume fraction (close-up)

Figure 3.24: Toumi's shock tube. The Harten entropy fix with varying δ and the LLF entropy fix for the Roe4 (MC) scheme on a 1001-point grid.

Roe5 scheme

It was just seen that the Roe4 scheme had problems calculating Toumi's shock tube, and that it was necessary to introduce additional diffusion. This was done by employing Harten's entropy fix (3.79) with $\delta = 50$, and also the combined model (3.108) for the interfacial pressure difference. For the Roe5 scheme, the use of the combined interfacial pressure-difference model was unnecessary, and, indeed, for $B_k = 0.999999$ and $B_k = 1$ (that is, a tiny bit and no additional diffusion), the results were the same to plotting accuracy. Regarding the entropy fix, since no eigenvalues changed sign, it had only a minor effect. That is, the amount of additional diffusion that was completely necessary for the Roe4 scheme, made no difference for the Roe5 scheme.

A comparison of the first-order (no limiter) Roe4 scheme employing Harten's entropy fix, and the first-order Roe5 scheme is shown in Figure 3.26 on page 94. The grid size was 10001 points, and the CFL number was $C = 0.9$. No limiter was employed in this case, since for the Roe5 scheme, both the minmod, the van Leer and the MC limiter introduced instabilities at the middle of the tube. For the temporal and spatial resolutions investigated, the results were different in the middle section of the shock tube, between about $x = 50\,\text{m}$ and $x = 60\,\text{m}$. For the Roe5 scheme, the volume fraction and the velocities in this section

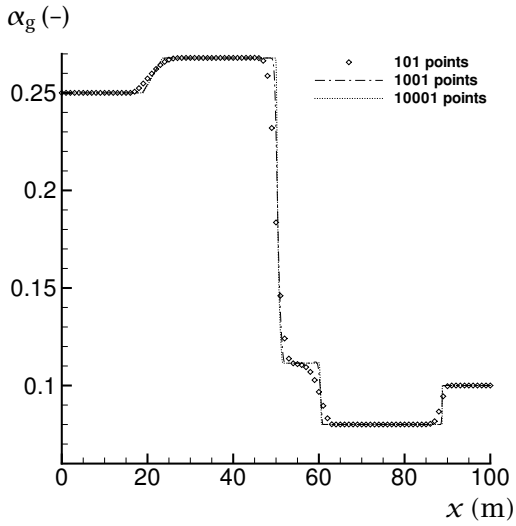

(a) Gas volume fraction

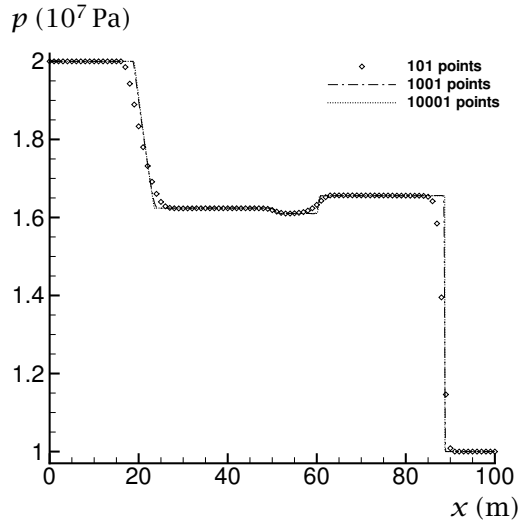

(b) Pressure

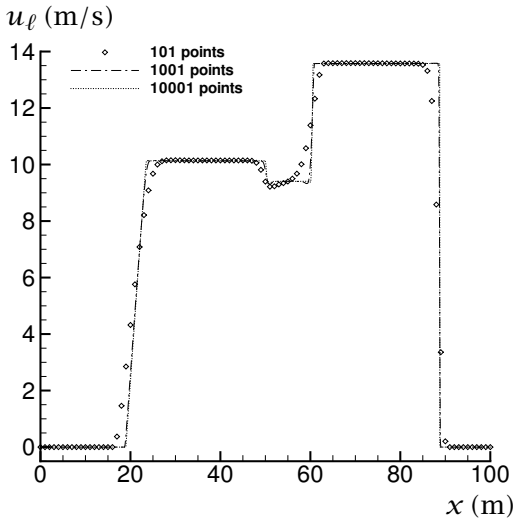

(c) Liquid velocity

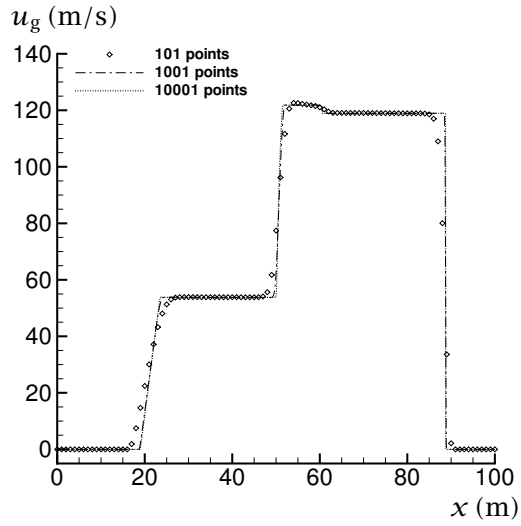

(d) Gas velocity

Figure 3.25: Toumi's shock tube. Grid refinement for the Roe4 (MC) scheme employing Harten's entropy fix with $\delta = 50$.

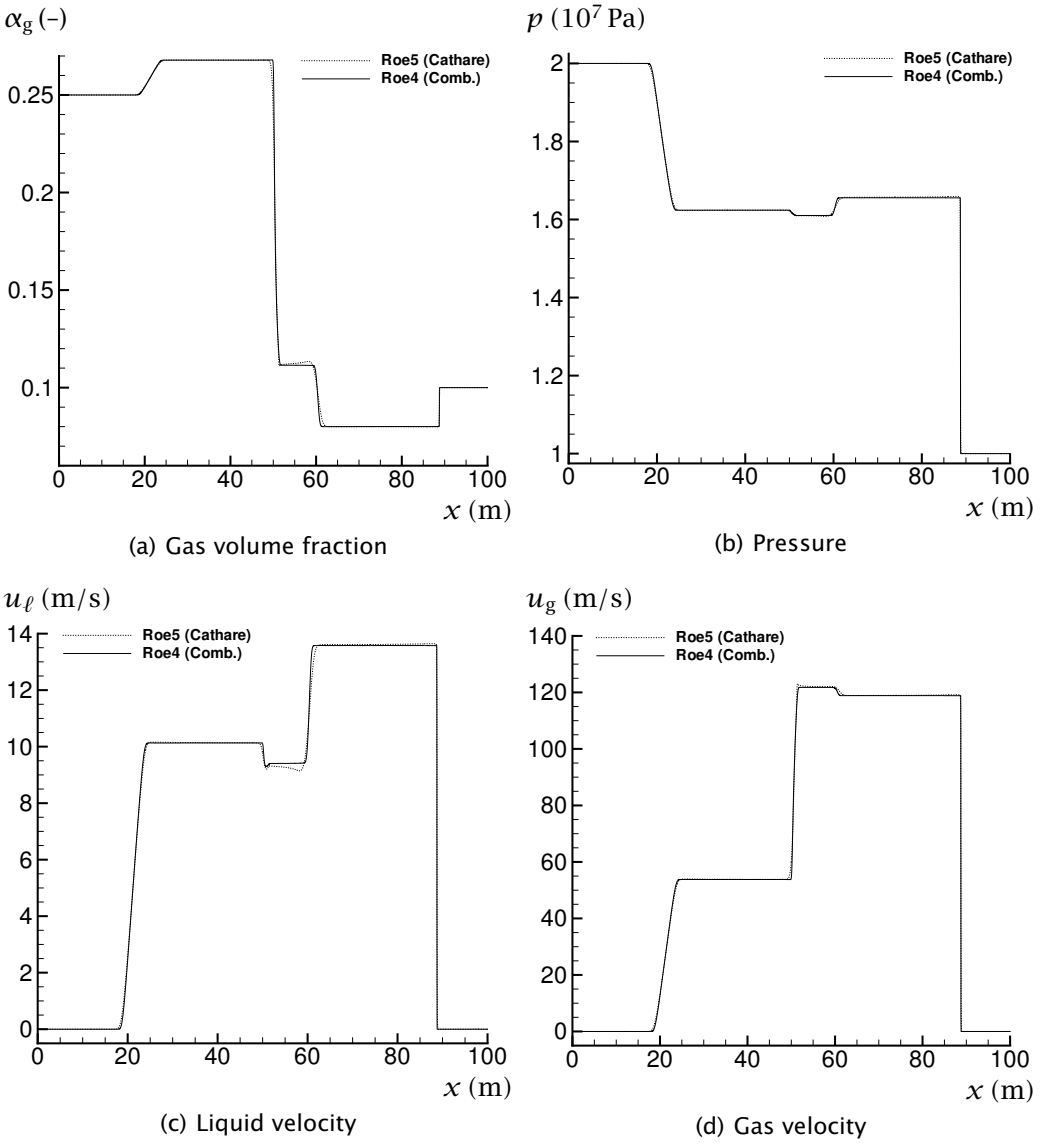

(a) Gas volume fraction

(b) Pressure

(c) Liquid velocity

(d) Gas velocity

Figure 3.26: Toumi's shock tube. Comparison of the Roe4 (first-order and entropy fix) and Roe5 (first-order) schemes on a grid of 10001 points.

all had gradients, whereas the Roe4 scheme produced plateaux. The latter behaviour corresponds to those of other methods (Evje and Flåtten, 2005a). Furthermore, the discontinuity at $x = 60\,\mathrm{m}$ is more sharply resolved by the Roe4 scheme.

3.4.6 Water–air separation

This phase-separation problem was proposed by Coquel *et al.* (1997). It consists of a vertical tube of length $L = 7.5\,\mathrm{m}$, closed at both ends. Initially it has a uniform pressure of $p = 1 \cdot 10^5\,\mathrm{Pa}$ and volume fraction of $\alpha_\ell = 0.5$. At $t = 0$, the phases start to separate under the influence of gravity, which is the only source term considered.

Evje and Flåtten (2003) derived approximate analytical solutions for the liquid velocity and volume fraction by assuming that the liquid is accelerated by gravity only, until it is abruptly brought into stagnation at the lower part of the tube:

$$\alpha_\ell(x,t) = \begin{cases} 0 & \text{for } x < 1/2gt^2, \\ 0.5 & \text{for } 1/2gt^2 \le x < L - 1/2gt^2, \\ 1 & \text{for } L - 1/2gt^2 < x, \end{cases} \tag{3.109}$$

and

$$u_\ell(x,t) = \begin{cases} \sqrt{2gx} & \text{for } x < 1/2gt^2, \\ gt & \text{for } 1/2gt^2 \le x < L - 1/2gt^2, \\ 0 & \text{for } L - 1/2gt^2 < x. \end{cases} \tag{3.110}$$

After the time

$$t = \sqrt{\frac{L}{g}} \approx 0.87\,\mathrm{s}, \tag{3.111}$$

the phases should be fully separated in the idealized case.

The water-air separation problem is in fact a difficult one. The presently implemented Roe4 scheme breaks down unless considerable amounts of artificial diffusion are added. As far as I know, no one has successfully calculated this problem using a Roe-type scheme.

One problem with the Roe scheme is that the positivity of the solution is not guaranteed (LeVeque, 2002, Section 15.3.6). However, in this case, the calculations did not break down because of negative volume fractions. The instabilities occurred at the large volume-fraction gradient. The eigenvalues of the coefficient matrix are a strong function of the volume fraction, and this could be a reason for the failure of the Roe4 scheme in this case.

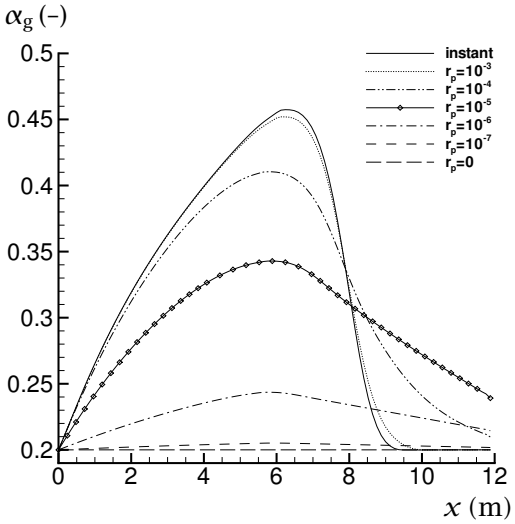

Figure 3.27: Gas volume fraction for the water faucet. Effect of pressure-relaxation parameter r_p on the Roe5 (MC) scheme for a grid of 101 points.

The Roe5 scheme failed, too, but for a different reason: At the bottom of the tube, the air volume fraction approached zero in a steep way, causing it to become negative, and hence the numerical method to fail.

3.4.7 Effect of the pressure-relaxation parameter

In the preceding subsections, instantaneous pressure relaxation was always used in the Roe5 method. Now we will investigate the effect of varying the pressure-relaxation parameter, r_p, in the equation (2.96).

Water faucet case

Consider Figure 3.27, showing the gas volume fraction for the water faucet case. The calculations have been performed using a 101-point grid, the MC limiter and a time-step length of $\Delta t = 1.06 \cdot 10^{-6}$ s. The curve labelled 'instant' has been calculated with instantaneous pressure relaxation, and it is equal to that already shown in Figure 3.7(a). The other curves have been calculated using the fractional-step method outlined in Section 2.5.3 for a finite pressure-relaxation coefficient. The effect of the pressure-relaxation parameter, r_p, is clearly seen in the figure: The smaller the r_p, the flatter the volume-fraction

profile becomes. For $r_p = 0$, the volume-fraction remains constant. This can be understood by considering the volume-fraction evolution equation (2.96). Initially, $\partial \alpha_g / \partial x = 0$, and since $r_p = 0$, $\partial \alpha_g / \partial t = 0$, which means that the volume fraction does not change.

It should also be noted that the transition between instantaneous and finite-rate pressure relaxation is smooth.

Toumi's shock tube

A further example of the effect of the pressure-relaxation parameter is shown in Figure 3.28 on the next page. Here, Toumi's shock tube has been calculated on a grid of 1001 points using no limiter and a time-step length of $\Delta t = 8.87 \cdot 10^{-6}$ s. However, as opposed to the case of the one-pressure calculations, here, the results are shown at $t = 0.04$ s. This has been done to avoid interaction with the boundaries.

Figure 3.28(b) shows an interesting plot of the liquid velocity. For a low value of the pressure-relaxation parameter, r_p, the two sonic waves can be seen to have reached about $x = 10$ m and $x = 90$ m. As r_p is increased, those two fast sonic waves are gradually suppressed, and the effect of the gas phase becomes more and more visible.

The approximate speed of the sonic waves can be read from the figure. For a low r_p, the average speed of the right-going wave is $40\,\text{m}/0.04\,\text{s} = 1000\,\text{m/s}$, which closely corresponds to the eigenvalue $u_\ell + c_\ell$. As the pressure-relaxation coefficient is increased, the sonic speed is reduced to that of the four-equation model, as was seen for instance in Figure 3.26 on page 94.

The discontinuity at the middle of the tube moves to the right with a speed corresponding to the interfacial velocity, u_i, (see (2.94)), which is practically equal to the liquid velocity.

The gas and liquid pressures are displayed in Figures 3.28(d) and 3.28(e), and it can be observed how the two independent pressures converge to one as r_p is increased.

3.4.8 Summary

A Roe-type scheme for the four-equation system (Roe4) has been tested on various cases from the literature. In the present work, the high-resolution approach of LeVeque (2002) has been successfully applied to the multifluid equations. For discontinuity problems such as the water-faucet case, a significant improvement was achieved compared to the conventional first-order Roe scheme.

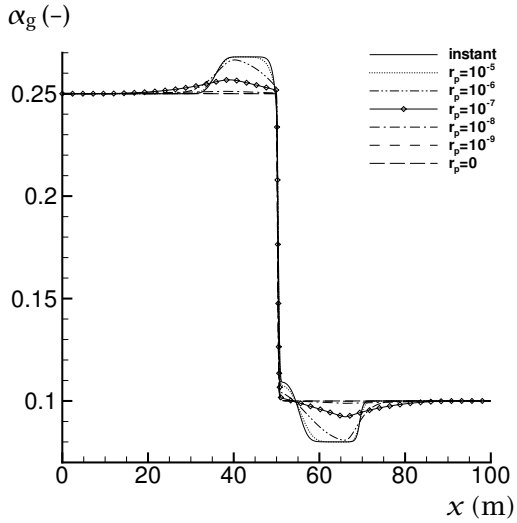

(a) Gas volume fraction

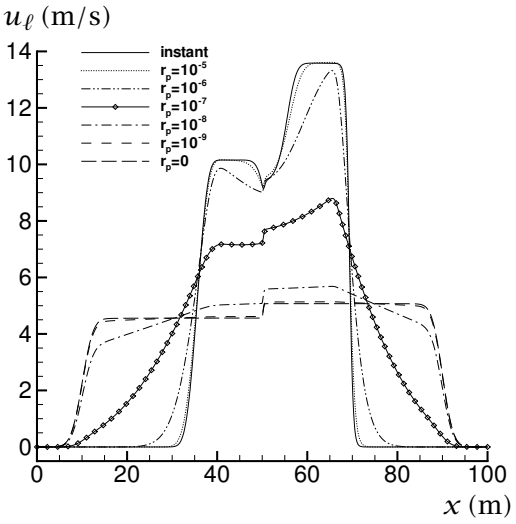

(b) Liquid velocity

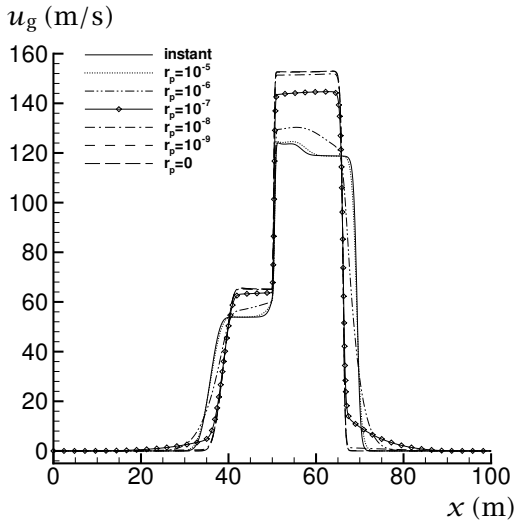

(c) Gas velocity

Figure 3.28: Toumi's shock tube at $t = 0.04\,\mathrm{s}$. Effect of the pressure-relaxation parameter r_p in the Roe5 (first-order) method for a grid of 1001 points.

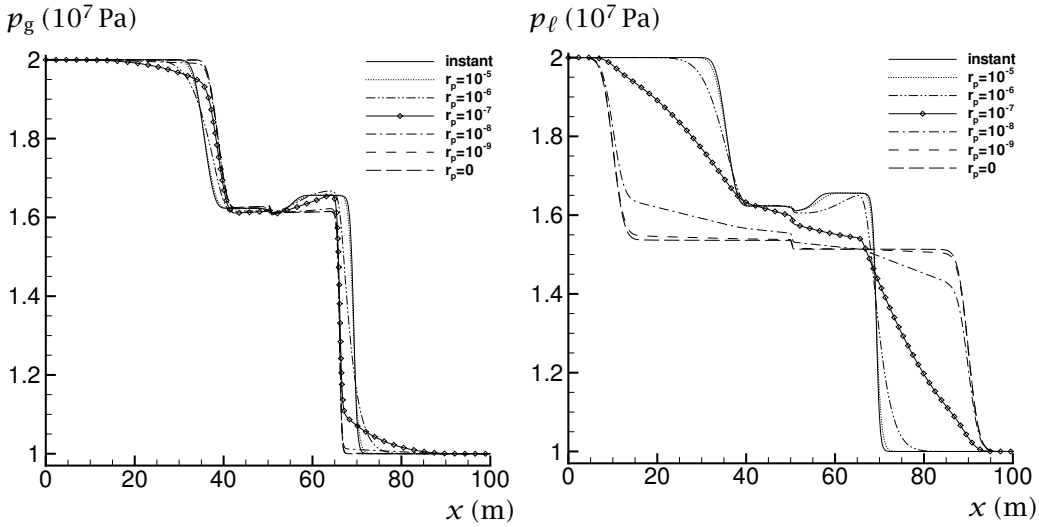

(d) Gas pressure (e) Liquid pressure

Figure 3.28: (Continued) Toumi's shock tube at $t = 0.04\,\mathrm{s}$. Effect of the pressure-relaxation parameter r_p in the Roe5 (first-order) method for a grid of 1001 points.

In the large relative velocity (LRV) and modified LRV shock tube problems, the effect of the high-resolution correction was less pronounced than for the faucet case. The resolution of sonic waves was seen to be time-step dependent.

A Roe-type scheme for the five-equation system has been derived (Sections 3.2 and 3.3): The two-velocity, two-pressure two-fluid model is first advanced in time, then a pressure-relaxation procedure is performed, yielding the same pressure in the two phases. The resulting scheme, Roe5, has been tested and compared to Roe4.

The Roe5 scheme was found to be significantly more diffusive than the Roe4 scheme. The diffusion is a strong function of the chosen time-step length, the grid size, whether a limiter function is employed or not, and also the liquid speed of sound.

Interestingly, for the faucet case, the MC-limited Roe5 scheme performed better than the Roe4 scheme for the very coarse grid of 26 points.

For fine grids and short time steps, the Roe5 scheme mostly converges to the same results as the Roe4 scheme. The differences seen are thought to be mainly due to the high diffusivity of the Roe5 scheme.

It was found that the sonic wave-propagation speed is the same in the Roe4 and the Roe5 schemes.

For Toumi's shock tube, it was required to use an entropy fix with the Roe4 scheme. For the Roe5 scheme, on the other hand, no fix was necessary, but the produced results were slightly less plausible.

The coefficient matrix employed in the Roe5 scheme is diagonalizable with real eigenvalues even in the case of zero interfacial pressure difference. This is a main difference between the Roe5 and the Roe4 schemes. Even so, oscillations normally associated with complex eigenvalues were produced for a low liquid speed of sound in the water-faucet test case. This may indicate that the Roe5 scheme and similar methods provide no easy remedy against complex eigenvalues in the two-fluid model.

The effect of finite-rate pressure relaxation in the Roe5 method was tested. As the pressure-relaxation parameter was increased, the solution gradually approached that obtained using instantaneous pressure relaxation.

The good correspondence between the results obtained using the Roe4 scheme and those of the Roe5 scheme with instantaneous pressure relaxation, indicates that the latter may be regarded as a numerical method to solve the four-equation system.

3.5 Conclusions

- The Roe5 scheme with instantaneous pressure relaxation can be regarded as a numerical method to solve the four-equation system. It is significantly more diffusive than the Roe4 scheme. This is true with or without the use of high-resolution limiters.

- As the pressure-relaxation parameter in the Roe5 scheme is increased, the instantaneous-relaxation results are recovered. Instantaneous pressure relaxation annihilates the fastest waves, so that the solution approaches that of the four-equation system.

- It appears that the approach of two pressures and instantaneous pressure relaxation does not provide an easy way to overcome the problem of complex eigenvalues in the four-equation system.

4 The flux-limiter centred scheme

The numerical schemes presented in Section 3.3 are computationally quite expensive, especially for the four-equation system, where the coefficient matrix is diagonalized numerically on every cell-interface on every time step. Therefore, the flux-limiter centred (FLIC) scheme of Toro (1999, Section 14.5.2) (see also Toro and Billett, 2000), with an adaptation for the non-conservative term, was tested for the four-equation system. This scheme does neither make direct use of wave-propagation information in the construction of the numerical flux, nor, indeed, does it explicitly employ the coefficient matrix.

4.1 Description of the scheme

The system was written in the form

$$\frac{\partial \boldsymbol{q}}{\partial t} + \frac{\partial \tilde{\boldsymbol{f}}(\boldsymbol{q})}{\partial x} = \tilde{\boldsymbol{s}}(\boldsymbol{q}), \tag{4.1}$$

with the 'modified' flux function

$$\tilde{\boldsymbol{f}} = \begin{bmatrix} \alpha_\mathrm{g}\rho_\mathrm{g}u_\mathrm{g} \\ \alpha_\ell\rho_\ell u_\ell \\ \alpha_\mathrm{g}\rho_\mathrm{g}u_\mathrm{g}^2 + \alpha_\mathrm{g}p_\mathrm{g} \\ \alpha_\ell\rho_\ell u_\ell^2 + \alpha_\ell p_\ell \end{bmatrix}, \tag{4.2}$$

and the right-hand side

$$\tilde{\boldsymbol{s}} = \begin{bmatrix} 0 \\ 0 \\ p_\mathrm{ig}\frac{\partial \alpha_\mathrm{g}}{\partial x} + \alpha_\mathrm{g}\rho_\mathrm{g}g_x \\ p_{\mathrm{i}\ell}\frac{\partial \alpha_\ell}{\partial x} + \alpha_\ell\rho_\ell g_x \end{bmatrix}. \tag{4.3}$$

The $\nabla\alpha_k$ terms were discretized using second-order central differences.

The scheme can be stated as

$$\boldsymbol{Q}_i^{n+1} = \boldsymbol{Q}_i^n - \frac{\Delta t}{\Delta x}\left(\boldsymbol{F}_{i+1/2} - \boldsymbol{F}_{i-1/2}\right) + \Delta t\boldsymbol{S}_i, \tag{4.4}$$

where $\boldsymbol{F}$ is the numerical approximation of $\tilde{\boldsymbol{f}}$ and $\boldsymbol{S}$ is the numerical approximation of $\tilde{\boldsymbol{s}}$.

The centred flux-limiter approach is different from the method presented in Section 3.3 in that the characteristic variables are not considered. Instead, the numerical fluxes $\boldsymbol{F}_{i-1/2}$ are taken as a combination of a low-order monotone flux $\boldsymbol{F}^{\mathrm{l}}_{i-1/2}$ and a high-order flux $\boldsymbol{F}^{\mathrm{h}}_{i-1/2}$ as

$$\boldsymbol{F}_{i-1/2} = \boldsymbol{F}^{\mathrm{l}}_{i-1/2} + \tilde{\phi}(\tilde{\theta}_{i-1/2})(\boldsymbol{F}^{\mathrm{h}}_{i-1/2} - \boldsymbol{F}^{\mathrm{l}}_{i-1/2}), \tag{4.5}$$

where $\tilde{\phi}$ is a centred flux limiter, described below.

Here, the low-order flux is the first-order centred (FORCE) flux, given by

$$\boldsymbol{F}^{\mathrm{l}}_{i-1/2} = \frac{1}{2}\left(\boldsymbol{F}^{\mathrm{LF}}_{i-1/2} + \boldsymbol{F}^{\mathrm{R}}_{i-1/2}\right), \tag{4.6}$$

where $\boldsymbol{F}^{\mathrm{LF}}_{i-1/2}$ is the Lax–Friedrichs flux

$$\boldsymbol{F}^{\mathrm{LF}}_{i-1/2} = \frac{1}{2}(\tilde{\boldsymbol{f}}(\boldsymbol{Q}_{i-1}) + \tilde{\boldsymbol{f}}(\boldsymbol{Q}_i)) - \frac{1}{2}\frac{\Delta x}{\Delta t}(\boldsymbol{Q}_i - \boldsymbol{Q}_{i-1}), \tag{4.7}$$

and $\boldsymbol{F}^{\mathrm{R}}_{i-1/2}$ is the Richtmyer flux. It is computed by first defining an intermediate state

$$\boldsymbol{Q}^{\mathrm{R}}_{i-1/2} = \frac{1}{2}(\boldsymbol{Q}_{i-1} + \boldsymbol{Q}_i) - \frac{1}{2}\frac{\Delta t}{\Delta x}(\tilde{\boldsymbol{f}}(\boldsymbol{Q}_i) - \tilde{\boldsymbol{f}}(\boldsymbol{Q}_{i-1})), \tag{4.8}$$

and then setting

$$\boldsymbol{F}^{\mathrm{R}}_{i-1/2} = \tilde{\boldsymbol{f}}(\boldsymbol{Q}^{\mathrm{R}}_{i-1/2}). \tag{4.9}$$

The high-order flux is taken to be the Richtmyer flux:

$$\boldsymbol{F}^{\mathrm{h}}_{i-1/2} = \boldsymbol{F}^{\mathrm{R}}_{i-1/2}. \tag{4.10}$$

Toro (1999, Section 14.5.2) lists some centred flux-limiter functions. They

are analogous to the corresponding upwind flux limiters.

$$\text{minbee/minmod}: \quad \tilde{\phi}(\tilde{\theta}) = \begin{cases} 0 & \text{if } \tilde{\theta} \le 0, \\ \tilde{\theta} & \text{if } 0 < \tilde{\theta} \le 1, \\ 1 & \text{if } \tilde{\theta} > 1, \end{cases}$$

$$\text{van Albada}: \quad \tilde{\phi}(\tilde{\theta}) = \begin{cases} 0 & \text{if } \tilde{\theta} \le 0, \\ \frac{\tilde{\theta}(1+\tilde{\theta})}{1+\tilde{\theta}^2} & \text{if } 0 < \tilde{\theta} \le 1, \\ \phi_g + \frac{(1-\phi_g)\tilde{\theta}(1+\tilde{\theta})}{1+\tilde{\theta}^2} & \text{if } \tilde{\theta} > 1, \end{cases}$$

$$\text{van Leer}: \quad \tilde{\phi}(\tilde{\theta}) = \begin{cases} 0 & \text{if } \tilde{\theta} \le 0, \\ \frac{2\tilde{\theta}}{1+\tilde{\theta}} & \text{if } 0 < \tilde{\theta} \le 1, \\ \phi_g + \frac{2(1-\phi_g)\tilde{\theta}}{1+\tilde{\theta}} & \text{if } \tilde{\theta} > 1, \end{cases}$$

$$\text{superbee}: \quad \tilde{\phi}(\tilde{\theta}) = \begin{cases} 0 & \text{if } \tilde{\theta} \le 0, \\ 2\tilde{\theta} & \text{if } 0 < \tilde{\theta} \le 1/2, \\ 1 & \text{if } 1/2 < \tilde{\theta} \le 1, \\ \min(2, \phi_g + (1-\phi_g)\tilde{\theta}) & \text{if } \tilde{\theta} > 1. \end{cases} \tag{4.11}$$

The function ϕ_g is given by

$$\phi_g = \frac{1-C}{1+C}, \tag{4.12}$$

where C is the CFL number.

One chooses a component q^j in the vector of unknowns, on which to apply the smoothness measure. Then the smoothness measure is calculated to the left and to the right

$$\tilde{\theta}^{\text{left}}_{i-1/2} = \frac{\Delta q^j_{i-3/2}}{\Delta q^j_{i-1/2}} \quad \text{and} \quad \tilde{\theta}^{\text{right}}_{i-1/2} \frac{\Delta q^j_{i+1/2}}{\Delta q^j_{i-1/2}}, \tag{4.13}$$

where $\Delta q^j_{i-1/2} = q^j_i - q^j_{i-1}$. The limiter to be applied in equation (4.5) is

$$\tilde{\phi} = \min(\tilde{\phi}(\tilde{\theta}^{\text{left}}_{i-1/2}), \tilde{\phi}(\tilde{\theta}^{\text{right}}_{i-1/2})). \tag{4.14}$$

For the Euler equations, Toro recommends taking q^j to be the total energy. For other systems, some experimentation might be necessary. Toro suggests applying (4.13)–(4.14) to every component, $q^j, j = 1, \ldots, m$, of the vector of

conserved variables to obtain m limiters $\tilde{\phi}_j$, and then selecting the final limiter as

$$\tilde{\phi} = \min(\tilde{\phi}_j), \quad j = 1, \ldots, m. \tag{4.15}$$

4.2 Numerical tests of the FLIC scheme

In the present section, we will perform numerical tests of the FLIC scheme.

Neither the coefficient matrix (3.34) nor its eigenvalues appear explicitly in the FLIC scheme. To estimate the time-step length from the CFL criterion, we used the approximate eigenvalue expressions presented by Evje and Flåtten (2003), and which are reproduced in Appendix A on page 251.

4.2.1 Water faucet test case

We commence the discussion by considering the water faucet test case (see Section 3.4.1 on page 58).

Choice of limiting procedure

It is first necessary to consider the choice of a limiter function, and a variable on which to apply it. Toro (1999, Section 14.5.2) considered various shock-tube cases for the Euler equations. As mentioned in Section 4.1, he reported satisfactory results when the total energy was used as the basis variable for the limiting procedure. Here, on the other hand, since we consider an isentropic model, we cannot make that choice. Instead, Toro's second recommendation was tried, that is, to calculate the limiter based on each of the composite variables, and then selecting the final limiter as the smallest one. Unfortunately, this did not work well. Then each of the composite variables, and the volume fraction, were tried individually as a basis for finding the limiter, but no stable calculations of the faucet case could be made. Hence it seems that further work is required to make the FLIC scheme work for the multifluid equations. Henceforth we therefore use the FLIC scheme without any limiter, that is, we use the FORCE scheme.

One small improvement was found to work, though: The Lax–Friedrichs flux was substituted by the Rusanov flux, that is, instead of employing (4.6), the FORCE flux was calculated from the formula

$$\boldsymbol{F}^{\mathrm{l}}_{i-1/2} = \frac{1}{2}\left(\boldsymbol{F}^{\mathrm{Ru}}_{i-1/2} + \boldsymbol{F}^{\mathrm{R}}_{i-1/2}\right), \tag{4.16}$$

where $\boldsymbol{F}^{\mathrm{Ru}}_{i-1/2}$ is the Rusanov flux

$$\boldsymbol{F}^{\mathrm{Ru}}_{i-1/2} = \frac{1}{2}(\tilde{\boldsymbol{f}}(\boldsymbol{Q}_{i-1}) + \tilde{\boldsymbol{f}}(\boldsymbol{Q}_i)) - \frac{1}{2}|\lambda|_{\max}(\boldsymbol{Q}_i - \boldsymbol{Q}_{i-1}), \tag{4.17}$$

where $|\lambda|_{\max}$ is the maximum eigenvalue in the computational domain. If the CFL number is $C = 1$, then the Rusanov and the Lax–Friedrichs fluxes are equal.

Grid refinement

The effect of grid refinement is shown in Figure 4.1 on the next page. The time-step length was $\Delta t = 3.16 \cdot 10^{-6}$ s, corresponding to $C = 0.9$ for the finest grid. It is clear that the FORCE scheme is rather diffusive. However, a comparison with Figure 3.8 on page 68 reveals that it is less so than the first-order Roe5 scheme. For the finest grid of 10001 points, it is also less diffusive than the MC-limited Roe5 scheme, as can be seen by likening with Figure 3.7 on page 67.

Effect of liquid speed of sound and time-step length

Contrary to the case of the Roe5 scheme, in FORCE, there is hardly anything to gain with respect to the volume-fraction profile from reducing the liquid speed of sound. This is mainly since the FORCE scheme is a central scheme. The small effect there is, is due to the appearance of $|\lambda|_{\max}$ in the equation (4.17). However, the maximum (approximate) eigenvalue at $t = 0.6$ s is only reduced from 342 m/s to 320 m/s by reducing the liquid speed of sound from 1000 m/s to 55.5 m/s. If the Lax–Friedrichs flux is employed instead of the Rusanov flux, then the effect of a reduction in the liquid velocity is not noticeable in the volume-fraction plot.

There *is*, of course, an effect on the pressure, due to the change of liquid compressibility.

Regarding the time-step length, the FORCE scheme behaves similarly to the Roe4 scheme; for small-enough time steps, the effect of the time-step length is moderate.

Comparison with the Roe4 scheme

In Figure 4.2 on page 107, we have plotted the data for the finest grid of 10001 points from Figure 4.1 on top of the corresponding results obtained from the MC-limited Roe4 scheme on a grid of 201 points and $C = 0.9$. For the gas volume fraction in Figure 4.2(a), the Roe4 scheme is clearly superior. As for the pressure shown in Figure 4.2(b), it is not completely clear which scheme is

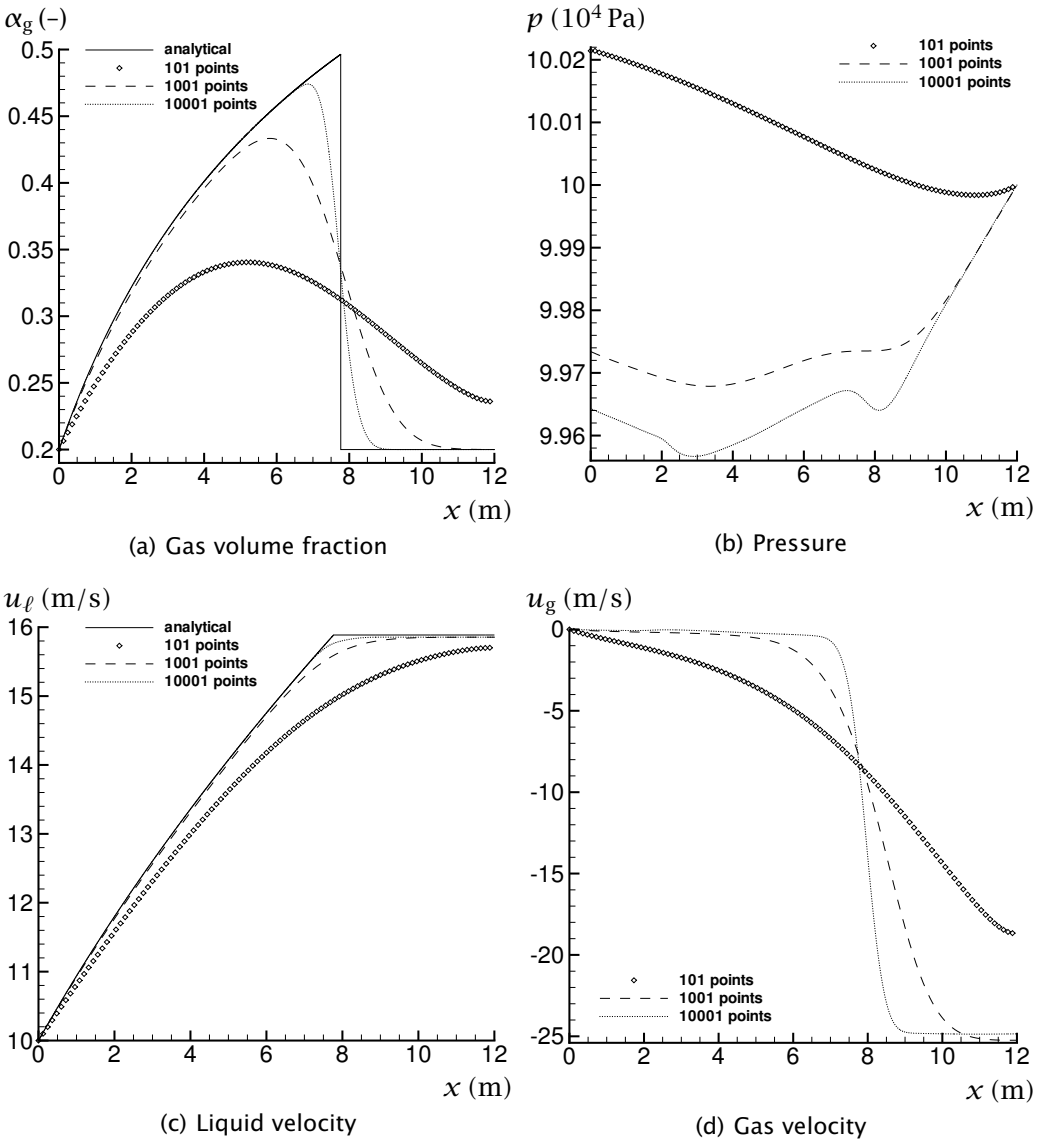

(a) Gas volume fraction

(b) Pressure

(c) Liquid velocity

(d) Gas velocity

Figure 4.1: Water faucet. Grid refinement for the FORCE scheme.

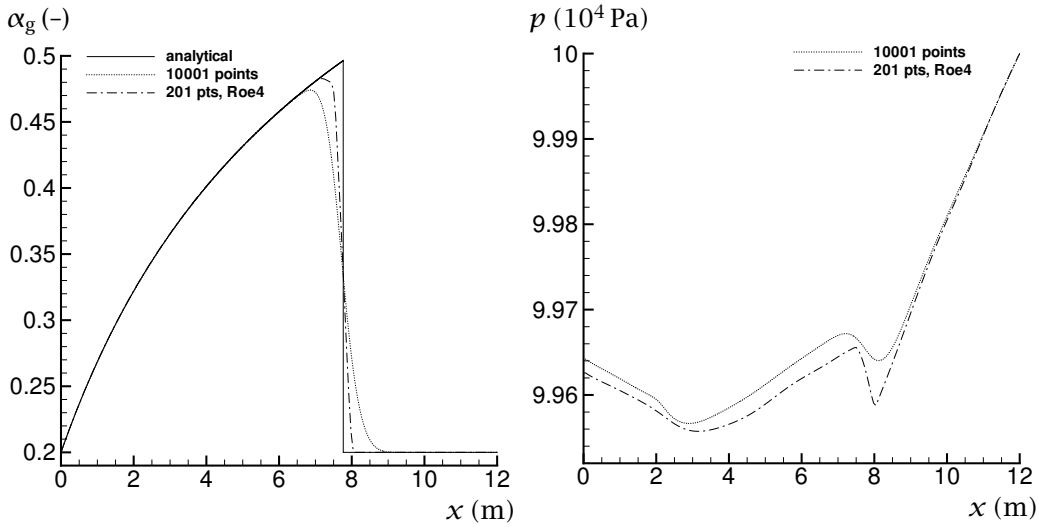

(a) Gas volume fraction (b) Pressure

Figure 4.2: Water faucet. Comparison of the FORCE scheme and the Roe4 scheme.

better, but the results are at least comparable. Hence, for the faucet case, the Roe4 scheme is able to produce equal or better results than the FORCE scheme using a fraction of the grid size and far longer time steps. This more than outweighs the fact that the Roe4 scheme is computationally expensive. For the results presented here, the CPU time of the Roe4 scheme was less than 1 % of that of the FORCE scheme.

Non-hyperbolic underlying model

In the original FORCE scheme, using the Lax–Friedrichs flux (4.7), neither the coefficient matrix (3.34) nor its eigenvalues appear explicitly. Hence one might be tempted to employ the scheme for solving a non-hyperbolic model. This has been done in Figure 4.3 on the next page, where the 0 model (3.106) has been taken for the interfacial pressure difference. The figure shows the effect of grid refinement using a time step of $\Delta t = 3.16 \cdot 10^{-6}$ s. For the coarse and intermediate grids, the results seem trustworthy, albeit diffusive. As one can see, for the 101-point grid, the scheme has been rendered almost totally diffusive. This is due to the $\Delta x/\Delta t$ term of the Lax–Friedrichs flux. By grid refinement, however, high-frequency disturbances are introduced, and they are not damped out. The liquid velocity is similarly oscillatory, and the gas velocity

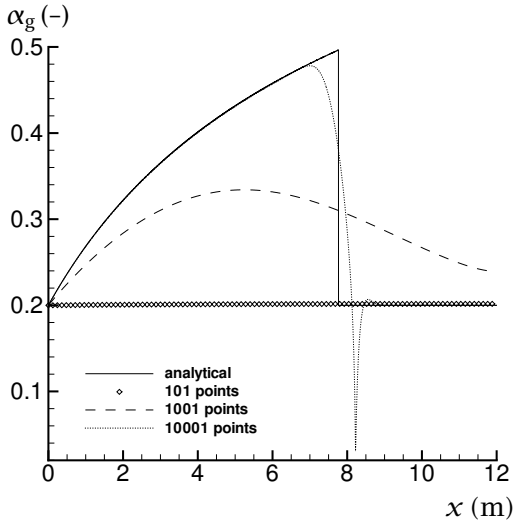

Figure 4.3: Gas volume fraction for the water faucet. Grid refinement for the FORCE scheme with the Lax–Friedrichs flux, using the the 0 model for the interfacial pressure difference.

and the pressure even worse.

The arising of instabilities by grid refinement is expected for a model with complex eigenvalues (see e.g. Ramshaw and Trapp, 1978). This indicates that the coefficient matrix and its complex eigenvalues do indeed stay lurking in the background, even if we try to forget them. What is more, for a model which does not converge by grid (and time-step) refinement, it is impossible to separate the numerical errors from the ones incurred by simplified physical modelling.

4.2.2 Toumi's shock tube

Recall Toumi's shock tube presented in Section 3.4.5 on page 89. A comparison between the FORCE, the Roe4 and the Roe5 schemes for a 101-point grid is shown in Figure 4.4 on the next page. The employed CFL number was $C = 0.5$. Both Roe-type schemes were used together with the MC limiter.

It was seen in the previous subsection that the FORCE scheme strongly smeared contact discontinuities. Figure 4.4 shows that the FORCE scheme also smeared the rarefaction wave (to the left), but perhaps less dramatically than for contact discontinuities. For the present shock (to the right), however, the FORCE scheme is too sharp (compressive), and hence becomes oscillatory, even

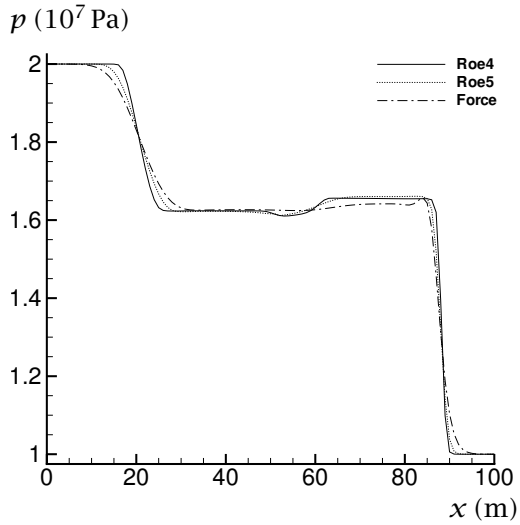

Figure 4.4: Pressure for Toumi's shock tube. Comparison of the FORCE, the Roe4 and the Roe5 schemes on a 101-point grid.

for a somewhat reduced CFL number of 0.5.

Another comparison of the three schemes is shown in Figure 4.5 on the following page, here for a finer grid of 10001 points. The CFL number was 0.5. Still, as can be seen in the figure, a small spike persists for the pressure and the velocities for the FORCE scheme. The CFL number had to be reduced to 0.1 to (almost) get rid of those.

It can be observed that the schemes converge to similar results. The largest differences between the schemes occur in the middle of the tube: The Roe4 scheme gives the sharpest resolution, and the Roe5 scheme produces slight gradients in the volume fraction and in the velocities.

4.2.3 Water–air separation

The water–air separation problem was presented in Section 3.4.6 on page 95. It is a challenging problem for two reasons:

1. The occurrence of sharp gradients, and

2. The tendency of the volume fractions to approach 0 and 1.

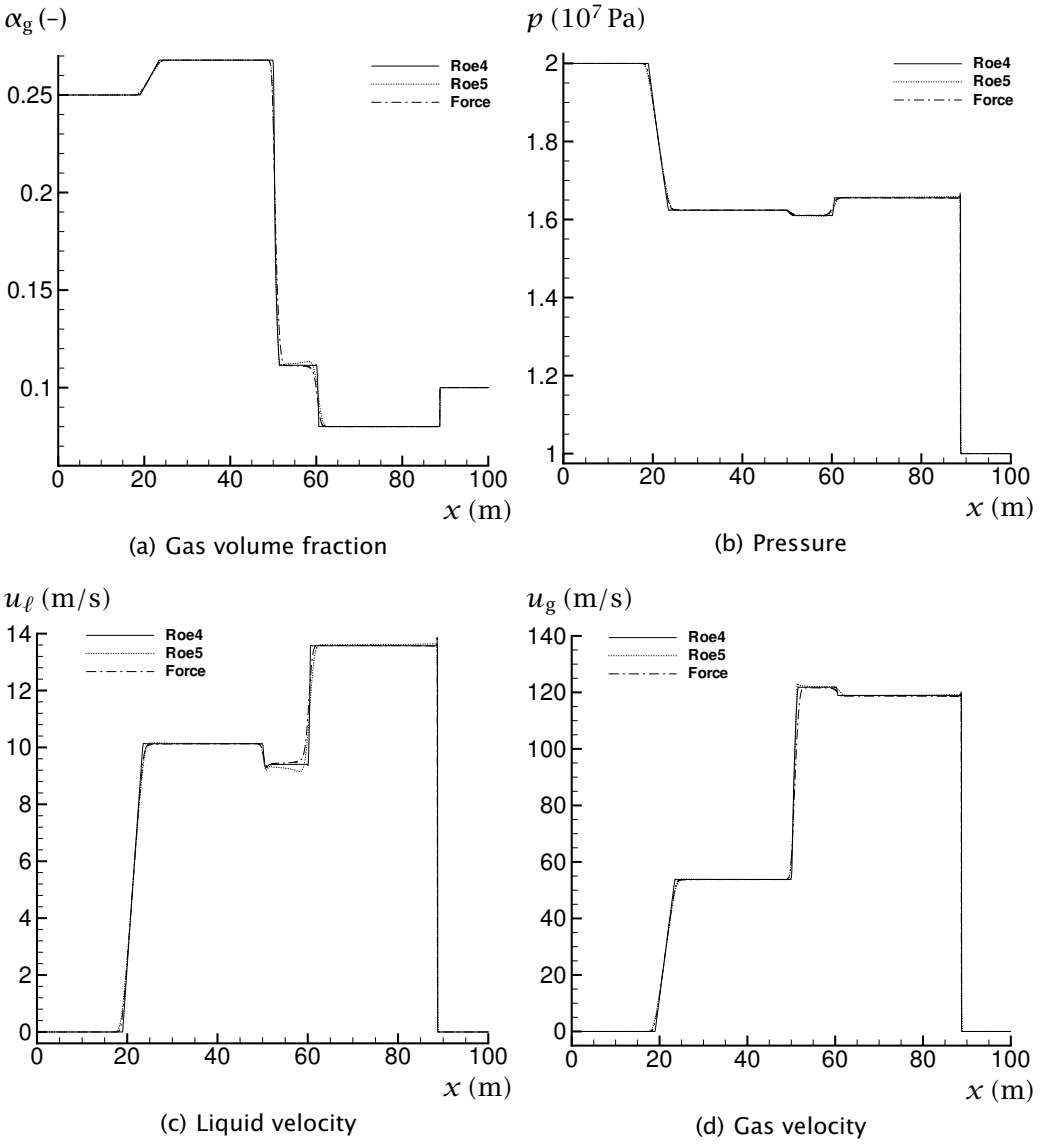

(a) Gas volume fraction

(b) Pressure

(c) Liquid velocity

(d) Gas velocity

Figure 4.5: Toumi's shock tube. Comparison of the FORCE, the Roe4 (MC limiter and entropy fix) and the Roe5 (first-order) schemes on a grid of 10001 points.

Interphasic friction

In a frictionless model, the gas velocity may attain very large values at the end of the tube, where the gas is disappearing. In the present case, it approached values of several thousand metres per second, leading to stability problems. Similar problems were also noted by Flåtten (2003, paper 2). Here we follow the Flåtten approach and include an interfacial drag term as a source term in the momentum equations:

$$F_{\mathrm{g}}^{\mathrm{d}} = -\Phi \alpha_{\mathrm{g}} \alpha_{\ell} \rho_{\mathrm{g}} (u_{\mathrm{g}} - u_{\ell}), \tag{4.18}$$

where Φ is positive and $F_{\ell}^{\mathrm{d}} = -F_{\mathrm{g}}^{\mathrm{d}}$. A similar formulation was also used by Paillère *et al.* (2003).

We adopt the friction parameter Φ of Flåtten (2003, paper 2). It is given by

$$\Phi = C \mathrm{e}^{-k\alpha_{\mathrm{g}}}, \tag{4.19}$$

where $C = 5 \cdot 10^4\,1/\mathrm{s}$ and $k = 50$. The values of the latter parameters were not discussed by Flåtten. Here we do likewise. The purpose, however, of the above choice of Φ is to impose the interfacial friction in the near-one-phase liquid regions, where the gas is expected to dissolve in the liquid.

Grid and time-step convergence

Figure 4.6 on the following page displays the results of grid refinement. Since the CFL number was held constant at $C = 0.5$, the effect of time-step refinement is also present. The data are for $t = 0.6\,\mathrm{s}$, that is, before a steady state is reached. It should be noted that the plotted analytical solution (given in Section 3.4.6) is approximate, and more so than the solution to the water faucet case.

Consider Figure 4.6(a) for the liquid volume fraction. Notice that the resolution of the shock (to the right) is significantly sharper than that of the discontinuity (to the left). The results for the fine grid of 10001 points are not too far away from the analytical solutions, but it should be noted that other methods (Evje and Flåtten, 2003; Flåtten, 2003; Paillère *et al.*, 2003) attain similar profiles on grids being one to two orders of magnitude coarser.

Results for $t = 1\,\mathrm{s}$, that is, when the steady state has ideally been reached, are shown in Figure 4.7 on page 113. For fine grids, the expected sharp volume-fraction profile is attained (Figure 4.7(a)), and likewise for the hydrostatic pressure profile (Figure 4.7(b)). The physical interpretation of the calculated velocity profiles is not obvious, since the velocity is non-zero mainly where the phase is practically absent (Figures 4.7(c) and 4.7(d)).

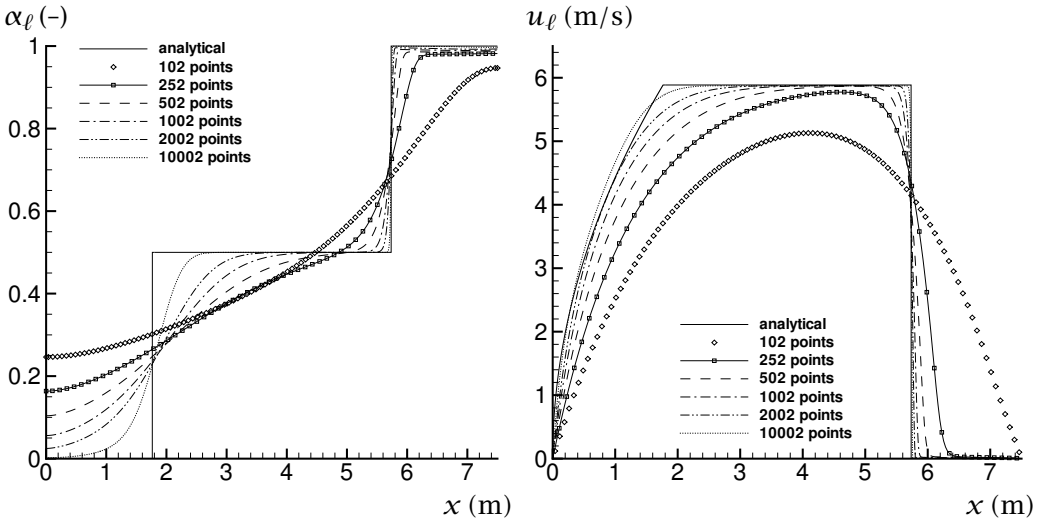

(a) Liquid volume fraction (b) Liquid velocity

Figure 4.6: Water–air separation at $t = 0.6\,\mathrm{s}$. Grid and time-step refinement for the FORCE scheme. $C = 0.5$.

Figure 4.7(d) shows that the interfacial friction model has succeeded reasonably well in limiting the gas velocity. One exception is at the interface, that is, where the volume fraction varies strongly. There, the gas is still present, but the interfacial friction is low due to the exponential term in the equation (4.19).

For the 101-point grid, spurious oscillations occurred at the water-side of the tube. This is clearly visible for the gas velocity, and also for the pressure.

It should be remarked that for the separation case, it is important that the tube is not leaking from the ends, particularly at the water side. Here this was achieved by simple extrapolation of the variables to the boundaries, such that the mass fluxes at the boundaries were zero. Fortunately, it is easy to check that the tube is water and air tight: The integral

$$\int_0^L \alpha_k \rho_k \, \mathrm{d}x,$$

where L is the tube length, should remain constant for each phase.

4.2.4 Summary

The FLIC scheme of Toro (1999, Section 14.5.2) has been adapted to the four-equation system. The suggested centred flux-limiter approaches have been

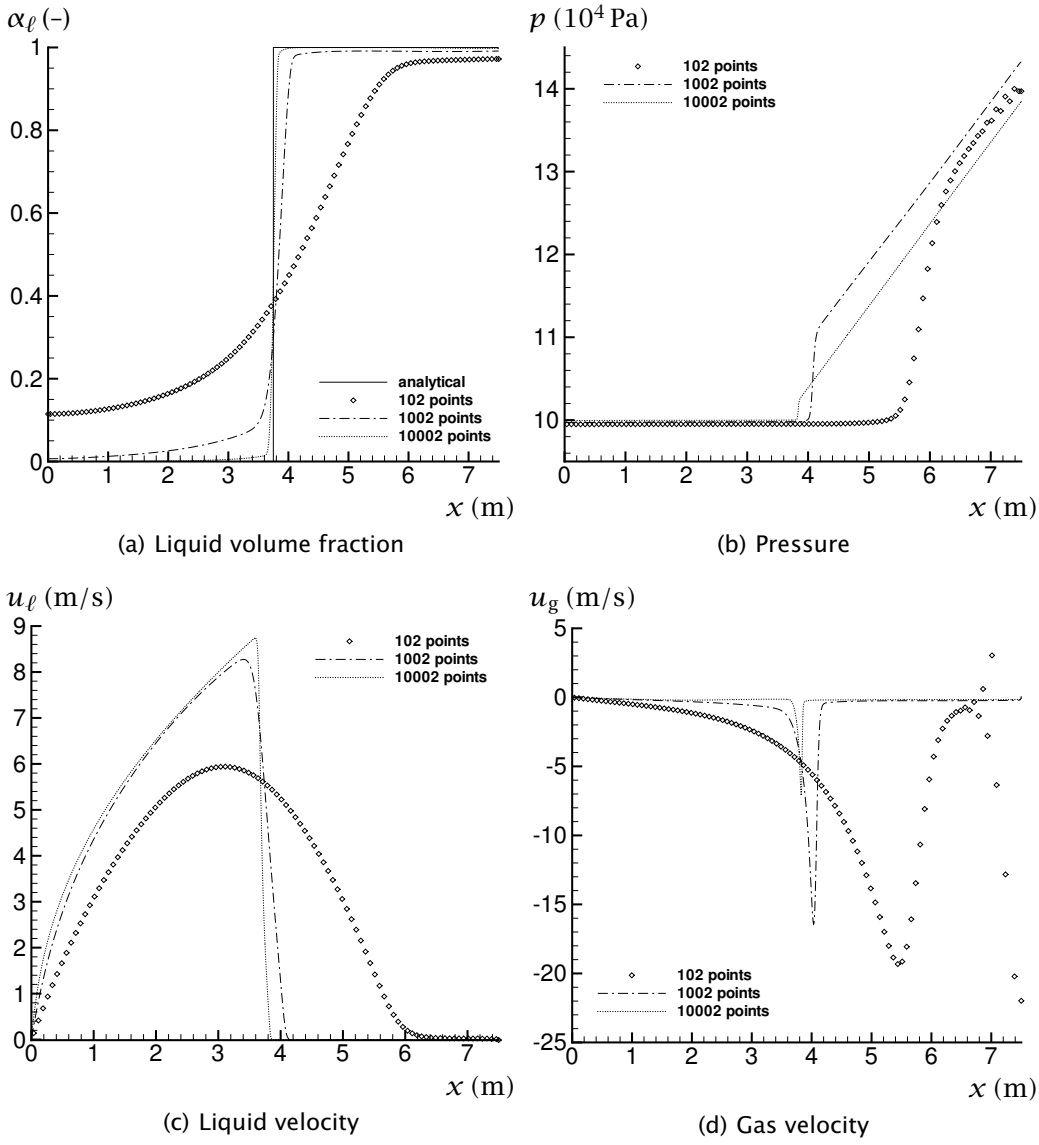

(a) Liquid volume fraction

(b) Pressure

(c) Liquid velocity

(d) Gas velocity

Figure 4.7: Water–air separation at $t = 1\,\mathrm{s}$. Grid and time-step refinement for the FORCE scheme. $C = 0.5$.

tested, but none has been found to work well. Hence, the first-order version (FORCE) of the scheme has been used. Herein, the Rusanov flux was employed instead of the Lax–Friedrichs flux, since that was found to give somewhat better results.

The FORCE scheme resolves shocks reasonably well, but sometimes introduces spurious oscillations. The scheme is highly diffusive on contact discontinuities. However, it succeeded in calculating the water–air separation case, where the Roe-type schemes failed.

4.3 Discretization of the non-conservative terms

As was observed in Section 4.2.2 on page 108, the FORCE scheme has a tendency to produce oscillations at shocks. This is in part related to the discretization of the non-conservative terms, which will be shown in the present section.

In Section 4.1, the non-conservative terms were discretized centrally. At the cost of having to consider the discrete equations in detail, we can instead write the scheme on a quasi-conservation form. Recall the continuity equation

$$\frac{\partial}{\partial t}(\alpha\rho) + \frac{\partial}{\partial x}(\alpha\rho u) = 0, \tag{4.21}$$

and the momentum equation

$$\frac{\partial}{\partial t}(\alpha\rho u) + \frac{\partial}{\partial x}(\alpha\rho u^2) + \alpha_k \frac{\partial p}{\partial x} + \Delta p \frac{\partial \alpha}{\partial x} = 0, \tag{4.22}$$

where phasic indices have been dropped and source terms neglected. Herein, Δp refers to the interfacial pressure difference.

In the following, superscripts refer to time steps, and subscripts to the spatial grid.

4.3.1 Lax–Friedrichs scheme

The Lax–Friedrichs scheme (see e.g. Toro, 1999, Section 5.2.2) for (4.21)–(4.22) can be written as follows:

Continuity equation

The continuity equation (4.21) is discretized as

$$(\alpha\rho)_i^{n+1} = \frac{1}{2}\Big[(\alpha\rho)_{i-1}^n + (\alpha\rho)_{i+1}^n\Big] + \frac{\Delta t}{2\Delta x}\Big[(\alpha\rho u)_{i-1}^n - (\alpha\rho u)_{i+1}^n\Big], \tag{4.23}$$

which can be written in conservation form,

$$\frac{(\alpha\rho)_i^{n+1} - (\alpha\rho)_i^n}{\Delta t} + \frac{F_{i+1/2} - F_{i-1/2}}{\Delta x} = 0, \tag{4.24}$$

with

$$F_{i+1/2} = \frac{1}{2}\Big[(\alpha\rho u)_i^n + (\alpha\rho u)_{i+1}^n\Big] + \frac{1}{2}\frac{\Delta x}{\Delta t}\Big[(\alpha\rho)_i^n - (\alpha\rho)_{i+1}^n\Big]. \tag{4.25}$$

Momentum equation

The momentum equation (4.22) is analogously discretized as

$$\begin{aligned}(\alpha\rho u)_i^{n+1} = \frac{1}{2}\Big[(\alpha\rho u)_{i-1}^n + (\alpha\rho u)_{i+1}^n\Big] + \frac{\Delta t}{2\Delta x}\Big[(\alpha\rho u^2)_{i-1}^n - (\alpha\rho u^2)_{i+1}^n\Big] \\ + \frac{\Delta t}{2\Delta x}\Big\{(\Delta p)_i^n\Big[\alpha_{i-1}^n - \alpha_{i+1}^n\Big] + \alpha_i^n\Big[p_{i-1}^n - p_{i+1}^n\Big]\Big\},\end{aligned} \tag{4.26}$$

but it cannot be written in conservation form. However, it can be written in the quasi-conservation form

$$\frac{(\alpha\rho u)_i^{n+1} - (\alpha\rho u)_i^n}{\Delta t} + \frac{F_{i+1/2}^{\text{right}} - F_{i-1/2}^{\text{left}}}{\Delta x} = 0, \tag{4.27}$$

with

$$F_{i+1/2}^{\text{right}} = F_{i+1/2} + \frac{1}{2}(\Delta p)_i^n\Big[\alpha_i^n + \alpha_{i+1}^n\Big] + \frac{1}{2}\alpha_i^n\Big[p_i^n + p_{i+1}^n\Big], \tag{4.28}$$

and

$$F_{i+1/2}^{\text{left}} = F_{i+1/2} + \frac{1}{2}(\Delta p)_{i+1}^n\Big[\alpha_i^n + \alpha_{i+1}^n\Big] + \frac{1}{2}\alpha_{i+1}^n\Big[p_i^n + p_{i+1}^n\Big], \tag{4.29}$$

where

$$F_{i+1/2} = \frac{1}{2}\Big[(\alpha\rho u^2)_i^n + (\alpha\rho u^2)_{i+1}^n\Big] + \frac{1}{2}\frac{\Delta x}{\Delta t}\Big[(\alpha\rho u)_i^n - (\alpha\rho u)_{i+1}^n\Big]. \tag{4.30}$$

4.3.2 Richtmyer scheme

The Richtmyer scheme (see e.g. Toro, 1999, Section 14.5.1) is a two-step version of the Lax–Wendroff scheme. One can interpret it as taking two steps with the Lax–Friedrichs scheme detailed in the preceding subsection. The first step (predictor step) determines the state $\boldsymbol{Q}_{i+1/2}^{n+1/2}$, and in the second step (corrector step), the sought state $\boldsymbol{Q}_i^n$ is found.

Predictor step

Note that that in the following, the stencils are narrow, whereas they where broad for the Lax–Friedrichs scheme. Hence this is a kind of staggering.

Continuity equation

$$(\alpha\rho)_{i+1/2}^{n+1/2} = \frac{1}{2}\Big[(\alpha\rho)_i^n + (\alpha\rho)_{i+1}^n\Big] + \frac{\Delta t}{2\Delta x}\Big[(\alpha\rho u)_i^n - (\alpha\rho u)_{i+1}^n\Big]. \tag{4.31}$$

Momentum equation

$$\begin{aligned}(\alpha\rho u)_{i+1/2}^{n+1/2} = {} & \frac{1}{2}\Big[(\alpha\rho u)_i^n + (\alpha\rho u)_{i+1}^n\Big] + \frac{\Delta t}{2\Delta x}\Big[(\alpha\rho u^2)_i^n - (\alpha\rho u^2)_{i+1}^n\Big] \\ & + \frac{\Delta t}{2\Delta x}\Big\{(\Delta p)_{i+1/2}^n\Big[\alpha_i^n - \alpha_{i+1}^n\Big] + \alpha_{i+1/2}^n\Big[p_i^n - p_{i+1}^n\Big]\Big\}. \end{aligned} \tag{4.32}$$

Herein, the cell-interface values are found by linear interpolation:

$$(\Delta p)_{i+1/2}^n = \frac{1}{2}\Big[(\Delta p)_i^n + (\Delta p)_{i+1}^n\Big], \tag{4.33}$$

and

$$\alpha_{i+1/2}^n = \frac{1}{2}\Big[\alpha_i^n + \alpha_{i+1}^n\Big]. \tag{4.34}$$

Corrector step

In the corrector step, the intermediate state from the predictor step is employed to yield the state at the next time step.

Continuity equation The continuity equation can be written in the conservation form (4.24) with the numerical mass flux given by

$$F_{i+1/2} = (\alpha\rho u)_{i+1/2}^{n+1/2}. \tag{4.35}$$

Momentum equation The momentum equation is now written as

$$\begin{aligned}\frac{(\alpha\rho u)_i^{n+1} - (\alpha\rho u)_i^n}{\Delta t} + \frac{(\alpha\rho u^2)_{i+1/2}^{n+1/2} - (\alpha\rho u^2)_{i-1/2}^{n+1/2}}{\Delta x} \\ + (\Delta p)_i^n \frac{\alpha_{i+1/2}^{n+1/2} - \alpha_{i-1/2}^{n+1/2}}{\Delta x} + \alpha_i^n \frac{p_{i+1/2}^{n+1/2} - p_{i-1/2}^{n+1/2}}{\Delta x} = 0, \end{aligned} \tag{4.36}$$

which can be written in the quasi-conservation form (4.27) with

$$F^{\text{right}}_{i+1/2} = (\alpha\rho u^2)^{n+1/2}_{i+1/2} + (\Delta p)^n_i \alpha^{n+1/2}_{i+1/2} + \alpha^n_i p^{n+1/2}_{i+1/2}, \tag{4.37}$$

and

$$F^{\text{left}}_{i+1/2} = (\alpha\rho u^2)^{n+1/2}_{i+1/2} + (\Delta p)^n_{i+1} \alpha^{n+1/2}_{i+1/2} + \alpha^n_{i+1} p^{n+1/2}_{i+1/2}. \tag{4.38}$$

4.3.3 FORCE2 scheme

The FORCE scheme is assembled as

$$\boldsymbol{Q}^{n+1}_i = \boldsymbol{Q}^n_i - \frac{\Delta t}{\Delta x}\left(\boldsymbol{F}^{\text{right}}_{i+1/2} - \boldsymbol{F}^{\text{left}}_{i-1/2}\right), \tag{4.39}$$

taking

$$F_{i+1/2} = \frac{1}{2}\left(F^{\text{LF}}_{i+1/2} + F^{\text{R}}_{i+1/2}\right) \tag{4.40}$$

for the numerical mass fluxes, where the Lax–Friedrichs flux, $F^{\text{LF}}_{i+1/2}$, is calculated using (4.25), and the Richtmyer flux, $F^{\text{R}}_{i+1/2}$, is given by (4.35).

For the non-conservative numerical momentum 'fluxes' one takes

$$F_{\text{right/left}} = \frac{1}{2}\left(F^{\text{LF}}_{\text{right/left}} + F^{\text{R}}_{\text{right/left}}\right), \tag{4.41}$$

with the Lax–Friedrichs flux from (4.28) or (4.29), and the Richtmyer flux from (4.37) or (4.38).

This scheme will be referred to as 'FORCE2'. It differs from the FORCE scheme described in Section 4.1 regarding the discretization of the non-conservative terms. In particular,

1. The need for the interpolation (4.33)–(4.34) introduces some numerical diffusion.

2. The non-conservative terms count in the calculation of the intermediate state (4.32).

4.3.4 Toumi's shock tube revisited

The influence of the discretization of the non-conservative terms is illustrated in Figure 4.8 on the next page. The calculations have been performed on a 101-point grid with a CFL number of $C = 0.9$. The label 'LxF' means that the Lax–Friedrichs flux has been used, while the label 'Rus' denotes that the

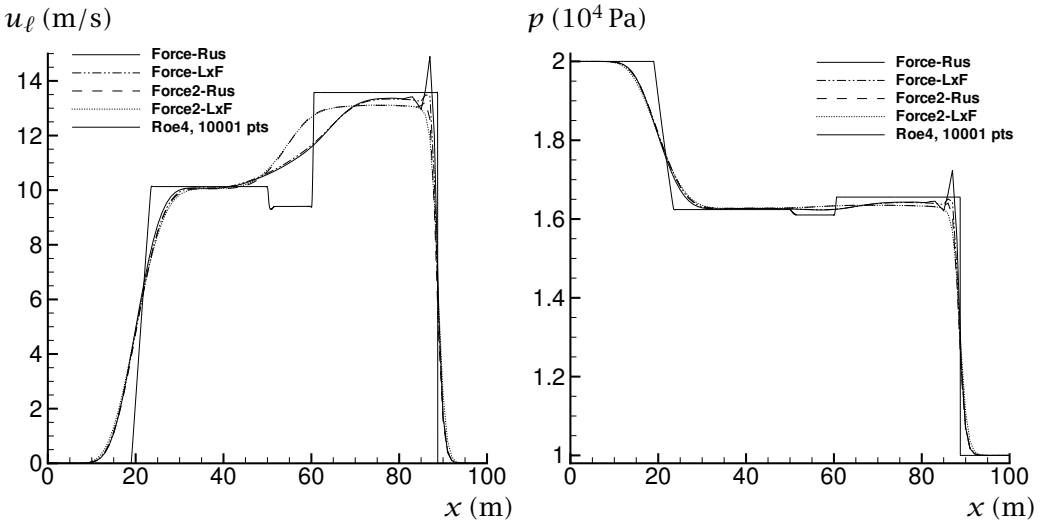

(a) Liquid velocity (b) Pressure

Figure 4.8: Toumi's shock tube. FORCE-scheme variants. Influence of the discretization of the non-conservative terms, as well as 'base flux', on a 101-point grid.

Rusanov flux has been taken as the low-order flux, that is, for FORCE2, $\Delta x/\Delta t$ has been substituted by $\lambda_{\max}$ in the equations (4.25) and (4.30), and similarly for FORCE.

The figure shows that when the Rusanov flux is used with the FORCE scheme, an overshoot occurs at the shock. This is reduced by employing the Lax–Friedrichs flux instead. The overshoot is further reduced for the combination of the FORCE2 scheme with the Rusanov flux. However, in this case, it is only the FORCE2 scheme with the Lax–Friedrichs flux that avoids overshoots.

It is perhaps surprising that for the liquid velocity in Figure 4.8(a), the FORCE2 scheme seems to give a sharper resolution than FORCE of the discontinuity at about $x = 60\,\mathrm{m}$, but situated a bit too far to the left. For the pressure in Figure 4.8(b), on the other hand, the FORCE2 profile appears more smeared. This latter tendency, however, is reversed by grid refinement.

At the rarefaction on the left-hand side, the differences are small, but FORCE2 is slightly more diffusive.

4.4 Summary

The FORCE scheme could be employed where the Roe4 and Roe5 schemes failed. Another use of it is for quick tests, since it is computationally less expensive for a given grid. However, it is not necessarily computationally cheaper for a given accuracy; an example was found of the opposite.

The tendency to produce oscillations at shocks is influenced by the discretization of the non-conservative terms. The approach of including the non-conservative terms in the numerical fluxes (FORCE2) produced preferable results for Toumi's shock tube.

5 The discrete-equation multiphase model*

Abgrall and Saurel (2003) presented a discrete-equation two-pressure two-phase model of seven equations. A main characteristic of that model is that the Riemann problems are solved between two pure fluids, and that phase interaction is determined by the Riemann solver.

Here we propose a five-equation isentropic simplification of the discrete-equation model, and by examples we show how existing and new models for interfacial closures can be incorporated into it. The interfacial pressure has a determining effect on the final solution.

We further show that the discrete-equation model can reproduce results for two-phase shock tubes given in the literature when the adequate interfacial-pressure model is employed. Finally, we compare the present results with those obtained using the Roe5 scheme on a continuous model, and obtain very good agreement.

The notation in this chapter is slightly different from that of the rest of the thesis, in that the phases are indicated by superscripts, to avoid 'conflict' with the often-needed spatial and other subscripts.

5.1 Introduction

5.1.1 Background

Multiphase flows are relevant in a large and increasing amount of applications, including in the oil and gas industries, in the chemical and process industries, in heat pumping applications and in nuclear power plants. Still, the mathematical modelling and numerical simulation of multiphase flows is, as a whole, not a mature science. Only in specialized areas is the state of the art satisfactory.

In the present work, we focus on two-phase flows. In recent years, progress has been made regarding the understanding of the mathematical properties and the proper spatial discretization of two-phase models. However, these questions are challenging, and hence, in the research papers presented, one has often not been able to attend to the constitutive terms in need of physical modelling and experimental verification.

*This chapter is based on the article by Munkejord and Papin (2005).

Here we investigate ways to model the interfacial pressure in the framework of the discrete-equation model of Abgrall and Saurel (2003).

5.1.2 Previous work

Saurel and Abgrall (1999) presented a two-velocity two-pressure two-phase model of seven equations, where pressure and / or velocity relaxation could be performed after the hyperbolic time step. The model was expanded to several space dimensions by Saurel and LeMetayer (2001), and it was stated to be suitable for compressible multiphase flows with interfaces, shocks, detonation waves and cavitation.

The approximate Riemann solver employed by Saurel and Abgrall (1999) was a modified Harten, Lax and van Leer (HLL) scheme. Other authors have later presented similar methods using other solvers. Niu (2001) applied a modified advection upstream splitting method (AUSMD) and solved the seven-equation model in one and two dimensions, also adding a k–ε turbulence model. A Roe-type scheme for the seven-equation model was presented by Karni *et al.* (2004).

One of the main difficulties of the above-mentioned two-phase model, is the occurrence of non-conservative products. Abgrall and Saurel (2003) proposed a discrete-equation two-phase model aiming to avoid the problems of the non-conservative terms by considering Riemann problems between pure phases. This approach leads to the phase interaction being defined through the Riemann solver.

5.1.3 Outline of chapter

The present chapter analyses the interfacial pressure and the discrete-equation model. Section 5.2 briefly repeats the multiphase model. The discrete-equation numerical scheme of Abgrall and Saurel (2003) is revisited in Section 5.3. Furthermore, similarities to, and differences from, the continuous model are pointed out, and the pure-phase Riemann problem is explained. The continuous model used for comparisons is briefly referred to in Section 5.4. Test calculations are presented in Section 5.5, and conclusions are drawn in Section 5.6.

5.2 Multiphase model

We recall that the one-dimensional, inviscid, isentropic multiphase flow is customarily described by the continuity equation

$$\frac{\partial}{\partial t}(\alpha^{(k)}\rho^{(k)}) + \frac{\partial}{\partial x}(\alpha^{(k)}\rho^{(k)}u^{(k)}) = 0, \tag{5.1}$$

and the momentum equation

$$\frac{\partial}{\partial t}(\alpha^{(k)}\rho^{(k)}u^{(k)}) + \frac{\partial}{\partial x}\left(\alpha^{(k)}\rho^{(k)}(u^{(k)})^2\right) + \alpha^{(k)}\frac{\partial p^{(k)}}{\partial x} + (p^{(k)} - p_{\text{int}}^{(k)})\frac{\partial \alpha^{(k)}}{\partial x} = 0, \tag{5.2}$$

when gravity, mass transfer, wall friction, interface friction and other effects are neglected. This model is arrived at by volume-averaging the governing equations for each phase, and by considering a cross-section of a pipe. Due to the term $p_{\text{int}}^{(k)}\partial\alpha^{(k)}/\partial x$, the equation system cannot be written in conservative form. The Riemann problem for non-conservative systems is not always unique, and it is in general difficult to define its solution (Andrianov and Warnecke, 2004).

A discrete mathematical and numerical model for compressible multiphase flows was introduced by Abgrall and Saurel (2003). Since the two-phase mixture was considered at the discrete, pure-phase level, the problem of the $\nabla\alpha$ terms, which render the system of equations non-conservative (Saurel and Abgrall, 1999), was avoided. For the sake of clarification, the main elements of the Abgrall and Saurel (2003) model are given here in detail. Further, we adapt their model to isentropic problems, something which represents a simplification.

5.2.1 Transport equations

For an inviscid, isentropic flow, each pure fluid k is governed by the (isentropic) Euler equations:

$$\frac{\partial \boldsymbol{q}^{(k)}}{\partial t} + \nabla \cdot \boldsymbol{F}^{(k)} = 0, \tag{5.3}$$

where $\boldsymbol{q}^{(k)}$ is the vector containing the 'conservative' variables,

$$\boldsymbol{q}^{(k)} = \left[\rho^{(k)}, \quad \rho^{(k)}\boldsymbol{u}^{(k)}\right]^T, \tag{5.4}$$

and $\boldsymbol{F}^{(k)}$ is the corresponding flux matrix:

$$\boldsymbol{F}^{(k)} = \left[\rho^{(k)}\boldsymbol{u}^{(k)}, \quad \rho^{(k)}\boldsymbol{u}^{(k)} \otimes \boldsymbol{u}^{(k)} + p^{(k)}\boldsymbol{I}\right]^T. \tag{5.5}$$

Denote the phase-indicator function (characteristic function) for phase k as $\chi^{(k)}$. It is equal to one inside phase k and zero otherwise. It is obvious that phase k is advected with the velocity of phase k. Hence the same is true for the phase-indicator function, which gives

$$\frac{\partial \chi^{(k)}}{\partial t} + \boldsymbol{u}^{(k)} \cdot \boldsymbol{\nabla} \chi^{(k)} = 0. \tag{5.6}$$

$\boldsymbol{\nabla} \chi^{(k)} = 0$, except at the interface of phase k. Therefore it is natural to write

$$\frac{\partial \chi^{(k)}}{\partial t} + \boldsymbol{u}_{\text{int}}^{(k)} \cdot \boldsymbol{\nabla} \chi^{(k)} = 0, \tag{5.7}$$

where $\boldsymbol{u}_{\text{int}}^{(k)}$ is the interface velocity of phase k. The above equation is derived in detail by Drew and Passman (1999, Section 9.1.3). For two phases, we have $\boldsymbol{u}_{\text{int}}^{(1)} = \boldsymbol{u}_{\text{int}}^{(2)} = \boldsymbol{u}_{\text{int}}$.

Here we follow the ensemble-averaging approach of Drew and Passman (1999, see Section 9.1 and Chapter 11). The ensemble-averaging operator, $\mathcal{E}(\cdot)$, is assumed to commute with differentiation in space and time, so that

$$\mathcal{E}(\boldsymbol{\nabla} \psi) = \boldsymbol{\nabla} \mathcal{E}(\psi), \tag{5.8}$$

and

$$\mathcal{E}\left(\frac{\partial \psi}{\partial t}\right) = \frac{\partial}{\partial t} \mathcal{E}(\psi), \tag{5.9}$$

where ψ is a general function. Further, we have, for example

$$\int \mathcal{E}(\psi)\, \mathrm{d}x\, \mathrm{d}t = \mathcal{E}\left(\int \psi\, \mathrm{d}x\, \mathrm{d}t\right). \tag{5.10}$$

Drew and Passman (1999) derived a relation for the ensemble average of the gradient (or divergence) of a general function ψ:

$$\mathcal{E}\left(\chi^{(k)} \boldsymbol{\nabla} \psi\right) = \boldsymbol{\nabla}\left(\mathcal{E}\left(\chi^{(k)} \psi\right)\right) - \mathcal{E}\left(\psi_{\text{int}}^{(k)} \boldsymbol{\nabla} \chi^{(k)}\right), \tag{5.11}$$

which is similar to the Slattery averaging theorem (Slattery, 1967; Whitaker, 1969) for volume averaging. The subscript 'int' denotes the value at the interface, which is 'picked up' by the $\boldsymbol{\nabla} \chi^{(k)}$ operator.

The expression for the ensemble average of a time derivative is

$$\mathcal{E}\left(\chi^{(k)} \frac{\partial \psi}{\partial t}\right) = \frac{\partial}{\partial t}\left(\mathcal{E}\left(\chi^{(k)} \psi\right)\right) - \mathcal{E}\left(\psi_{\text{int}}^{(k)} \frac{\partial \chi^{(k)}}{\partial t}\right). \tag{5.12}$$

Thus we can write the averaged balance equations for each phase as

$$\frac{\partial \mathcal{E}\left(\chi^{(k)}\rho^{(k)}\right)}{\partial t} + \nabla \cdot \mathcal{E}\left(\chi^{(k)}\rho^{(k)}\boldsymbol{u}^{(k)}\right) = \mathcal{E}\left(\rho^{(k)}(\boldsymbol{u}^{(k)} - \boldsymbol{u}_{\text{int}}^{(k)}) \cdot \nabla\chi^{(k)}\right), \quad (5.13)$$

and

$$\frac{\partial \mathcal{E}\left(\chi^{(k)}\rho^{(k)}\boldsymbol{u}^{(k)}\right)}{\partial t} + \nabla \cdot \left[\mathcal{E}\left(\chi^{(k)}\rho^{(k)}\boldsymbol{u}^{(k)} \otimes \boldsymbol{u}^{(k)}\right) + \mathcal{E}\left(\chi^{(k)}p^{(k)}\right)\right] = \mathcal{E}\left((\rho^{(k)}\boldsymbol{u}^{(k)} \otimes (\boldsymbol{u}^{(k)} - \boldsymbol{u}_{\text{int}}^{(k)}) + p^{(k)}\boldsymbol{I}) \cdot \nabla\chi^{(k)}\right). \quad (5.14)$$

Defining the volume fraction of phase k as

$$\alpha^{(k)} = \mathcal{E}\left(\chi^{(k)}\right), \quad (5.15)$$

the average density as

$$\overline{\rho}^{(k)} = \frac{\mathcal{E}\left(\chi^{(k)}\rho^{(k)}\right)}{\alpha^{(k)}}, \quad (5.16)$$

the average velocity as

$$\overline{\boldsymbol{u}}^{(k)} = \frac{\mathcal{E}\left(\chi^{(k)}\rho^{(k)}\boldsymbol{u}^{(k)}\right)}{\alpha^{(k)}\overline{\rho}^{(k)}}, \quad (5.17)$$

etc., assuming

$$\mathcal{E}\left(\chi^{(k)}\rho^{(k)}\boldsymbol{u}^{(k)} \otimes \boldsymbol{u}^{(k)}\right) = \alpha^{(k)}\overline{\rho}^{(k)}\overline{\boldsymbol{u}}^{(k)} \otimes \overline{\boldsymbol{u}}^{(k)}, \quad (5.18)$$

and omitting the overline symbol for notational convenience, we get:

$$\frac{\partial \alpha^{(k)}\rho^{(k)}}{\partial t} + \nabla \cdot [\alpha^{(k)}\rho^{(k)}\boldsymbol{u}^{(k)}] = \mathcal{E}\left(\rho^{(k)}(\boldsymbol{u}^{(k)} - \boldsymbol{u}_{\text{int}}^{(k)}) \cdot \nabla\chi^{(k)}\right), \quad (5.19)$$

and

$$\frac{\partial \alpha^{(k)}\rho^{(k)}\boldsymbol{u}^{(k)}}{\partial t} + \nabla \cdot [\alpha^{(k)}\rho^{(k)}\boldsymbol{u}^{(k)} \otimes \boldsymbol{u}^{(k)} + \alpha^{(k)}p^{(k)}\boldsymbol{I}] = \mathcal{E}\left((\rho^{(k)}\boldsymbol{u}^{(k)} \otimes (\boldsymbol{u}^{(k)} - \boldsymbol{u}_{\text{int}}^{(k)}) + p^{(k)}\boldsymbol{I}) \cdot \nabla\chi^{(k)}\right). \quad (5.20)$$

Herein, the quantities on the left-hand side are averaged. The averaged topological equation is

$$\frac{\partial \alpha^{(k)}}{\partial t} + \mathcal{E}\left(\boldsymbol{u}_{\text{int}}^{(k)} \cdot \nabla\chi^{(k)}\right) = 0. \quad (5.21)$$

5.2.2 Thermodynamics

In the present work, the energy equation is not considered, and the following equation of state is employed:

$$p^{(k)} = (c^{(k)})^2(\rho^{(k)} - \rho_\circ^{(k)}), \tag{5.22}$$

where the speed of sound $c^{(k)}$ and the 'reference density' $\rho_\circ^{(k)}$ are constants for each phase. The above equation corresponds to the stiffened-gas equation of state, $p = (\gamma - 1)\rho e - \gamma p_\circ$, where e is the internal energy, if one takes $c^2 = (\gamma - 1)e$ and $\gamma p_\circ = c^2\rho_\circ$.

This equation of state (5.22) has been derived under the assumption of an isentropic flow. In fact, it also implies isothermal flow, as was shown in Section 2.5.5 on page 34.

Since we are interested in two-phase mixtures, pure single-phase flow has not been explicitly accounted for. This restriction is not thought to be of practical importance in most applications.

5.3 Numerical scheme

Henceforth we treat only one spatial dimension for simplicity. Consider the non-averaged balance equations (5.3) for each phase. They are multiplied by the phase-indicator function $\chi^{(k)}$ and integrated over a control volume C_i as follows:

$$\int_{C_i} \chi^{(k)} \frac{\partial \boldsymbol{q}^{(k)}}{\partial t}\,\mathrm{d}x + \int_{C_i} \chi^{(k)} \nabla \cdot \boldsymbol{F}^{(k)}\,\mathrm{d}x = 0, \tag{5.23}$$

or

$$\int_{C_i} \chi^{(k)} \frac{\partial \boldsymbol{q}^{(k)}}{\partial t}\,\mathrm{d}x + \int_{\partial[C_i \cap \{\chi^{(k)}=1\}]} \chi^{(k)} \boldsymbol{F}^{(k)} \cdot \boldsymbol{n}\,\mathrm{d}s = 0, \tag{5.24}$$

where $\boldsymbol{n}$ is the outward-pointing unit normal vector. Using the commutation property (5.10), we can ensemble-average (5.23):

$$\mathcal{E}\left(\int_{C_i} \left\{ \frac{\partial \chi^{(k)} \boldsymbol{q}^{(k)}}{\partial t} + \nabla \cdot (\chi^{(k)} \boldsymbol{F}^{(k)}) - \boldsymbol{q}^{(k)} \frac{\partial \chi^{(k)}}{\partial t} - \boldsymbol{F}^{(k)} \cdot \nabla \chi^{(k)} \right\} \mathrm{d}x \right) = 0, \tag{5.25}$$

and using (5.7), to obtain, analogously to (5.19) and (5.20):

$$\int_{C_i} \frac{\partial \alpha^{(k)} \boldsymbol{q}^{(k)}}{\partial t}\,\mathrm{d}x + \int_{C_i} \nabla \cdot (\alpha^{(k)} \boldsymbol{F}^{(k)})\,\mathrm{d}x = \int_{C_i} \mathcal{E}\left(\boldsymbol{S}^{(k)}\right)\mathrm{d}x, \tag{5.26}$$

where

$$\boldsymbol{S}^{(k)} = \begin{bmatrix} \rho^{(k)}(\boldsymbol{u}^{(k)} - \boldsymbol{u}_{\mathrm{int}}^{(k)}) \cdot \nabla \chi^{(k)} \\ (\rho^{(k)} \boldsymbol{u}^{(k)} \otimes (\boldsymbol{u}^{(k)} - \boldsymbol{u}_{\mathrm{int}}^{(k)}) + p^{(k)} \boldsymbol{I}) \cdot \nabla \chi^{(k)} \end{bmatrix}. \tag{5.27}$$

However, the topological equation (5.7) cannot be written in the form (5.3), and must therefore be treated differently. Still, we may integrate it,

$$\int_{C_i} \frac{\partial \chi^{(k)}}{\partial t} \, \mathrm{d}x + \int_{C_i} \boldsymbol{u}_{\mathrm{int}}^{(k)} \cdot \boldsymbol{\nabla} \chi^{(k)} \, \mathrm{d}x, \tag{5.28}$$

and take the ensemble average:

$$\int_{C_i} \frac{\partial \mathcal{E}\left(\chi^{(k)}\right)}{\partial t} \, \mathrm{d}x = -\int_{C_i} \mathcal{E}\left(\boldsymbol{u}_{\mathrm{int}}^{(k)} \cdot \boldsymbol{\nabla} \chi^{(k)}\right) \mathrm{d}x. \tag{5.29}$$

Since we consider a two-phase flow at the discrete level, $\mathcal{E}\left(\chi^{(k)}\right) = \chi^{(k)} = 1$ inside phase k and 0 otherwise, and the above equation reads $0 = 0$ except at the interface, where the *size* of the jump in $\chi^{(k)}$ equals 1.

5.3.1 Lagrangian fluxes

The right-hand sides of (5.26) and (5.29) give rise to the Lagrangian fluxes $\boldsymbol{F}^{\mathrm{lag},(k)}$ treated in Abgrall and Saurel (2003). They are sometimes called transfer integrals in the multiphase literature. For example, in 1D we have

$$\boldsymbol{S}^{(k)} = \boldsymbol{F}^{\mathrm{lag},(k)} \frac{\partial \chi^{(k)}}{\partial x}, \tag{5.30}$$

where

$$\boldsymbol{F}^{\mathrm{lag},(k)} = \boldsymbol{F}^{(k)} - u_{\mathrm{int}}^{(k)} \boldsymbol{q}^{(k)}. \tag{5.31}$$

The phase velocity $\boldsymbol{u}^{(k)}$ at the interface and the corresponding interface velocity $\boldsymbol{u}_{\mathrm{int}}^{(k)}$ are different if there is mass transfer between the phases. Since in the present work we assume that no interphase mass transfer takes place, we get:

$$\boldsymbol{S}^{(k)} = \begin{bmatrix} 0 \\ p^{(k)} \boldsymbol{I} \cdot \boldsymbol{\nabla} \chi^{(k)}. \end{bmatrix}. \tag{5.32}$$

Integrate (5.26) over $C_i \times [t_0, t_0 + \Delta t]$:

$$\iint_{C_i \times [t_0, t_0+\Delta t]} \left(\frac{\partial \alpha^{(k)} \boldsymbol{q}^{(k)}}{\partial t} + \frac{\partial \alpha^{(k)} \boldsymbol{F}^{(k)}}{\partial x} \right) \mathrm{d}x \, \mathrm{d}t = \iint_{C_i \times [t_0, t_0+\Delta t]} \mathcal{E}\left(\boldsymbol{S}^{(k)}\right) \mathrm{d}x \, \mathrm{d}t. \tag{5.33}$$

Consider the space–time control volume shown in Figure 5.1 on the next page. The shaded areas are pure fluid k, where $\alpha^{(k)} = \chi^{(k)} = 1$, and the white areas

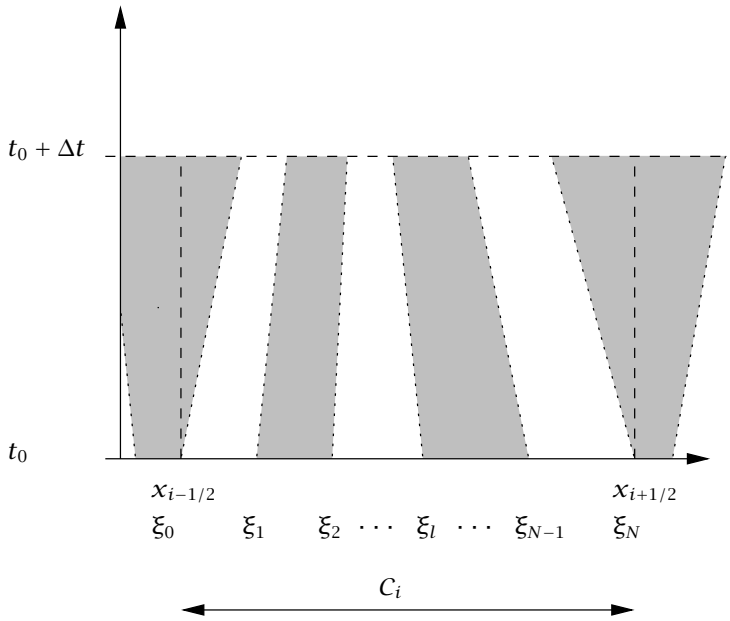

Figure 5.1: Space–time control volume.

represent the other fluid, where $\chi^{(k)} = 0$. The dashed lines at $x_{i-1/2}$ and $x_{i+1/2}$ are the control-volume boundaries fixed in space. The dotted lines represent the trajectories of the interfaces between the two fluids. We can use Green's theorem, and the left-hand side of (5.33) becomes

$$\begin{aligned}
&\iint_{C_i\times[t_0,t_0+\Delta t]} \left(\frac{\partial \alpha^{(k)} \boldsymbol{q}^{(k)}}{\partial t} + \frac{\partial \alpha^{(k)} \boldsymbol{F}^{(k)}}{\partial x} \right) \mathrm{d}x\,\mathrm{d}t \\
&= \int_{C_i(t_0+\Delta t)} \alpha^{(k)}(x, t_0+\Delta t)\boldsymbol{q}^{(k)}(x, t_0+\Delta t)\,\mathrm{d}x - \int_{C_i(t_0)} \alpha^{(k)}(x, t_0)\boldsymbol{q}^{(k)}(x, t_0)\,\mathrm{d}x \\
&\quad + \int_{t_0}^{t_0+\Delta t} \left(\alpha^{(k)}(x_{i+1/2}, t)\boldsymbol{F}^{(k)}(x_{i+1/2}, t) - \alpha^{(k)}(x_{i-1/2}, t)\boldsymbol{F}^{(k)}(x_{i-1/2}, t) \right) \mathrm{d}t.
\end{aligned} \tag{5.34}$$

Inserting (5.34) in (5.33), dividing by Δx and by Δt and taking the limit as $\Delta t \to 0$ gives:

$$\frac{\mathrm{d}}{\mathrm{d}t}\left(\alpha_i^{(k)} \boldsymbol{q}_i^{(k)}\right) + \frac{1}{\Delta x}\left(\mathcal{E}\left(\chi \boldsymbol{F}\right)_{i+1/2}^{(k)} - \mathcal{E}\left(\chi \boldsymbol{F}\right)_{i-1/2}^{(k)}\right) = \frac{1}{\Delta x}\int_{C_i} \mathcal{E}\left(\boldsymbol{S}^{(k)}\right) \mathrm{d}x. \tag{5.35}$$

The right-hand side of the above equation can be estimated by assuming a distribution of $\boldsymbol{S}^{(k)}$ in the control volume C_i. First, we assume that $\boldsymbol{S}^{(k)}$ is

constant in C_i, to obtain a first-order approximation. The second-order scheme will be outlined in Section 5.3.3 on page 131.

The volume-fraction evolution equation (5.29) may also be integrated over $C_i \times [t_0, t_0 + \Delta t]$:

$$\iint_{C_i \times [t_0, t_0+\Delta t]} \frac{\partial \alpha^{(k)}}{\partial t} \, \mathrm{d}x \, \mathrm{d}t = - \iint_{C_i \times [t_0, t_0+\Delta t]} \mathcal{E}\left(\boldsymbol{u}_{\mathrm{int}}^{(k)} \cdot \nabla \chi^{(k)} \right) \mathrm{d}x \, \mathrm{d}t, \quad (5.36)$$

or

$$\int_{C_i(t_0+\Delta t)} \alpha^{(k)}(x, t_0 + \Delta t) \, \mathrm{d}x - \int_{C_i(t_0)} \alpha^{(k)}(x, t_0) \, \mathrm{d}x = - \iint_{C_i \times [t_0, t_0+\Delta t]} \mathcal{E}\left(\boldsymbol{u}_{\mathrm{int}}^{(k)} \cdot \nabla \chi^{(k)} \right) \mathrm{d}x \, \mathrm{d}t. \quad (5.37)$$

Divide by Δx and Δt and take the limit as $\Delta t \to 0$:

$$\frac{\mathrm{d}\alpha_i^{(k)}}{\mathrm{d}t} = - \int_{C_i} \mathcal{E}\left(\boldsymbol{u}_{\mathrm{int}}^{(k)} \cdot \nabla \chi^{(k)} \right) \mathrm{d}x \, \mathrm{d}t. \quad (5.38)$$

This permits us to include the volume-fraction evolution equation into our system of equations, by writing

$$\frac{\mathrm{d}}{\mathrm{d}t}\left(\alpha_i^{(k)} \tilde{\boldsymbol{q}}_i^{(k)} \right) + \frac{1}{\Delta x}\left(\mathcal{E}\left(\chi \tilde{\boldsymbol{F}} \right)_{i+1/2}^{(k)} - \mathcal{E}\left(\chi \tilde{\boldsymbol{F}} \right)_{i-1/2}^{(k)} \right) = \frac{1}{\Delta x} \int_{C_i} \mathcal{E}\left(\tilde{\boldsymbol{S}}^{(k)} \right) \mathrm{d}x, \quad (5.39)$$

where

$$\tilde{\boldsymbol{q}}^{(k)} = \begin{bmatrix} 1, & \boldsymbol{q}^{(k)} \end{bmatrix}^T, \quad (5.40)$$

$$\tilde{\boldsymbol{F}}^{(k)} = \begin{bmatrix} 0, & \boldsymbol{F}^{(k)} \end{bmatrix}^T, \quad (5.41)$$

and

$$\tilde{\boldsymbol{S}}^{(k)} = \begin{bmatrix} -\boldsymbol{u}_{\mathrm{int}}^{(k)} \cdot \nabla \chi^{(k)}, & \boldsymbol{S}^{(k)} \end{bmatrix}^T. \quad (5.42)$$

The discretization of the volume-fraction evolution equation is explained by Abgrall and Saurel (2003). Henceforth we use $\tilde{\boldsymbol{q}}^{(k)}$, $\tilde{\boldsymbol{F}}^{(k)}$ and $\tilde{\boldsymbol{S}}^{(k)}$, but drop the tilde for convenience.

A main hypothesis in the Abgrall and Saurel (2003) article is that it is reasonable to approximate the interface velocity $\boldsymbol{u}_{\mathrm{int}}^{(k)}(\xi_l)$ by the velocity of the contact discontinuity given by the Riemann problem between the states to the left and right of ξ_l. This is denoted by

$$\boldsymbol{S}^{(k)}(x) = \begin{cases} -\boldsymbol{F}^{\mathrm{lag},(k)}\left(\boldsymbol{q}^{(k)}(x^-), \boldsymbol{q}^{(l)}(x^+) \right) & \text{if } [\chi^{(k)}] = -1, \\ \boldsymbol{F}^{\mathrm{lag},(k)}\left(\boldsymbol{q}^{(l)}(x^-), \boldsymbol{q}^{(k)}(x^+) \right) & \text{if } [\chi^{(k)}] = 1, \end{cases} \quad (5.43)$$

where k is the phase under consideration and l is the other phase. x^- is the coordinate to the left of x and x^+ is to the right. The jump in $\chi^{(k)}$ at x, $[\chi^{(k)}] = \chi^{(k),+} - \chi^{(k),-} = \pm 1$ is negative when we have phase k to the left and phase l to the right, since then, $\chi^{(k)} = 0$ to the left and $\chi^{(k)} = 1$ to the right.

To estimate the right-hand side of (5.35), we must consider the boundaries and the interior of the control volume C_i separately. At the boundary $x_{i-1/2}$, the discontinuity will only count if the interfacial velocity is positive, else it will be counted in the control volume to the left. Conversely, at the boundary $x_{i+1/2}$ the discontinuity will only count if the interfacial velocity is negative.

It is also necessary to consider the probability of having phase k to the left of $x_{i+1/2}$ and phase l to the right, etc. These probabilities are denoted by $\mathcal{P}_{i+1/2}(k,l)$, and, as explained by Abgrall and Saurel (2003), reasonable estimates are

$$\begin{aligned}
\mathcal{P}_{i+1/2}(k,k) &= \min(\alpha_i^{(k)}, \alpha_{i+1}^{(k)}),\\
\mathcal{P}_{i+1/2}(k,l) &= \max(\alpha_i^{(k)} - \alpha_{i+1}^{(k)}, 0),\\
\mathcal{P}_{i+1/2}(l,k) &= \max(\alpha_i^{(l)} - \alpha_{i+1}^{(l)}, 0),\\
\mathcal{P}_{i+1/2}(l,l) &= \min(\alpha_i^{(l)}, \alpha_{i+1}^{(l)}).
\end{aligned} \tag{5.44}$$

Using all this, we get for the boundary part of the right-hand side of (5.35):

$$\begin{aligned}
&\int_{C_i} \mathcal{E}\left(\boldsymbol{S}^{(k)}\right)_{\text{bound}} \mathrm{d}x = \int_{C_i} \mathcal{E}\left(\boldsymbol{F}^{\text{lag},(k)} \frac{\partial \chi^{(k)}}{\partial x}\right)_{\text{bound}} \mathrm{d}x\\
&= -\max\left\{0, \operatorname{sgn}[\boldsymbol{u}_{\text{int}}^{(k)}(\boldsymbol{q}_{i-1/2}^{(k),-}, \boldsymbol{q}_{i-1/2}^{(l),+})]\right\} \mathcal{P}_{i-1/2}(k,l) \boldsymbol{F}^{\text{lag},(k)}(\boldsymbol{q}_{i-1/2}^{(k),-}, \boldsymbol{q}_{i-1/2}^{(l),+})\\
&\quad + \max\left\{0, \operatorname{sgn}[\boldsymbol{u}_{\text{int}}^{(k)}(\boldsymbol{q}_{i-1/2}^{(l),-}, \boldsymbol{q}_{i-1/2}^{(k),+})]\right\} \mathcal{P}_{i-1/2}(l,k) \boldsymbol{F}^{\text{lag},(k)}(\boldsymbol{q}_{i-1/2}^{(l),-}, \boldsymbol{q}_{i-1/2}^{(k),+})\\
&\quad + \min\left\{0, \operatorname{sgn}[\boldsymbol{u}_{\text{int}}^{(k)}(\boldsymbol{q}_{i+1/2}^{(k),-}, \boldsymbol{q}_{i+1/2}^{(l),+})]\right\} \mathcal{P}_{i+1/2}(k,l) \boldsymbol{F}^{\text{lag},(k)}(\boldsymbol{q}_{i+1/2}^{(k),-}, \boldsymbol{q}_{i+1/2}^{(l),+})\\
&\quad - \min\left\{0, \operatorname{sgn}[\boldsymbol{u}_{\text{int}}^{(k)}(\boldsymbol{q}_{i+1/2}^{(l),-}, \boldsymbol{q}_{i+1/2}^{(k),+})]\right\} \mathcal{P}_{i+1/2}(l,k) \boldsymbol{F}^{\text{lag},(k)}(\boldsymbol{q}_{i+1/2}^{(l),-}, \boldsymbol{q}_{i+1/2}^{(k),+}).
\end{aligned} \tag{5.45}$$

The part of the right-hand side of (5.35) arising from internal interfaces, is called relaxation terms by Abgrall and Saurel (2003). Denote the expected number of internal interfaces by $N_{\text{int},i}$. Similarly to what was done above, and using the midpoint rule, this gives:

$$\begin{aligned}
\int_{C_i} \mathcal{E}\left(\boldsymbol{S}^{(k)}\right)_{\text{relax}} \mathrm{d}x &= \int_{C_i} \mathcal{E}\left(\boldsymbol{F}^{\text{lag},(k)} \frac{\partial \chi^{(k)}}{\partial x}\right)_{\text{relax}} \mathrm{d}x\\
&= \frac{N_{\text{int},i}}{2}\left(\boldsymbol{F}^{\text{lag},(k)}(\boldsymbol{q}_i^{(l)}, \boldsymbol{q}_i^{(k)}) - \boldsymbol{F}^{\text{lag},(k)}(\boldsymbol{q}_i^{(k)}, \boldsymbol{q}_i^{(l)})\right),
\end{aligned} \tag{5.46}$$

where the second equality depends on the assumption that $\boldsymbol{F}^{\mathrm{lag},(k)}\partial\chi^{(k)}/\partial x$ is constant in C_i. Hence,

$$\int_{C_i}\mathcal{I}\left(\boldsymbol{S}^{(k)}\right)\mathrm{d}x=\int_{C_i}\mathcal{I}\left(\boldsymbol{S}^{(k)}\right)_{\mathrm{bound}}\mathrm{d}x+\int_{C_i}\mathcal{I}\left(\boldsymbol{S}^{(k)}\right)_{\mathrm{relax}}\mathrm{d}x, \tag{5.47}$$

using (5.45) and (5.46).

5.3.2 Conservative fluxes

Now consider the flux terms on the right-hand side of (5.35). For the control-volume boundary at $x_{i+1/2}$, we have, of course, a contribution to the phase k-equation if there is phase k on both sides. Moreover, there is a contribution if phase k exists on the left-hand side and phase l on the right-hand side, if the interface velocity is positive (phase k exits), and finally there is a contribution if phase l exists on the left-hand side and k on the right-hand side, if the interface velocity is negative (phase k enters). If we have phase l on both sides, there is no contribution to the phase k-equation. Hence,

$$\begin{aligned}\mathcal{I}\left(\chi\boldsymbol{F}\right)_{i+1/2}^{(k)}=&\,\mathcal{P}_{i+1/2}(k,k)\boldsymbol{F}^{(k)}(\boldsymbol{q}_i^{(k)},\boldsymbol{q}_{i+1}^{(k)})\\&+\max\left\{0,\operatorname{sgn}[\boldsymbol{u}_{\mathrm{int}}^{(k)}(\boldsymbol{q}_i^{(k)},\boldsymbol{q}_{i+1}^{(l)})]\right\}\mathcal{P}_{i+1/2}(k,l)\boldsymbol{F}^{(k)}(\boldsymbol{q}_i^{(k)},\boldsymbol{q}_{i+1}^{(l)})\\&+\max\left\{0,\operatorname{sgn}[-\boldsymbol{u}_{\mathrm{int}}^{(k)}(\boldsymbol{q}_i^{(l)},\boldsymbol{q}_{i+1}^{(k)})]\right\}\mathcal{P}_{i+1/2}(l,k)\boldsymbol{F}^{(k)}(\boldsymbol{q}_i^{(l)},\boldsymbol{q}_{i+1}^{(k)}).\end{aligned} \tag{5.48}$$

At the control-volume boundary at $x_{i-1/2}$ the situation is similar, that is,

$$\begin{aligned}\mathcal{I}\left(\chi\boldsymbol{F}\right)_{i-1/2}^{(k)}=&\,\mathcal{P}_{i-1/2}(k,k)\boldsymbol{F}^{(k)}(\boldsymbol{q}_{i-1}^{(k)},\boldsymbol{q}_i^{(k)})\\&+\max\left\{0,\operatorname{sgn}[\boldsymbol{u}_{\mathrm{int}}^{(k)}(\boldsymbol{q}_{i-1}^{(k)},\boldsymbol{q}_i^{(l)})]\right\}\mathcal{P}_{i-1/2}(k,l)\boldsymbol{F}^{(k)}(\boldsymbol{q}_{i-1}^{(k)},\boldsymbol{q}_i^{(l)})\\&+\max\left\{0,\operatorname{sgn}[-\boldsymbol{u}_{\mathrm{int}}^{(k)}(\boldsymbol{q}_{i-1}^{(l)},\boldsymbol{q}_i^{(k)})]\right\}\mathcal{P}_{i-1/2}(l,k)\boldsymbol{F}^{(k)}(\boldsymbol{q}_{i-1}^{(l)},\boldsymbol{q}_i^{(k)}).\end{aligned} \tag{5.49}$$

5.3.3 Second-order scheme

With (5.45)–(5.49), we can advance (5.35) in time using an appropriate scheme. Abgrall and Saurel (2003) proposed to use a modified MUSCL-Hancock scheme (van Leer, 1984) (see Toro, 1999, Section 14.4) to get second-order accuracy in space and time. This will not be repeated here, except that one point will be made: Extra terms arise in $\mathcal{I}\left(\boldsymbol{S}^{(k)}\right)_{\mathrm{bound}}$ for the second-order scheme. This is due to the fact that for a first-order Godunov method, the variables are

assumed to be constant in each control volume C_i, whereas in the second-order method, they are assumed to be linearly varying.

To see how the extra terms arise, divide the cell C_i into $M+1$ sub-cells ($x_{i-1/2} = \eta_{0-1/2}, \ldots, \eta_{j-1/2}, \ldots, \eta_{M+1/2} = x_{i+1/2}$; $j \in \{0, 1, \ldots, M+1\}$; $\Delta\eta = \eta_{j+1/2} - \eta_{j-1/2} = \Delta x/(M+1)$) in which the volume fraction $\alpha_j^{(k)}$ is supposed to be constant. Both fluids can exist in each of these $M+1$ sub-cells. Then divide each of the sub-cells into N sub-sub-cells containing pure phase k or l. Hence the first-order scheme previously found can be directly applied to each of the $M+1$ sub-cells. However, since the volume fraction $\alpha_j^{(k)}$ is supposed to be constant for each j, it is necessary to let $M \to \infty$ to obtain the assumed linear distribution.

Apply the semi-discrete scheme to the $M+1$ sub-cells:

$$\frac{\mathrm{d}}{\mathrm{d}t}\left(\alpha_j^{(k)}\boldsymbol{q}_j^{(k)}\right) + \frac{1}{\Delta\eta}\left(\mathcal{E}\left(\chi\boldsymbol{F}\right)_{j+1/2}^{(k)} - \mathcal{E}\left(\chi\boldsymbol{F}\right)_{j-1/2}^{(k)}\right) = \frac{1}{\Delta\eta}\int_{x\in[\eta_{j-1/2},\eta_{j+1/2}]}\left\{\mathcal{E}\left(\boldsymbol{S}^{(k)}\right)_{\text{bound}} + \mathcal{E}\left(\boldsymbol{S}^{(k)}\right)_{\text{relax}}\right\}\mathrm{d}x. \quad (5.50)$$

To obtain an equation for the cell C_i, multiply the above equation with $\Delta\eta$ and sum it term-wise. The first term becomes

$$\sum_{j=0}^{M}\Delta\eta\frac{\mathrm{d}}{\mathrm{d}t}\left(\alpha_j^{(k)}\boldsymbol{q}_j^{(k)}\right) = \sum_{j=0}^{M}\frac{\Delta x}{M+1}\frac{\mathrm{d}}{\mathrm{d}t}\left(\alpha_j^{(k)}\boldsymbol{q}_j^{(k)}\right) = \Delta x\frac{\mathrm{d}}{\mathrm{d}t}\left(\frac{1}{M+1}\sum_{j=0}^{M}\alpha_j^{(k)}\boldsymbol{q}_j^{(k)}\right), \quad (5.51)$$

that is, we calculate the mean of the conserved variables. The Eulerian fluxes are evaluated in the following way:

$$\sum_{j=0}^{M}\left(\mathcal{E}\left(\chi\boldsymbol{F}\right)_{j+1/2}^{(k)} - \mathcal{E}\left(\chi\boldsymbol{F}\right)_{j-1/2}^{(k)}\right) = \mathcal{E}\left(\chi\boldsymbol{F}\right)_{M+1/2}^{(k)} - \mathcal{E}\left(\chi\boldsymbol{F}\right)_{1/2}^{(k)}, \quad (5.52)$$

that is, the sum telescopes. The right-hand side becomes

$$\sum_{j=0}^{M}\int_{x\in[\eta_{j-1/2},\eta_{j+1/2}]}\left\{\mathcal{E}\left(\boldsymbol{S}^{(k)}\right)_{\text{bound}} + \mathcal{E}\left(\boldsymbol{S}^{(k)}\right)_{\text{relax}}\right\}\mathrm{d}x, \quad (5.53)$$

where

$$\begin{aligned}\int_{x\in[\eta_{j-1/2},\eta_{j+1/2}]} &\left\{\mathcal{E}\left(\boldsymbol{S}^{(k)}\right)_{\text{bound}}+\mathcal{E}\left(\boldsymbol{S}^{(k)}\right)_{\text{relax}}\right\}\mathrm{d}x = \\ &-\max\left\{0,\operatorname{sgn}[\boldsymbol{u}_{\text{int}}^{(k)}(\boldsymbol{q}_{j-1}^{(k)},\boldsymbol{q}_{j}^{(l)})]\right\}\mathcal{P}_{j-1/2}(k,l)\boldsymbol{F}^{\text{lag},(k)}(\boldsymbol{q}_{j-1}^{(k)},\boldsymbol{q}_{j}^{(l)}) \\ &+\max\left\{0,\operatorname{sgn}[\boldsymbol{u}_{\text{int}}^{(k)}(\boldsymbol{q}_{j-1}^{(l)},\boldsymbol{q}_{j}^{(k)})]\right\}\mathcal{P}_{j-1/2}(l,k)\boldsymbol{F}^{\text{lag},(k)}(\boldsymbol{q}_{j-1}^{(l)},\boldsymbol{q}_{j}^{(k)}) \\ &+\min\left\{0,\operatorname{sgn}[\boldsymbol{u}_{\text{int}}^{(k)}(\boldsymbol{q}_{j}^{(k)},\boldsymbol{q}_{j+1}^{(l)})]\right\}\mathcal{P}_{j+1/2}(k,l)\boldsymbol{F}^{\text{lag},(k)}(\boldsymbol{q}_{j}^{(k)},\boldsymbol{q}_{j+1}^{(l)}) \\ &-\min\left\{0,\operatorname{sgn}[\boldsymbol{u}_{\text{int}}^{(k)}(\boldsymbol{q}_{j}^{(l)},\boldsymbol{q}_{j+1}^{(k)})]\right\}\mathcal{P}_{j+1/2}(l,k)\boldsymbol{F}^{\text{lag},(k)}(\boldsymbol{q}_{j}^{(l)},\boldsymbol{q}_{j+1}^{(k)}) \\ &+\frac{N_{\text{int},j}}{2}\left(\boldsymbol{F}^{\text{lag},(k)}(\boldsymbol{q}_{j}^{(l)},\boldsymbol{q}_{j}^{(k)})-\boldsymbol{F}^{\text{lag},(k)}(\boldsymbol{q}_{j}^{(k)},\boldsymbol{q}_{j}^{(l)})\right). \end{aligned} \tag{5.54}$$

First consider the terms of the type $\boldsymbol{F}^{\text{lag},(k)}(\boldsymbol{q}_{m}^{(k)},\boldsymbol{q}_{m+1}^{(l)})$, that is,

$$\begin{aligned}&\sum_{j=0}^{M}\Big\{\min\left\{0,\operatorname{sgn}[\boldsymbol{u}_{\text{int}}^{(k)}(\boldsymbol{q}_{j}^{(k)},\boldsymbol{q}_{j+1}^{(l)})]\right\}\mathcal{P}_{j+1/2}(k,l)\boldsymbol{F}^{\text{lag},(k)}(\boldsymbol{q}_{j}^{(k)},\boldsymbol{q}_{j+1}^{(l)}) \\ &\qquad-\max\left\{0,\operatorname{sgn}[\boldsymbol{u}_{\text{int}}^{(k)}(\boldsymbol{q}_{j-1}^{(k)},\boldsymbol{q}_{j}^{(l)})]\right\}\mathcal{P}_{j-1/2}(k,l)\boldsymbol{F}^{\text{lag},(k)}(\boldsymbol{q}_{j-1}^{(k)},\boldsymbol{q}_{j}^{(l)})\Big\} \\ &=\sum_{j=0}^{M}\Big\{\min\left\{0,\operatorname{sgn}[\boldsymbol{u}_{\text{int}}^{(k)}(\boldsymbol{q}_{j}^{(k)},\boldsymbol{q}_{j+1}^{(l)})]\right\}\max(\alpha_{j}^{(k)}-\alpha_{j+1}^{(k)},0)\boldsymbol{F}^{\text{lag},(k)}(\boldsymbol{q}_{j}^{(k)},\boldsymbol{q}_{j+1}^{(l)}) \\ &\quad-\max\left\{0,\operatorname{sgn}[\boldsymbol{u}_{\text{int}}^{(k)}(\boldsymbol{q}_{j-1}^{(k)},\boldsymbol{q}_{j}^{(l)})]\right\}\max(\alpha_{j-1}^{(k)}-\alpha_{j}^{(k)},0)\boldsymbol{F}^{\text{lag},(k)}(\boldsymbol{q}_{j-1}^{(k)},\boldsymbol{q}_{j}^{(l)})\Big\}. \end{aligned} \tag{5.55}$$

Define

$$V_m=\max(\alpha_{m}^{(k)}-\alpha_{m+1}^{(k)},0)\boldsymbol{F}^{\text{lag},(k)}(\boldsymbol{q}_{m}^{(k)},\boldsymbol{q}_{m+1}^{(l)}), \tag{5.56}$$

$$\left(\beta_{m-1/2}^{(k,l)}\right)^{+}=\max\left\{0,\operatorname{sgn}[\boldsymbol{u}_{\text{int}}^{(k)}(\boldsymbol{q}_{m-1}^{(k)},\boldsymbol{q}_{m}^{(l)})]\right\}, \tag{5.57}$$

and

$$\left(\beta_{m+1/2}^{(k,l)}\right)^{-}=\min\left\{0,\operatorname{sgn}[\boldsymbol{u}_{\text{int}}^{(k)}(\boldsymbol{q}_{m}^{(k)},\boldsymbol{q}_{m+1}^{(l)})]\right\}, \tag{5.58}$$

so that the sum in (5.55) can be written as

$$\sum_{j=0}^{M}\left\{\left(\beta_{j+1/2}^{(k,l)}\right)^{-}V_j-\left(\beta_{j-1/2}^{(k,l)}\right)^{+}V_{j-1}\right\}=\sum_{j=0}^{M}\left(\beta_{j+1/2}^{(k,l)}\right)^{-}V_j-\sum_{j=-1}^{M-1}\left(\beta_{j+1/2}^{(k,l)}\right)^{+}V_j$$
$$=\left(\beta_{M+1/2}^{(k,l)}\right)^{-}V_M-\left(\beta_{-1/2}^{(k,l)}\right)^{+}V_0+\sum_{j=0}^{M-1}\left\{\left(\beta_{j+1/2}^{(k,l)}\right)^{-}-\left(\beta_{j+1/2}^{(k,l)}\right)^{+}\right\}V_j$$
$$=\left(\beta_{M+1/2}^{(k,l)}\right)^{-}V_M-\left(\beta_{-1/2}^{(k,l)}\right)^{+}V_0-\sum_{j=0}^{M-1}V_j. \quad (5.59)$$

The two first terms on the right-hand side above correspond to the interactions with the cells C_{i+1} and C_{i-1}, respectively. The last term is

$$\sum_{j=0}^{M-1}V_j=\sum_{j=0}^{M-1}\max(\alpha_j^{(k)}-\alpha_{j+1}^{(k)},0)\boldsymbol{F}^{\mathrm{lag},(k)}(\boldsymbol{q}_j^{(k)},\boldsymbol{q}_{j+1}^{(l)})$$
$$=\sum_{j=0}^{M-1}(\eta_{j+1}-\eta_j)\max(-\delta_i\alpha_i^{(k)},0)\boldsymbol{F}^{\mathrm{lag},(k)}(\boldsymbol{q}_j^{(k)},\boldsymbol{q}_{j+1}^{(l)})$$
$$=\max(-\delta_i\alpha_i^{(k)},0)\sum_{j=0}^{M-1}(\eta_{j+1}-\eta_j)\boldsymbol{F}^{\mathrm{lag},(k)}(\boldsymbol{q}_j^{(k)},\boldsymbol{q}_{j+1}^{(l)})$$
$$=\max(\delta_i\alpha_i^{(l)},0)\sum_{j=0}^{M-1}(\eta_{j+1}-\eta_j)\boldsymbol{F}^{\mathrm{lag},(k)}(\boldsymbol{q}_j^{(k)},\boldsymbol{q}_{j+1}^{(l)}), \quad (5.60)$$

where $\delta_i\alpha_i^{(k)}$ is the slope of the volume fraction in the ith cell, given by the chosen limiter function. The last sum is a Riemann sum, and therefore

$$\lim_{M\to\infty}\sum_{j=0}^{M-1}V_j=\max(\delta_i\alpha_i^{(l)},0)\int_{x_{i-1/2}}^{x_{i+1/2}}\boldsymbol{F}^{\mathrm{lag},(k)}(\boldsymbol{q}^{(k)}(\eta),\boldsymbol{q}^{(l)}(\eta))\,\mathrm{d}\eta. \quad (5.61)$$

The above integral can be estimated using the second-order midpoint method:

$$\int_{x_{i-1/2}}^{x_{i+1/2}}\boldsymbol{F}^{\mathrm{lag},(k)}(\boldsymbol{q}^{(k)}(\eta),\boldsymbol{q}^{(l)}(\eta))\,\mathrm{d}\eta\approx\boldsymbol{F}^{\mathrm{lag},(k)}(\boldsymbol{q}_i^{(k)},\boldsymbol{q}_i^{(l)})\Delta x. \quad (5.62)$$

Here, $\boldsymbol{q}_i^{(k)}$ is evaluated at $(x_{i+1/2}-x_{i-1/2})/2=x_i$.

Using exactly the same arguments, but reversing the phasic indices k and l, we arrive at the corresponding expression for $\boldsymbol{F}^{\mathrm{lag},(k)}(\boldsymbol{q}_m^{(l)}, \boldsymbol{q}_{m+1}^{(k)})$, namely,

$$\begin{aligned}\sum_{j=0}^{M} \Big\{ &\max\Big\{0, \operatorname{sgn}[\boldsymbol{u}_{\mathrm{int}}^{(k)}(\boldsymbol{q}_{j-1}^{(l)}, \boldsymbol{q}_j^{(k)})]\Big\} \mathcal{P}_{j-1/2}(l,k) \boldsymbol{F}^{\mathrm{lag},(k)}(\boldsymbol{q}_{j-1}^{(l)}, \boldsymbol{q}_j^{(k)}) \\ &- \min\Big\{0, \operatorname{sgn}[\boldsymbol{u}_{\mathrm{int}}^{(k)}(\boldsymbol{q}_j^{(l)}, \boldsymbol{q}_{j+1}^{(k)})]\Big\} \mathcal{P}_{j+1/2}(l,k) \boldsymbol{F}^{\mathrm{lag},(k)}(\boldsymbol{q}_j^{(l)}, \boldsymbol{q}_{j+1}^{(k)}) \Big\} \\ &\approx \max(\delta_i \alpha_i^{(k)}, 0) \boldsymbol{F}^{\mathrm{lag},(k)}(\boldsymbol{q}_i^{(l)}, \boldsymbol{q}_i^{(k)}) \Delta x + \text{ boundary terms.} \end{aligned} \tag{5.63}$$

For the relaxation terms, we obtain analogously, using the midpoint rule:

$$\begin{aligned}\sum_{j=0}^{M} \Big\{ &\frac{N_{\mathrm{int},j}}{2} \Big(\boldsymbol{F}^{\mathrm{lag},(k)}(\boldsymbol{q}_j^{(l)}, \boldsymbol{q}_j^{(k)}) - \boldsymbol{F}^{\mathrm{lag},(k)}(\boldsymbol{q}_j^{(k)}, \boldsymbol{q}_j^{(l)}) \Big) \Big\} \\ &\approx \frac{N_{\mathrm{int},i}}{2} \Big(\boldsymbol{F}^{\mathrm{lag},(k)}(\boldsymbol{q}_i^{(l)}, \boldsymbol{q}_i^{(k)}) - \boldsymbol{F}^{\mathrm{lag},(k)}(\boldsymbol{q}_i^{(k)}, \boldsymbol{q}_i^{(l)}) \Big), \end{aligned} \tag{5.64}$$

so that the final, second-order expression for phase-interaction terms becomes:

$$\begin{aligned}&\sum_{j=0}^{M} \int_{x \in [\eta_{j-1/2}, \eta_{j+1/2}]} \Big\{ \mathcal{E}\left(\boldsymbol{S}^{(k)}\right)_{\mathrm{bound}} + \mathcal{E}\left(\boldsymbol{S}^{(k)}\right)_{\mathrm{relax}} \Big\} \, \mathrm{d}x \approx \\ &\mathrm{I} \left\{ \begin{array}{l} - \max\Big\{0, \operatorname{sgn}[\boldsymbol{u}_{\mathrm{int}}^{(k)}(\boldsymbol{q}_{i-1/2}^{(k),-}, \boldsymbol{q}_{i-1/2}^{(l),+})]\Big\} \mathcal{P}_{i-1/2}(k,l) \boldsymbol{F}^{\mathrm{lag},(k)}(\boldsymbol{q}_{i-1/2}^{(k),-}, \boldsymbol{q}_{i-1/2}^{(l),+}) \\ + \max\Big\{0, \operatorname{sgn}[\boldsymbol{u}_{\mathrm{int}}^{(k)}(\boldsymbol{q}_{i-1/2}^{(l),-}, \boldsymbol{q}_{i-1/2}^{(k),+})]\Big\} \mathcal{P}_{i-1/2}(l,k) \boldsymbol{F}^{\mathrm{lag},(k)}(\boldsymbol{q}_{i-1/2}^{(l),-}, \boldsymbol{q}_{i-1/2}^{(k),+}) \\ + \min\Big\{0, \operatorname{sgn}[\boldsymbol{u}_{\mathrm{int}}^{(k)}(\boldsymbol{q}_{i+1/2}^{(k),-}, \boldsymbol{q}_{i+1/2}^{(l),+})]\Big\} \mathcal{P}_{i+1/2}(k,l) \boldsymbol{F}^{\mathrm{lag},(k)}(\boldsymbol{q}_{i+1/2}^{(k),-}, \boldsymbol{q}_{i+1/2}^{(l),+}) \\ - \min\Big\{0, \operatorname{sgn}[\boldsymbol{u}_{\mathrm{int}}^{(k)}(\boldsymbol{q}_{i+1/2}^{(l),-}, \boldsymbol{q}_{i+1/2}^{(k),+})]\Big\} \mathcal{P}_{i+1/2}(l,k) \boldsymbol{F}^{\mathrm{lag},(k)}(\boldsymbol{q}_{i+1/2}^{(l),-}, \boldsymbol{q}_{i+1/2}^{(k),+}) \\ + \dfrac{N_{\mathrm{int},i}}{2} \Big(\boldsymbol{F}^{\mathrm{lag},(k)}(\boldsymbol{q}_i^{(l)}, \boldsymbol{q}_i^{(k)}) - \boldsymbol{F}^{\mathrm{lag},(k)}(\boldsymbol{q}_i^{(k)}, \boldsymbol{q}_i^{(l)}) \Big) \end{array} \right. \\ &\mathrm{II} \left\{ \begin{array}{l} - \max(\delta_i \alpha_i^{(l)}, 0) \boldsymbol{F}^{\mathrm{lag},(k)}(\boldsymbol{q}_i^{(k)}, \boldsymbol{q}_i^{(l)}) \Delta x \\ + \max(\delta_i \alpha_i^{(k)}, 0) \boldsymbol{F}^{\mathrm{lag},(k)}(\boldsymbol{q}_i^{(l)}, \boldsymbol{q}_i^{(k)}) \Delta x. \end{array} \right. \end{aligned} \tag{5.65}$$

Herein, (I) represent the MUSCL method and relaxation terms, and (II) are correction terms. Note that they involve Riemann problems between the two phases, centred in the computational cells and not at the cell interfaces. As shown above, they arise from the non-conservative terms, $\boldsymbol{F}^{\mathrm{lag},(k)}$, in (I). Further details are discussed by Papin (2005, Part II, Chapter 3).

5.3.4 Comparison with 'conventional' model

The 'conventional', continuous model given by (5.1) and (5.2) can be written as

$$\frac{\partial \alpha^{(k)} \check{\boldsymbol{q}}^{(k)}}{\partial t} + \boldsymbol{\nabla} \cdot (\alpha^k \check{\boldsymbol{F}}^{(k)}) = \check{\boldsymbol{S}}^{(k)}, \tag{5.66}$$

where

$$\check{\boldsymbol{q}}^{(k)} = \left[\rho^{(k)}, \quad \rho^{(k)} u^{(k)}\right]^T, \tag{5.67}$$

$$\check{\boldsymbol{F}}^{(k)} = \left[\rho^{(k)} u^{(k)}, \quad \rho^{(k)} (u^{(k)})^2 + p^{(k)}\right]^T, \tag{5.68}$$

and

$$\check{\boldsymbol{S}}^{(k)} = \left[0, \quad p_{\text{int}}^{(k)} \frac{\partial \alpha^{(k)}}{\partial x}\right]^T. \tag{5.69}$$

Recall the present (semi-) discrete model (5.39):

$$\frac{\mathrm{d}}{\mathrm{d}t}\left(\alpha_i^{(k)} \boldsymbol{q}_i^{(k)}\right) + \frac{1}{\Delta x}\left(\mathcal{F}\,(\chi \boldsymbol{F})_{i+1/2}^{(k)} - \mathcal{F}\,(\chi \boldsymbol{F})_{i-1/2}^{(k)}\right) = \frac{1}{\Delta x}\int_{C_i}\left\{\mathcal{F}\left(\boldsymbol{S}^{(k)}\right)_{\text{bound}} + \mathcal{F}\left(\boldsymbol{S}^{(k)}\right)_{\text{relax}}\right\}\mathrm{d}x, \tag{5.70}$$

where

$$\boldsymbol{q}^{(k)} = \left[1, \quad \rho^{(k)}, \quad \rho^{(k)} u^{(k)}\right]^T, \tag{5.71}$$

$$\boldsymbol{F}^{(k)} = \left[0, \quad \rho^{(k)} u^{(k)}, \quad \rho^{(k)} (u^{(k)})^2 + p^{(k)}\right]^T, \tag{5.72}$$

and

$$\boldsymbol{S}^{(k)} = \left[-u_{\text{int}}^{(k)} \frac{\partial \chi^{(k)}}{\partial x}, \quad 0, \quad p^{(k)} \frac{\partial \chi^{(k)}}{\partial x}\right]^T. \tag{5.73}$$

The system (5.70) has one more equation than (5.66); it is the volume-fraction equation. Hence, (5.70) has a priori two independent pressures, while (5.66) has only one (See Section 5.3.6 on page 141). In the 'conventional' model, the volume fraction can be found using the equation of state (5.22), the pressure equality and the relation $\alpha_{\text{g}} + \alpha_\ell = 1$, whereas in the discrete-equation model, the volume fraction is found from a transport equation.

Except for the above-mentioned differences, the left-hand sides are analogous. $\check{\boldsymbol{q}}^{(k)}$ is (implicitly) volume-averaged, while $\boldsymbol{q}^{(k)}$ is ensemble-averaged. $\check{\boldsymbol{F}}^{(k)}$ is implicitly volume-averaged, while the ensemble-averaging of $\boldsymbol{F}^{(k)}$ is shown explicitly.

The correspondence between the right-hand sides is more subtle. The right-hand side of (5.70) can be substituted by the right-hand side of (5.65). The expression $\check{\boldsymbol{S}}^{(k)}$ for the 'conventional' model is simpler, but a lot of necessary modelling effort is hidden away in the interfacial pressure $p_{\text{int}}^{(k)}$. Several of the interfacial-pressure models presented in the literature seem to be chosen such that the eigenvalues of the resulting system coefficient matrix are real for a range of suitable flow conditions. One of the main advantages of the present method, on the other hand, is that it avoids several problems regarding hyperbolicity. This is discussed somewhat further in Section 5.3.7.

Note that the pressure $p^{(k)}$ in (5.73) is the pressure at the interface, hence there is a connection to the 'conventional' model (5.69). However, in the discrete model, the interfacial pressure and velocity come from the solution of Riemann problems at the interface. We hypothesize that this might be a useful point of view with respect to the modelling of the interfacial quantities.

5.3.5 The Riemann problem

Due to the discrete nature of the present model, the Riemann problems to be solved are between two pure fluids. Hence, the equations defining the Riemann problems are the isentropic Euler equations with the addition of an advection equation for the phase-indicator function. The employed equation of state may have different parameters in the two states.

The solution to the Riemann problem for fluid dynamics is described by Toro (1999); LeVeque (2002). However, LeVeque (1990) gives details with respect to the isentropic Euler equations.

For the isentropic Euler equations, there is no contact discontinuity, therefore one cannot distinguish between the fluids on the right-hand and on the left-hand sides. However, in the present case there is also an advection equation for the phase-indicator function, which adds the required contact discontinuity. Hence the hypothesis of Abgrall and Saurel (2003) that the volume fraction is advected by the speed given by the corresponding Riemann problem, often denoted by u^*, see Figure 5.2 on the following page. On each side of the point moving with speed u^*, we have pure phase k or l. Moreover, the Rankine-Hugoniot relations imply that at this point, there must be equality of pressure (denoted by p^*) between the left-hand and right-hand states. Therefore, the Riemann problem can be solved.

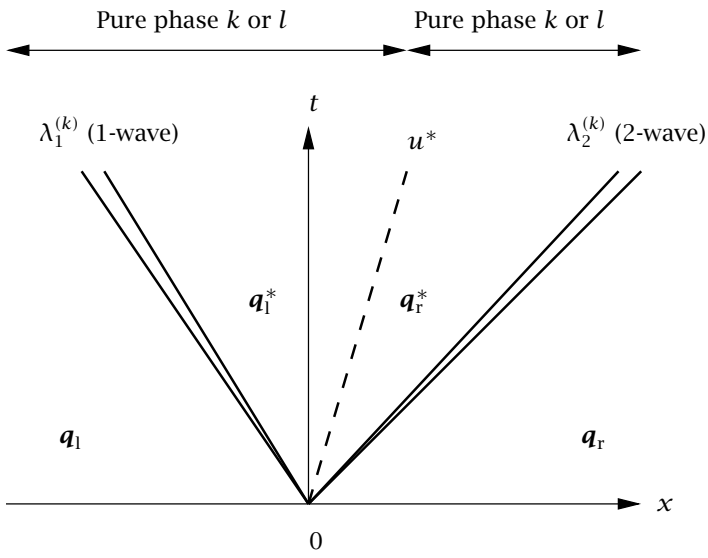

Figure 5.2: Structure of the solution to the Riemann problem.

The equations defining the Riemann problem are

$$\begin{aligned}
\frac{\partial \chi^{(k)}}{\partial t} + u_{\mathrm{int}}^{(k)} \frac{\partial \chi^{(k)}}{\partial x} &= 0, \\
\frac{\partial}{\partial t}(\chi^{(k)}\rho^{(k)}) + \frac{\partial}{\partial x}(\chi^{(k)}\rho^{(k)}u^{(k)}) &= 0, \\
\frac{\partial}{\partial t}(\chi^{(l)}\rho^{(l)}) + \frac{\partial}{\partial x}(\chi^{(l)}\rho^{(l)}u^{(l)}) &= 0, \\
\frac{\partial}{\partial t}(\chi^{(k)}\rho^{(k)}u^{(k)}) + \frac{\partial}{\partial x}(\chi^{(k)}\rho^{(k)}u^{(k)}u^{(k)} + \chi^{(k)}p^{(k)}) &= 0, \\
\frac{\partial}{\partial t}(\chi^{(l)}\rho^{(l)}u^{(l)}) + \frac{\partial}{\partial x}(\chi^{(l)}\rho^{(l)}u^{(l)}u^{(l)} + \chi^{(l)}p^{(l)}) &= 0,
\end{aligned} \tag{5.74}$$

where we take $u_{\mathrm{int}}^{(k)} = u^*$. Since either $\chi^{(k)}$ or $\chi^{(l)}$ is zero on each side of the contact discontinuity, it suffices to solve the Riemann problem corresponding to the pure-phase isentropic Euler equations, using the appropriate equation of state.

Another way to look at (5.74), is to write

$$\begin{aligned} \frac{\partial \chi^{(k)}}{\partial t} + u_{\text{int}} \frac{\partial \chi}{\partial x} &= 0, \\ \frac{\partial}{\partial t}(\rho) + \frac{\partial}{\partial x}(\rho u) &= 0, \\ \frac{\partial}{\partial t}(\rho u) + \frac{\partial}{\partial x}(\rho u u + p) &= 0, \end{aligned} \tag{5.75}$$

where the equation of state is $p = p(\rho, \chi^{(k)})$, that is, the equation of state of phase k is employed when $\chi^{(k)} = 1$ and the equation of state of phase l is used otherwise. The velocity u is constant across the contact discontinuity, that is, $u_{\text{l}}^* = u_{\text{r}}^*$. Moreover $u = u_{\text{int}}$ there. Hence the Rankine-Hugoniot conditions

$$\begin{aligned} [\rho(u - u_{\text{int}})] &= 0, \\ [\rho u(u - u_{\text{int}}) + p] &= 0, \end{aligned} \tag{5.76}$$

imply that $p_{\text{l}}^* = p_{\text{r}}^*$.

The velocity as a function of pressure through a rarefaction wave is given by

$$u^{(k)}(p^{(k)}) = u_s^{(k)} \pm c^{(k)} \ln\left\{ \frac{p^{(k)} + \rho_\circ^{(k)} (c^{(k)})^2}{p_s^{(k)} + \rho_\circ^{(k)} (c^{(k)})^2} \right\}, \tag{5.77}$$

where the negative sign corresponds to the eigenvalue $\lambda_1^{(k)} = u^{(k)} - c^{(k)}$ and the positive sign corresponds to $\lambda_2^{(k)} = u^{(k)} + c^{(k)}$. The subscript s denotes the known state, that is, the left state for $\lambda_1^{(k)}$ and the right state for $\lambda_2^{(k)}$.

Across a shock, the velocity function is

$$u^{(k)}(p^{(k)}) = u_s^{(k)} \pm \frac{p^{(k)} - p_s^{(k)}}{c^{(k)} \sqrt{\left(p^{(k)} + \rho_\circ^{(k)} (c^{(k)})^2\right)\left(p_s^{(k)} + \rho_\circ^{(k)} (c^{(k)})^2\right)}}, \tag{5.78}$$

when the equation of state (5.22) is used, where again the negative sign corresponds to the eigenvalue $\lambda_1^{(k)} = u^{(k)} - c^{(k)}$ and the positive sign corresponds to $\lambda_2^{(k)} = u^{(k)} + c^{(k)}$. If $p^* > p_{\text{l}}$, then the 1-wave is a shock, else it is a rarefaction. Similarly, if $p^* > p_{\text{r}}$, then the 2-wave is a shock, else it is a rarefaction. Using this, equations (5.77) and (5.78), as well as the procedure described by Toro (1999, Section 4.5), an exact Riemann solver has been written. However, for the presently-considered test problems, an acoustic solver, or 'primitive-variables Riemann solver' (PVRS), (Toro, 1999, Section 9.3) gave very similar results, and shorter (in the order of 50 %) CPU times.

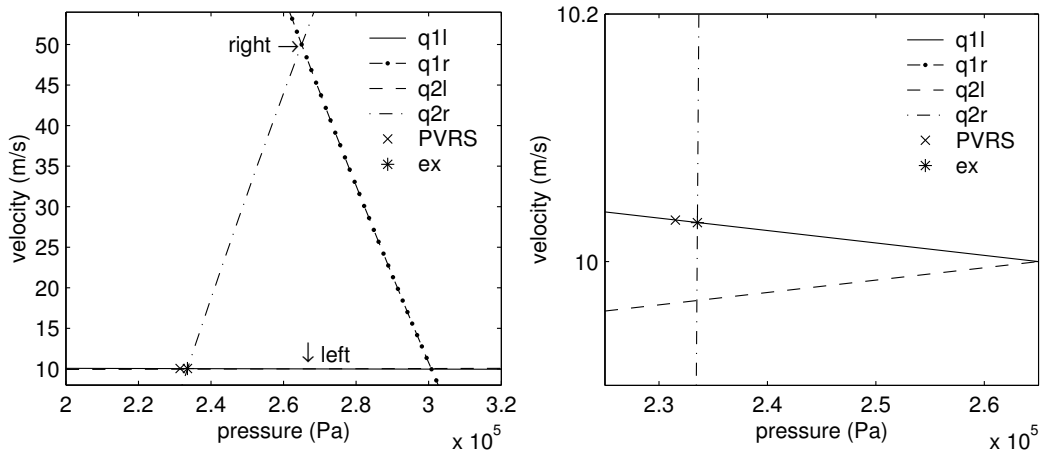

Figure 5.3: Solution to a liquid–gas Riemann problem.

The principle of the acoustic solver is a linearization of the shock and rarefaction waves. In the present work, we have chosen to use the acoustic solver for two reasons: Simplicity and robustness. The robustness is required since we solve Riemann problems between two pure fluids with possibly very different equation-of-state parameters. Other possible choices for approximate Riemann solvers are HLL-type schemes, relaxation schemes, etc.

Consider the solution to the liquid–gas Riemann problem shown in Figure 5.3(a). The left-hand state is gas, whereas the right-hand state is liquid. The input data correspond to the 'Shock tube 2' test case, described in Section 5.5.2 on page 147. The curves in the figure are plots of (5.77). The legend 'q1l' denotes the curve corresponding to λ_1 going through the left-hand state. Analogously, 'q2r' is for λ_2 and goes through the right-hand state, etc. The curves for the liquid have a much smaller gradient than those for the gas, since the liquid has a higher speed of sound. The exact solution to the Riemann problem, denoted by 'ex' in the figure, lies, in this case, on the intersection between the 1-rarefaction from the left and the 2-rarefaction from the right. As can be observed in Figure 5.3(b), the solution given by the acoustic solver ('PVRS') was not much off; the predicted velocity was 0.02% too high and the pressure was 0.9% too low. The curves plotted using (5.77) and (5.78) were very nearly linear and hardly distinguishable.

More physical phenomena, for instance surface tension, can be accounted for in the discrete-equation model by including them in the Riemann-problem

definition. This, as well as viscous flows and other equations of state, is discussed in more detail by Papin (2005). It is also possible to treat phase transition (Le Métayer *et al.*, 2005).

5.3.6 Pressure relaxation

For the two-phase flows considered here, neglecting surface tension and other effects, it is reasonable to assume pressure equality between the phases. This has been achieved by performing an instantaneous pressure relaxation at each time step, as described by Saurel and Abgrall (1999). The present case was simpler, however, since the energy equation needed not be accounted for. In short, after the hyperbolic operator has been applied, the volume fraction is modified so as to render the two pressures equal, keeping $\alpha^{(k)}\rho^{(k)}$ and $\alpha^{(k)}\rho^{(k)}u^{(k)}$ constant. This leads to a second-degree equation with positive solution

$$\alpha^{(\ell)} = \frac{-\psi_2 - \sqrt{\psi_2^2 - 4\psi_1\psi_3}}{2\psi_1}, \tag{5.79}$$

where

$$\psi_1 = (c^{(\ell)})^2\rho_\circ^{(\ell)} - (c^{(\mathrm{g})})^2\rho_\circ^{(\mathrm{g})}, \tag{5.80}$$

$$\psi_2 = -(c^{(\ell)})^2(\alpha^{(\ell)}\rho^{(\ell)} + \rho_\circ^{(\ell)}) + (c^{(\mathrm{g})})^2(-\alpha^{(\mathrm{g})}\rho^{(\mathrm{g})} + \rho_\circ^{(\mathrm{g})}), \tag{5.81}$$

and

$$\psi_3 = (c^{(\ell)})^2\alpha^{(\ell)}\rho^{(\ell)}. \tag{5.82}$$

The instantaneous pressure relaxation can be thought of as eliminating the volume-fraction equation. The present model is conditionally hyperbolic, whereas the equal-pressure models are dependent upon a suitable choice for the interfacial pressure $p_{\mathrm{int}}^{(k)}$, that is, they have more restrictive conditions.

5.3.7 Interfacial-pressure modelling

When the expected number of internal interfaces N_{int} in a control volume is larger than 0, the last term of (I) in (5.65) will tend to drive the velocities and pressures of the two phases together, hence the name ‘relaxation term’. The effect increases with increasing N_{int}. In other words, N_{int} is a relaxation parameter for both velocity and pressure, such that a large N_{int} will cause equality of pressure and no slip (relative velocity) between the phases. This

is so because the present model is purely one-dimensional: Fluid particles moving in only one dimension cannot pass each other. The 'conventional' multiphase model has been averaged over a control volume (or cross-section) and is therefore able to account for some two-dimensional phenomena, such as slip. A similar cross-sectional averaging could be performed for the present model. However, the calculations would be tedious and are outside the scope of the present work. Instead, we introduce these 'two-dimensional' effects in a more simplistic manner, as described in the following, by setting $N_{\text{int}} = 0$ and by modifying the expression for p^*.

Standard p^*

A simple and linearized solution to the Riemann problem is given by the acoustic solver, or 'primitive variable Riemann solver (PVRS)' (Toro, 1999, Section 9.3). The expression for the 'star value' of the pressure (see Figure 5.2 on page 138) is

$$p^* = \frac{1}{a_\text{l} + a_\text{r}}\left[a_\text{r} p_\text{l} + a_\text{l} p_\text{r} + a_\text{l} a_\text{r}(u_\text{l} - u_\text{r})\right], \tag{5.83}$$

where $a \equiv \rho c$ can be called the acoustic impedance and the subscripts 'l' and 'r' denote the left-hand and right-hand states, respectively. This expression will be referred to as the 'standard p^*'.

CATHARE model for p^*

In the CATHARE code, the following expression was employed for non-stratified flows 'simply to provide the hyperbolicity of the system' (Bestion, 1990):

$$p^{(\text{g})} - p^{(\text{g})}_{\text{int}} = p^{(\ell)} - p^{(\ell)}_{\text{int}} = \gamma \frac{\alpha^{(\text{g})}\alpha^{(\ell)}\rho^{(\text{g})}\rho^{(\ell)}}{\alpha^{(\text{g})}\rho^{(\ell)} + \alpha^{(\ell)}\rho^{(\text{g})}}(u^{(\text{g})} - u^{(\ell)})^2. \tag{5.84}$$

In Bestion (1990), the factor γ does not appear explicitly. Evje and Flåtten (2003) took $\gamma = 1.2$.

Even though it might be difficult to derive the above expression in a rigorous way, we propose setting

$$p^* = p - \gamma \frac{\alpha^{(\text{g})}\alpha^{(\ell)}\rho^{(\text{g})}\rho^{(\ell)}}{\alpha^{(\text{g})}\rho^{(\ell)} + \alpha^{(\ell)}\rho^{(\text{g})}}(u^{(\text{g})} - u^{(\ell)})^2, \tag{5.85}$$

with $\gamma = 1.2$ in the gas–liquid Riemann problems.

The 0 model for p^*

It is often beneficial to take a simple model when the applicability of more complex models is unknown or difficult to evaluate. Consider the following simple model for the interfacial pressure:

$$p^{(k)} - p_{\text{int}}^{(k)} = 0. \tag{5.86}$$

It is not in widespread use, however, for it yields complex eigenvalues in the four-equation equal-pressure model. The present model, on the other hand, does not, a priori, share this problem. Instead of the expression (5.85), one may take

$$p^* = \frac{1}{2}(p^{(\ell)} + p^{(\mathrm{g})}) = p, \tag{5.87}$$

where the last equality stems from the fact that we use instantaneous pressure relaxation in the present work.

5.4 Reference method

To verify the numerical results obtained using the discrete-equation model, we will compare them with those of an independent numerical method, the 'Roe5' scheme, presented in Chapter 3. That scheme is based on the continuous multiphase equations and instantaneous pressure relaxation, and it uses a Roe-type Riemann solver.

Some care has to be taken when seeking to compare the results obtained using the standard p^* model (5.83) with those of a continuous model. It is necessary to provide the continuous model with interface-models corresponding to the ones of the discrete model in the limit of a fine grid. The continuous limit of the discrete-equation model has been studied by Papin (2005, Part II, Chapter 3) in two spatial dimensions, for Riemann solvers whose 'star values' can be written in the form

$$p^* = \frac{1}{a_1 + a_2}[a_1 p_2 + a_2 p_1 + a_1 a_2 (u_2 - u_1)], \tag{5.88}$$

and

$$u^* = \frac{1}{a_1 + a_2}[a_1 u_1 + a_2 u_2 + p_2 - p_1], \tag{5.89}$$

for some choice of a_1 and a_2. Among the Riemann solvers fitting into the above scheme are the acoustic solver, the HLLC solver and the relaxation solver (Papin, 2005).

Table 5.1: Parameters used in the shock tube test problems.

Quantity	Value	Unit
CFL number, C	0.9	–
Liquid speed of sound, $c^{(\ell)}$	1000	m/s
Gas speed of sound, $c^{(\mathrm{g})}$	$\sqrt{10^5}$	m/s
Liquid reference density, $\rho_\circ^{(\ell)}$	999.9	kg/m^3
Gas reference density, $\rho_\circ^{(\mathrm{g})}$	0	kg/m^3
Number of interfaces per control volume, N_{int}	0	–

Here we present the limit expressions for 1D, and the case of no surface tension. The interfacial pressure is

$$p_{\mathrm{int}}^{(\mathrm{g})} = p_{\mathrm{int}}^{(\ell)} = \frac{1}{a^{(\mathrm{g})} + a^{(\ell)}}[a^{(\mathrm{g})}p^{(\ell)} + a^{(\ell)}p^{(\mathrm{g})} + a^{(\ell)}a^{(\mathrm{g})}(u^{(\ell)} - u^{(\mathrm{g})})\,\mathrm{sgn}(\partial\alpha^{(\mathrm{g})}/\partial x)], \quad (5.90)$$

whereas the interfacial velocity is given by

$$u_{\mathrm{int}}^{(\mathrm{g})} = u_{\mathrm{int}}^{(\ell)} = \frac{1}{a^{(\mathrm{g})} + a^{(\ell)}}[a^{(\mathrm{g})}u^{(\mathrm{g})} + a^{(\ell)}u^{(\ell)} + (p^{(\ell)} - p^{(\mathrm{g})})\,\mathrm{sgn}(\partial\alpha^{(\mathrm{g})}/\partial x)]. \quad (5.91)$$

Here we take a to be the acoustic impedance, and the above expressions are equal to those for the 'star values' of the acoustic solver, except for the appearance of the sign function.

In the following, results from the Roe5 scheme will be shown together with the present results for comparison.

5.5 Test calculations

Here we consider the two two-phase shock-tube problems investigated by Evje and Flåtten (2003). They were presented in Chapter 3, but are repeated here fore convenience. The problems consist of a 100 m long tube, where the initial state is constant in each half. These test problems enable the investigation of various properties of the numerical scheme. However, it is difficult to envisage a laboratory setup that might realize them.

The employed parameters are given in Table 5.1. The values for the speed of sound and reference density used in the equation of state are equivalent to the ones used by Evje and Flåtten (2003). The calculations have been performed using the acoustic Riemann solver, our second-order scheme and the van Leer

Table 5.2: Initial states in the large relative velocity (LRV) shock tube problem.

Quantity	Left value	Right value	Unit
Liquid volume fraction, $\alpha^{(\ell)}$	0.71	0.70	–
Liquid velocity, $u^{(\ell)}$	1.0	1.0	m/s
Gas velocity, $u^{(\mathrm{g})}$	65	50	m/s
Liquid density, $\rho^{(\ell)}$	1000.165	1000.165	kg/m^3
Gas density, $\rho^{(\mathrm{g})}$	2.65	2.65	kg/m^3
Pressures, $p^{(\ell)} = p^{(\mathrm{g})}$	$2.65 \cdot 10^5$	$2.65 \cdot 10^5$	Pa

slope-limiter function. The Courant–Friedrichs–Lewy (CFL) number is defined by

$$C = \frac{\Delta t}{\Delta x} \max_{\forall k, \forall i} (|u_i^{(k),*}| + c_i^{(k)}). \tag{5.92}$$

5.5.1 Large relative velocity shock tube

The large relative velocity (LRV) shock was introduced by Cortes *et al.* (1998). However, since they plotted other variables, a direct comparison with their results is not feasible. The initial states can be found in Table 5.2.

Standard p^*

The results are plotted in Figure 5.4 on the following page at time $t = 0.1$ s. Here, the 'standard' expression (5.83) for p^* has been employed. The graph of the liquid volume fraction in Figure 5.4(a) is focused on the middle of the tube, where differences between the grids appear more clearly.

Compared to the results of Evje and Flåtten (2003) (see also the results for the CATHARE p^* model in the next subsection), some differences can be seen:

- The present method has less numerical diffusion (see e.g. the gas-velocity profile for the 100-cell grid).
- There is an instability at $x = 50$ m in the liquid velocity plot, Figure 5.4(c) on the next page.
- The 'plateaux' in the velocities are somewhat different.
- The jump in pressure at $x = 50$ m is larger in the present case, and contrary to the case of Evje and Flåtten (2003), the highest pressure is on the left-hand side.

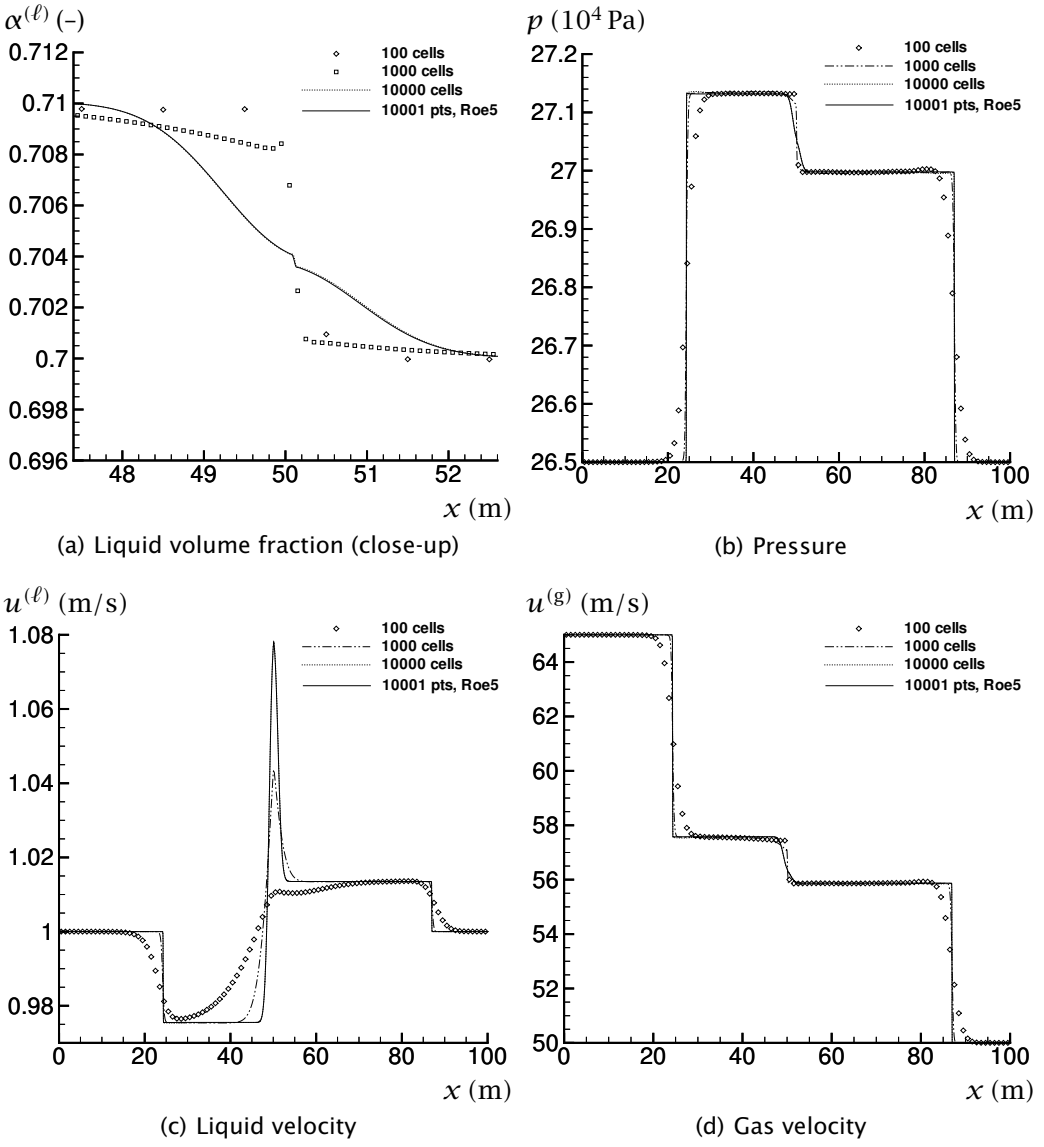

(a) Liquid volume fraction (close-up)

(b) Pressure

(c) Liquid velocity

(d) Gas velocity

Figure 5.4: LRV shock tube, calculated using the 'standard' p^*.

Figure 5.4 also shows results obtained using the Roe5 method on an equidistant grid with a grid spacing, Δx, equal to that of the 10000-cell grid of the discrete-equation model. The employed interfacial closures were the ones in (5.90)–(5.91). It is clear that the discrete-equation model and the Roe5 method give the same solution for fine grids.

CATHARE model for p^*

The case of the previous subsection has been recalculated employing the CATHARE model (5.85) for p^*. The results are shown in Figure 5.5 on the following page. The clearest difference from the preceding case, is that the pressure jump at $x = 50\,\text{m}$ is much smaller. Moreover, the plateaux in the velocities and in the pressure are straight, and in the case of the gas velocity, the levels of the middle plateaux are slightly higher.

Figure 5.5 shows very close agreement between the present model and the Roe5 scheme.

The 0 model for p^*

Results for the 0 model (5.87) are plotted in Figure 5.6 on page 149. As can be observed, they are similar to the results in Figure 5.5 obtained using the CATHARE model, except that the 0 model yields an undershoot in all variables at $x = 50\,\text{m}$, particularly in the liquid volume fraction and in the liquid velocity. Furthermore, the undershoot increases with grid refinement. The results agree closely with those of the Roe5 scheme, which, indeed, also displays undershoots at $x = 50\,\text{m}$. This behaviour might be a result of the complex eigenvalues of the 'underlying' one-pressure four-equation two-phase model.

5.5.2 Modified large relative velocity shock tube

The second shock tube problem features a liquid velocity jump, as well as a larger jump in the volume fraction, that is, it is a modified large relative velocity (LRV) shock tube problem. The initial states are displayed in Table 5.3 on page 151.

Standard p^*

Numerical results for the 'standard' expression for p^* are shown in Figure 5.7 on page 150. Again, the calculations performed using the discrete-equation model agree very well with those of the Roe5 scheme. However, the pressure

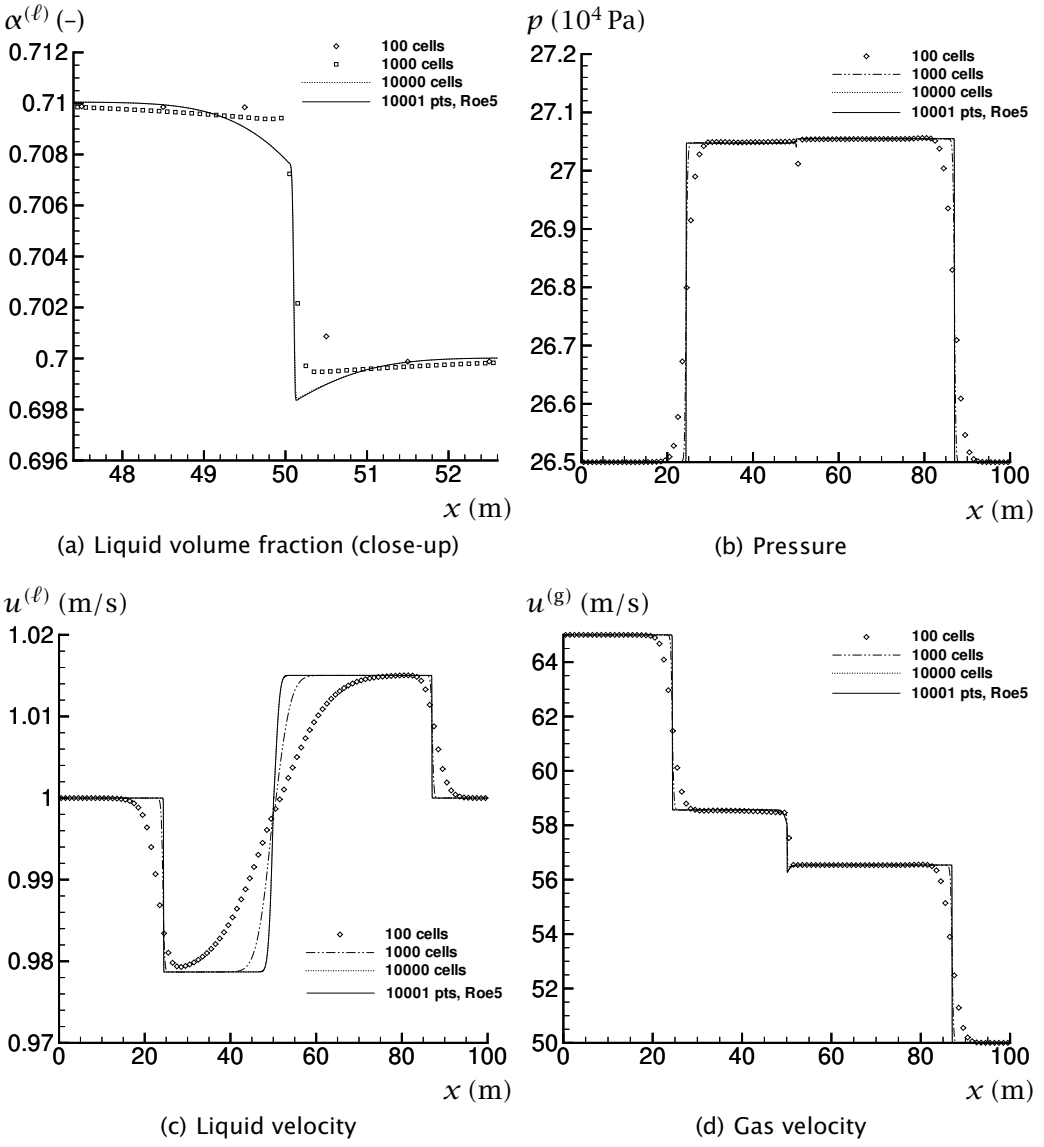

(a) Liquid volume fraction (close-up)

(b) Pressure

(c) Liquid velocity

(d) Gas velocity

Figure 5.5: LRV shock tube, calculated using the CATHARE model for p^*.

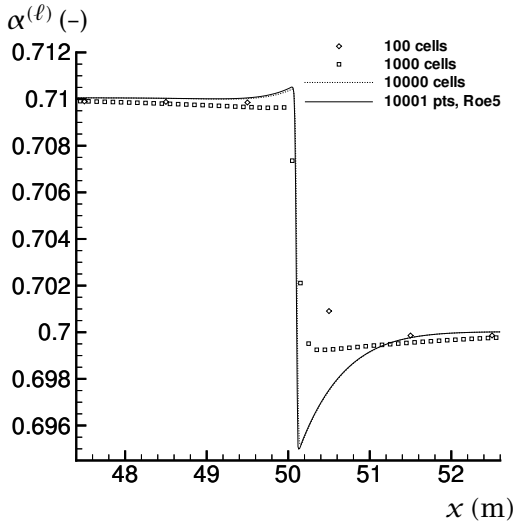

(a) Liquid volume fraction (close-up)

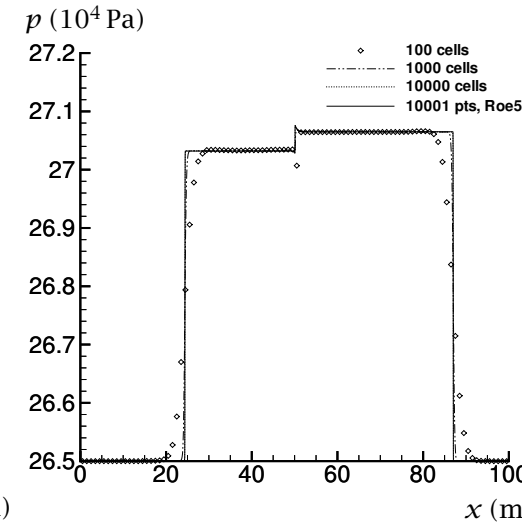

(b) Pressure

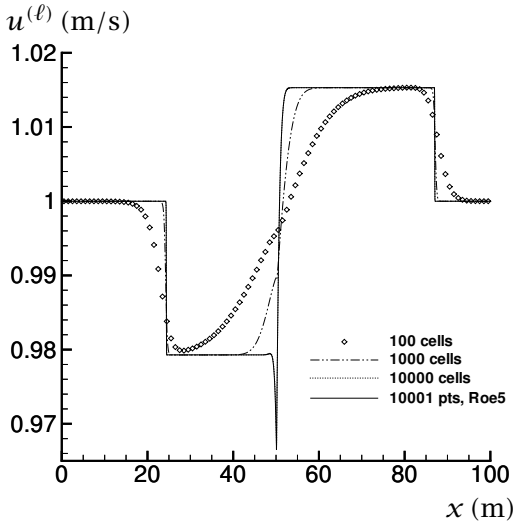

(c) Liquid velocity

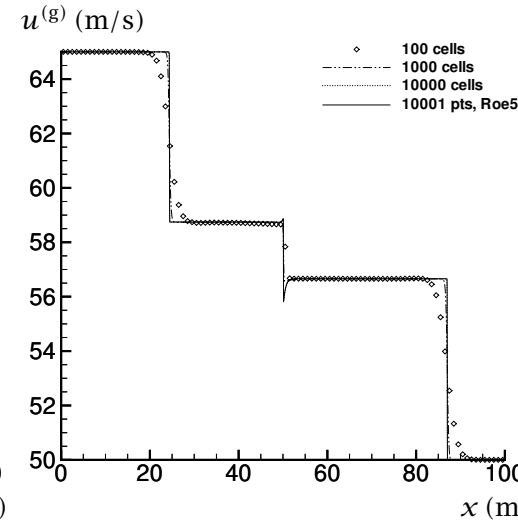

(d) Gas velocity

Figure 5.6: LRV shock tube, calculated using the 0 model for p^*.

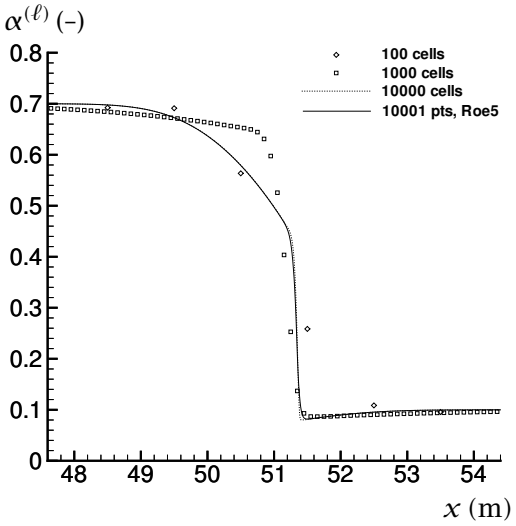

(a) Liquid volume fraction (close-up)

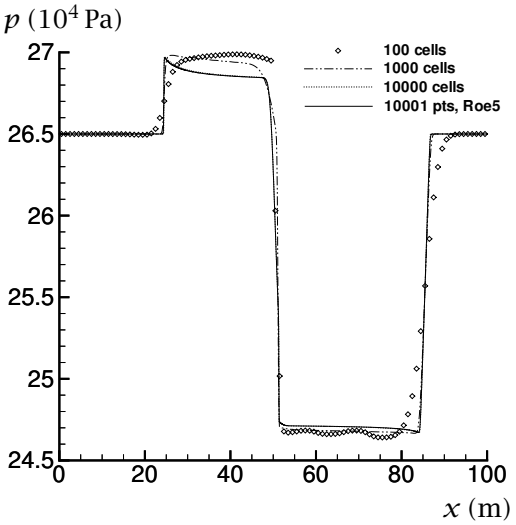

(b) Pressure

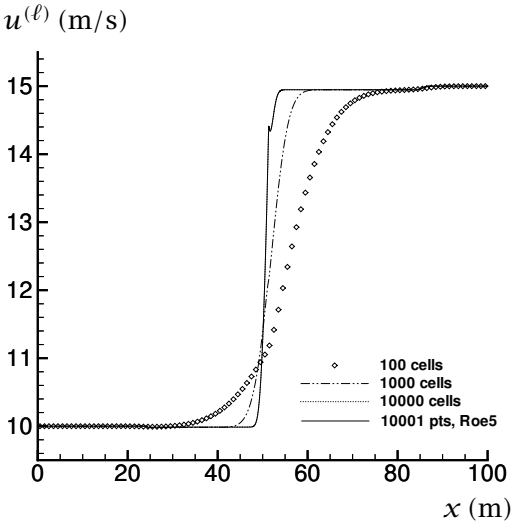

(c) Liquid velocity

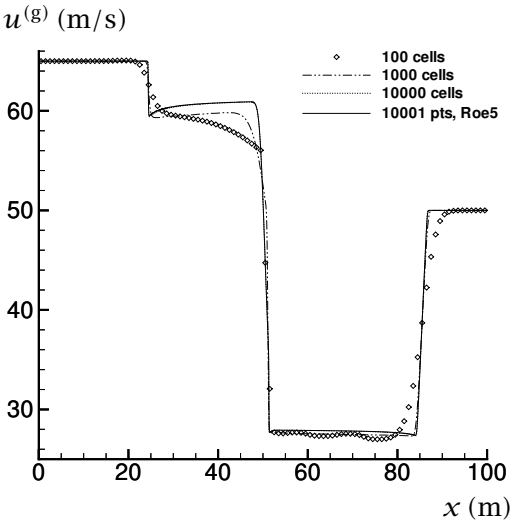

(d) Gas velocity

Figure 5.7: Modified LRV shock tube problem, calculated using the 'standard' p^*.

Table 5.3: Initial states in the modified large relative velocity (LRV) shock tube problem.

Quantity	Left value	Right value	Unit
Liquid volume fraction, $\alpha^{(\ell)}$	0.70	0.10	–
Liquid velocity, $u^{(\ell)}$	10	15	m/s
Gas velocity, $u^{(\mathrm{g})}$	65	50	m/s
Liquid density, $\rho^{(\ell)}$	1000.165	1000.165	$\mathrm{kg/m^3}$
Gas density, $\rho^{(\mathrm{g})}$	2.65	2.65	$\mathrm{kg/m^3}$
Pressures, $p^{(\ell)} = p^{(\mathrm{g})}$	$2.65 \cdot 10^5$	$2.65 \cdot 10^5$	Pa

and gas-velocity profiles are quite different from those of Evje and Flåtten (2003). This has numerical, but above all, modelling reasons, as can be seen by comparing with the results obtained using the CATHARE interfacial-pressure model in the following subsection.

CATHARE model for p^*

The results for the CATHARE model for p^* are given in Figure 5.8 on the following page. The fine-grid results are quite similar to those of Evje and Flåtten (2003).

Comparing with the results obtained using the standard p^* in Figure 5.7 reveals that the main differences occur for the pressure (Figures 5.8(b) and 5.7(b)) and the gas velocity (Figures 5.8(d) and 5.7(d)), where the plateaux in the middle section of the tube are on different levels. For the CATHARE model, the pressure in the tube is nowhere higher than the initial value of $26.5 \cdot 10^4$ Pa. For the standard p^* model, on the other hand, the pressure in the middle-left section is $27 \cdot 10^4$ Pa. The situation for the gas velocity is reversed: It is for the CATHARE model that gas velocities occur which are higher than the initial value.

These differences are a result of the interfacial closure models, and therefore it would have been interesting to be able to compare the calculations to experimental data.

The 0 model for p^*

Figure 5.9 on page 153 shows the results obtained using the 0 model (5.87) for p^*. Like in the case of the LRV shock tube, the results are similar to those of the CATHARE model for p^*. There are some differences, however: The pressure plateau to the left of $x = 50\,\mathrm{m}$ (Figure 5.9(b)) is lower than that of Figure 5.8(b),

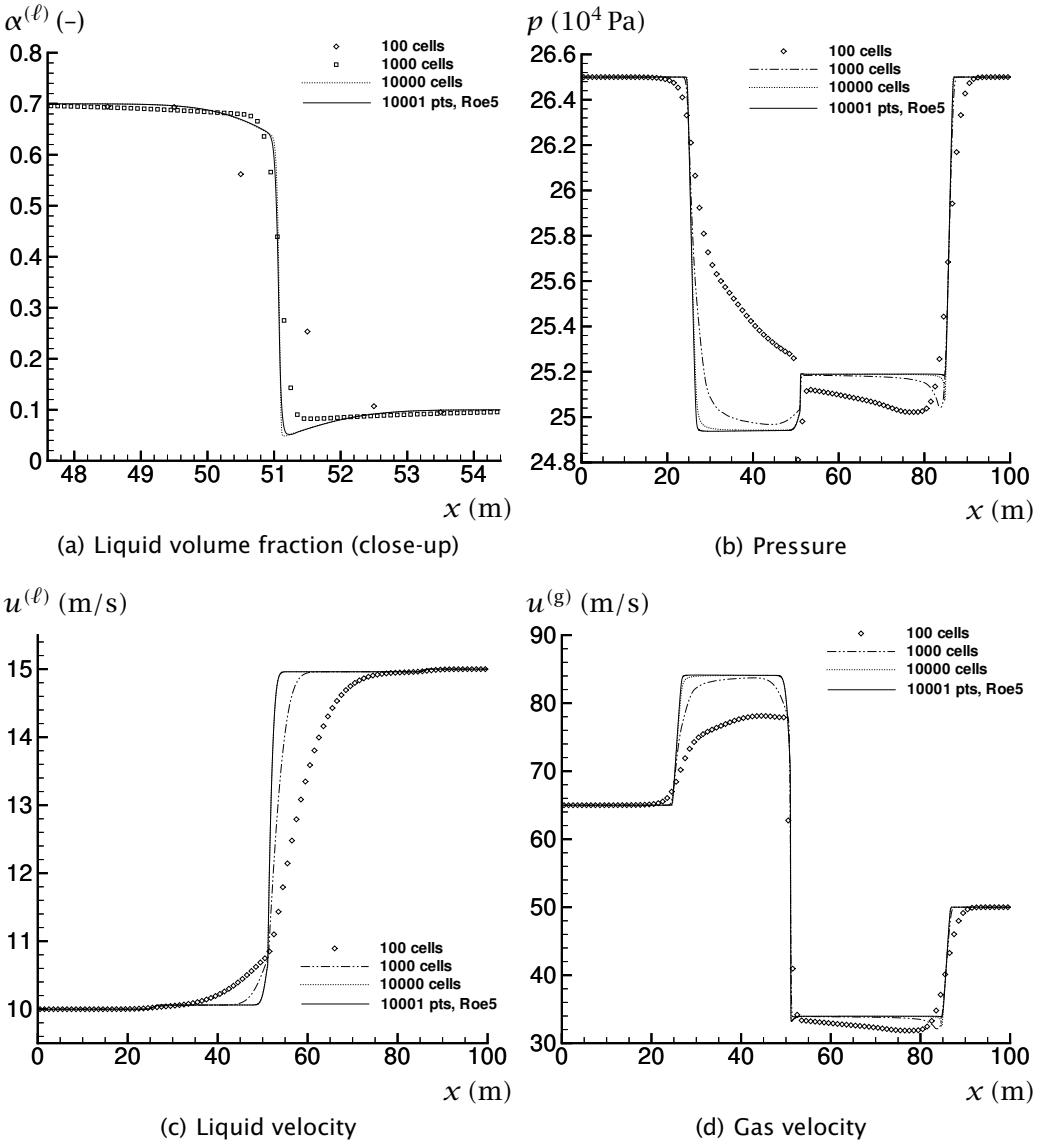

(a) Liquid volume fraction (close-up)

(b) Pressure

(c) Liquid velocity

(d) Gas velocity

Figure 5.8: Modified LRV shock tube problem, calculated using the CATHARE model for p^*.

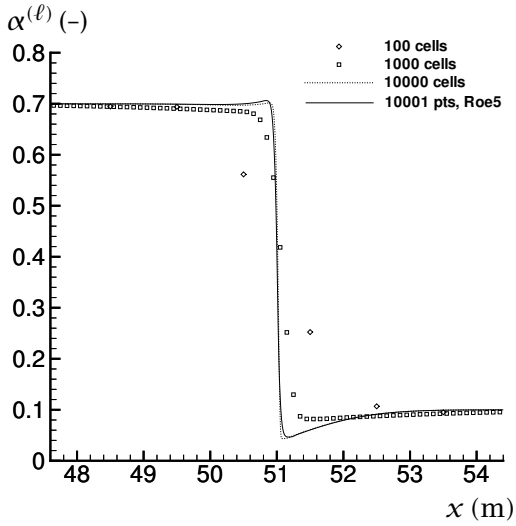

(a) Liquid volume fraction (close-up)

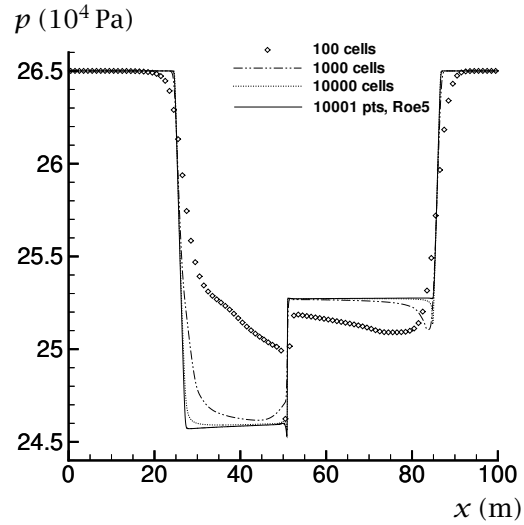

(b) Pressure

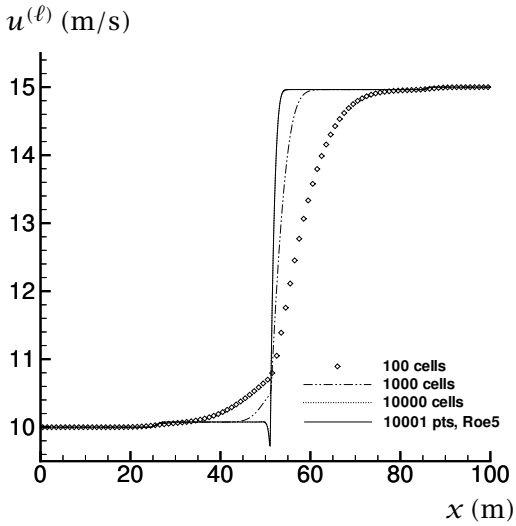

(c) Liquid velocity

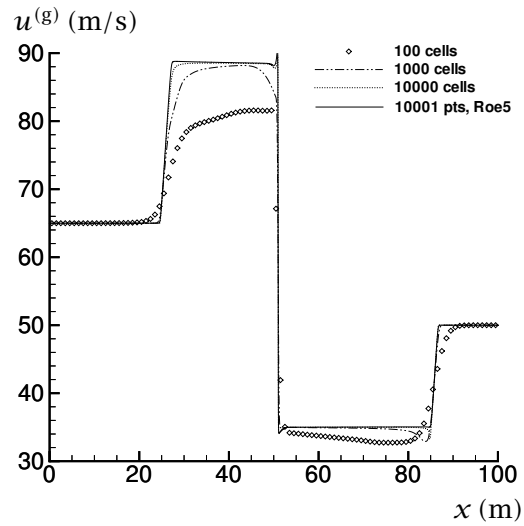

(d) Gas velocity

Figure 5.9: Modified LRV shock tube problem, calculated using the 0 model for p^*.

so that the pressure jump at $x = 50\,\text{m}$ is higher. Further, the plateau in the gas velocity to the left of the middle of the tube in Figure 5.9(d) is higher than that in Figure 5.8(d).

The plots for the 0 model in Figure 5.9 have more under- and overshoots than those for the CATHARE model in Figure 5.8, but this is somewhat less noticeable than for the LRV shock tube (Figures 5.6 and 5.5).

5.6 Conclusions

We have presented a five-equation isentropic version of the discrete seven-equation two-phase model of Abgrall and Saurel (2003). In the discrete-equation model, Riemann problems are solved between pure fluids. Hence, the difficulty of non-conservative products is avoided while solving the Riemann problem. Another characteristic of the discrete-equation model is that the properties of the Riemann solver influence the phasic interaction.

We have shown how different interfacial-pressure expressions can be incorporated into the discrete-equation model. One example is the CATHARE expression, often cited in the literature.

Two shock-tube problems from the literature (Evje and Flåtten, 2003) have been considered. The numerical results were strongly dependent on the employed expression for the interfacial pressure. The convergence properties of the scheme were also affected.

When the CATHARE interfacial-pressure model was employed, our results were similar to those presented by Evje and Flåtten (2003).

The correspondence between the discrete-equation model and the 'conventional' continuous model has been discussed. Continuous-limit expressions for the interfacial pressure and velocity were given for the discrete model. These expressions were employed in the Roe5 scheme (Chapter 3), a continuous model. Very good agreement between the discrete-equation model and the Roe5 scheme was obtained.

6 Characteristic-based boundary treatment

This chapter deals with partially-reflecting boundary conditions for the four-equation, one-pressure, isentropic two-fluid model. Using PID controllers, this boundary treatment allows waves to pass the boundaries, while keeping the boundary values close to their set-point values, even when the equation system contains source terms.

We consider the water faucet test case. Using the partially-reflecting boundary conditions, the method reaches the correct steady-state solution, and, moreover, in the transient period, the pressure profiles closely resemble the ones produced using non-reflecting boundary conditions.

A version of this chapter will be published as an article (Munkejord, 2005b).

6.1 Introduction

Physical systems with inlets and outlets, have, unlike the numerical models used to describe them, no abrupt boundaries. Therefore, the numerical boundary conditions may be called artificial, but anyhow, they are required to arrive at a numerical solution.

The specification of open boundaries for flow systems without source terms is relatively straightforward (see e.g. Toro, 1999, Section 6.3.3). However, source terms, such as gravity, often have to be considered. In such cases, the use of the simple, open boundary conditions will most often lead to drifting boundary values. Hence, for example, one cannot maintain a constant pressure at the outlet boundary.

Here we consider the four-equation, one-pressure, isentropic two-fluid model, assuming both phases to be compressible. Little work has been published regarding open boundary conditions for this system. Indeed, when numerical methods are tested in the literature, the computations are usually halted before the important waves reach the boundaries, to avoid reflected waves interacting with the solution in the inner domain. While that is perfectly justifiable for testing a numerical method, it is not difficult to conceive cases where it would be of interest to conduct longer simulations of the system.

In the present chapter, we employ the boundary-specification method of Olsen (2004, Chapter 3), who extended the single-phase method of Thompson

(1987, 1990) to the two-fluid model, and introduced Proportional-Integral-Derivative (PID) controllers to maintain the boundary quantities close to their desired values. This boundary treatment can be called 'partially-reflecting', since a part of the waves reaching the boundary is reflected. The theory of PID controllers can be found in a control-engineering textbook (e.g. Haugen, 1994).

The focus of Olsen (2004) was on essentially stationary cases. The *primary aim* of the present contribution is to demonstrate the applicability of the Olsen method for a transient case. Furthermore, the PID-controller approach involves three parameters. Hence it is our *secondary aim* to give an example of how these parameters can be estimated.

Section 6.2 reviews the characteristic-based boundary treatment, while in Section 6.3, an alternate way of reaching the steady-state solution is outlined. Numerical tests are performed in Section 6.4, with the water-faucet case as the main example. Conclusions are drawn in Section 6.5.

The reader might want to review the two-fluid model formulation described in Section 2.5 on page 28, and the characteristic form of the equations detailed in Section 3.2 on page 41.

6.2 The theory

The present boundary treatment is based on the work of Olsen (2004, Chapter 3), who applied the method of Thompson (1987, 1990) to the four-equation system, and introduced a PID controller to specify the conditions at the partially-reflecting boundaries. Here we briefly review the key points of the Olsen approach.

While Olsen (2004) wrote the coefficient matrix $\boldsymbol{A}$ in terms of the primitive variables $\boldsymbol{v}$, here the composite variables $\boldsymbol{q}$ are employed instead, and this is found to work equally well. This choice is based on practical reasons: The wish to use the same vector of unknowns in the inner domain and at the boundaries.

Since $\boldsymbol{A}$ is diagonalizable with real eigenvalues, we have:

$$\boldsymbol{R}^{-1}\boldsymbol{A}\boldsymbol{R} = \boldsymbol{\Lambda} = [\lambda_j \delta_{ij}], \tag{6.1}$$

that is, $\boldsymbol{\Lambda}$ is a diagonal matrix with the eigenvalues of $\boldsymbol{A}$ along its diagonal.

Multiply the equation (3.2) by $\boldsymbol{R}^{-1}$ from the left:

$$\boldsymbol{R}^{-1}\frac{\partial \boldsymbol{q}}{\partial t} + \boldsymbol{R}^{-1}\boldsymbol{A}\frac{\partial \boldsymbol{q}}{\partial x} = \boldsymbol{R}^{-1}\boldsymbol{s}, \tag{6.2}$$

and define the vector

$$\mathcal{L} \equiv \boldsymbol{\Lambda}\boldsymbol{R}^{-1}\frac{\partial \boldsymbol{q}}{\partial x} \equiv \boldsymbol{R}^{-1}\boldsymbol{A}\frac{\partial \boldsymbol{q}}{\partial x}. \tag{6.3}$$

Then component j of $\mathcal{L}$ becomes

$$\mathcal{L}_j \equiv \lambda_j \boldsymbol{l}_j^T \frac{\partial \boldsymbol{q}}{\partial x}. \tag{6.4}$$

The equation for the (time dependent) boundary conditions is

$$\frac{\partial \boldsymbol{q}}{\partial t} + \boldsymbol{R}\mathcal{L} = \boldsymbol{s}. \tag{6.5}$$

We define the vector of characteristic variables, $\boldsymbol{w}$, by the relation

$$\mathrm{d}\boldsymbol{w} = \boldsymbol{R}^{-1}\,\mathrm{d}\boldsymbol{q}. \tag{6.6}$$

Using the chain rule, we obtain from (3.2), neglecting source terms:

$$\frac{\partial \boldsymbol{q}}{\partial \boldsymbol{w}}\frac{\partial \boldsymbol{w}}{\partial t} + \boldsymbol{A}\frac{\partial \boldsymbol{q}}{\partial \boldsymbol{w}}\frac{\partial \boldsymbol{w}}{\partial x} = \boldsymbol{0}, \tag{6.7}$$

Multiply from the left by $\partial \boldsymbol{w}/\partial \boldsymbol{q} = \boldsymbol{R}^{-1}$:

$$\frac{\partial \boldsymbol{w}}{\partial t} + \boldsymbol{\Lambda}\frac{\partial \boldsymbol{w}}{\partial x} = \boldsymbol{0}, \tag{6.8}$$

or

$$\frac{\partial w_j}{\partial t} + \lambda_j \frac{\partial w_j}{\partial x} = 0 \tag{6.9}$$

in component form. This is an advection equation for each w_j with λ_j as the characteristic (advection) speed. A system of advection equations represents waves, and λ_j is the wave speed. Therefore, the solution of the nonlinear system (3.2) consists of several interacting waves.

The interpretation of $\mathcal{L}$ is less obvious, but the equations (6.8) and (6.3) show that in the case with no source terms, $\mathcal{L}$ is equal to the negative of the time-derivative of the vector of characteristic variables, $\boldsymbol{w}$. Thus $\mathcal{L}$ is related to the time-variation of the wave amplitude. The boundary conditions are therefore specified in terms of $\mathcal{L}$.

Boundary conditions can only be specified for incoming characteristics. Hence split the boundary-condition equation (6.5) in the following way:

$$\frac{\partial \boldsymbol{q}}{\partial t} + \boldsymbol{R}^+\mathcal{L}^+ + \boldsymbol{R}^-\mathcal{L}^- = \boldsymbol{s}. \tag{6.10}$$

$\boldsymbol{R}^+$ contains the eigenvectors corresponding to the positive eigenvalues (and zero-vectors otherwise), while $\boldsymbol{R}^-$ does the converse.

Hence, for the *left* boundary, the $\mathcal{L}_j^+ s$ must be specified as boundary conditions, while the $\mathcal{L}_j^- s$ are calculated from the definition (6.4). Conversely, on the *right* boundary, the $\mathcal{L}_j^- s$ are the boundary conditions, while the $\mathcal{L}_j^+ s$ are calculated from their definition (6.4).

To specify a function value $\boldsymbol{q}_j$ at the boundary, one sets $\partial \boldsymbol{q}_j / \partial t = \mathbf{0}$, so that the equation (6.10) in component form gives:

$$\boldsymbol{R}_j^{\mp} \mathcal{L}^{\mp} = -\boldsymbol{R}_j^{\pm} \mathcal{L}^{\pm} + \boldsymbol{s}_j. \tag{6.11}$$

Here, $\boldsymbol{R}_j$ denotes row j of $\boldsymbol{R}$.

It is also possible to specify a spatial gradient. The equation (6.3) implies that

$$(\boldsymbol{A}^{-1}\boldsymbol{R})_j \mathcal{L} = \frac{\partial \boldsymbol{q}_j}{\partial x} \tag{6.12}$$

or

$$(\boldsymbol{A}^{-1}\boldsymbol{R}^{\mp})_j \mathcal{L}^{\mp} = \frac{\partial \boldsymbol{q}_j}{\partial x} - (\boldsymbol{A}^{-1}\boldsymbol{R}^{\pm})_j \mathcal{L}^{\pm}. \tag{6.13}$$

Non-reflecting boundaries are set by specifying $\mathcal{L}^{\mp} \equiv \mathbf{0}$. However, in several cases with non-zero source terms, this may lead to 'drifting', or undetermined, values at the boundaries (Olsen, 2004, Section 3.3).

Drifting values can be avoided by making the boundaries partially-reflecting. A good way of doing that, is by thinking of the boundary treatment in terms of PID controllers (Olsen, 2004, Chapter 3). Hence write

$$\boldsymbol{R}_j^{\mp} \mathcal{L}^{\mp} = (\boldsymbol{R}_j^{\mp} \mathcal{L}^{\mp})^{\circ} + \frac{k_{\mathrm{P}}}{T} \Delta \boldsymbol{q}_j + \frac{k_{\mathrm{I}}}{T^2} \int_0^t \Delta \boldsymbol{q}_j \, \mathrm{d}\tau + k_{\mathrm{D}} \frac{\partial \boldsymbol{q}_j}{\partial t}. \tag{6.14}$$

Herein, $(\boldsymbol{R}_j^{\mp} \mathcal{L}^{\mp})^{\circ}$ is a start term. If the initial conditions are 'good', a suitable value for the start term is $-\boldsymbol{R}_j^{\pm} \mathcal{L}^{\pm} + \boldsymbol{s}_j$. $\Delta \boldsymbol{q}_j = \boldsymbol{q}_j - \boldsymbol{q}_j^{\mathrm{ref}}$ is the discrepancy between the desired value $\boldsymbol{q}_j^{\mathrm{ref}}$ and the actual one. k_{P}, k_{I} and k_{D} are the proportional, integral and differential constants, respectively. T is an integral time scale.

Substitute $\partial \boldsymbol{q}_j / \partial t$ in (6.14) by using the equation (6.10) in component form:

$$\frac{\partial \boldsymbol{q}_j}{\partial t} = -\boldsymbol{R}_j^{\pm} \mathcal{L}^{\pm} - \boldsymbol{R}_j^{\mp} \mathcal{L}^{\mp} + \boldsymbol{s}_j. \tag{6.15}$$

This gives:

$$\boldsymbol{R}_j^{\mp} \mathcal{L}^{\mp} = (1 + k_{\mathrm{D}})^{-1} \left[(\boldsymbol{R}_j^{\mp} \mathcal{L}^{\mp})^{\circ} + \frac{k_{\mathrm{P}}}{T} \Delta \boldsymbol{q}_j + \frac{k_{\mathrm{I}}}{T^2} \int_0^t \Delta \boldsymbol{q}_j \, \mathrm{d}\tau - k_{\mathrm{D}} (\boldsymbol{R}_j^{\pm} \mathcal{L}^{\pm} - \boldsymbol{s}_j) \right]. \tag{6.16}$$

Using the above equations for the boundary conditions is here, as in Olsen (2004), referred to as the MPCBC (multiphase characteristic-based boundary conditions) method.

6.3 Steady-state solution

A steady-state solution of the governing equations may, if it exists, be found by carrying out a simulation until the variation in the solution is small enough to be called steady. Another, and computationally far cheaper method, is by making a dedicated steady-state solver. In the present work, this was done for the four-equation system by deleting the transient term of the equation (3.3). The resulting system

$$\frac{\mathrm{d}\boldsymbol{v}}{\mathrm{d}x} = \boldsymbol{B}^{-1}(\boldsymbol{v})\boldsymbol{\varsigma}(\boldsymbol{v}) \tag{6.17}$$

can then solved using a suitable ODE solver if $\boldsymbol{B}$ is invertible. It is invertible if it has non-zero eigenvalues.

Finding the steady-state solution using this method has advantages due to its efficiency, for instance when one wants to test the effect of interface relations. It is also instructive to test whether transient methods are able to attain the steady-state solution.

6.4 Numerical tests

We have chosen the water faucet of Ransom as a test case for the multiphase characteristic-based boundary conditions (MPCBC). The water-faucet test case is described in Section 3.4.1 on page 58. Since gravity is included, simply setting $\mathcal{L}^{\mp} \equiv \mathbf{0}$ would not work for specifying open boundary conditions, as that would cause a drifting outlet pressure. Hence the approach of the equation (6.16) is needed.

The results shown in the following have been calculated using the monotonized central-difference (MC) limiter function in (3.57). It approaches second order when the solution is smooth. Details and calculations regarding limiter functions, and convergence order of the schemes, can be found in Chapter 3. Further, the Roe4 method was employed with a CFL number of $C = 0.9$ and a 101-point grid, unless otherwise stated.

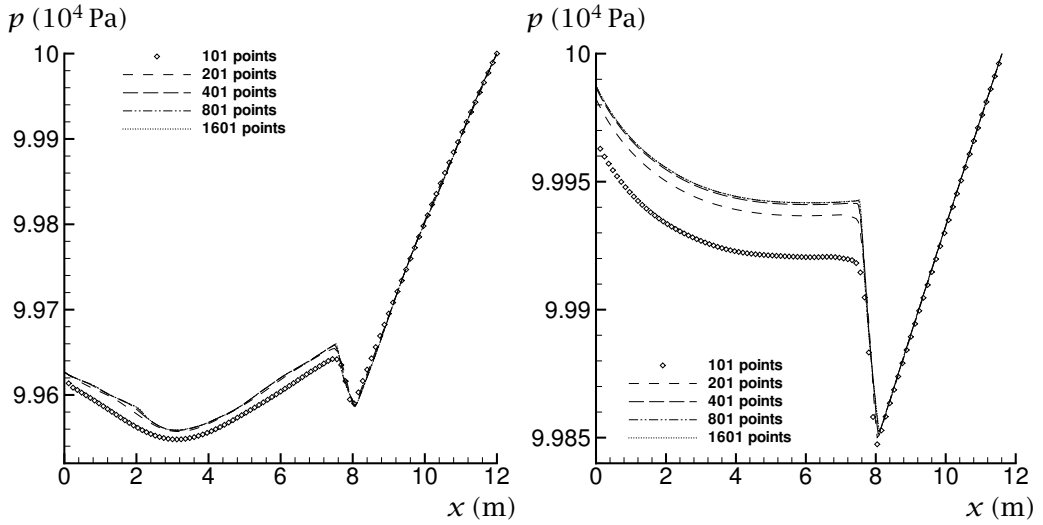

(a) Fixed BC (b) MPCBC

Figure 6.1: Pressure for the water faucet. Grid convergence of the Roe4 method for fixed and characteristic-based boundary conditions (MPCBC).

6.4.1 Pressure

As was already shown in Figure 3.4 on page 64, the pressure is by far the most sensitive variable in the faucet case. It is shown in Figure 6.1 for the for simple, fixed boundary conditions, and MPCBC. As in Section 3.4.1 on page 61, the time step was set to $\Delta t = 1.97 \cdot 10^{-5}$ s, which corresponds to a CFL number of $C = 0.9$ for the finest grid. It can be observed that the solution is quite different, depending on how the boundary conditions are specified. The fixed boundary conditions employed in Figure 6.1(a) give a larger pressure difference across the computational domain than the MPCBC method shown in Figure 6.1(b). This is further discussed in the following.

For the volume fraction and the velocities, on the other hand, the effect of the boundary treatment is not obvious until the volume-fraction discontinuity reaches the outlet.

6.4.2 Estimation of controller parameters

Recall the equation (6.16) on page 158 for the PID-controller boundary condition. It is necessary to estimate some reasonable values for the controller parameters appearing there. Here, this was done by using a slightly modified version of

Table 6.1: Controller parameters used for calculating the faucet case by the Roe4 method

k_P	k_I	k_D	T (s)
150	1667	3.3	1

the closed-loop method by Ziegler and Nichols (1942) as presented in the control-engineering textbook by Haugen (1994, Section 7.3).

In the present work, we assign the value $T = 1$ s for the time scale in the equation (6.16), which is sufficient, since we shall not discuss the controller-parameter values and the time scale independently. Assume that the 'critical gain', k_c, and the corresponding 'critical period', T_c, can be estimated. Then the Ziegler–Nichols method corresponds to setting

$$k_P = 0.6k_c, \qquad k_I = \frac{2k_P T}{T_c}, \quad \text{and} \quad k_D = \frac{k_P T_c}{8T}, \tag{6.18}$$

where k_P, k_I and k_D, are defined by the equation (6.16).

The pressure, p, was used as the 'control variable' for determining k_P, k_I and k_D. In normal control theory, the critical gain, k_c, is determined by setting k_I and k_D equal to zero and increasing the gain (corresponding to k_P) until the appearance of standing waves. Here, however, it is not the pressure, p, that is controlled, but its time derivative. Hence a steady state could not be attained without the integral term, and the proportional term was found instead by trial and error.

The period T_c was estimated by setting reasonably good 'trial-and-error' values for the controller parameters, and then measuring the period of the pressure fluctuations at the outlet. Values of $k_P = 300$, $k_I = 650$ and $k_D = 0$ were taken. This gave a value for the period of $T_c \approx 0.18$ s. The period was only a weak function of the controller parameters in this region.

Setting $k_P = 150$ gave, using $T_c = 0.18$ s, $k_I = 1667$ and $k_D = 3.3$, (repeated in Table 6.1). These values gave satisfactory results, that is, not too large initial fluctuations, and small fluctuations in the steady state. Doubling and halving k_P was also tried, calculating the corresponding k_I and k_D using $T_c = 0.18$ s each time. However, $k_P = 300$ gave unacceptably large fluctuations in the 'steady' state, and $k_P = 75$ gave rather large initial fluctuations. Hence, $k_P = 150$ was found to be a good compromise and retained for all the faucet-case calculations by the Roe4 method.

The above method for determining the controller parameters is undoubtedly improvable, but, as will be demonstrated in the following, it did indeed give reasonable results.

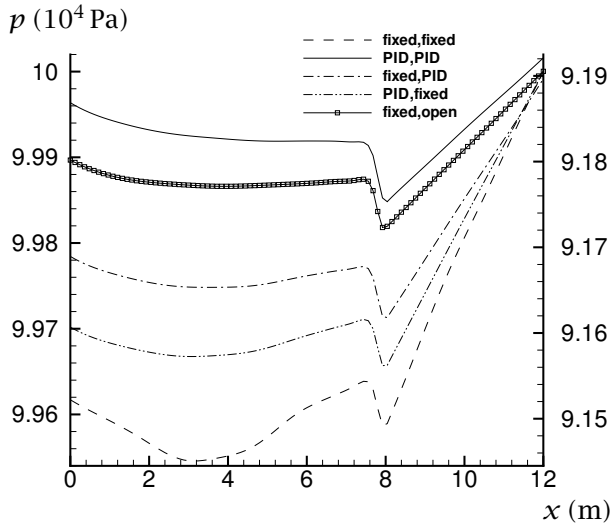

Figure 6.2: Pressure for the water faucet. Dependence on choice of inlet and outlet boundary conditions. The 'fixed,open' curve is related to the right-hand ordinate.

6.4.3 Influence of boundary-condition 'reflectiveness'

Consider Figure 6.2. It is similar to Figure 6.1 on page 160, but instead of grid refinement, it shows the dependence on the choice of boundary conditions on the inlet and the outlet. The label pairs shown in the figure, for instance 'fixed,PID', indicate the boundary conditions on the left-hand and on the right-hand sides, respectively. 'PID' means that the boundary conditions are set using the equation (6.16), while 'fixed' indicates that the equation (6.11) is used, that is, that the boundaries are reflecting. 'Open' means that the $\mathcal{L}_j$s are set to zero for incoming characteristics.

When the outlet boundary condition is 'open' (the $\boxplus$ curve), the pressure will drop. Hence the curve for the open outlet condition is drawn using the right-hand ordinate. The other curves relate to the left-hand ordinate. Both ordinates have the same span of 480 Pa, and the right-hand ordinate has been set such that the outlet pressure corresponds to $10 \cdot 10^4$ Pa on the left-hand ordinate.

The boundary-specification method giving by far the lowest pressure change across the domain, at the particular time of $t = 0.6$ s, was the use of PID controllers at both boundaries. The use of fixed boundary conditions produced the largest pressure changes at the inlet. When an open boundary was set at

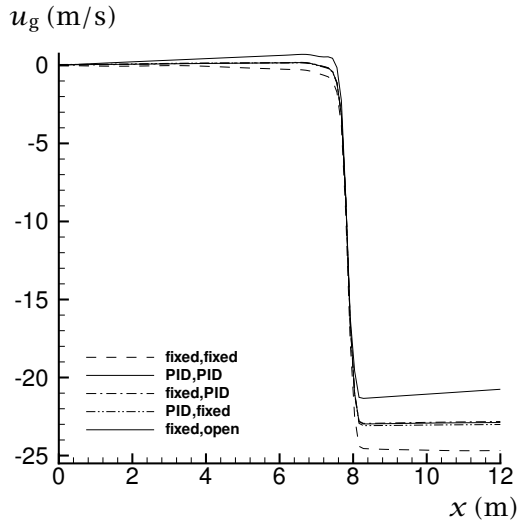

Figure 6.3: Gas velocity for the water faucet. Dependence on choice of inlet and outlet boundary conditions.

the outlet, it did not matter whether the inlet condition was fixed or PID.

Among the different combinations of reflecting and partially-reflecting boundary conditions, the one with a PID controller at both ends was the one that gave a pressure profile that best matched the shape of the profile calculated using the open boundary condition at the outlet. This shows that for the faucet case, the PID-controller boundary conditions succeeded in

- Keeping the outlet pressure from deviating too far from the set-point pressure of $1.0 \cdot 10^5$ Pa, and

- Giving results closely resembling those obtained using open boundary conditions at the outlet.

For the volume fraction and the liquid velocity, all the boundary conditions gave virtually the same result. Regarding the gas velocity, however, there were some differences, as shown in Figure 6.3. The three combinations of PID conditions gave very similar gas-velocity profiles, whereas the most negative velocity occurred for the fixed inlet–fixed outlet condition, and the least negative velocity was calculated using the open-outlet condition.

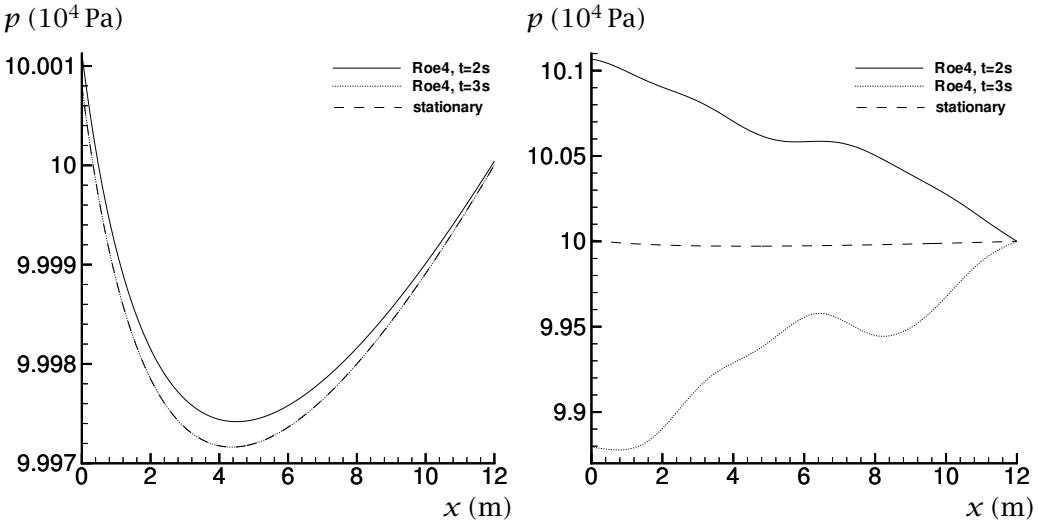

(a) Roe4 with PID-controller (b) Roe4 with fixed boundary conditions

Figure 6.4: Pressure for the water faucet. Comparison of steady-state solution as obtained with the Roe4 solver with and without PID-controller boundary conditions, and with the stationary solver.

6.4.4 Calculations towards steady state

The steady-state solution of the faucet case was calculated by two different methods:

1. By carrying out simulations with the Roe4 method until $t = 3$ s, and
2. By solving the steady-state system (6.17) on page 159 using a standard ODE solver.

Again the pressure was the most sensitive variable, and the result is displayed in Figure 6.4. For Figure 6.4(a), the Roe4 method was run using PID controllers at both boundaries. At $t = 3$ s, the correspondence between the Roe4 solution and the stationary solution is very good, and this result is not obtained by chance: Using a non-PID boundary condition at any boundary would lead to the Roe4 method utterly failing to produce the stationary pressure profile. This is shown in Figure 6.4(b). Note that the scale of the ordinate is different; in Figure 6.4(b), the shown pressure interval is 2400 Pa, while it is 41.25 Pa in Figure 6.4(a).

The pressure profiles obtained in Figure 6.4(a) are different from the linear shape one would expect in a case where gravity is the only source term. In

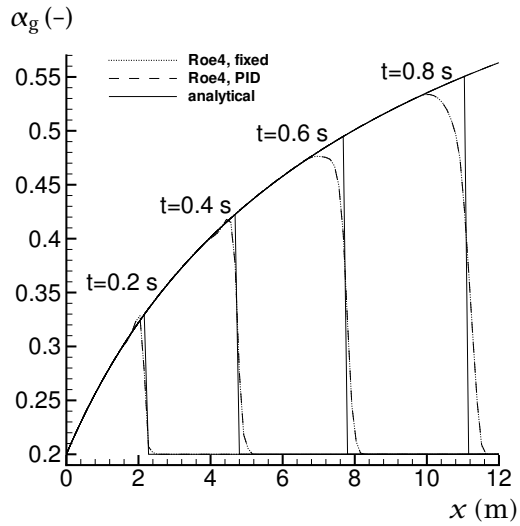

Figure 6.5: Gas volume fraction for the water faucet. Time series for fixed and PID-controller boundary conditions.

fact, this is a result of the use of the CATHARE correlation (see page 34) for the interfacial pressure difference. Indeed, when calculations were performed with a vanishing interfacial pressure difference, the pressure profile approached a linear shape. Physically, this can be explained by considering the liquid falling in stagnant air. The air is stagnant, and it will have a hydrostatic pressure profile. At the same time, it is reasonable that the air and water have the same pressure at each cross section, since no surface tension or other effects causing different phasic pressures are present.

Figure 6.5 displays a time series of the volume fraction calculated using the Roe4 method. The different boundary conditions do not influence the volume-fraction profiles on a scale that is visible on the plot.

The difference in pressure arising from the use of PID or fixed boundary conditions is noticeable, however, and it is further illustrated in Figure 6.6, showing a time series calculated using the Roe4 method. In Figure 6.6(a), a PID controller has been used at both boundaries, and in Figure 6.6(b), fixed conditions were employed. As can be seen, the amplitude of the pressure fluctuation at the inlet is about three times larger in the case of fixed boundary conditions compared to PID-controller conditions. Hence, if the pressure is important in itself, or if one wants, for instance, to calculate mass transfer due to flashing, a proper choice of boundary conditions is of significance.

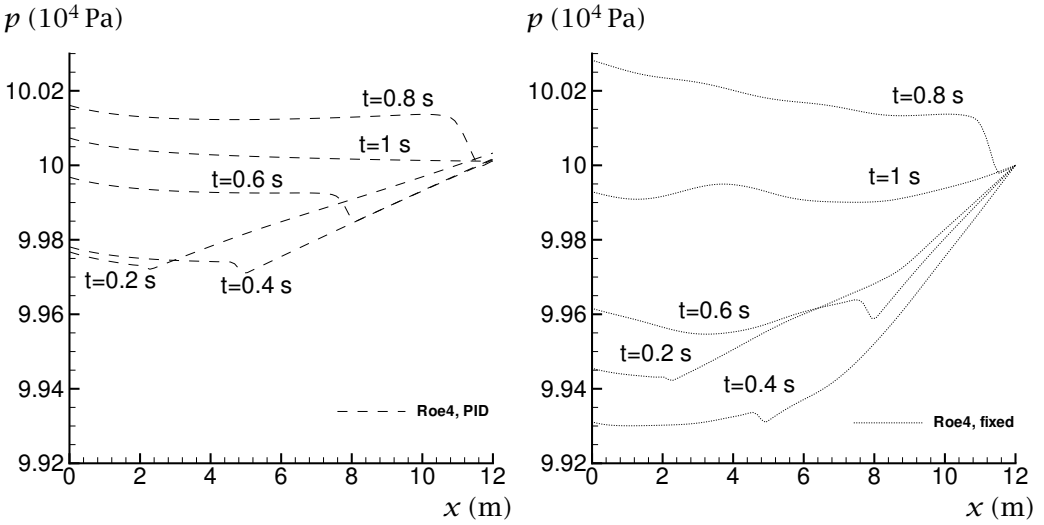

(a) PID controller at both boundaries

(b) Fixed conditions at both boundaries

Figure 6.6: Pressure for the water faucet. Time series showing the influence of boundary conditions.

À propos Another question is how the pressure calculated using different boundary conditions would compare with the pressure in the physical system for which the faucet case is a simplified model. Furthermore, as can be seen from the equation (6.4), the $\mathcal{L}_j$s are proportional to the left eigenvectors, which are not unique. Hence, the transient behaviour at a PID-controlled boundary is dependent on the choice of eigenvectors as well as on the controller parameters. These are two interesting issues beyond the scope of the present work.

6.5 Conclusions

For compressible flow, the specification of open boundary conditions is non-straightforward when the system of equations contains source terms, because they can cause drifting boundary values.

In this work, we have studied the one-dimensional one-pressure two-fluid model, solving it using a Roe-type method. The multiphase characteristic-based boundary condition (MPCBC) method of Olsen (2004) was employed. It uses PID controllers at the boundaries to avoid drifting values, while keeping the solution close to the desired set-point values.

We have aimed to demonstrate that the MPCBC method is applicable to transi-

ent cases. Furthermore, we have illustrated how the PID-controller parameters can be estimated. With the water-faucet case of Ransom (1987) as an example, it has been shown that MPCBC can yield a reasonable approximation to physically 'open' boundary conditions. Specifically, during the transient period, the MPCBC method gave a pressure profile closely resembling that of open boundary conditions, and the correct steady-state solution was attained. The pressure profile obtained using fixed boundary conditions was noticeably different from that obtained using PID controllers at the boundaries.

It is believed that the MPCBC method can be used for the simulation of systems with open boundaries, even after important waves have reached the boundaries.

7 A Roe scheme for the drift-flux model*

We construct a Roe-type numerical scheme for approximating the solutions of a drift-flux two-phase flow model. The model incorporates a set of highly complex closure laws, and the fluxes are generally not algebraic functions of the conserved variables. Hence, the classical approach of constructing a Roe solver by means of parameter vectors is unfeasible.

Alternative approaches for analytically constructing the Roe solver are discussed, and a formulation of the Roe solver valid for general closure laws is derived. In particular, a fully analytical Roe matrix is obtained for the special case of the Zuber–Findlay law describing bubbly flows.

First and second-order accurate versions of the scheme are demonstrated by numerical examples.

7.1 Introduction

To avoid excessive computational complexity, workable models describing two-phase flows in pipe networks are conventionally obtained by means of some averaging procedure. Models thus obtained are mathematically tractable, but there is a significant loss of information associated with the averaging process.

Hence additional information must be supplied to the system in the form of *closure laws*. The different physical assumptions leading to such laws result in different formulations of the two-phase flow models (Murrone and Guillard, 2005; Abgrall and Saurel, 2003; Ransom and Hicks, 1984; Stewart and Wendroff, 1984). It is useful to divide such models into two main classes:

- *Two-fluid* models, where equations are written for mass, momentum and energy balances for each fluid separately.
- *Mixture* models, where balance equations are written for the two-phase mixture.

For reasons of accuracy and robustness, it is desirable to use a numerical method able to provide an upwind resolution of all wave phenomena inherent

*This chapter corresponds to the article by Flåtten and Munkejord (2006).

in the models. The approximate Riemann solver of Roe (1981) is an attractive candidate, as it requires only the solution of a *linear* Riemann problem at each cell interface.

In the context of two-phase flows, this method has been extensively used. Sainsaulieu (1995) proposed a Roe-type Riemann solver for a model describing incompressible liquid droplets suspended in a gas. Karni *et al.* (2004) implemented a Roe scheme for a two-fluid model with velocity and pressure relaxation (Saurel and Abgrall, 1999).

A classical two-fluid model (Stewart and Wendroff, 1984) assumes pressure equilibrium between the phases. Toumi and Kumbaro (1996) presented a Roe scheme for such a model including a virtual mass force term. A generalization allowing for a pressure-modification term at the gas-liquid interface was presented in Toumi (1996). An alternative Roe scheme for this model was presented by Evje and Flåtten (2003). Furthermore, Cortes *et al.* (1998) proposed an efficient method for calculating the wave structure of the Roe linearization for such a model.

In this work, we consider a *mixture* model describing two-phase flows where the motions of the phases are strongly coupled. The model, commonly denoted as the *drift-flux* model, consists of a mass conservation equation for each phase, in addition to a momentum balance equation for the two-phase mixture. Supplementary relations are required to obtain the information necessary for determining the motion of each phase separately.

These relations are most often expressed in terms of a *hydrodynamic closure law* giving the relative velocity between the phases as a function of the flow parameters:

$$u_{\mathrm{g}} - u_{\ell} = \Phi(m_{\mathrm{g}}, m_{\ell}, u_{\mathrm{g}}), \tag{7.1}$$

where u_k is the velocity and m_k is the volumetric mass of phase k. The relative velocity $u_{\mathrm{r}} = u_{\mathrm{g}} - u_{\ell}$ between the phases is often referred to as the *slip velocity*; for this reason, the closure law (7.1) is also known as the *slip relation*.

In general, the closure law Φ is commonly stated as a complex combination of analytic expressions valid for particular flow regimes, experimental correlations, and various switching operators. To the investigator, it may be viewed as a black box. In addition, *thermodynamic closure laws* must be specified for each phase to relate the phasic density to the mixture pressure. These relations are often given only in tabular form.

As has been pointed out by several researchers (Baudin *et al.*, 2005a,b; Evje and Fjelde, 2002, 2003; Faille and Heintzé, 1999; Romate, 1998), the complexity of these laws severely restricts the possibilities for constructing a Roe solver by purely algebraic manipulations. Nevertheless, Roe-type schemes have been proposed for this model. Romate (1998) presented a method for constructing

a Roe matrix using a fully numerical approach. This method was used as the conservative part of the *hybrid primitive-conservative* method of Fjelde and Karlsen (2002). Faille and Heintzé (1999) proposed a linearized Riemann solver which may be interpreted as a simplified version of the approach of Romate. However, their suggested scheme does not satisfy the Roe conditions, with the consequence that the numerical fluxes are generally discontinuous if there is a change of sign in an eigenvalue between neighbouring cells.

A more formal approach was undertaken by Toumi and Caruge (1998) for a related model involving a mixture mass equation and a mixture energy equation. Based on a splitting of the flux into a 'mixture' and 'drift' part, they described how a Roe matrix could be obtained using the parameter-vector approach of Roe (1981). Unfortunately, the success of this approach relies heavily on the simplicity of the flux Jacobian of their model. Furthermore, their framework leads to integrals over the closure laws for which closed-form solutions do not generally exist.

Baudin *et al.* (2005a,b) suggested a *relaxation* scheme of the type proposed by Jin and Xin (1995). This is somewhat related to the Roe scheme in that one needs only to solve a linear Riemann problem at each cell interface. However, the relaxation procedure introduces two additional artifical wave phenomena, which complicate the matrix calculations required to advance the numerical solution. In addition, the relaxation parameters must be chosen with care to avoid excessive numerical dissipation.

In this work, we propose an alternative method for constructing a Roe solver for the drift-flux model. To as large a degree as possible, we construct our Roe solver based on *analytically derived* averages. By this, we address computational complexity issues associated with previously derived Roe solvers. Furthermore, we are able to isolate the effect of the closure law on the mathematical structure of the Roe linearization.

The chapter is organized as follows: In Section 7.2, we describe the two-phase flow model that we will be working with. In Section 7.2.2, we derive an analytical expression for the flux Jacobian of the model. In Section 7.3.1, we discuss various strategies for analytically constructing a Roe solver for systems of conservation laws. In Section 7.3.2, we adapt these strategies to the drift-flux model supplied with general closure laws. In Section 7.3.3, we present a method for obtaining a fully analytical Roe matrix for the special case of the Zuber–Findlay closure law. In Section 7.3.4, the main results of Section 7.3 are summarized. The numerical algorithm is described in Section 7.4.

In Section 7.5 we present numerical simulations, demonstrating accuracy and robustness properties of the scheme. Finally, our results are summarized in Section 7.6.

7.2 The drift-flux model

7.2.1 Model formulation

The model that we will be concerned with may be written in the following vector form

$$\frac{\partial \boldsymbol{q}}{\partial t} + \frac{\partial \boldsymbol{f}(\boldsymbol{q})}{\partial x} = \boldsymbol{s}(\boldsymbol{q}), \tag{7.2}$$

where $\boldsymbol{q}$ is the vector of conserved variables, $\boldsymbol{f}$ is the vector of fluxes, and $\boldsymbol{s}(\boldsymbol{q})$ is the vector of sources. They are given by

$$\boldsymbol{q} = \begin{bmatrix} \rho_g \alpha_g \\ \rho_\ell \alpha_\ell \\ \rho_g \alpha_g u_g + \rho_\ell \alpha_\ell u_\ell \end{bmatrix} = \begin{bmatrix} m_g \\ m_\ell \\ I_g + I_\ell \end{bmatrix}, \tag{7.3}$$

$$\boldsymbol{f}(\boldsymbol{q}) = \begin{bmatrix} \rho_g \alpha_g u_g \\ \rho_\ell \alpha_\ell u_\ell \\ \rho_g \alpha_g u_g^2 + \rho_\ell \alpha_\ell u_\ell^2 + p \end{bmatrix} = \begin{bmatrix} I_g \\ I_\ell \\ I_g u_g + I_\ell u_\ell + p \end{bmatrix} \tag{7.4}$$

and

$$\boldsymbol{s}(\boldsymbol{q}) = \begin{bmatrix} 0 \\ 0 \\ -F_w \end{bmatrix}. \tag{7.5}$$

The volume fractions satisfy

$$\alpha_g + \alpha_\ell = 1. \tag{7.6}$$

Dynamic mass andenergy transfers are neglected; we consider isentropic or isothermal flows. In particular, this means that the pressure may be obtained as

$$p = p(\rho_g) = p(\rho_\ell). \tag{7.7}$$

Thermodynamic submodels

For the numerical simulations presented in this chapter, we assume that both the gas and liquid phases are compressible, described by the simplified thermodynamic relations

$$\rho_\ell = \rho_{\ell,0} + \frac{p - p_{\ell,0}}{c_\ell^2} \tag{7.8}$$

and

$$\rho_g = \rho_{g,0} + \frac{p - p_{g,0}}{c_g^2}, \tag{7.9}$$

where

$$p_{k,0} = p(\rho_{k,0}).$$

Hydrodynamic submodels

By far the most important aspect of the model is the *hydrodynamic closure law*, which is commonly expressed in the following general form

$$u_g - u_\ell = \Phi(m_g, m_\ell, u_g). \tag{7.10}$$

The formulation of this law has a large effect on the flux Jacobian of the drift-flux model, and hence on the construction of the linearized Roe solver. A general approach for handling this difficulty is described in Section 7.3.2, where we explicitly express the Roe matrix as a function of Φ.

A special case of interest is the Zuber and Findlay (1965) relation

$$u_g = K(\alpha_g u_g + \alpha_\ell u_\ell) + S, \tag{7.11}$$

where K and S are flow-dependent parameters. The validity of (7.11) has been experimentally established for a broad range of parameters for both bubbly and slug flows (Bendiksen, 1984; França and Lahey, 1992; Hibiki and Ishii, 2002).

In the following calculations, the wall-friction term, F_w, is set equal to zero unless otherwise stated.

7.2.2 The Jacobian matrix

An alternative formulation of the system (7.2) is the *quasi-linear* form

$$\frac{\partial \boldsymbol{q}}{\partial t} + \boldsymbol{A}(\boldsymbol{q})\frac{\partial \boldsymbol{q}}{\partial x} = \boldsymbol{s}(\boldsymbol{q}), \tag{7.12}$$

where the flux Jacobian $\boldsymbol{A}(\boldsymbol{q})$ is defined as

$$\boldsymbol{A} \equiv \frac{\partial \boldsymbol{f}}{\partial \boldsymbol{q}} = \left[\frac{\partial f_i}{\partial q_j}\right]. \tag{7.13}$$

In the following, we will derive an expression for $\boldsymbol{A}$. Towards this aim, we will follow the common practice of thermodynamics and take

$$\left(\frac{\partial X}{\partial Y}\right)_{a,b} \tag{7.14}$$

to mean the partial derivative of X with respect to Y under the assumption of constant a and b.

Some definitions

We now define the following basic abbreviations:

$$\mu_{\mathrm{g}} = \left(\frac{\partial \Phi}{\partial m_{\mathrm{g}}}\right)_{m_\ell, u_{\mathrm{g}}} \tag{7.15}$$

$$\mu_\ell = \left(\frac{\partial \Phi}{\partial m_\ell}\right)_{m_{\mathrm{g}}, u_{\mathrm{g}}} \tag{7.16}$$

$$\mu_{\mathrm{v}} = \left(\frac{\partial \Phi}{\partial u_{\mathrm{g}}}\right)_{m_{\mathrm{g}}, m_\ell} \tag{7.17}$$

$$\zeta = \left(\frac{\partial u_\ell}{\partial u_{\mathrm{g}}}\right)_{m_{\mathrm{g}}, m_\ell}. \tag{7.18}$$

We further define the *pseudo mass* ϱ as

$$\varrho = m_{\mathrm{g}} + \zeta m_\ell. \tag{7.19}$$

Remark 1 We observe that by writing (7.1) as

$$\mathrm{d}\Phi = \mathrm{d}u_{\mathrm{g}} - \mathrm{d}u_\ell, \tag{7.20}$$

we obtain from (7.17) and (7.18) the basic relation

$$\mu_{\mathrm{v}} = 1 - \zeta. \tag{7.21}$$

□

We may now derive the following differentials:

Differential 1 (Gas velocity) We may expand $\mathrm{d}q_3$ as

$$\mathrm{d}q_3 = m_{\mathrm{g}}\,\mathrm{d}u_{\mathrm{g}} + u_{\mathrm{g}}\,\mathrm{d}m_{\mathrm{g}} + u_\ell\,\mathrm{d}m_\ell + m_\ell\,\mathrm{d}u_\ell. \tag{7.22}$$

Using (7.20) and

$$\mathrm{d}\Phi = \mu_{\mathrm{g}}\,\mathrm{d}m_{\mathrm{g}} + \mu_\ell\,\mathrm{d}m_\ell + \mu_{\mathrm{v}}\,\mathrm{d}u_{\mathrm{g}}, \tag{7.23}$$

we obtain

$$\mathrm{d}u_{\mathrm{g}} = \frac{1}{\varrho}\left(\left(m_\ell\mu_{\mathrm{g}} - u_{\mathrm{g}}\right)\mathrm{d}q_1 + \left(m_\ell\mu_\ell - u_\ell\right)\mathrm{d}q_2 + \mathrm{d}q_3\right). \tag{7.24}$$

□

Differential 2 (Gas momentum) Using

$$\mathrm{d}I_{\mathrm{g}} = m_{\mathrm{g}}\,\mathrm{d}u_{\mathrm{g}} + u_{\mathrm{g}}\,\mathrm{d}m_{\mathrm{g}} \tag{7.25}$$

we obtain from (7.24)

$$\mathrm{d}I_{\mathrm{g}} = \frac{1}{\varrho}\left(\left(m_{\mathrm{g}}m_{\ell}\mu_{\mathrm{g}} + \zeta m_{\ell}u_{\mathrm{g}}\right)\mathrm{d}q_1 + \left(m_{\mathrm{g}}m_{\ell}\mu_{\ell} - m_{\mathrm{g}}u_{\ell}\right)\mathrm{d}q_2 + m_{\mathrm{g}}\,\mathrm{d}q_3\right). \tag{7.26}$$

□

Differential 3 (Liquid momentum) Using

$$\mathrm{d}q_3 = \mathrm{d}I_{\mathrm{g}} + \mathrm{d}I_{\ell} \tag{7.27}$$

we obtain from (7.26)

$$\mathrm{d}I_{\ell} = \frac{1}{\varrho}\left(-\left(m_{\mathrm{g}}m_{\ell}\mu_{\mathrm{g}} + \zeta m_{\ell}u_{\mathrm{g}}\right)\mathrm{d}q_1 - \left(m_{\mathrm{g}}m_{\ell}\mu_{\ell} - m_{\mathrm{g}}u_{\ell}\right)\mathrm{d}q_2 + \zeta m_{\ell}\,\mathrm{d}q_3\right). \tag{7.28}$$

□

Differential 4 (Pressure) Writing $\alpha_{\mathrm{g}} + \alpha_{\ell} = 1$ as

$$\frac{m_{\mathrm{g}}}{\rho_{\mathrm{g}}(p)} + \frac{m_{\ell}}{\rho_{\ell}(p)} = 1, \tag{7.29}$$

we obtain by differentiation

$$\mathrm{d}p = \kappa\left(\rho_{\ell}\,\mathrm{d}q_1 + \rho_{\mathrm{g}}\,\mathrm{d}q_2\right), \tag{7.30}$$

where

$$\kappa = \frac{1}{\left(\partial\rho_{\mathrm{g}}/\partial p\right)\rho_{\ell}\alpha_{\mathrm{g}} + \left(\partial\rho_{\ell}/\partial p\right)\rho_{\mathrm{g}}\alpha_{\ell}}. \tag{7.31}$$

□

Differential 5 (Gas momentum convection) We have

$$\mathrm{d}\left(I_{\mathrm{g}}u_{\mathrm{g}}\right) = I_{\mathrm{g}}\,\mathrm{d}u_{\mathrm{g}} + u_{\mathrm{g}}\,\mathrm{d}I_{\mathrm{g}}. \tag{7.32}$$

Hence from (7.24) and (7.26) we obtain

$$\begin{aligned}\mathrm{d}\left(I_{\mathrm{g}}u_{\mathrm{g}}\right) = \frac{1}{\varrho}\Big(&\left(2m_{\mathrm{g}}m_{\ell}u_{\mathrm{g}}\mu_{\mathrm{g}} + (\zeta m_{\ell} - m_{\mathrm{g}})u_{\mathrm{g}}^2\right)\mathrm{d}q_1 \\ &+ \left(2m_{\mathrm{g}}m_{\ell}u_{\mathrm{g}}\mu_{\ell} - 2m_{\mathrm{g}}u_{\mathrm{g}}u_{\ell}\right)\mathrm{d}q_2 + 2m_{\mathrm{g}}u_{\mathrm{g}}\,\mathrm{d}q_3\Big).\end{aligned} \tag{7.33}$$

□

Differential 6 (Liquid momentum convection) We have

$$\mathrm{d}u_\ell = \mathrm{d}u_\mathrm{g} - \mathrm{d}\Phi = \zeta\,\mathrm{d}u_\mathrm{g} - \mu_\mathrm{g}\,\mathrm{d}m_\mathrm{g} - \mu_\ell\,\mathrm{d}m_\ell. \tag{7.34}$$

From (7.24) we obtain

$$\mathrm{d}u_\ell = \frac{1}{\varrho}\left(\zeta\,\mathrm{d}I - \left(m_\mathrm{g}\mu_\mathrm{g} + \zeta u_\mathrm{g}\right)\mathrm{d}m_\mathrm{g} - \left(m_\mathrm{g}\mu_\ell + \zeta u_\ell\right)\mathrm{d}m_\ell\right). \tag{7.35}$$

Hence from

$$\mathrm{d}(I_\ell u_\ell) = I_\ell\,\mathrm{d}u_\ell + u_\ell\,\mathrm{d}I_\ell \tag{7.36}$$

we obtain

$$\begin{aligned}\mathrm{d}(I_\ell u_\ell) = \frac{1}{\varrho}\Big(&-\left(2m_\mathrm{g}m_\ell u_\ell\mu_\mathrm{g} + 2\zeta m_\ell u_\mathrm{g}u_\ell\right)\mathrm{d}q_1\\ &-\left(2m_\mathrm{g}m_\ell u_\ell\mu_\ell + (\zeta m_\ell - m_\mathrm{g})u_\ell^2\right)\mathrm{d}q_2 + 2\zeta m_\ell u_\ell\,\mathrm{d}q_3\Big).\end{aligned} \tag{7.37}$$

□

The Jacobian matrix

Using these differentials, we see that the Jacobian matrix can be written as

$$\boldsymbol{A}(\boldsymbol{q}) = \frac{1}{\varrho}\begin{bmatrix} m_\mathrm{g}m_\ell\mu_\mathrm{g} + \zeta m_\ell u_\mathrm{g} & m_\mathrm{g}m_\ell\mu_\ell - m_\mathrm{g}u_\ell & m_\mathrm{g} \\ -(m_\mathrm{g}m_\ell\mu_\mathrm{g} + \zeta m_\ell u_\mathrm{g}) & m_\mathrm{g}u_\ell - m_\mathrm{g}m_\ell\mu_\ell & \zeta m_\ell \\ a_{31} & a_{32} & 2(m_\mathrm{g}u_\mathrm{g} + \zeta m_\ell u_\ell)\end{bmatrix}, \tag{7.38}$$

where

$$a_{31} = \kappa\varrho\rho_\ell + 2m_\mathrm{g}m_\ell\mu_\mathrm{g}(u_\mathrm{g} - u_\ell) + (\zeta m_\ell - m_\mathrm{g})u_\mathrm{g}^2 - 2\zeta m_\ell u_\mathrm{g}u_\ell \tag{7.39}$$

and

$$a_{32} = \kappa\varrho\rho_\mathrm{g} + 2m_\mathrm{g}m_\ell\mu_\ell(u_\mathrm{g} - u_\ell) - (\zeta m_\ell - m_\mathrm{g})u_\ell^2 - 2m_\mathrm{g}u_\mathrm{g}u_\ell. \tag{7.40}$$

7.3 The Roe linearization

7.3.1 Linearization strategies

The essence of Roe's method (Roe, 1981) is the replacement of the original nonlinear problem

$$\frac{\partial \boldsymbol{q}}{\partial t} + \frac{\partial}{\partial x}\boldsymbol{f}(\boldsymbol{q}) = \boldsymbol{0} \tag{7.41}$$

by a *linearized* problem defined locally at each cell interface;

$$\frac{\partial \hat{\boldsymbol{q}}}{\partial t} + \hat{\boldsymbol{A}}_{i-1/2}\frac{\partial \hat{\boldsymbol{q}}}{\partial x} = \boldsymbol{0}. \tag{7.42}$$

In the context of Roe's method, the matrix $\hat{\boldsymbol{A}}_{i-1/2}$ is expressed as a function of the left and right states as $\hat{\boldsymbol{A}}(\boldsymbol{q}^{\mathrm{L}}, \boldsymbol{q}^{\mathrm{R}})$, and must satisfy the following conditions:

R1: $\hat{\boldsymbol{A}}(\boldsymbol{q}^{\mathrm{L}}, \boldsymbol{q}^{\mathrm{R}})(\boldsymbol{q}^{\mathrm{R}} - \boldsymbol{q}^{\mathrm{L}}) = \boldsymbol{f}(\boldsymbol{q}^{\mathrm{R}}) - \boldsymbol{f}(\boldsymbol{q}^{\mathrm{L}})$

R2: $\hat{\boldsymbol{A}}(\boldsymbol{q}^{\mathrm{L}}, \boldsymbol{q}^{\mathrm{R}})$ is diagonalizable with real eigenvalues

R3: $\hat{\boldsymbol{A}}(\boldsymbol{q}^{\mathrm{L}}, \boldsymbol{q}^{\mathrm{R}}) \to \boldsymbol{A}(\boldsymbol{q})$ smoothly as $\boldsymbol{q}^{\mathrm{L}}, \boldsymbol{q}^{\mathrm{R}} \to \boldsymbol{q}$.

The main difficulty with the construction of such a matrix $\hat{\boldsymbol{A}}$ resides with the condition R1. In the event that the flux function $\boldsymbol{f}$ is a rational function of the components of $\boldsymbol{q}$, Roe (1981) discusses two strategies to meet the condition R1:

Strategy 1 (Direct algebraic manipulation) The following are discrete variants of the differential rules for rational functions:

$$\Delta(p+q) = \Delta p + \Delta q, \tag{7.43}$$

$$\Delta(pq) = \bar{p}\Delta q + \bar{q}\Delta p, \tag{7.44}$$

$$\Delta(1/q) = -\Delta q/\tilde{q}^2, \tag{7.45}$$

where $\bar{(\cdot)}$ denotes an arithmetic and $\tilde{(\cdot)}$ denotes a geometric mean value. Hence the flux difference can be written as a sum of terms

$$f_i(\boldsymbol{q}^{\mathrm{R}}) - f_i(\boldsymbol{q}^{\mathrm{L}}) = \sum_r \hat{A}_{ij}\left(q_j^{\mathrm{R}} - q_j^{\mathrm{L}}\right), \tag{7.46}$$

where $\hat{A}_{ij}$, constructed by application of (7.43)–(7.45), are the entries of $\hat{\boldsymbol{A}}$. □

Strategy 2 (Parameter vectors) We assume that $\boldsymbol{f}$ and $\boldsymbol{q}$ may be expressed as

$$\boldsymbol{f} = \boldsymbol{f}(\boldsymbol{w}) \tag{7.47}$$

$$\boldsymbol{q} = \boldsymbol{q}(\boldsymbol{w}), \tag{7.48}$$

for some *parameter vector* $\boldsymbol{w}$, where the components of $\boldsymbol{f}$ are at most quadratic polynomials in the components of $\boldsymbol{w}$. Then, by (7.43) and (7.44), any jump in $\boldsymbol{f}$ is related to jumps in $\boldsymbol{w}$ exclusively through **arithmetic** averages, and the Roe matrix may be obtained as

$$\hat{\boldsymbol{A}} = \boldsymbol{A}\left(q\left(\frac{1}{2}(\boldsymbol{w}_1 + \boldsymbol{w}_2)\right)\right). \tag{7.49}$$

□

Roe (1981) presented a successful application of the parameter-vector approach to the three-dimensional Euler equations. He also made the observation that several other systems of conservation laws possess a sufficiently simple structure allowing for a generalization of the approach.

When applicable, the parameter-vector approach has the advantage of satisfying an additional assumption which we may write as

R4: $\hat{\boldsymbol{A}}(\boldsymbol{q}^{\mathrm{L}}, \boldsymbol{q}^{\mathrm{R}}) = \boldsymbol{A}(\hat{\boldsymbol{q}})$ for some Roe-averaged state $\hat{\boldsymbol{q}}(\boldsymbol{q}^{\mathrm{L}}, \boldsymbol{q}^{\mathrm{R}})$.

Here

$$\hat{\boldsymbol{q}} = \boldsymbol{q}\left(\frac{1}{2}(\boldsymbol{w}_1 + \boldsymbol{w}_2)\right). \tag{7.50}$$

Although not a formal requirement of a Roe matrix, the satisfaction of R4 can nevertheless be advantageous. For instance, if the eigenstructure of $\boldsymbol{A}$ is analytically available, the same is also true for $\hat{\boldsymbol{A}}$. This property R4 is by no means guaranteed by the application of Strategy 1.

Strategies 1 and 2 are both based on the assumption that the flux vector is a rational function of the conserved variables. We would here like to draw attention to the fact that for the most general case, an alternative approach exists where the Roe matrix may be expressed as a function of $\boldsymbol{f}$ and $\boldsymbol{q}$ directly. This may be achieved by replacing the Jacobian by suitable *numerical flux derivatives*, as described below.

Strategy 3 (Flux Differences) Assuming that $\boldsymbol{q}$ is an N-vector, we may write the flux function $\boldsymbol{f}$ as

$$\boldsymbol{f}(\boldsymbol{q}) = \boldsymbol{f}(q_1, q_2, \ldots, q_N). \tag{7.51}$$

We now introduce the p-component flux difference symbol $\Delta_{(p)}$, defined by

$$\Delta_{(p)}\boldsymbol{f}(\boldsymbol{q}^{\mathrm{L}}, \boldsymbol{q}^{\mathrm{R}}) = \boldsymbol{f}(q_1^{\mathrm{R}}, \ldots, q_p^{\mathrm{R}}, q_{p+1}^{\mathrm{L}}, \ldots, q_N^{\mathrm{L}}) - \boldsymbol{f}(q_1^{\mathrm{R}}, \ldots, q_{p-1}^{\mathrm{R}}, q_p^{\mathrm{L}}, \ldots, q_N^{\mathrm{L}}), \tag{7.52}$$

for left and right states $\boldsymbol{q}^{\mathrm{L}}$ and $\boldsymbol{q}^{\mathrm{R}}$, where $p \in [1, \ldots, N]$.

We may now state the following theorem:

Theorem 1 *The $N \times N$ matrix $\hat{\boldsymbol{A}}$ given by*

$$\hat{\boldsymbol{A}}(\boldsymbol{q}^{\mathrm{L}}, \boldsymbol{q}^{\mathrm{R}}) = \left[\hat{A}_{ij}\right], \tag{7.53}$$

where

$$\hat{A}_{ij} = \begin{cases} \dfrac{\Delta_{(j)} f_i(\boldsymbol{q}^{\mathrm{L}}, \boldsymbol{q}^{\mathrm{R}})}{q_j^{\mathrm{R}} - q_j^{\mathrm{L}}} & \text{for } q_j^{\mathrm{L}} \neq q_j^{\mathrm{R}} \\ \dfrac{\partial f_i}{\partial q_j}(q_1^{\mathrm{R}}, \ldots, q_j^{\mathrm{R}}, q_{j+1}^{\mathrm{L}}, \ldots, q_N^{\mathrm{L}}) & \text{otherwise,} \end{cases} \tag{7.54}$$

satisfies the Roe conditions R1 and R3 for all sufficiently smooth functions $\boldsymbol{f}(\boldsymbol{q})$.□

PROOF By substitution of (7.53)–(7.54) into the Roe condition R1, all flux terms except $\boldsymbol{f}(\boldsymbol{q}^{\mathrm{L}})$ and $\boldsymbol{f}(\boldsymbol{q}^{\mathrm{R}})$ cancel, leaving us with a trivial identity.

Furthermore, by writing

$$\boldsymbol{q}^{\mathrm{R}} = \boldsymbol{q}^{\mathrm{L}} + \varepsilon, \tag{7.55}$$

it follows from the definition of the partial derivative that

$$\lim_{\varepsilon \to 0} \hat{A}_{ij} = \frac{\partial f_i}{\partial q_j}, \tag{7.56}$$

which is the requirement R3. ■

Remark 2 The requirement R2 cannot be proved in general, as it depends on the particular functional relationship $\boldsymbol{f}(\boldsymbol{q})$. In principle, this applies to all Strategies 1–3.

However, Harten and Lax (Harten *et al.*, 1983) have shown that if (7.41) has an entropy function, there exists a choice of parameter vector such that a matrix $\hat{\boldsymbol{A}}$, satisfying all requirements R1–R3, can always be obtained using Strategy 2. In this case, (7.49) is not necessarily satisfied. □

Remark 3 Strategy 3 has the advantage of not making any assumptions about the flux function. On the other hand, if Strategies 1 and 2 are applicable, they generally lead to computationally cheaper algorithms. □

7.3.2 Considerations for the drift-flux model

As previously discussed, the formulations of the hydrodynamic and thermodynamic closure laws are in general not available as analytical expressions. This leads to the conclusion that the parameter-vector approach will not be fruitful for the drift-flux model in general.

Instead, we will base our approach on Strategies 1 and 3 above. In this work, we wish to emphasize a somewhat unrecognized advantage associated with Strategy 1 – the large amount of freedom it presents us with in the construction of the Roe solver. In particular, we will take advantage of the following theorem:

Theorem 2 *Let the flux vector $\boldsymbol{f}(\boldsymbol{q})$ be written as a sum of individual contributions*

$$\boldsymbol{f}(\boldsymbol{q}) = \sum_r \boldsymbol{f}_r(\boldsymbol{q}). \tag{7.57}$$

Assume that with each $\boldsymbol{f}_r$, there is an associated matrix $\hat{\boldsymbol{A}}_r$ satisfying the Roe conditions R1 and R3 with respect to $\boldsymbol{f}_r$. Then the matrix

$$\hat{\boldsymbol{A}} = \sum_r \hat{\boldsymbol{A}}_r \tag{7.58}$$

satisfies both

(i) the Roe condition R1

(ii) the Roe condition R3

with respect to $\boldsymbol{f}(\boldsymbol{q})$. □

PROOF From the Roe condition R1, (i) directly follows by linearity of matrix multiplication. Furthermore, (ii) follows from the limit rule

$$\lim_{a\to b}\big(x(a)+y(a)\big) = \lim_{a\to b} x(a) + \lim_{a\to b} y(a) \tag{7.59}$$

applied to the definition of the partial derivative. ■

A flux-splitting strategy

To derive our scheme, we apply the Roe condition R1 sequentially to the various parts of the equation system (7.2). In particular, by Theorem 2 we express the Roe matrix $\hat{\boldsymbol{A}}$ as a sum of individual contributions

$$\hat{\boldsymbol{A}} = \hat{\boldsymbol{A}}_m + \hat{\boldsymbol{A}}_{\mathrm{g}} + \hat{\boldsymbol{A}}_\ell + \hat{\boldsymbol{A}}_p. \tag{7.60}$$

Hence, by not insisting that the Roe matrix must satisfy the condition R4, we are able to construct a valid matrix that

- consists almost entirely of simple arithmetic averages;
- allows the Roe-averaging of the closure laws to be isolated as fully independent problems.

We then demonstrate that Strategy 3 allows us to obtain a Roe-averaging of the closure laws with general validity. For the special case of the Zuber–Findlay closure law (7.11), an approach based on Strategy 1 allows us to directly obtain a fully analytical Roe matrix expressed in terms of the physical variables.

Mass equations

We first look for appropriate Roe averages for the mass conservation part of the system, i.e. we seek the submatrix

$$\hat{\boldsymbol{A}}_m = \frac{1}{\hat{\varrho}} \begin{bmatrix} \hat{m}_\mathrm{g}\hat{m}_\ell\hat{\mu}_\mathrm{g} + \hat{\zeta}\hat{m}_\ell\hat{u}_\mathrm{g} & \hat{m}_\mathrm{g}\hat{m}_\ell\hat{\mu}_\ell - \hat{m}_\mathrm{g}\hat{u}_\ell & \hat{m}_\mathrm{g} \\ -(\hat{m}_\mathrm{g}\hat{m}_\ell\hat{\mu}_\mathrm{g} + \hat{\zeta}\hat{m}_\ell\hat{u}_\mathrm{g}) & \hat{m}_\mathrm{g}\hat{u}_\ell - \hat{m}_\mathrm{g}\hat{m}_\ell\hat{\mu}_\ell & \hat{\zeta}\hat{m}_\ell \\ 0 & 0 & 0 \end{bmatrix} \tag{7.61}$$

corresponding to the convective mass-flux vector

$$\boldsymbol{f}_m = \begin{bmatrix} m_\mathrm{g}u_\mathrm{g} \\ m_\ell u_\ell \\ 0 \end{bmatrix}. \tag{7.62}$$

The Roe condition R1 yields two equations, which in vector form become

$$\hat{\boldsymbol{A}}_m(\boldsymbol{q}^\mathrm{R} - \boldsymbol{q}^\mathrm{L}) = \boldsymbol{f}_m(\boldsymbol{q}^\mathrm{R}) - \boldsymbol{f}_m(\boldsymbol{q}^\mathrm{L}). \tag{7.63}$$

Following (7.19) and (7.21), we insist that

$$\hat{\varrho} = \hat{m}_\mathrm{g} + \hat{\zeta}\hat{m}_\ell \tag{7.64}$$

$$\hat{\mu}_\mathrm{v} = 1 - \hat{\zeta}. \tag{7.65}$$

Given that the flux function $\boldsymbol{f}_m$ is quadratic in the variables (m_k, u_k), the following averages are suggested by (7.44):

$$\hat{m}_\mathrm{g} = \frac{1}{2}\left(m_\mathrm{g}^\mathrm{L} + m_\mathrm{g}^\mathrm{R}\right) \tag{7.66}$$

$$\hat{m}_\ell = \frac{1}{2}\left(m_\ell^\mathrm{L} + m_\ell^\mathrm{R}\right) \tag{7.67}$$

$$\hat{u}_\mathrm{g} = \frac{1}{2}\left(u_\mathrm{g}^\mathrm{L} + u_\mathrm{g}^\mathrm{R}\right) \tag{7.68}$$

$$\hat{u}_\ell = \frac{1}{2}\left(u_\ell^\mathrm{L} + u_\ell^\mathrm{R}\right). \tag{7.69}$$

By these substitutions, (7.63) reduces to

$$\hat{\mu}_\mathrm{g}\left(m_\mathrm{g}^\mathrm{R} - m_\mathrm{g}^\mathrm{L}\right) + \hat{\mu}_\ell\left(m_\ell^\mathrm{R} - m_\ell^\mathrm{L}\right) + \hat{\mu}_\mathrm{v}\left(u_\mathrm{g}^\mathrm{R} - u_\mathrm{g}^\mathrm{L}\right) = \Phi^\mathrm{R} - \Phi^\mathrm{L}, \tag{7.70}$$

which is directly satisfied when $(\mu_\mathrm{g}, \mu_\ell, \mu_\mathrm{v})$ are constant, by the definitions (7.15)–(7.17). Non-constant $(\mu_\mathrm{g}, \mu_\ell, \mu_\mathrm{v})$ are discussed in Sections 7.3.2 and 7.3.3.

Momentum convection

We split the convective momentum flux as follows:

$$\boldsymbol{f}_I = \begin{bmatrix} 0 \\ 0 \\ m_{\mathrm{g}} u_{\mathrm{g}}^2 + m_\ell u_\ell^2 \end{bmatrix} = \boldsymbol{f}_{\mathrm{g}} + \boldsymbol{f}_\ell, \tag{7.71}$$

where

$$\boldsymbol{f}_{\mathrm{g}} = \begin{bmatrix} 0 \\ 0 \\ m_{\mathrm{g}} u_{\mathrm{g}}^2 \end{bmatrix} \tag{7.72}$$

and

$$\boldsymbol{f}_\ell = \begin{bmatrix} 0 \\ 0 \\ m_\ell u_\ell^2 \end{bmatrix}. \tag{7.73}$$

Gas momentum convection

We now seek Roe averages for the Jacobian submatrix

$$\boldsymbol{A}_{\mathrm{g}} = \frac{\partial \boldsymbol{f}_{\mathrm{g}}}{\partial \boldsymbol{q}} = \frac{1}{\varrho} \begin{bmatrix} 0 & 0 & 0 \\ 0 & 0 & 0 \\ a_{\mathrm{g},31} & a_{\mathrm{g},32} & 2 m_{\mathrm{g}} u_{\mathrm{g}} \end{bmatrix}, \tag{7.74}$$

where

$$a_{\mathrm{g},31} = 2 m_{\mathrm{g}} m_\ell u_{\mathrm{g}} \mu_{\mathrm{g}} + (\zeta m_\ell - m_{\mathrm{g}}) u_{\mathrm{g}}^2 \tag{7.75}$$

and

$$a_{\mathrm{g},32} = 2 m_{\mathrm{g}} m_\ell u_{\mathrm{g}} \mu_\ell - 2 m_{\mathrm{g}} u_{\mathrm{g}} u_\ell. \tag{7.76}$$

In particular, we observe that if we look for Roe averages of the form

$$\hat{A}_{\mathrm{g},31} = \frac{1}{\hat{\varrho}} \left(2 \hat{m}_{\mathrm{g}} \hat{m}_\ell \tilde{u}_{\mathrm{g}} \hat{\mu}_{\mathrm{g}} + 2 \hat{\zeta} \hat{m}_\ell \hat{u}_{\mathrm{g}} \tilde{u}_{\mathrm{g}} - (\hat{\zeta} \hat{m}_\ell + \hat{m}_{\mathrm{g}}) \tilde{u}_{\mathrm{g}}^2 \right) \tag{7.77}$$

$$\hat{A}_{\mathrm{g},32} = \frac{1}{\hat{\varrho}} \left(2 \hat{m}_{\mathrm{g}} \hat{m}_\ell \tilde{u}_{\mathrm{g}} \hat{\mu}_\ell - 2 \hat{m}_{\mathrm{g}} \tilde{u}_{\mathrm{g}} \hat{u}_\ell \right) \tag{7.78}$$

$$\hat{A}_{\mathrm{g},33} = \frac{1}{\hat{\varrho}} \left(2 \hat{m}_{\mathrm{g}} \tilde{u}_{\mathrm{g}} \right), \tag{7.79}$$

involving the assumption of *two* different Roe-averaged gas velocities $\tilde{u}_{\mathrm{g}}$ and $\hat{u}_{\mathrm{g}}$, we may write (7.77)–(7.79) as

$$\hat{A}_{\mathrm{g},31} = 2 \tilde{u}_{\mathrm{g}} \hat{A}_{m,11} - \tilde{u}_{\mathrm{g}}^2 \tag{7.80}$$

$$\hat{A}_{\mathrm{g},32} = 2 \tilde{u}_{\mathrm{g}} \hat{A}_{m,12} \tag{7.81}$$

$$\hat{A}_{\mathrm{g},33} = 2 \tilde{u}_{\mathrm{g}} \hat{A}_{m,13}, \tag{7.82}$$

where $\hat{\boldsymbol{A}}_m$ is the *mass* Roe matrix (7.61).

Remark 4 Note that $\hat{A}_{\mathrm{g},31}$ can equivalently be written as

$$\hat{A}_{\mathrm{g},31} = \frac{1}{\hat{\varrho}}\left(2\hat{m}_{\mathrm{g}}\hat{m}_\ell\tilde{u}_{\mathrm{g}}\hat{\mu}_{\mathrm{g}} + (\hat{\zeta}\hat{m}_\ell - \hat{m}_{\mathrm{g}})\tilde{u}_{\mathrm{g}}^2 + 2\hat{\zeta}\hat{m}_\ell\tilde{u}_{\mathrm{g}}(\hat{u}_{\mathrm{g}} - \tilde{u}_{\mathrm{g}})\right), \tag{7.83}$$

where the last term vanishes when $\hat{u}_{\mathrm{g}} = \tilde{u}_{\mathrm{g}}$ (in accordance with the condition R3). □

By the gas mass equation (7.63), the condition R1 on $\hat{\boldsymbol{A}}_{\mathrm{g}}$ simply becomes

$$\tilde{u}_{\mathrm{g}}^2\left(m_{\mathrm{g}}^{\mathrm{R}} - m_{\mathrm{g}}^{\mathrm{L}}\right) - 2\tilde{u}_{\mathrm{g}}\left(m_{\mathrm{g}}^{\mathrm{R}}u_{\mathrm{g}}^{\mathrm{R}} - m_{\mathrm{g}}^{\mathrm{L}}u_{\mathrm{g}}^{\mathrm{L}}\right) + (m_{\mathrm{g}}u_{\mathrm{g}}^2)^{\mathrm{R}} - (m_{\mathrm{g}}u_{\mathrm{g}}^2)^{\mathrm{L}} = 0, \tag{7.84}$$

the solution of which is the standard Roe-averaged velocity, familiar from the Euler equations:

$$\tilde{u}_{\mathrm{g}} = \frac{\sqrt{m_{\mathrm{g}}^{\mathrm{L}}}u_{\mathrm{g}}^{\mathrm{L}} + \sqrt{m_{\mathrm{g}}^{\mathrm{R}}}u_{\mathrm{g}}^{\mathrm{R}}}{\sqrt{m_{\mathrm{g}}^{\mathrm{L}}} + \sqrt{m_{\mathrm{g}}^{\mathrm{R}}}}. \tag{7.85}$$

Here the gas mass m_{g} takes the place of the density ρ.

Hence a Roe average $\hat{\boldsymbol{A}}_{\mathrm{g}}$ for the gas momentum convection submatrix (7.74) is obtained rather nicely; the 'hat' averages of (7.77)–(7.79) are the simple arithmetic averages (7.66)–(7.69), whereas the 'tilde'-averaged gas velocity $\tilde{u}_{\mathrm{g}}$ of (7.77)–(7.79) is given by (7.85).

Remark 5 The simultaneous application of two different velocity averages $\tilde{u}_{\mathrm{g}}$ and $\hat{u}_{\mathrm{g}}$ allows for a significantly simplified algebraic structure of the Roe matrix $\hat{\boldsymbol{A}}$. Imposing the conditon R4, hereby forcing a unique expression for the velocity average, would in this case have led to highly complicated expressions. □

Liquid momentum convection

We seek Roe averages for the Jacobian submatrix

$$\boldsymbol{A}_\ell = \frac{\partial \boldsymbol{f}_\ell}{\partial \boldsymbol{q}} = \frac{1}{\varrho}\begin{bmatrix} 0 & 0 & 0 \\ 0 & 0 & 0 \\ a_{\ell,31} & a_{\ell,32} & 2\zeta m_\ell u_\ell \end{bmatrix}, \tag{7.86}$$

where

$$a_{\ell,31} = -(2m_{\mathrm{g}}m_\ell u_\ell\mu_{\mathrm{g}} + 2\zeta m_\ell u_{\mathrm{g}}u_\ell) \tag{7.87}$$

and

$$a_{\ell,32} = -(2m_{\mathrm{g}}m_\ell u_\ell\mu_\ell + (\zeta m_\ell - m_{\mathrm{g}})u_\ell^2). \tag{7.88}$$

We proceed in a fully equivalent fashion as for the gas momentum convection, i.e. we look for Roe averages of the form

$$\hat{A}_{\ell,31} = -\frac{1}{\hat{\varrho}}\left(2\hat{m}_{\mathrm{g}}\hat{m}_\ell\tilde{u}_\ell\hat{\mu}_{\mathrm{g}} + 2\hat{\zeta}\hat{m}_\ell\hat{u}_{\mathrm{g}}\tilde{u}_\ell\right) \tag{7.89}$$

$$\hat{A}_{\ell,32} = \frac{1}{\hat{\varrho}}\left(2\hat{m}_{\mathrm{g}}\tilde{u}_\ell\hat{u}_\ell - 2\hat{m}_{\mathrm{g}}\hat{m}_\ell\tilde{u}_\ell\hat{\mu}_\ell - (\hat{m}_{\mathrm{g}} + \hat{\zeta}\hat{m}_\ell)\tilde{u}_\ell^2\right) \tag{7.90}$$

$$\hat{A}_{\ell,33} = \frac{1}{\hat{\varrho}}\left(2\hat{\zeta}\hat{m}_\ell\tilde{u}_\ell\right). \tag{7.91}$$

Remark 6 Note that $\hat{A}_{\ell,32}$ can equivalently be written as

$$\hat{A}_{\ell,32} = \frac{1}{\hat{\varrho}}\left(-(2\hat{m}_{\mathrm{g}}\hat{m}_\ell\tilde{u}_\ell\hat{\mu}_\ell + (\hat{\zeta}\hat{m}_\ell - \hat{m}_{\mathrm{g}})\tilde{u}_\ell^2) + 2\hat{m}_{\mathrm{g}}\tilde{u}_\ell(\hat{u}_\ell - \tilde{u}_\ell)\right), \tag{7.92}$$

where the last term vanishes when $\hat{u}_\ell = \tilde{u}_\ell$ (in accordance with the condition R3). □

As for the gas momentum convection, we may express (7.89)–(7.91) in terms of the mass Roe matrix $\hat{\boldsymbol{A}}_m$ (7.61) as

$$\hat{A}_{\ell,31} = 2\tilde{u}_\ell\hat{A}_{m,21} \tag{7.93}$$

$$\hat{A}_{\ell,32} = 2\tilde{u}_\ell\hat{A}_{m,22} - \tilde{u}_\ell^2 \tag{7.94}$$

$$\hat{A}_{\ell,33} = 2\tilde{u}_\ell\hat{A}_{m,23}. \tag{7.95}$$

By the liquid mass equation (7.63), the Roe momentum equation now reduces to

$$\tilde{u}_\ell^2\left(m_\ell^{\mathrm{R}} - m_\ell^{\mathrm{L}}\right) - 2\tilde{u}_\ell\left(m_\ell^{\mathrm{R}}u_\ell^{\mathrm{R}} - m_\ell^{\mathrm{L}}u_\ell^{\mathrm{L}}\right) + (m_\ell u_\ell^2)^{\mathrm{R}} - (m_\ell u_\ell^2)^{\mathrm{L}} = 0, \tag{7.96}$$

with corresponding solution

$$\tilde{u}_\ell = \frac{\sqrt{m_\ell^{\mathrm{L}}}u_\ell^{\mathrm{L}} + \sqrt{m_\ell^{\mathrm{R}}}u_\ell^{\mathrm{R}}}{\sqrt{m_\ell^{\mathrm{L}}} + \sqrt{m_\ell^{\mathrm{R}}}}. \tag{7.97}$$

In summary, a Roe average $\hat{\boldsymbol{A}}_\ell$ for the liquid momentum convection submatrix (7.86) is obtained as follows; the 'hat' averages of (7.89)–(7.91) are the simple arithmetic averages (7.66)–(7.69), whereas the 'tilde'-averaged liquid velocity $\tilde{u}_\ell$ of (7.89)–(7.91) is given by (7.97).

Pressure terms

We here seek the Roe submatrix

$$\hat{\boldsymbol{A}}_p = \begin{bmatrix} 0 & 0 & 0 \\ 0 & 0 & 0 \\ \hat{\kappa}\hat{\rho}_\ell & \hat{\kappa}\hat{\rho}_\mathrm{g} & 0 \end{bmatrix} \tag{7.98}$$

corresponding to the flux vector

$$\boldsymbol{f}_p = \begin{bmatrix} 0 \\ 0 \\ p \end{bmatrix}. \tag{7.99}$$

Writing (7.31) as

$$\hat{\kappa} = \left(\widehat{\partial_p \rho_\mathrm{g}}\hat{\rho}_\ell\hat{\alpha}_\mathrm{g} + \widehat{\partial_p \rho_\ell}\hat{\rho}_\mathrm{g}\hat{\alpha}_\ell\right)^{-1}, \tag{7.100}$$

we obtain the equation

$$\frac{\hat{\rho}_\ell\left(m_\mathrm{g}^\mathrm{R} - m_\mathrm{g}^\mathrm{L}\right) + \hat{\rho}_\mathrm{g}\left(m_\ell^\mathrm{R} - m_\ell^\mathrm{L}\right)}{\widehat{\partial_p \rho_\mathrm{g}}\hat{\rho}_\ell\hat{\alpha}_\mathrm{g} + \widehat{\partial_p \rho_\ell}\hat{\rho}_\mathrm{g}\hat{\alpha}_\ell} = p^\mathrm{R} - p^\mathrm{L} \tag{7.101}$$

by the Roe condition R1.

The averages $\widehat{\partial_p \rho_k}$ indirectly involve the thermodynamic closure law, which, as previously discussed, may not be available in algebraic form. We hence suggest to apply Strategy 3 for the Roe-averaging of these terms. Taking advantage of the fact that we assume density models of the form (7.7), we suggest approximating these compressibility terms as

$$\widehat{\partial_p \rho_k} = \begin{cases} \dfrac{\rho_k^\mathrm{R} - \rho_k^\mathrm{L}}{p^\mathrm{R} - p^\mathrm{L}} & \text{for } p^\mathrm{L} \neq p^\mathrm{R} \\ \left(\partial_p \rho_k\right)^\mathrm{L} & \text{otherwise.} \end{cases} \tag{7.102}$$

Substituting (7.102) in (7.101) we obtain

$$\hat{\rho}_\ell\left(m_\mathrm{g}^\mathrm{R} - m_\mathrm{g}^\mathrm{L}\right) + \hat{\rho}_\mathrm{g}\left(m_\ell^\mathrm{R} - m_\ell^\mathrm{L}\right) = \hat{\rho}_\mathrm{g}\hat{\alpha}_\ell\left(\rho_\ell^\mathrm{R} - \rho_\ell^\mathrm{L}\right) + \hat{\rho}_\ell\hat{\alpha}_\mathrm{g}\left(\rho_\mathrm{g}^\mathrm{R} - \rho_\mathrm{g}^\mathrm{L}\right), \tag{7.103}$$

which is satisfied by the arithmetic averages

$$\hat{\alpha}_\ell = \frac{1}{2}(\alpha_\ell^\mathrm{L} + \alpha_\ell^\mathrm{R}) \tag{7.104}$$

$$\hat{\alpha}_\mathrm{g} = \frac{1}{2}(\alpha_\mathrm{g}^\mathrm{L} + \alpha_\mathrm{g}^\mathrm{R}) \tag{7.105}$$

$$\hat{\rho}_\mathrm{g} = \frac{1}{2}(\rho_\mathrm{g}^\mathrm{L} + \rho_\mathrm{g}^\mathrm{R}) \tag{7.106}$$

$$\hat{\rho}_\ell = \frac{1}{2}(\rho_\ell^\mathrm{L} + \rho_\ell^\mathrm{R}), \tag{7.107}$$

where we have used that

$$m_k = \rho_k \alpha_k. \tag{7.108}$$

The slip relation

We now aim to obtain Roe averages $(\hat{\mu}_\mathrm{g}, \hat{\mu}_\ell, \hat{\mu}_\mathrm{v})$ valid for *general* hydrodynamic closure laws $\Phi(m_\mathrm{g}, m_\ell, u_\mathrm{g})$. Remark 3 consequently suggests that we should apply Strategy 3 to obtain these averages.

As noted in Section 7.3.2, the condition R1 dictates that the averages must satisfy

$$\hat{\mu}_\mathrm{g}\left(m_\mathrm{g}^\mathrm{R} - m_\mathrm{g}^\mathrm{L}\right) + \hat{\mu}_\ell\left(m_\ell^\mathrm{R} - m_\ell^\mathrm{L}\right) + \hat{\mu}_\mathrm{v}\left(u_\mathrm{g}^\mathrm{R} - u_\mathrm{g}^\mathrm{L}\right) = \Phi^\mathrm{R} - \Phi^\mathrm{L}. \tag{7.109}$$

Application of Strategy 3 directly yields

$$\hat{\mu}_\mathrm{g} = \begin{cases} \dfrac{\Phi(m_\mathrm{g}^\mathrm{R}, m_\ell^\mathrm{L}, u_\mathrm{g}^\mathrm{L}) - \Phi(m_\mathrm{g}^\mathrm{L}, m_\ell^\mathrm{L}, u_\mathrm{g}^\mathrm{L})}{m_\mathrm{g}^\mathrm{R} - m_\mathrm{g}^\mathrm{L}} & \text{for } m_\mathrm{g}^\mathrm{L} \neq m_\mathrm{g}^\mathrm{R} \\ \mu_\mathrm{g}(m_\mathrm{g}^\mathrm{L}, m_\ell^\mathrm{L}, u_\mathrm{g}^\mathrm{L}) & \text{otherwise} \end{cases} \tag{7.110}$$

$$\hat{\mu}_\ell = \begin{cases} \dfrac{\Phi(m_\mathrm{g}^\mathrm{R}, m_\ell^\mathrm{R}, u_\mathrm{g}^\mathrm{L}) - \Phi(m_\mathrm{g}^\mathrm{R}, m_\ell^\mathrm{L}, u_\mathrm{g}^\mathrm{L})}{m_\ell^\mathrm{R} - m_\ell^\mathrm{L}} & \text{for } m_\ell^\mathrm{L} \neq m_\ell^\mathrm{R} \\ \mu_\ell(m_\mathrm{g}^\mathrm{R}, m_\ell^\mathrm{L}, u_\mathrm{g}^\mathrm{L}) & \text{otherwise} \end{cases} \tag{7.111}$$

$$\hat{\mu}_\mathrm{v} = \begin{cases} \dfrac{\Phi(m_\mathrm{g}^\mathrm{R}, m_\ell^\mathrm{R}, u_\mathrm{g}^\mathrm{R}) - \Phi(m_\mathrm{g}^\mathrm{R}, m_\ell^\mathrm{R}, u_\mathrm{g}^\mathrm{L})}{u_\mathrm{g}^\mathrm{R} - u_\mathrm{g}^\mathrm{L}} & \text{for } u_\mathrm{g}^\mathrm{L} \neq u_\mathrm{g}^\mathrm{R} \\ \mu_\mathrm{v}(m_\mathrm{g}^\mathrm{R}, m_\ell^\mathrm{R}, u_\mathrm{g}^\mathrm{L}) & \text{otherwise.} \end{cases} \tag{7.112}$$

7.3.3 The Zuber–Findlay law

Although the averages derived in Section 7.3.2 are valid for general formulations of the hydrodynamic closure law, they may not always be optimal in terms of computational efficiency, as noted in Remark 3.

In this section, we derive explicit averages for the special case of the Zuber–Findlay slip relation (Zuber and Findlay, 1965)

$$u_\mathrm{g} = K(\alpha_\mathrm{g} u_\mathrm{g} + \alpha_\ell u_\ell) + S, \tag{7.113}$$

which may be equivalently expressed as

$$\Phi = \frac{(K-1)u_\mathrm{g} + S}{K\alpha_\ell}. \tag{7.114}$$

The slip derivatives for this particular relation are found to be

$$\mu_{\mathrm{v}} = \frac{K-1}{K\alpha_\ell} \tag{7.115}$$

$$\mu_{\mathrm{g}} = (u_{\mathrm{g}} - u_\ell)\kappa\frac{\partial \rho_\ell}{\partial p} \tag{7.116}$$

$$\mu_\ell = -(u_{\mathrm{g}} - u_\ell)\kappa\frac{\alpha_{\mathrm{g}}}{\alpha_\ell}\frac{\partial \rho_{\mathrm{g}}}{\partial p}. \tag{7.117}$$

Roe-averages for these slip derivatives are now found by applying Strategy 1 to the requirement (7.109), as described below.

A splitting of the slip relation

We first note that Φ can be written as

$$\Phi = f(u_{\mathrm{g}}) \cdot g(\alpha_\ell), \tag{7.118}$$

where

$$f(u_{\mathrm{g}}) = (K-1)u_{\mathrm{g}} + S \tag{7.119}$$

and

$$g(\alpha_\ell) = (K\alpha_\ell)^{-1}. \tag{7.120}$$

By (7.44) and (7.118) we obtain

$$\begin{aligned}\Phi^{\mathrm{R}} - \Phi^{\mathrm{L}} = \frac{1}{2}\left(f(u_{\mathrm{g}}^{\mathrm{L}}) + f(u_{\mathrm{g}}^{\mathrm{R}})\right)\left(g(\alpha_\ell^{\mathrm{R}}) - g(\alpha_\ell^{\mathrm{L}})\right) \\ + \frac{1}{2}\left(g(\alpha_\ell^{\mathrm{L}}) + g(\alpha_\ell^{\mathrm{R}})\right)\left(f(u_{\mathrm{g}}^{\mathrm{R}}) - f(u_{\mathrm{g}}^{\mathrm{L}})\right),\end{aligned} \tag{7.121}$$

which suggests a natural splitting of (7.109) into two separate equations:

$$\hat{\mu}_{\mathrm{g}}(m_{\mathrm{g}}^{\mathrm{R}} - m_{\mathrm{g}}^{\mathrm{L}}) + \hat{\mu}_\ell(m_\ell^{\mathrm{R}} - m_\ell^{\mathrm{L}}) = \frac{1}{2}\left(f(u_{\mathrm{g}}^{\mathrm{L}}) + f(u_{\mathrm{g}}^{\mathrm{R}})\right)\left(g(\alpha_\ell^{\mathrm{R}}) - g(\alpha_\ell^{\mathrm{L}})\right) \tag{7.122}$$

and

$$\hat{\mu}_{\mathrm{v}}(u_{\mathrm{g}}^{\mathrm{R}} - u_{\mathrm{g}}^{\mathrm{L}}) = \frac{1}{2}\left(g(\alpha_\ell^{\mathrm{L}}) + g(\alpha_\ell^{\mathrm{R}})\right)\left(f(u_{\mathrm{g}}^{\mathrm{R}}) - f(u_{\mathrm{g}}^{\mathrm{L}})\right). \tag{7.123}$$

The velocity slip derivative

We now express the Roe-average of (7.115) as

$$\hat{\mu}_{\mathrm{v}} = \frac{K-1}{K\tilde{\alpha}_\ell}. \tag{7.124}$$

By (7.119) and (7.120), (7.123) then becomes

$$\frac{K-1}{K\tilde{\alpha}_\ell} = \frac{K-1}{2K}\left(\frac{1}{\alpha_\ell^{\mathrm{L}}} + \frac{1}{\alpha_\ell^{\mathrm{R}}}\right), \tag{7.125}$$

which yields $\tilde{\alpha}_\ell(\alpha_\ell^{\mathrm{L}}, \alpha_\ell{}^{\mathrm{R}})$ as the *harmonic mean*:

$$\tilde{\alpha}_\ell = 2\frac{\alpha_\ell^{\mathrm{L}}\alpha_\ell^{\mathrm{R}}}{\alpha_\ell^{\mathrm{L}} + \alpha_\ell^{\mathrm{R}}}. \tag{7.126}$$

The mass slip derivatives

We write the Roe-averages of (7.116) and (7.117) as

$$\hat{\mu}_{\mathrm{g}} = \hat{\Phi}\hat{\kappa}\widehat{\partial_p \rho_\ell} \tag{7.127}$$

and

$$\hat{\mu}_\ell = -\hat{\Phi}\hat{\kappa}\frac{\hat{\alpha}_{\mathrm{g}}}{\hat{\alpha}_\ell}\widehat{\partial_p \rho_{\mathrm{g}}}. \tag{7.128}$$

By writing

$$\hat{\Phi} = \frac{(K-1)\hat{u}_{\mathrm{g}} + S}{K\tilde{\alpha}_\ell}, \tag{7.129}$$

where

$$\hat{u}_{\mathrm{g}} = \frac{1}{2}(u_{\mathrm{g}}^{\mathrm{L}} + u_{\mathrm{g}}^{\mathrm{R}}) \tag{7.130}$$

$$\tilde{\alpha}_\ell = 2\frac{\alpha_\ell^{\mathrm{L}}\alpha_\ell^{\mathrm{R}}}{\alpha_\ell^{\mathrm{L}} + \alpha_\ell^{\mathrm{R}}}, \tag{7.131}$$

(7.122) can, by use of (7.45), be rewritten as

$$-\hat{\Phi}\frac{\alpha_\ell^{\mathrm{R}} - \alpha_\ell^{\mathrm{L}}}{\hat{\alpha}_\ell} = \hat{\Phi}\hat{\kappa}\widehat{\partial_p \rho_\ell}(m_{\mathrm{g}}^{\mathrm{R}} - m_{\mathrm{g}}^{\mathrm{L}}) - \hat{\Phi}\hat{\kappa}\frac{\hat{\alpha}_{\mathrm{g}}}{\hat{\alpha}_\ell}\widehat{\partial_p \rho_{\mathrm{g}}}(m_\ell^{\mathrm{R}} - m_\ell^{\mathrm{L}}), \tag{7.132}$$

where we define

$$\hat{\alpha}_k = \frac{1}{2}(\alpha_k^{\mathrm{L}} + \alpha_k^{\mathrm{R}}). \tag{7.133}$$

We now observe that the averages $\hat{\kappa}$ and $\widehat{\partial_p \rho_k}$, obtained in Section 7.3.2, do in fact also satisfy (7.132); together with (7.129) they yield valid Roe averages (7.127) and (7.128).

7.3.4 The Roe matrix

The preceeding analysis of Sections 7.3.2–7.3.3 may be summed up by the following Proposition:

Proposition 1 *The matrix*

$$\hat{\boldsymbol{A}}(\boldsymbol{q}^{\mathrm{L}},\boldsymbol{q}^{\mathrm{R}}) = \frac{1}{\hat{\varrho}}\begin{bmatrix} \hat{m}_g\hat{m}_\ell\hat{\mu}_g + \hat{\zeta}\hat{m}_\ell\hat{u}_g & \hat{m}_g\hat{m}_\ell\hat{\mu}_\ell - \hat{m}_g\hat{u}_\ell & \hat{m}_g \\ -(\hat{m}_g\hat{m}_\ell\hat{\mu}_g + \hat{\zeta}\hat{m}_\ell\hat{u}_g) & \hat{m}_g\hat{u}_\ell - \hat{m}_g\hat{m}_\ell\hat{\mu}_\ell & \hat{\zeta}\hat{m}_\ell \\ \hat{a}_{31} & \hat{a}_{32} & 2(\hat{m}_g\tilde{u}_g + \hat{\zeta}\hat{m}_\ell\tilde{u}_\ell) \end{bmatrix}, \tag{7.134}$$

where

$$\hat{a}_{31} = \hat{\kappa}\hat{\varrho}\hat{\rho}_\ell + 2\hat{m}_g\hat{m}_\ell\tilde{u}_g\hat{\mu}_g + 2\hat{\zeta}\hat{m}_\ell\hat{u}_g\tilde{u}_g - \hat{\varrho}\tilde{u}_g^2 - 2\hat{m}_g\hat{m}_\ell\tilde{u}_\ell\hat{\mu}_g - 2\hat{\zeta}\hat{m}_\ell\hat{u}_g\tilde{u}_\ell, \tag{7.135}$$

$$\hat{a}_{32} = \hat{\kappa}\hat{\varrho}\hat{\rho}_g + 2\hat{m}_g\hat{m}_\ell\tilde{u}_g\hat{\mu}_\ell - 2\hat{m}_g\tilde{u}_g\hat{u}_\ell + 2\hat{m}_g\tilde{u}_\ell\hat{u}_\ell - 2\hat{m}_g\hat{m}_\ell\tilde{u}_\ell\hat{\mu}_\ell - \hat{\varrho}\tilde{u}_\ell^2 \tag{7.136}$$

and

$$\hat{\varrho} = \hat{m}_g + \hat{\zeta}\hat{m}_\ell, \tag{7.137}$$

obtained by the ***arithmetic*** *averages*

$$\hat{m}_g = \frac{1}{2}\left(m_g^{\mathrm{L}} + m_g^{\mathrm{R}}\right) \tag{7.138}$$

$$\hat{m}_\ell = \frac{1}{2}\left(m_\ell^{\mathrm{L}} + m_\ell^{\mathrm{R}}\right) \tag{7.139}$$

$$\hat{u}_g = \frac{1}{2}\left(u_g^{\mathrm{L}} + u_g^{\mathrm{R}}\right) \tag{7.140}$$

$$\hat{u}_\ell = \frac{1}{2}\left(u_\ell^{\mathrm{L}} + u_\ell^{\mathrm{R}}\right) \tag{7.141}$$

$$\hat{\rho}_g = \frac{1}{2}\left(\rho_g^{\mathrm{L}} + \rho_g^{\mathrm{R}}\right) \tag{7.142}$$

$$\hat{\rho}_\ell = \frac{1}{2}\left(\rho_\ell^{\mathrm{L}} + \rho_\ell^{\mathrm{R}}\right), \tag{7.143}$$

as well as the Roe-type averages

$$\tilde{u}_g = \frac{\sqrt{m_g^{\mathrm{L}}}u_g^{\mathrm{L}} + \sqrt{m_g^{\mathrm{R}}}u_g^{\mathrm{R}}}{\sqrt{m_g^{\mathrm{L}}} + \sqrt{m_g^{\mathrm{R}}}} \tag{7.144}$$

$$\tilde{u}_\ell = \frac{\sqrt{m_\ell^{\mathrm{L}}}u_\ell^{\mathrm{L}} + \sqrt{m_\ell^{\mathrm{R}}}u_\ell^{\mathrm{R}}}{\sqrt{m_\ell^{\mathrm{L}}} + \sqrt{m_\ell^{\mathrm{R}}}}, \tag{7.145}$$

and where $\hat{\kappa}$ is obtained as described in Section 7.3.2, satisfies the Roe conditions R1 and R3 for the drift-flux model described in Section 7.2, provided that the Roe-averaged slip derivatives $\hat{\mu}_g$, $\hat{\mu}_\ell$ and $\hat{\mu}_{\mathrm{v}} \equiv 1 - \hat{\zeta}$ satisfy

$$\hat{\mu}_g\left(m_g^{\mathrm{R}} - m_g^{\mathrm{L}}\right) + \hat{\mu}_\ell\left(m_\ell^{\mathrm{R}} - m_\ell^{\mathrm{L}}\right) + \hat{\mu}_{\mathrm{v}}\left(u_g^{\mathrm{R}} - u_g^{\mathrm{L}}\right) = \Phi^{\mathrm{R}} - \Phi^{\mathrm{L}}. \tag{7.146}$$

□

Furthermore, following the discussions of Sections 7.3.2 and 7.3.3, we make the following definitions:

Definition 1 The matrix $\hat{\boldsymbol{A}}$ described by Proposition 1, used in conjunction with the averages $\hat{\mu}_{\mathrm{g}}$, $\hat{\mu}_\ell$ and $\hat{\mu}_{\mathrm{v}}$ described by (7.110)–(7.112), satisfies the Roe conditions R1 and R3 for the drift-flux model supplied with a general, sufficiently smooth slip relation Φ. The Roe scheme obtained by solving the linearized Riemann problem defined by this matrix $\hat{\boldsymbol{A}}$ will in the following be termed the **RoeGen** scheme. □

Definition 2 The matrix $\hat{\boldsymbol{A}}$ described by Proposition 1, used in conjunction with the averages $\hat{\mu}_{\mathrm{g}}$, $\hat{\mu}_\ell$ and $\hat{\mu}_{\mathrm{v}}$ described in Section 7.3.3, satisfies the Roe conditions R1 and R3 for the drift-flux model supplied with a Zuber–Findlay type slip relation Φ, as expressed by (7.114). The Roe scheme obtained by solving the linearized Riemann problem defined by this matrix $\hat{\boldsymbol{A}}$ will in the following be termed the **RoeZF** scheme. □

Remark 7 We have not been able to obtain explicit conditions under which RoeGen and RoeZF satisfy the condition R2. In fact, this condition is non-trivial for the given drift-flux model for the following reasons:

– The eigenstructure, and hence the hyperbolicity, of the model itself is sensitive to the choice of closure laws. Even the rather simple Zuber–Findlay law (7.11) leads to highly complex expressions for the eigenvalues, and only conditional hyperbolicity (Benzoni-Gavage, 1991).

– As noted by Baudin *et al.* (2005a), the system cannot be provided with an entropy pair except for highly restrictive choices of Φ. Hence the approach of Harten and Lax, discussed in Remark 2, will not work in this case.

However, the numerical evidence indicates that if $\boldsymbol{q}^{\mathrm{L}}$ and $\boldsymbol{q}^{\mathrm{R}}$ are in the hyperbolic region of the model, the RoeGen and RoeZF solvers tend to produce real eigenvalues and a hyperbolic linearization. No instance of complex eigenvalues, i.e. violation of R2, occurred for any calculations performed in the preparation of this chapter. Approximate eigenvalues of the model can be found in Appendix B. □

7.4 Numerical algorithm

The present section provides a brief overview of the employed numerical algorithm, which is based on the wave-propagation (flux-difference splitting) form of Godunov's method presented by LeVeque (2002, Chapter 15). We start by giving a description of the general numerical method, and proceed with an explanation of how it relates to the Roe scheme.

7.4.1 Framework

A 'high-resolution' extension of Godunov's method can be written as

$$\boldsymbol{Q}_i^{n+1} = \boldsymbol{Q}_i^n - \frac{\Delta t}{\Delta x}\left(\mathcal{A}^-\Delta\boldsymbol{Q}_{i+1/2} + \mathcal{A}^+\Delta\boldsymbol{Q}_{i-1/2}\right) - \frac{\Delta t}{\Delta x}\left(\tilde{\boldsymbol{F}}_{i+1/2} - \tilde{\boldsymbol{F}}_{i-1/2}\right), \quad (7.147)$$

where $\boldsymbol{Q}_i^n$ denotes the numerical approximation to the cell average of the vector of unknowns $\boldsymbol{q}(x(i), t_n)$, that is, in control volume i at time step n. Quantities without a time index are evaluated at time step n. The symbol $\mathcal{A}^-\Delta\boldsymbol{Q}_{i+1/2}$ denotes the net effect of all left-going waves at $x_{i+1/2}$, that is, at the control-volume boundary midway between x_i and x_{i+1}, while $\mathcal{A}^+\Delta\boldsymbol{Q}_{i-1/2}$ measures the net effect of all right-going waves at $x_{i-1/2}$. The waves and wave speeds from the approximate Riemann solution are used to define

$$\begin{aligned} \mathcal{A}^-\Delta\boldsymbol{Q}_{i-1/2} &= \sum_{p=1}^{m} (s_{i-1/2}^p)^- \mathcal{W}_{i-1/2}^p, \\ \mathcal{A}^+\Delta\boldsymbol{Q}_{i-1/2} &= \sum_{p=1}^{m} (s_{i-1/2}^p)^+ \mathcal{W}_{i-1/2}^p, \end{aligned} \quad (7.148)$$

where $\mathcal{W}^p_{i-1/2}$ is the pth wave arising in the solution to the Riemann problem at $x_{i-1/2}$, that is, it is a vector with one component for each equation. m is the number of waves, and since we will be using a linearized Riemann solver, it is equal to the number of equations. $s^p_{i-1/2}$ is the wave speed of the pth wave and

$$(s^p_{i-1/2})^+ = \max(s^p_{i-1/2}, 0), \qquad (s^p_{i-1/2})^- = \min(s^p_{i-1/2}, 0). \tag{7.149}$$

The flux vector $\tilde{\boldsymbol{F}}_{i-1/2}$ is the higher-order correction. It is given by

$$\tilde{\boldsymbol{F}}_{i-1/2} = \frac{1}{2}\sum_{p=1}^{m} |s^p_{i-1/2}| \left(1 - \frac{\Delta t}{\Delta x}|s^p_{i-1/2}|\right) \widetilde{\mathcal{W}}^p_{i-1/2}, \tag{7.150}$$

where $\widetilde{\mathcal{W}}^p_{i-1/2}$ is a limited version of the wave $\mathcal{W}^p_{i-1/2}$. With the correction terms, the method approaches second order for smooth solutions.

In the present work, we have taken account of source terms by adding the term $\Delta t \boldsymbol{S}_i$ to the right-hand side of (7.147).

7.4.2 Considerations for the Roe solver

As noted in Section 7.3, the Roe scheme defines an approximate Riemann solution by replacing the nonlinear problem

$$\frac{\partial \boldsymbol{q}}{\partial t} + \frac{\partial}{\partial x}\boldsymbol{f}(\boldsymbol{q}) = \boldsymbol{0} \tag{7.151}$$

by a linearized problem defined locally at each cell interface;

$$\frac{\partial \hat{\boldsymbol{q}}}{\partial t} + \hat{\boldsymbol{A}}_{i-1/2}\frac{\partial \hat{\boldsymbol{q}}}{\partial x} = \boldsymbol{0}. \tag{7.152}$$

For the Roe solver, we have the interpretation that

$$\mathcal{A}^{\pm}\Delta \boldsymbol{Q}_{i-1/2} = \hat{\boldsymbol{A}}^{\pm}_{i-1/2}(\boldsymbol{Q}_i - \boldsymbol{Q}_{i-1}). \tag{7.153}$$

Herein,

$$\hat{\boldsymbol{A}}^{\pm}_{i-1/2} = \hat{\boldsymbol{R}}_{i-1/2}\hat{\Lambda}^{\pm}_{i-1/2}\hat{\boldsymbol{R}}^{-1}_{i-1/2}, \tag{7.154}$$

where $\hat{\boldsymbol{R}}_{i-1/2}$ is the matrix having the right eigenvectors $\hat{\boldsymbol{r}}_{i-1/2}$ of $\hat{\boldsymbol{A}}_{i-1/2}$ as its columns, and $\hat{\Lambda}^+_{i-1/2}$ and $\hat{\Lambda}^-_{i-1/2}$ are the diagonal matrices containing the positive and negative eigenvalues, respectively, of $\hat{\boldsymbol{A}}_{i-1/2}$. Further, to satisfy the condition R1, we must have that

$$\hat{\boldsymbol{A}}_{i-1/2}(\boldsymbol{Q}_i - \boldsymbol{Q}_{i-1}) = \sum_{p=1}^{m} s^p_{i-1/2}\mathcal{W}^p_{i-1/2}. \tag{7.155}$$

The approximate Riemann solution consists of m waves proportional to the right eigenvectors $\hat{\boldsymbol{r}}_{i-1/2}$, propagating with speeds

$$s^p_{i-1/2} = \hat{\lambda}^p_{i-1/2} \tag{7.156}$$

given by the eigenvalues. The proportionality coefficients $\beta^p_{i-1/2}$ can be found by solving the linear system

$$\boldsymbol{Q}_i - \boldsymbol{Q}_{i-1} = \sum_{p=1}^{m} \beta^p_{i-1/2} \hat{\boldsymbol{r}}^p_{i-1/2}, \tag{7.157}$$

and $\beta^p_{i-1/2}$ can be interpreted as wave strengths (Toro, 1999, Section 2.3.3). The solution of the equation (3.66) is

$$\boldsymbol{\beta}_{i-1/2} = \hat{\boldsymbol{R}}^{-1}_{i-1/2}(\boldsymbol{Q}_i - \boldsymbol{Q}_{i-1}), \tag{7.158}$$

whence the waves can be found as

$$\mathcal{W}^p_{i-1/2} = \beta^p_{i-1/2} \hat{\boldsymbol{r}}^p_{i-1/2}. \tag{7.159}$$

Eigenstructure

As noted in Remark 7, the eigenstructure of the Roe matrix $\hat{\boldsymbol{A}}_{i-1/2}$ is quite complicated, and it is difficult to obtain analytical expressions for the eigenvalues and eigenvectors. Hence, in the present work, the eigenstructure was found numerically.

Entropy solution

For transonic rarefactions, that is, when an eigenvalue λ^p is negative to the left of the p-wave, $\mathcal{W}^p$, and positive to the right, a scheme using a linearized Riemann solver may converge to an unphysical solution, violating the entropy condition (Osher, 1984).

Several remedies are conceivable, e.g. using Harten's entropy fix (Harten, 1983). However, for the calculations presented in the following, the problem of entropy-condition violations did not occur.

7.5 Numerical simulations

In this section, we illustrate the ability of the Roe method to produce accurate and non-oscillatory results for some numerical benchmark problems, including

Table 7.1: Initial states in the pure rarefaction test problem.

Quantity	symbol (unit)	left	right
Gas volume fraction	α_g (–)	0.6	0.68
Pressure	p (MPa)	1.66667	1.17647
Gas velocity	u_g (m/s)	34.4233	50.0
Liquid velocity	u_ℓ (m/s)	34.4233	50.0

Table 7.2: Parameters employed in the pure rarefaction test problem.

	c_k (m/s)	ρ_k° (kg/m^3)
gas (g)	100	0
liquid (ℓ)	1000	998.924

non-linear slip laws and transition to near-single-phase flow. Furthermore, for the case of the Zuber–Findlay slip relation, we show that the general method for the drift-flux model derived in Section 7.3.2 and the specific method of Section 7.3.3 give identical results.

The method (7.147) can be shown to be total variation diminishing (TVD) for scalar problems under the restriction that the Courant–Friedrichs–Lewy (CFL) number be smaller than $1/2$ (LeVeque, 2002, Section 12.8). The calculations presented here were thus run using a CFL number of $1/2$.

7.5.1 Pure rarefaction

The first test case is a Riemann problem constructed by Baudin *et al.* (2005a), and whose solution is a pure rarefaction. Baudin *et al.* took the liquid to have a constant density. Here, however, both phases are treated as compressible. The considered horizontal tube is 100 m long, and there is a jump in the initial state at $x = 50$ m. The initial values are given in Table 7.1, and the equation-of-state parameters are reported in Table 7.2. Herein,

$$\rho_k^\circ \equiv c_k^{-2}(p - p_{k,0}). \tag{7.160}$$

In the present problem, the no-slip law is used, that is, $\Phi \equiv 0$. In this case, the Roe average derived for the Zuber–Findlay slip relation (Section 7.3.3), and the general Roe average (Section 7.3.2), give the same numerical scheme.

Pressure profiles at $t = 0.8$ s are presented for various grid sizes in Figure 7.1. Figure 7.1(a) shows the results obtained using the first-order scheme, that is, without the use of a limiter function, while in Figure 7.1(b), the monotonized central-difference (MC) limiter has been employed. The first-order Roe scheme

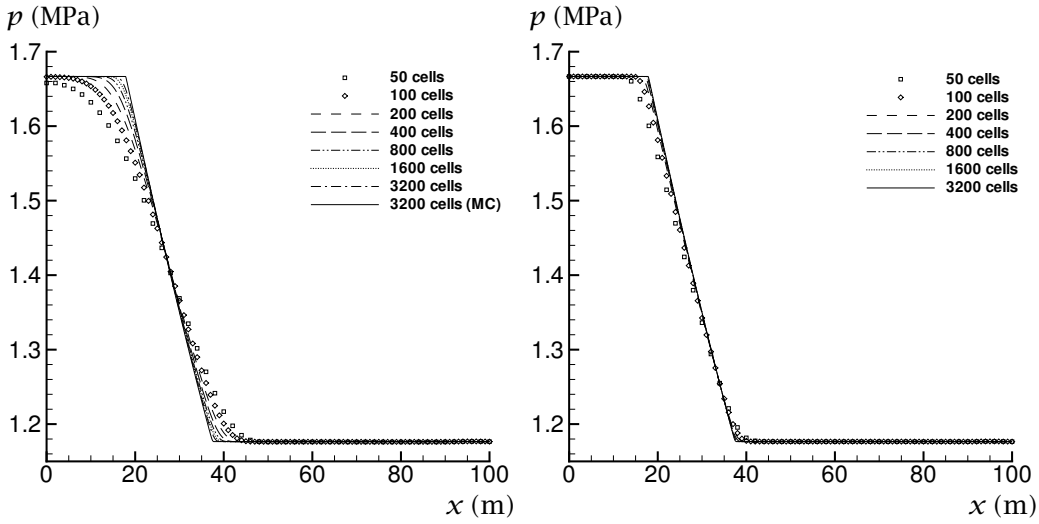

(a) No limiter (first-order) (b) MC limiter

Figure 7.1: Pressure for the pure rarefaction test problem. Convergence of the Roe method with and without a limiter function.

compares very well with the results presented in Baudin *et al.* (2005a), and it can be seen that the use of the MC limiter provides an improved resolution of the rarefaction wave. The remaining physical variables are shown in Figure 7.2.

7.5.2 Shock-tube problem 1

We next consider a shock-tube problem where the solution consists of a 1-shock, a 2-contact and a 3-shock. This case was also studied by Baudin *et al.* (2005a) for the case of constant liquid density. The initial states can be found in Table 7.3, and the equation-of-state parameters are given in Table 7.4. The slip is given by the Zuber–Findlay relation (7.11) with $K = 1.07$ and $S = 0.2162$. Therefore, we employ the Roe average derived in Section 7.3.3 (RoeZF).

The convergence of the RoeZF scheme employing the MC limiter is shown in Figure 7.3, where the results are plotted at $t = 0.5$ s. Both the shocks and the contact discontinuity are very sharply resolved.

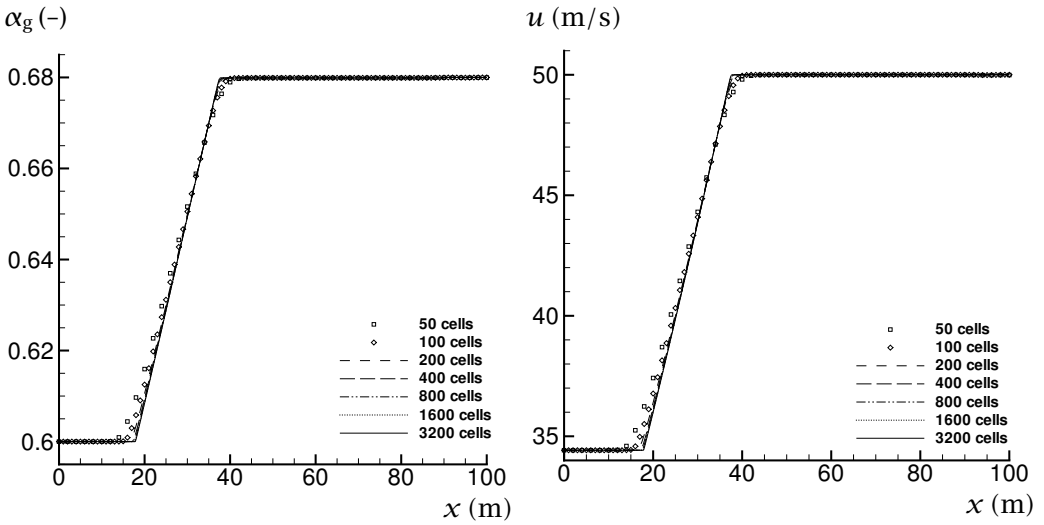

(a) Gas volume fraction (b) Velocity

Figure 7.2: Gas volume fraction and velocity for the pure rarefaction test problem. Convergence of the Roe method using the MC limiter.

Table 7.3: Initial states in the Shock Tube 1 problem.

Quantity	symbol (unit)	left	right
Gas volume fraction	α_g (-)	0.6	0.55
Pressure	p (kPa)	522.825	803.959
Gas velocity	u_g (m/s)	29.5138	2.5582
Liquid velocity	u_ℓ (m/s)	24.7741	1.7372

Table 7.4: Parameters employed in the Shock Tube 1 problem.

	c_k (m/s)	ρ_k° (kg/m^3)
gas (g)	300	0
liquid (ℓ)	1000	999.916

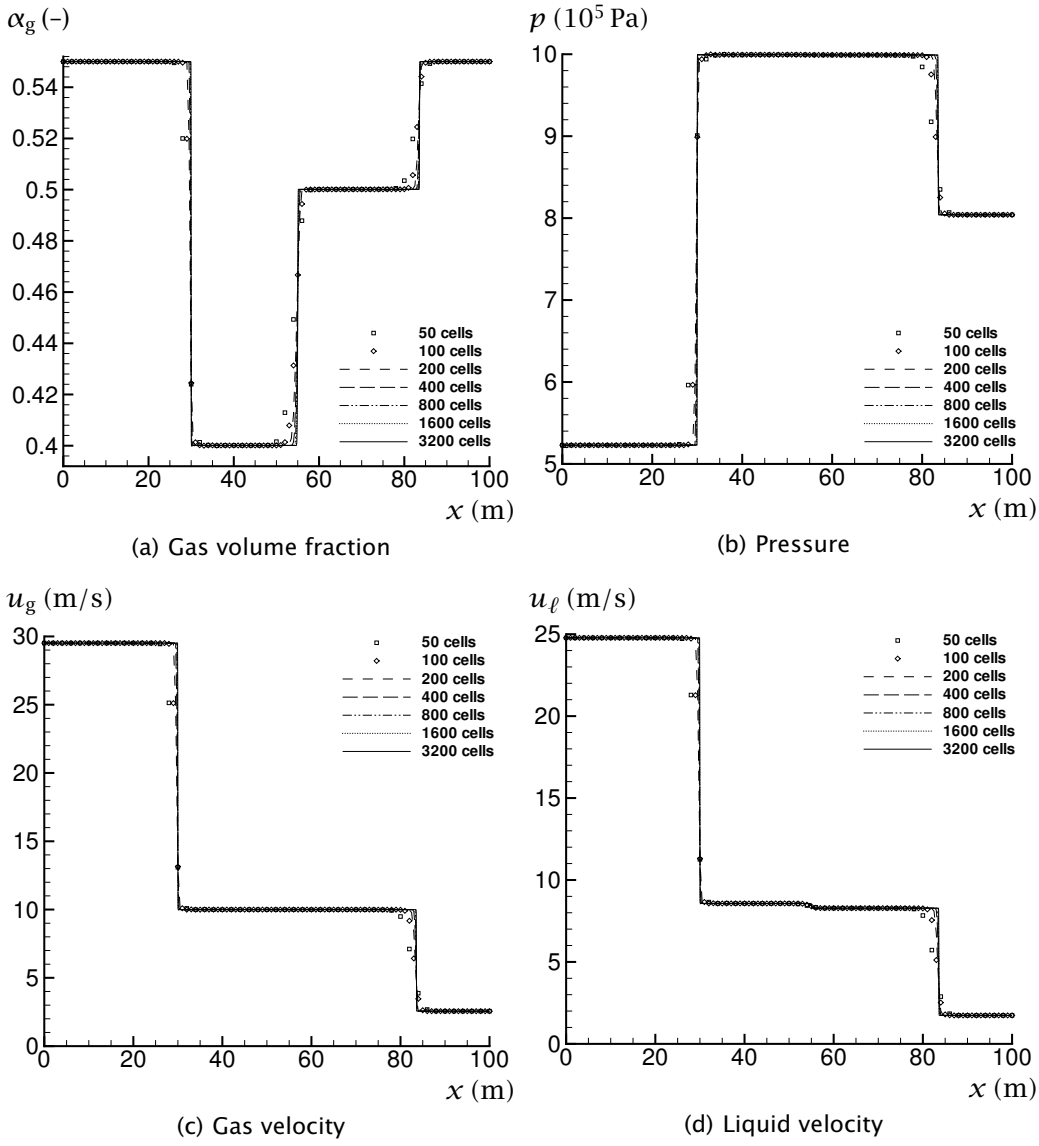

(a) Gas volume fraction

(b) Pressure

(c) Gas velocity

(d) Liquid velocity

Figure 7.3: Shock Tube 1. Convergence of the RoeZF method using the MC limiter.

Table 7.5: Initial states in the Shock Tube 2 problem.

Quantity	symbol (unit)	left	right
Gas volume fraction	α_g (–)	0.55	0.55
Pressure	p (kPa)	80.450	24.282
Gas velocity	u_g (m/s)	12.659	1.181
Liquid velocity	u_ℓ (m/s)	10.370	0.561

Table 7.6: Parameters employed in the Shock Tube 2 and pipe-flow problems.

	c_k (m/s)	ρ_k° (kg/m^3)
gas (g)	$\sqrt{10^5}$	0
liquid (ℓ)	1000	999.9

7.5.3 Shock-tube problem 2

An alternative shock-tube problem has previously been studied by Evje and Fjelde (2002) and Fjelde and Karlsen (2002), for the case of constant liquid density. The initial states are given in Table 7.5, whereas Table 7.6 shows the equation-of-state parameters. In this problem, the Zuber–Findlay slip relation (7.11) is employed with $K = 1.07$ and $S = 0.216$.

Numerical results for grid refinement are displayed in Figure 7.4 for $t = 1$ s. The solution at the shocks is non-oscillatory for all the variables, while the discontinuity is sharply resolved.

7.5.4 Comparison of RoeGen and RoeZF

In Section 7.3.3, we derived a Roe average specially for the Zuber–Findlay slip relation (RoeZF). Figure 7.5 shows numerical results for Shock Tube 1 obtained using RoeZF plotted on top of the solution calculated with the general Roe average (RoeGen) of Section 7.3.2. As can be seen, they are exactly the same.

Figure 7.6 shows a similar comparison between RoeZF and RoeGen for Shock Tube 2. Again, the results are exactly the same. This gives confidence in the applicability of RoeGen for general slip relations.

7.5.5 Pipe-flow problem

The final test simulates a practical pipe-flow problem, and includes such challenges as a more complex, non-linear slip relation and near-single-phase flow. The problem was introduced as Example 4 by Evje and Fjelde (2003).

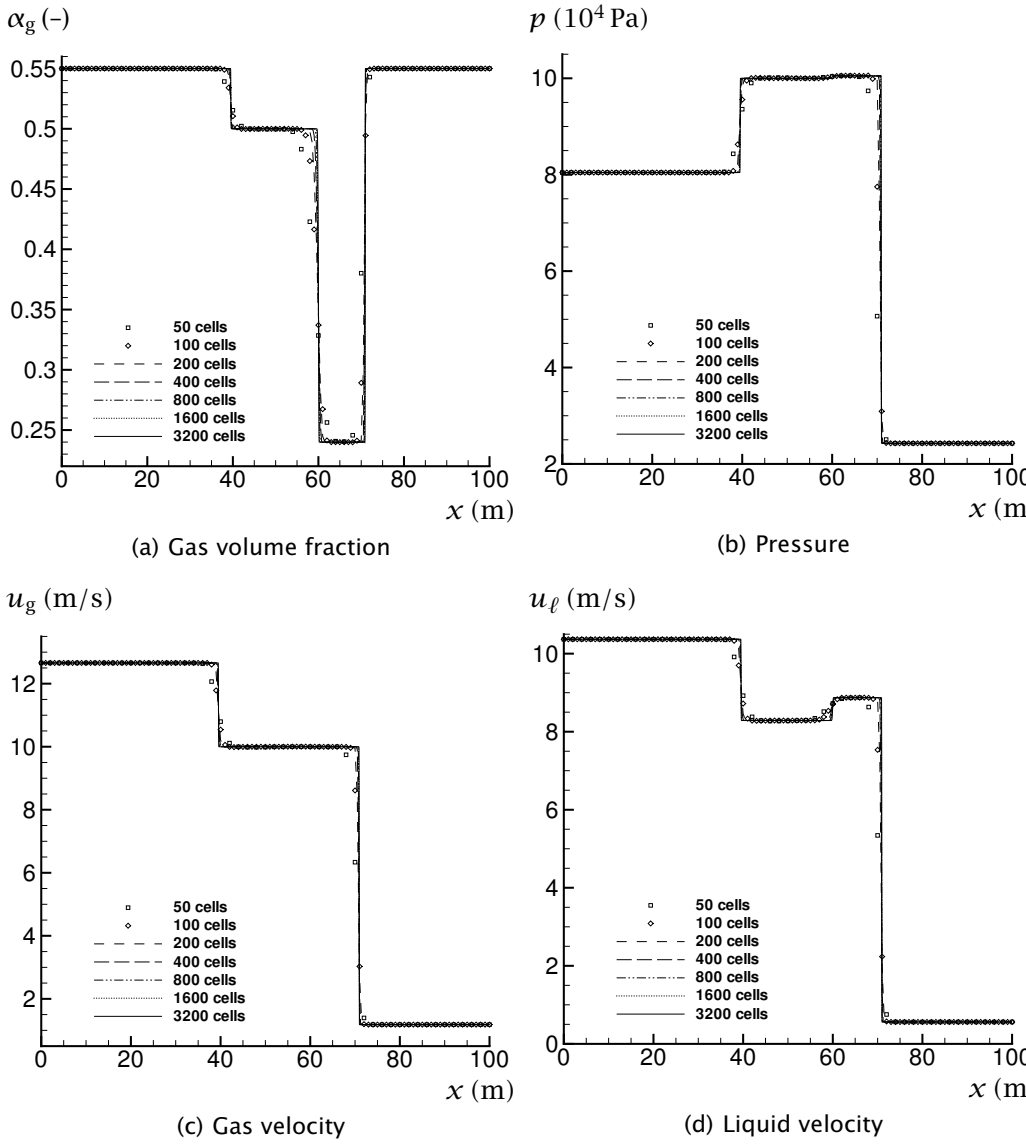

(a) Gas volume fraction

(b) Pressure

(c) Gas velocity

(d) Liquid velocity

Figure 7.4: Shock Tube 2. Convergence of the RoeZF method using the MC limiter.

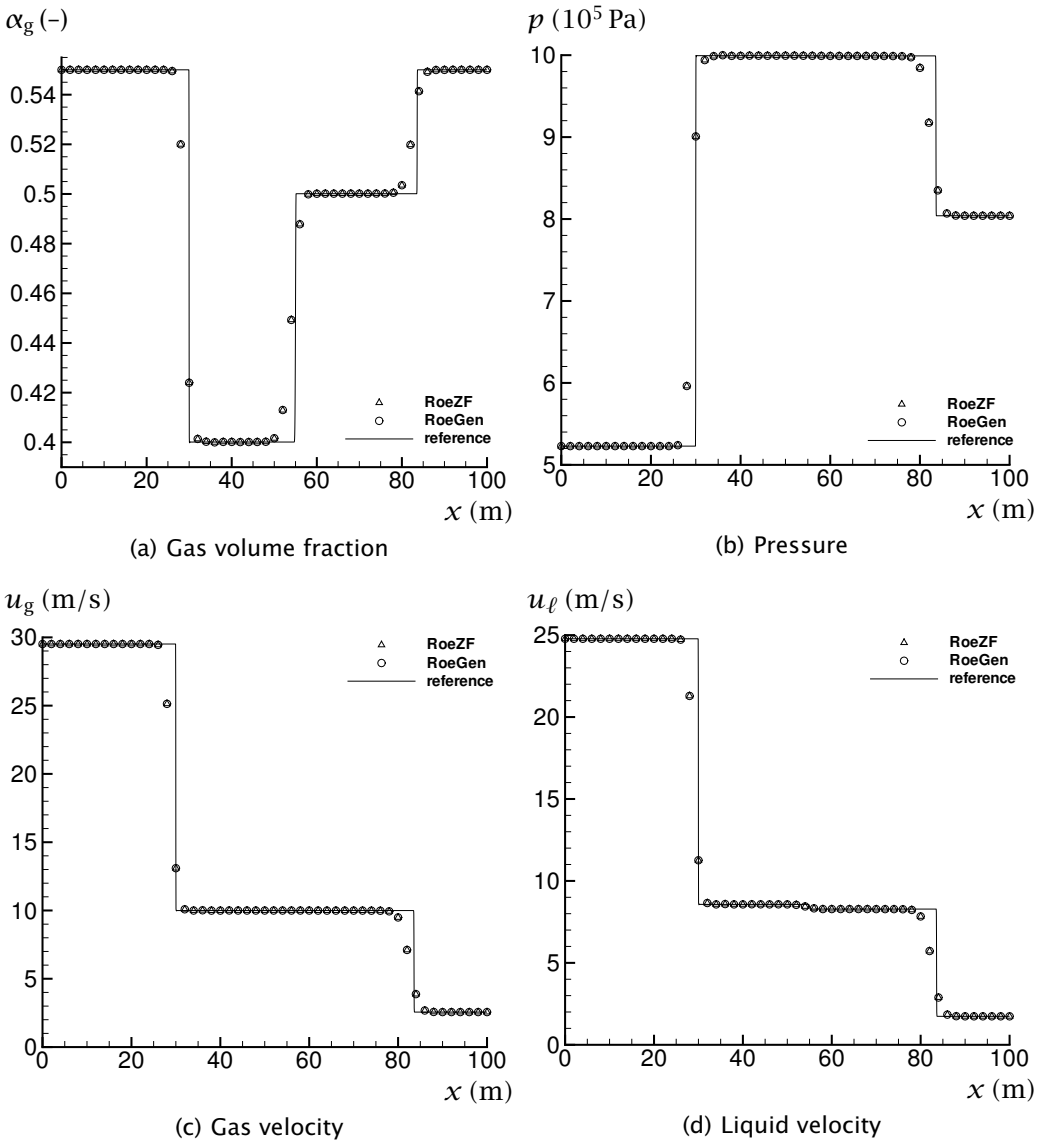

(a) Gas volume fraction

(b) Pressure

(c) Gas velocity

(d) Liquid velocity

Figure 7.5: Shock Tube 1. Comparison of the Zuber–Findlay average (RoeZF) and the general Roe-average (RoeGen) on a 50-cell grid, using the MC limiter. The 3200-cell solution is shown for reference.

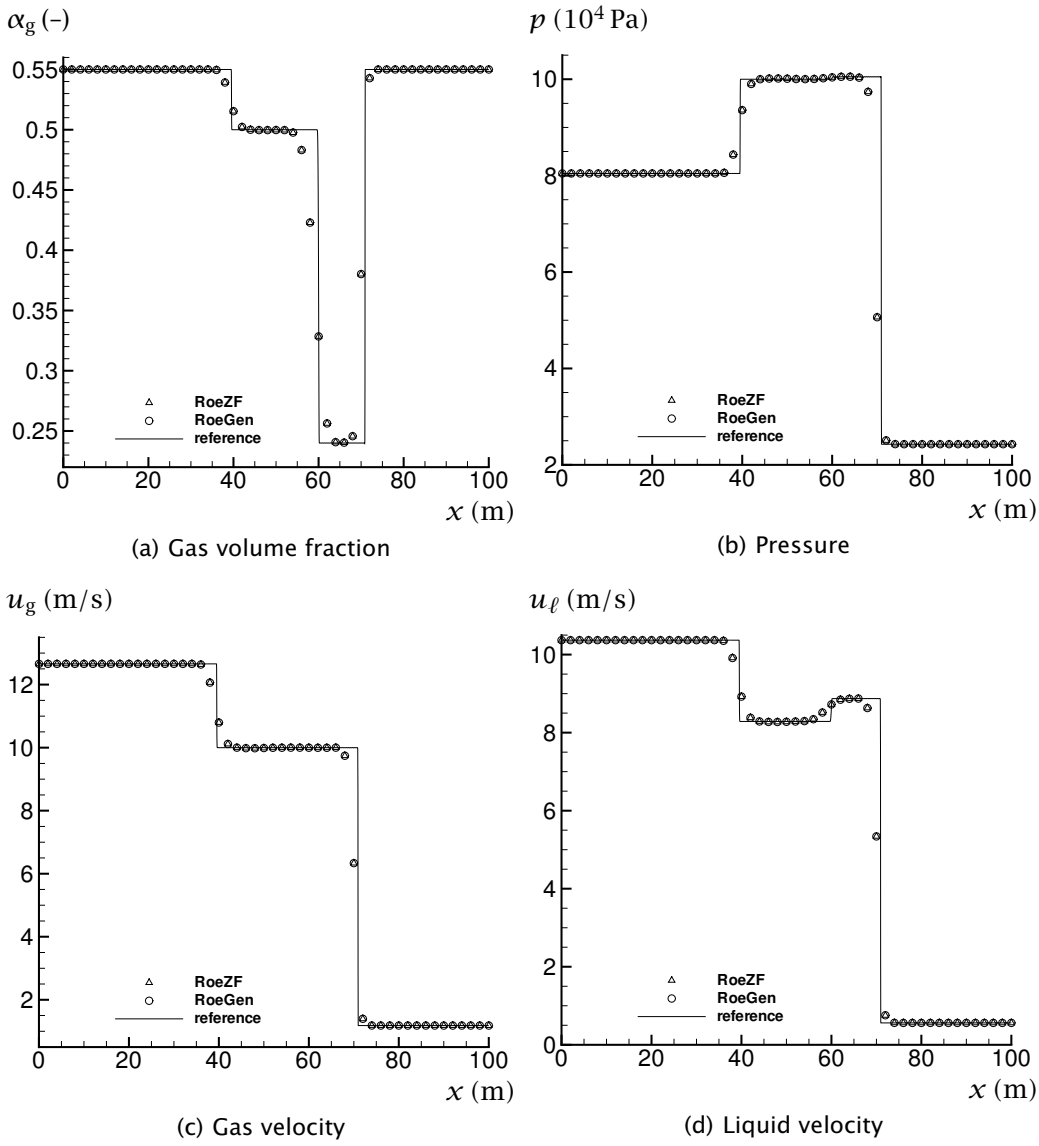

(a) Gas volume fraction

(b) Pressure

(c) Gas velocity

(d) Liquid velocity

Figure 7.6: Shock Tube 2. Comparison of the Zuber–Findlay average (RoeZF) and the general Roe-average (RoeGen) on a 50-cell grid, using the MC limiter. The 3200-cell solution is shown for reference.

The equation-of-state parameters are given by Table 7.6. In the slip relation (7.11), $K = 1$ is constant, but S is now a non-linear function of the volume fraction:

$$S = S(\alpha_g) = \frac{1}{2}\sqrt{1 - \alpha_g}. \tag{7.161}$$

Further, a wall-friction model is included:

$$F_w = \frac{32 u_m \eta_m}{d^2}, \tag{7.162}$$

where u_m is the mixture velocity,

$$u_m = \alpha_g u_g + \alpha_\ell u_\ell, \tag{7.163}$$

and the dynamic mixture viscosity, η_m, is taken to be

$$\eta_m = \alpha_g \eta_g + \alpha_\ell \eta_\ell, \tag{7.164}$$

with $\eta_g = 5 \cdot 10^{-6}\,\mathrm{Pa\,s}$ and $\eta_\ell = 5 \cdot 10^{-2}\,\mathrm{Pa\,s}$.

The problem consists of a horizontal pipe of length $l = 1000\,\mathrm{m}$ and inner diameter $d = 0.1\,\mathrm{m}$. Initially, it is filled with stagnant, almost-pure liquid, with $\alpha_g = 1 \cdot 10^{-5}$. Furthermore, the details of the simulation are specified as follows:

- The simulation lasts for 175 s.
- Between $t = 0$ and $t = 10\,\mathrm{s}$, the gas and liquid inlet mass-flow rates are linearly increased from zero to 0.08 kg/s and 12.0 kg/s, respectively.
- From $t = 10\,\mathrm{s}$ to $t = 175\,\mathrm{s}$, the inlet liquid mass-flow rate is kept constant.
- The inlet gas mass-flow rate is kept constant between $t = 10\,\mathrm{s}$ and $t = 50\,\mathrm{s}$.
- Between $t = 50\,\mathrm{s}$ and $t = 70\,\mathrm{s}$, the inlet gas mass-flow rate is linearly decreased from 0.08 kg/s to $1 \cdot 10^{-8}$ kg/s, after which it is kept constant.
- At the outlet, the pressure is kept constant at $p = 1 \cdot 10^5\,\mathrm{Pa}$.

Calculations were performed using the RoeGen method. The physical variables are plotted in Figure 7.7 for various grids. It can be observed that for the 200-cell grid, the numerical solution is already close to the one obtained on fine grids. The present results compare favourably with those presented in Evje and Fjelde (2003). Furthermore, one may note that the transition to near-single-phase flow is handled well.

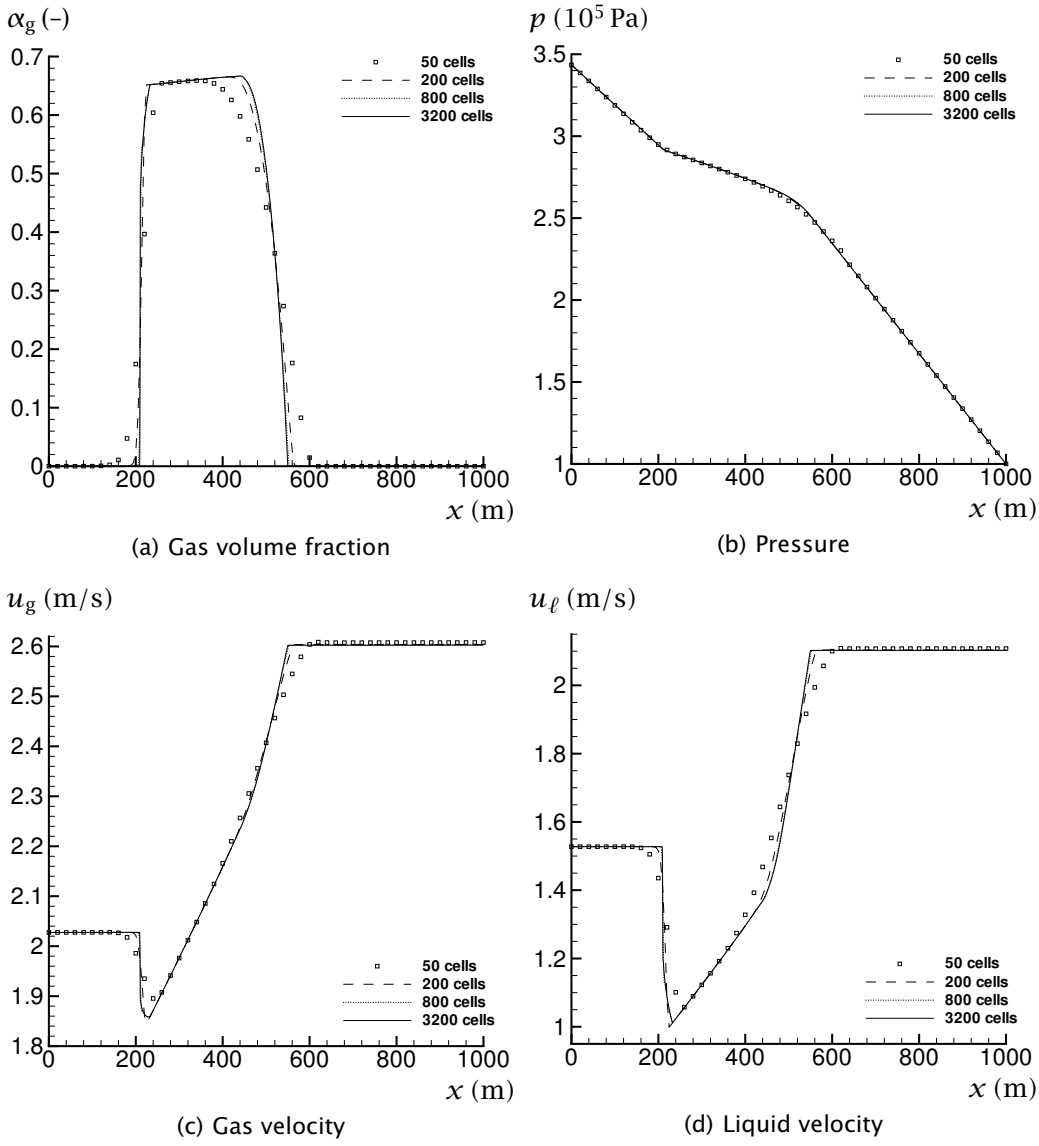

(a) Gas volume fraction

(b) Pressure

(c) Gas velocity

(d) Liquid velocity

Figure 7.7: Pipe-flow test problem. Convergence of the RoeGen method using the MC limiter.

7.6 Summary

A quasi-linear formulation of the general *drift-flux* model, describing the flow of two-phase mixtures in pipelines, has been presented. Based on this formulation, a linearized Riemann solver of the type proposed by Roe has been derived.

The complexity of the closure laws inherent in the model prevents us from using the parameter-vector strategy originally proposed by Roe. Instead, we satisfy the Roe conditions using alternative strategies, enabling us to

- split the problem into independently solvable parts;
- handle general formulations of the closure laws within a single framework.

Hence, we are able to construct a genuine Roe scheme purely by algebraic manipulation of the flux Jacobian.

Even for the most general case, our proposed linearized Riemann solver is to a large extent constructed from arithmetic averages; it is consequently relatively efficient. Numerical examples have been presented, illustrating that the solver possesses the accuracy and robustness properties one may expect from a Roe-type method.

Finally, we would like to put forth the suggestion that the approach here presented may be extensible to other systems of conservation laws where the flux vector is only partly available in algebraic form.

8 The multi-stage centred-scheme approach*

For two-phase flow models, upwind schemes are most often difficult do derive, and expensive to use. Centred schemes, on the other hand, are simple, but more dissipative. The multi-stage (MUSTA) method is aimed at coming close to the accuracy of upwind schemes while retaining the simplicity of centred schemes. So far, the MUSTA approach has been shown to work well for the Euler equations of inviscid, compressible single-phase flow. In this chapter, we explore the MUSTA scheme for a more complex system of equations: the drift-flux model, which describes one-dimensional two-phase flow where the motions of the phases are strongly coupled. As the number of stages is increased, the results of the MUSTA scheme approach those of the Roe method. The good results of the MUSTA scheme are dependent on the use of a large-enough local grid. Hence, the main benefit of the MUSTA scheme is its simplicity, rather than CPU-time savings.

8.1 Introduction

In this chapter, we consider the drift-flux model presented in Section 7.2. It is a two-phase model arising from averaging the equations for single-phase flow (see Chapter 2), and it consists of a continuity equation for each phase, and a momentum equation for the mixture, and it is employed to describe bubbly flows and other two-phase flows where the motions of the phases are strongly coupled.

Since the momentum equation is for the two-phase mixture, a supplementary *hydrodynamic closure law*, commonly denoted as the *slip relation*, is required to determine the velocity of each phase. In addition, *thermodynamic closure laws* are needed for each phase to relate the phasic density to the mixture pressure. The drift-flux model can be written on conservation form, and it has shown to be hyperbolic for a reasonable range of input parameters (Romate, 1998). However, even for simple closure relations, the Jacobian of the model becomes rather complicated.

*The content of this chapter has been submitted for publication as an article (Munkejord *et al.*, 2006)

8.1.1 Riemann solvers

A popular class of methods for solving systems of hyperbolic equations for flow problems are the Godunov-type methods (see e.g. LeVeque, 2002; Toro, 1999, for a review). The basic scheme involves the solution of the Riemann problem at each cell interface. This solution is used to compute the intercell flux. Since they employ wave-propagation information in the construction of the numerical flux, these schemes are often called *upwind* or *upstream* schemes. The Riemann problem can be exactly solved for models such as the Euler equations of inviscid, compressible single-phase flow. However, an exact Riemann solution for the drift-flux model may be derived only for some special cases, since the model is sensitive to the formulation of the closure laws.

It is often adequate to employ an approximate Riemann solver. An attractive candidate is that of Roe (1981), in which the original model is linearized at each cell interface, and a representation of all the wave phenomena in the model is provided. To that end, the Jacobian of the model is diagonalized.

As has been pointed out by several researchers (Baudin *et al.*, 2005a,b; Evje and Fjelde, 2002, 2003; Faille and Heintzé, 1999; Romate, 1998), the complexity resulting from the closure laws employed in the drift-flux model severely restricts the possibilities for constructing a Roe solver by purely algebraic manipulations. Nevertheless, Roe-type schemes have been proposed for this model. Romate (1998) presented a method for constructing a Roe matrix using a fully numerical approach, whereas in Chapter 7, an analytical Roe matrix was derived for fairly general closure laws. Still, that approach relied on a numerical diagonalization of the Roe matrix, and on the closure laws not including differential terms. Such terms were discussed e.g. by Bouré (1997).

8.1.2 Centred schemes

A simpler method for calculating the intercell flux is to employ *centred* stencils which do not explicitly make use of wave-propagation information in the construction of the numerical flux. However, the centred schemes are generally more dissipative than the upwind ones (see e.g. Toro, 1999).

The FORCE flux has been proposed by Toro as an interesting basic centred flux, and it is known that the FORCE scheme possesses various good properties (Toro, 1999; Toro and Billett, 2000; Chen and Toro, 2004). It has been shown to be monotone, to possess the optimal stability condition, and to have the smallest numerical viscosity among centred schemes when it is considered for a scalar, linear conservation law. Moreover, entropy consistence has also been shown for a general nonlinear system of conservation laws, and convergence results

have been obtained for special systems like the isentropic Euler equations and the shallow-water equations (Chen and Toro, 2004).

However, a main drawback of FORCE is clearly observed when considering its truncation error for a linear advection equation with constant speed a; $\partial u/\partial t + a\partial u/\partial x = 0$. In this case, the truncation error is inversely proportional to the Courant–Friedrichs–Lewy (CFL) number $C = a\Delta t/\Delta x$ (Titarev and Toro, 2005). In particular, the FORCE scheme cannot resolve a stationary discontinuity exactly.

8.1.3 The multi-stage approach

The multi-stage (MUSTA) method proposed by Toro (2003); Titarev and Toro (2005) is aimed at coming close to the accuracy of upwind schemes while retaining the simplicity of centred schemes. In this approach, the solution of the Riemann problem at the cell interface is approximated numerically by employing a first-order centred scheme on a local grid. More precisely, by using $2N$ spatial grid cells, M local time steps, and a local CFL number, $C_{\text{loc}} = a\Delta t_{\text{loc}}/\Delta x$, Titarev and Toro (2005) showed that the truncation error for the linear advection equation with constant wave speed could be strongly reduced. In particular, this MUSTA scheme was demonstrated to behave similarly to the upwind Godunov scheme for the linear advection equation. Motivated by this, the authors applied their scheme to the Euler equations and observed that the new MUSTA scheme could effectively match the accuracy of the Godunov method with state-of-the-art Riemann solvers.

An important motivation for the development of the MUSTA scheme was the possibility to use it for more complex systems, such as those occuring in multiphase fluid dynamics. The main purpose of this work is to take one step in this direction.

The analysis behind the construction of the MUSTA scheme proposed by Titarev and Toro (2005) is based on the linear advection equation and monotonicity considerations related to this simple equation. Therefore, it may not be obvious that the good properties of the MUSTA scheme for the scalar case in fact carry over to the case of more complicated systems of conservation laws. Titarev and Toro demonstrated that the MUSTA scheme works well for the Euler equations. However, in order to resolve the local Riemann problem, appropriate choices are needed for the parameters M and N for the local grid. These depend on the specific model under consideration. Consequently, there is a need for exploring the MUSTA approach also for other models than the Euler equations. The aim of this work is thus to explore the MUSTA approach for a two-phase model, the drift-flux model, and reveal more insight into the

potential of this approach when it is applied to a relatively complicated system.

8.1.4 The drift-flux model

A main feature of the drift-flux model is that it possesses two fast waves (sound waves) and one slowly moving wave (mass wave). In particular, if we have a transition from two-phase to pure liquid flow, the speed of sound can change from the order of 10 m/s to the order of 1000 m/s. Consequently, for such flow scenarios (which are highly relevant for the petroleum industry), one is forced to take very small time steps according to the CFL condition. A main purpose of this work is to demonstrate to what extent the improved MUSTA scheme of Titarev and Toro (2005) is able to give an accurate resolution of the important slowly moving mass waves. Due to the possible large gap between the smallest and largest eigenvalues, the drift-flux model may represent a harder test for the MUSTA scheme than the Euler equations. Specifically, we also want to explore in what way the resolution properties of the MUSTA scheme depend on choices related to the local grid represented by the parameters M and N.

The rest of this chapter is organized as follows: The numerical algorithm, including a second-order extension, is detailed in Section 8.2. Section 8.3 presents numerical simulations aimed at demonstrating the accuracy and robustness properties of the MUSTA scheme, as well as to highlight the importance of the involved parameters. Further, the section shows the differences between the MUSTA scheme and the Roe scheme. The main results are summarized in Section 8.4, and conclusions drawn in Section 8.5.

8.2 Numerical algorithm

The drift-flux model (7.2) can be integrated over a control volume to yield the semi-discrete formulation

$$\frac{\mathrm{d}}{\mathrm{d}t}\boldsymbol{Q}_i(t) = -\frac{1}{\Delta x}\left(\boldsymbol{F}_{i+1/2} - \boldsymbol{F}_{i-1/2}\right) + \boldsymbol{S}_i. \tag{8.1}$$

A simple way of integrating (8.1) in time is to use the Forward Euler method:

$$\boldsymbol{Q}_i^{j+1} - \boldsymbol{Q}_i^{j} = -\frac{\Delta t}{\Delta x}\left(\boldsymbol{F}_{i+1/2} - \boldsymbol{F}_{i-1/2}\right) + \Delta t \boldsymbol{S}_i. \tag{8.2}$$

Herein, $\boldsymbol{Q}_i^j$ denotes the numerical approximation to the cell average of the vector of unknowns, $\boldsymbol{q}(x(i), t_j)$, that is, in control volume i at time step j. Quantities without a time index are evaluated at time step j.

A method for specifying the cell fluxes $\boldsymbol{F}_{i-1/2}$ is needed. In the Godunov method, the solution of the local Riemann problem at the cell interfaces is employed. For two-phase flow models, an exact solution to the Riemann problem is not easy to find. Even the derivation of approximate Riemann solvers, such as those of the type of Roe (1981), involves a good deal of work.

8.2.1 FORCE flux

A simple method for calculating the numerical flux $\boldsymbol{F}_{i-1/2}$ is to use the first-order centred (FORCE) scheme of Toro (1999, Section 14.5.1) that was described in Chapter 4. We restate it here for convenience. The FORCE flux is given by

$$\boldsymbol{F}_{i-1/2} = \frac{1}{2}\left(\boldsymbol{F}^{\mathrm{LF}}_{i-1/2} + \boldsymbol{F}^{\mathrm{Ri}}_{i-1/2}\right), \tag{8.3}$$

where $\boldsymbol{F}^{\mathrm{LF}}_{i-1/2}$ is the Lax–Friedrichs flux

$$\boldsymbol{F}^{\mathrm{LF}}_{i-1/2} = \frac{1}{2}(\boldsymbol{f}(\boldsymbol{Q}_{i-1}) + \boldsymbol{f}(\boldsymbol{Q}_i)) - \frac{1}{2}\frac{\Delta x}{\Delta t}(\boldsymbol{Q}_i - \boldsymbol{Q}_{i-1}), \tag{8.4}$$

and $\boldsymbol{F}^{\mathrm{Ri}}_{i-1/2}$ is the Richtmyer flux. It is computed by first defining an intermediate state

$$\boldsymbol{Q}^{\mathrm{Ri}}_{i-1/2} = \frac{1}{2}(\boldsymbol{Q}_{i-1} + \boldsymbol{Q}_i) - \frac{1}{2}\frac{\Delta t}{\Delta x}(\boldsymbol{f}(\boldsymbol{Q}_i) - \boldsymbol{f}(\boldsymbol{Q}_{i-1})), \tag{8.5}$$

and then setting

$$\boldsymbol{F}^{\mathrm{Ri}}_{i-1/2} = \boldsymbol{f}(\boldsymbol{Q}^{\mathrm{Ri}}_{i-1/2}). \tag{8.6}$$

As was seen in Chapter 4, the FORCE scheme is rather dissipative.

8.2.2 The MUSTA approach

In the multi-stage (MUSTA) approach (Toro, 2003; Titarev and Toro, 2005), the solution of the Riemann problem at the cell interface is approximated numerically by employing a simple first-order centred method on a local grid. This solution can then be used in (8.2) or (8.1).

Here we employ the improved MUSTA scheme of Titarev and Toro (2005) using multiple cells on the local grid.

Note that the FORCE flux (8.3) can be written as

$$\boldsymbol{F}_{i-1/2} = \boldsymbol{F}(\boldsymbol{Q}_{i-1}, \boldsymbol{Q}_i) = \boldsymbol{F}(\boldsymbol{Q}_{\mathrm{L}}, \boldsymbol{Q}_{\mathrm{R}}). \tag{8.7}$$

That is, it is only a function of the value to the left and to the right of the cell interface, and it gives rise to a three-point scheme.

In the MUSTA approach, the numerical fluxes $\boldsymbol{F}_{i-1/2}$ in (8.2) or (8.1) are found by transforming the Riemann problem at $x_{i-1/2}$ to a local grid:

$$\frac{\partial \boldsymbol{Q}}{\partial t} + \frac{\partial \boldsymbol{F}}{\partial \xi} = \boldsymbol{0}, \qquad \boldsymbol{Q}(\xi, 0) = \begin{cases} \boldsymbol{Q}_{i-1} = \boldsymbol{Q}_{\mathrm{L}} & \text{if } \xi < 0, \\ \boldsymbol{Q}_{i} = \boldsymbol{Q}_{\mathrm{R}} & \text{if } \xi \geq 0. \end{cases} \tag{8.8}$$

Herein, the position $\xi = 0$ corresponds to $x_{i-1/2}$. This local Riemann problem is then solved approximately by employing the FORCE scheme. We index the local grid by n, and, following Titarev and Toro (2005), we set $\Delta\xi \equiv \Delta x$. Hence the FORCE flux $\boldsymbol{F}(\boldsymbol{Q}_{n-1}, \boldsymbol{Q}_n)$ is calculated using the formulae

$$\begin{gathered} \boldsymbol{F}(\boldsymbol{Q}_{n-1}, \boldsymbol{Q}_n) = \frac{1}{4}\Big(\boldsymbol{F}_{n-1} + 2\boldsymbol{F}^* + \boldsymbol{F}_n - \frac{\Delta x}{\Delta t_{\mathrm{loc}}}(\boldsymbol{Q}_n - \boldsymbol{Q}_{n-1})\Big), \\ \boldsymbol{F}_{n-1} = \boldsymbol{f}(\boldsymbol{Q}_{n-1}), \quad \boldsymbol{F}_n = \boldsymbol{f}(\boldsymbol{Q}_n), \\ \boldsymbol{F}^* = \boldsymbol{f}(\boldsymbol{Q}^*), \quad \boldsymbol{Q}^* = \frac{1}{2}(\boldsymbol{Q}_{n-1} + \boldsymbol{Q}_n) - \frac{1}{2}\frac{\Delta t_{\mathrm{loc}}}{\Delta x}(\boldsymbol{f}(\boldsymbol{Q}_n) - \boldsymbol{f}(\boldsymbol{Q}_{n-1})). \end{gathered} \tag{8.9}$$

First, the fluxes are computed using (8.9), where Δt_{loc} is the time-step length calculated using the CFL criterion on the local grid:

$$\Delta t_{\mathrm{loc}} = \frac{C_{\mathrm{loc}} \Delta x}{\max\limits_{1 \leq n \leq 2N} \Big(\max\limits_{1 \leq p \leq d} |\lambda_n^p| \Big)}, \tag{8.10}$$

where d is the dimension of the system (7.2), and the local CFL number, C_{loc}, is a parameter in the method. Next, the local solution is advanced by use of the formula

$$\boldsymbol{Q}_n^{m+1} - \boldsymbol{Q}_n^m = -\frac{\Delta t_{\mathrm{loc}}}{\Delta x}\Big(\boldsymbol{F}_{n+1/2} - \boldsymbol{F}_{n-1/2}\Big). \tag{8.11}$$

The local time-stepping is performed a fixed number of times, M, and the local grid has $2N$ cells, in addition to two boundary cells. The initial conditions and the numbering of the local grid are illustrated in Figure 8.1 on the facing page. The algorithm for the MUSTA flux can be summarized as follows:

1. For each local cell $n = 1, \ldots, 2N$, compute the fluxes on the data from stage m using (8.9).
2. If $m = M$ then return the FORCE flux $\boldsymbol{F}_{N+1/2}^M$, else continue.
3. Apply extrapolation boundary conditions; $\boldsymbol{Q}_0^m = \boldsymbol{Q}_1^m$ and $\boldsymbol{Q}_{2N+1}^m = \boldsymbol{Q}_{2N}^m$.
4. Update the local solution using (8.11) for $n = 1, \ldots, 2N$. Repeat from 1.

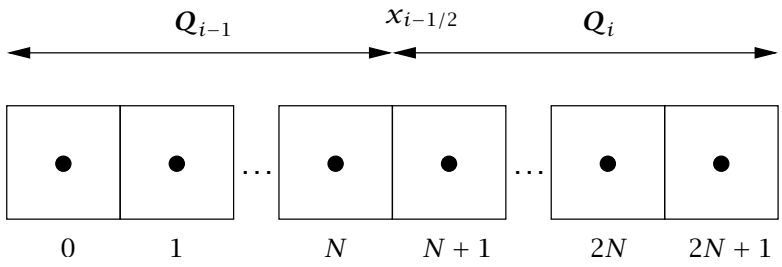

Figure 8.1: Initial values and cell numbering for the local MUSTA grid.

Thus the MUSTA flux $\boldsymbol{F}_{i-1/2}$ to be employed in (8.1) or (8.2) is the FORCE flux $\boldsymbol{F}^M_{N+1/2}$ found on the local grid.

In the above notation, the original FORCE scheme is nearly recovered for $M = 1$ and $2N = 2$. One notable difference, however, is that in the MUSTA approach, the fluxes in (8.9) are calculated using a *local* CFL criterion, while in the FORCE scheme, the *global* time-step length is used throughout. Here we follow Titarev and Toro (2005) and set the local CFL number to $C_{\text{loc}} = 0.9$ for all the calculations.

Note that the cell size of the local grid is without significance, since we are only interested in the solution $\boldsymbol{F}^M_{N+1/2}$ after a particular number of steps, and not at a particular 'time'.

The MUSTA scheme is constructed to have some of the advantages of upstream schemes. Indeed, for increasing M and N, the MUSTA flux is expected to approach the Godunov flux using the exact Riemann solver (Titarev and Toro, 2005).

In the following, we will denote the M-stage MUSTA scheme with $2N$ local cells by MUSTA$_{M-2N}$.

8.2.3 Higher-order extension

Titarev and Toro (2004) suggested to employ weighted essentially non-oscillatory (WENO) schemes in conjunction with MUSTA to produce higher spatial order. Here we propose a different and simpler approach, namely to use a semi-discrete version of the monotone upwind-centred scheme for conservation laws (MUSCL) (van Leer, 1979; Osher, 1985).

In the MUSCL approach, we construct a piecewise linear function using the data $\{\boldsymbol{Q}_i(t)\}$. Then at the interface $x_{i-1/2}$ we have values on the left and right from the two linear approximations in each of the neighbouring cells. These

are denoted by

$$Q_{i-1}^{\mathrm{R}} = Q_{i-1} + \frac{\Delta x}{2}\sigma_{i-1} \quad \text{and} \quad Q_i^{\mathrm{L}} = Q_i - \frac{\Delta x}{2}\sigma_i, \tag{8.12}$$

where σ_i is a slope calculated using a suitable slope-limiter function. Some are listed by LeVeque (2002, Section 9.2). The *minmod* slope is

$$\sigma_i = \mathrm{minmod}\left(\frac{Q_i - Q_{i-1}}{\Delta x}, \frac{Q_{i+1} - Q_i}{\Delta x}\right), \tag{8.13}$$

where the minmod function is defined by (3.86) on page 57. The *superbee* slope is

$$\sigma_i = \mathrm{maxmod}\left(\sigma_i^{(1)}, \sigma_i^{(2)}\right), \tag{8.14}$$

where

$$\sigma_i^{(1)} = \mathrm{minmod}\left(\left(\frac{Q_{i+1} - Q_i}{\Delta x}\right), 2\left(\frac{Q_i - Q_{i-1}}{\Delta x}\right)\right),$$
$$\sigma_i^{(2)} = \mathrm{minmod}\left(2\left(\frac{Q_{i+1} - Q_i}{\Delta x}\right), \left(\frac{Q_i - Q_{i-1}}{\Delta x}\right)\right),$$

and the maxmod function is given by

$$\mathrm{maxmod}(a,b) = \begin{cases} 0 & \text{if } ab \le 0, \\ a & \text{if } |a| > |b| \text{ and } ab > 0, \\ b & \text{if } |a| \le |b| \text{ and } ab > 0. \end{cases} \tag{8.15}$$

The *monotonized central-difference (MC)* slope (van Leer, 1977) is

$$\sigma_i = \mathrm{minmod}\left(\left(\frac{Q_{i+1} - Q_{i-1}}{2\Delta x}\right), 2\left(\frac{Q_i - Q_{i-1}}{\Delta x}\right), 2\left(\frac{Q_{i+1} - Q_i}{\Delta x}\right)\right). \tag{8.16}$$

We also have the van Leer (1974) (see van Leer, 1977) limiter

$$\sigma_i = \begin{cases} \dfrac{2(Q_i - Q_{i-1})(Q_{i+1} - Q_i)}{(Q_i - Q_{i-1}) + (Q_{i+1} - Q_i)} & \text{if } \mathrm{sgn}(Q_i - Q_{i-1}) = \mathrm{sgn}(Q_{i+1} - Q_i), \\ 0 & \text{otherwise.} \end{cases} \tag{8.17}$$

The slope limiting is applied component-wise to the vector of unknowns. There are different possible choices regarding which variables to use in the slope-limiting procedure, for instance; the composite variables, the primitive variables, or the characteristic variables. The latter would correspond more

closely to the scalar case, but would require the diagonalization of the Jacobian matrix, thus defying the purpose of the MUSTA scheme, which is to be simple. Here we use the primitive variables $[\alpha_g, p, u_g]$.

When the piecewise linear reconstruction has been performed, the MUSTA flux $\boldsymbol{F}_{i-1/2} = \boldsymbol{F}(\boldsymbol{Q}^{\mathrm{R}}_{i-1}, \boldsymbol{Q}^{\mathrm{L}}_{i})$ is computed as described in the previous subsection. To obtain a second-order solution in time, we employ the semi-discrete formulation (8.1) in combination with the two-stage second-order strong-stability-preserving (SSP) Runge–Kutta (RK) method (see e.g. Ketcheson and Robinson, 2005).

With the semi-discrete formulation (8.1) of the form

$$\frac{\mathrm{d}\boldsymbol{Q}}{\mathrm{d}t} = \mathcal{H}(\boldsymbol{Q}), \tag{8.18}$$

the two-stage second-order SSP-RK method can be written as

$$\begin{aligned} \boldsymbol{Q}^{(1)} &= \boldsymbol{Q}^{j} + \frac{1}{2}\Delta t \mathcal{H}(\boldsymbol{Q}^{j}) \\ \boldsymbol{Q}^{j+1} &= \frac{1}{2}\boldsymbol{Q}^{j} + \frac{1}{2}\boldsymbol{Q}^{(1)} + \frac{1}{2}\Delta t \mathcal{H}(\boldsymbol{Q}^{(1)}). \end{aligned} \tag{8.19}$$

Herein, $\boldsymbol{Q}^{j}$ is the vector of unknowns from time step j, $\boldsymbol{Q}^{j+1}$ is the sought values at the next time step, while $\boldsymbol{Q}^{(1)}$ represents intermediate values.

Wave-speed estimates

To obtain the local and global time-step lengths, it is necessary to employ the CFL criterion. The CFL number is

$$C = \frac{\|\lambda\|_\infty \Delta t}{\Delta x}, \tag{8.20}$$

where $\|\lambda\|_\infty$ is the maximum eigenvalue in the computational domain. This shows that even though no information of the eigenstructure of the model is directly used in the calculation of the MUSTA flux, an estimate of the maximum eigenvalue is still needed.

In this work, we employed the approximate eigenvalues derived by Evje and Flåtten (2005b) using a perturbation technique, see Appendix B. It should be noted that the computed results are not very sensitive to the eigenvalue estimate. For instance, we have carried out some experiments using the simple estimate by Evje and Fjelde (2003) based on a no-slip assumption, and only minor differences were observed in the numerical results.

8.3 Numerical simulations

In this section, we will analyse the performance of the MUSTA scheme and its MUSCLE extension by conducting basic numerical tests and by running benchmark cases from the literature. Comparisons with the Roe scheme of Chapter 7 and the FORCE scheme will also be provided. The main aim of the section is to

- Clarify the dependence of the MUSTA scheme on the parameters M and N,
- Explore the performance of the MUSTA scheme for cases where there is a large difference between the largest and the smallest eigenvalue. In particular, we want do demonstrate the importance of the fact that the MUSTA scheme is semi-discrete, which is an essential difference compared to the FORCE scheme.

All the computations in this work have been performed using a local CFL number of $C_{\text{loc}} = 0.9$ in (8.10).

8.3.1 Advection of a 'hat'

First we perform a basic validation of the MUSCL-MUSTA scheme by testing its convergence properties when the solution is smooth. The test case was introduced in Section 3.4.2 on page 76 and it consists of a 'smoothed hat' volume-fraction profile which is advected with the flow (see Figure 3.14 on page 77). In the present calculations, the no-slip law was employed.

Grid refinement with constant time-step length

Calculations were performed for various grid sizes, each using a time-step length of $\Delta t = 9.82 \cdot 10^{-6}$ s. The volume-fraction profiles obtained after $t = 0.12$ s were compared to that calculated on a fine grid of 10000 cells using the minmod limiter. Table 8.1 on the facing page displays the 1-norms and the corresponding convergence rates obtained when using the minmod limiter and the MC limiter. The MC limiter gave second-order convergence, but the convergence rate calculated when using the minmod limiter was slightly lower. This is due to the latter limiter's stronger clipping of the solution. The difference might have been smaller for an even smoother initial solution.

This test seems to indicate that it is preferable to employ the MC limiter, but unfortunately, as will be shown in the following, the MC limiter and other sharp limiters gave oscillatory solutions for the shock-tube benchmark test.

Table 8.1: Smooth volume-fraction advection test case. 1-norm of the relative error in gas volume fraction by grid refinement with a constant time-step length of $\Delta t = 9.82 \cdot 10^{-6}$ s.

	minmod limiter		MC limiter	
Δx(m)	$\|E(\alpha_g)\|_1$	n	$\|E(\alpha_g)\|_1$	n
0.24	$9.951 \cdot 10^{-2}$	–	$7.323 \cdot 10^{-2}$	–
0.12	$2.990 \cdot 10^{-2}$	1.73	$1.823 \cdot 10^{-2}$	2.01
0.06	$9.219 \cdot 10^{-3}$	1.70	$4.452 \cdot 10^{-3}$	2.03
0.03	$2.705 \cdot 10^{-3}$	1.77	$1.097 \cdot 10^{-3}$	2.02
0.012	$4.759 \cdot 10^{-4}$	1.90	$1.740 \cdot 10^{-4}$	2.01

Table 8.2: Smooth volume-fraction advection test case. 1-norm of the relative error in gas volume fraction by time-step refinement with a 101-point grid.

Δt(s)	$\|E(\alpha_g)\|_1$	n
$1.0 \cdot 10^{-3}$	$2.046 \cdot 10^{-4}$	–
$5.0 \cdot 10^{-4}$	$5.121 \cdot 10^{-5}$	2.00
$2.5 \cdot 10^{-4}$	$1.280 \cdot 10^{-5}$	2.00
$1.25 \cdot 10^{-4}$	$3.196 \cdot 10^{-6}$	2.00
$6.25 \cdot 10^{-5}$	$7.930 \cdot 10^{-7}$	2.01

Time-step refinement with a given grid

The convergence-rate was also calculated for time-step refinement on a grid of 100 cells, and the results are given in Table 8.2. Here, the minmod limiter was employed, and the reference solution was computed using $\Delta t = 6.25 \cdot 10^{-6}$ s. As can be seen, the convergence-rate was of second order, and hence it can be concluded that the MUSCL-MUSTA scheme is second order in space and time when the two-stage second-order SSP-RK method is used for the time integration.

8.3.2 Shock tube

This subsection presents calculations of the shock-tube test case of Baudin *et al.* (2005a) described in Section 7.5.2 on page 195. First, we will investigate the dependence upon the parameters M and N, that is, the number of stages and the number of local cells. Thereafter, the convergence of the basic MUSTA scheme and the MUSCL-MUSTA scheme will be tested.

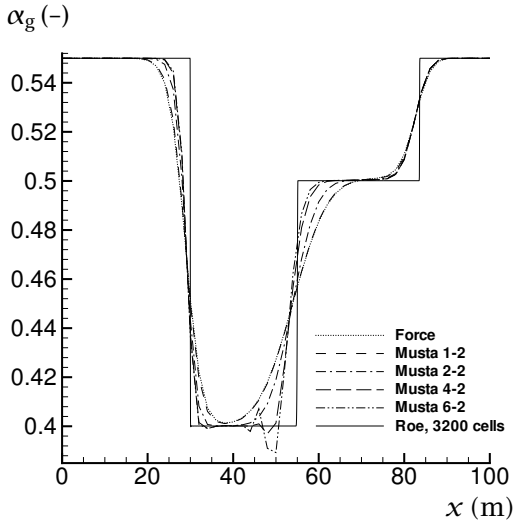

Figure 8.2: Gas volume fraction for the shock-tube test case. Dependency on the number of stages, M, for the MUSTA$_{M-2}$ scheme.

Effect of number of stages and local cells

Figure 8.2 shows the volume fraction calculated on a 50-cell grid using a CFL number of $C = 0.9$ in (8.20). The solution obtained with the MC-limited Roe method on a 3200-cell grid is shown for reference. The data in the figure have been calculated using two local cells, or $N = 1$, and the number of local time steps, M, has been varied. The difference between MUSTA$_{1-2}$ and FORCE is that in FORCE, only the global time-step length is employed, while MUSTA$_{1-2}$ uses a local CFL criterion for the calculation of the intercell fluxes. This is also the difference between the MUSTA$_{M-2}$ scheme discussed here and the two-cell MUSTA scheme proposed by Toro (2003). For the present case, there is only a small difference between the results produced with MUSTA$_{1-2}$ and those from FORCE.

When M is increased from 1 to 2, the performance of the scheme is clearly improved. However, as M is further increased, the monotonicity is lost and grave oscillations occur. This is in contrast to what was reported by Toro (2003) for the Euler equations. There, satisfactory results were shown for the four-stage two-cell MUSTA scheme.

Figure 8.3 on the facing page shows why MUSTA cannot be expected to give good results in general when the number of stages, M, is greater than the number of cells, N, on each side of the discontinuity. The figure displays the gas velocity as calculated in the local MUSTA procedure for a varying number

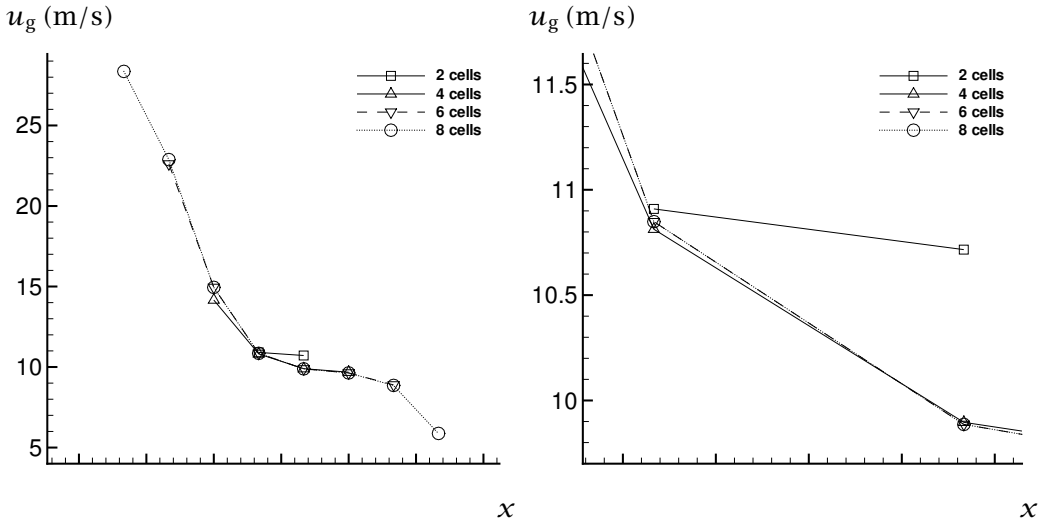

(a) Whole domain (b) Close-up on $x_{N+1/2}$

Figure 8.3: Gas velocity on the local MUSTA grid for the shock tube. Results after four local MUSTA time steps for varying number of local cells.

of local cells, $2N$. The right and left states are the same as in the shock-tube test case, and the results are shown after $M = 4$ local time steps. Figure 8.3(a) shows the whole domain, while Figure 8.3(b) highlights the results for the middle cells. It is the values from these cells that are used to compute the intercell flux. As can be seen in Figure 8.3(a), the calculation domain grows as the number of local cells is increased.

Figure 8.3(b) shows a clear discrepancy between the values obtained with $N = 1$ (two local cells) and $N = 2$ (four local cells). On the left-hand side, a small difference can also be seen between the values calculated for $N = 2$ and $N = 3$ (six local cells). The results for $N = 3$ and $N = 4$ are identical in the two middle cells.

Due to the CFL criterion, a wave can travel one cell per time step. For $N = 2$, that is, with two internal cells on each side of the Riemann discontinuity, a wave may travel to the boundary, be (partially) reflected, and return to the origin in four time steps. On the other hand, for $N = 3$, the wave has no longer the time to return. This is why there is a difference between the $N = 2$ and $N = 3$ results, while the results for $N = 3$ and $N = 4$ are equal.

As a conclusion, we may say that to be certain that boundary effects do not interfere in the calculation of the MUSTA flux, one must choose $M < 2N$. However, the results in Figure 8.3 indicate that $M = 2N$ may also give good

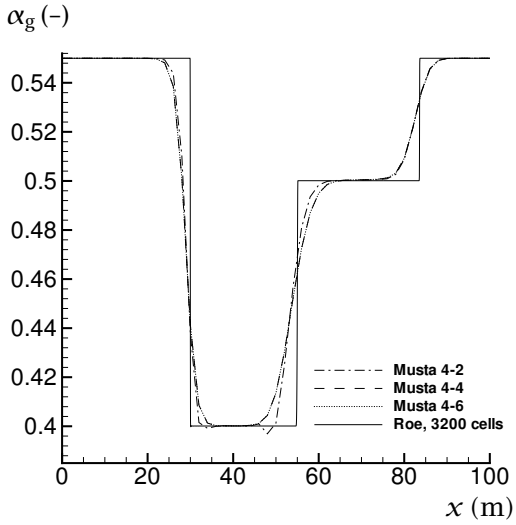

Figure 8.4: Gas volume fraction for the shock-tube test case. Dependency on the number of local cells, $2N$, for the four-stage MUSTA$_{4-2N}$ scheme.

results.

The bad results for $M > 2N$ may be due to the rather simplified boundary treatment in the local MUSTA procedure, which has as a consequence that when N is set too low, information disappears from the calculation domain in an unmotivated way. This is because every variable at the boundaries is found from the inner domain by zeroth-order extrapolation. Hence the boundary conditions are not set according to the number of positive and negative characteristics, as they ought to be. However, instead of enforcing a rigorous boundary treatment in the local MUSTA procedure, it is adequate simply to choose a sufficiently large local grid.

Figure 8.4 shows the effect of the number of local cells, $2N$, for the four-stage MUSTA$_{4-2N}$ scheme. Again, a 50-cell grid has been employed, and the CFL number was $C = 0.9$. As already shown, oscillations are produced in the case of $N = 1$ (two local cells). Even though a boundary effect can be present for $N = 2$, in this case, the results for $N = 2$ and $N = 3$ are equal to plotting accuracy.

The effect of the simultaneous increase of the number of stages, M, and the number of local cells, $2N$, is shown in Figure 8.5 on the facing page. As can be seen from the plot, it is primarily the resolution of the contact discontinuity that is improved for an increased number of stages. However, the difference between four and eight stages is small. In the graph we have also plotted data

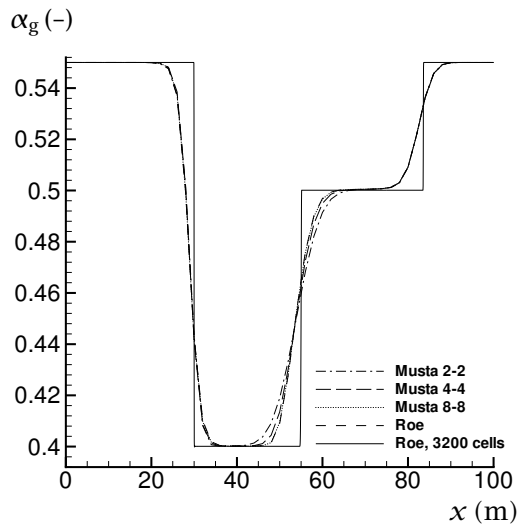

Figure 8.5: Gas volume fraction for the shock-tube test case. Effect of varying number of stages and local cells in the MUSTA$_{M-2N}$ scheme.

obtained with the first-order Roe method on the same grid and using the same CFL number. It is noticeable that the MUSTA results approach those of the Roe scheme when the number of stages is increased. For eight stages, the results obtained with the MUSTA scheme are very similar to those calculated using the Roe method.

Some comparisons with the FORCE scheme

Figure 8.6 on the next page shows volume-fraction profiles for computations performed on a 50-cell grid using various time-step lengths (CFL numbers). Results for MUSTA$_{1-2}$ are displayed in Figure 8.6(a), while Figure 8.6(b) gives profiles for the FORCE scheme. It can be seen that the FORCE scheme becomes increasingly diffusive as the time-step length is decreased. This is due to the $\Delta x/\Delta t$ term of the Lax–Friedrichs flux, and it reflects the fact that the FORCE scheme has no semi-discrete form. The results of the MUSTA$_{1-2}$ scheme, on the other hand, converge for decreasing time-step lengths, and there is only a small difference between the results for $C = 0.1$ and those for $C = 0.01$. This behaviour is expected from a semi-discrete scheme, even though it does not prove in itself that the scheme is semi-discrete.

There are two main reasons for the differences between MUSTA and FORCE. In MUSTA, as opposed to in FORCE, the intercell fluxes are calculated using a *local*

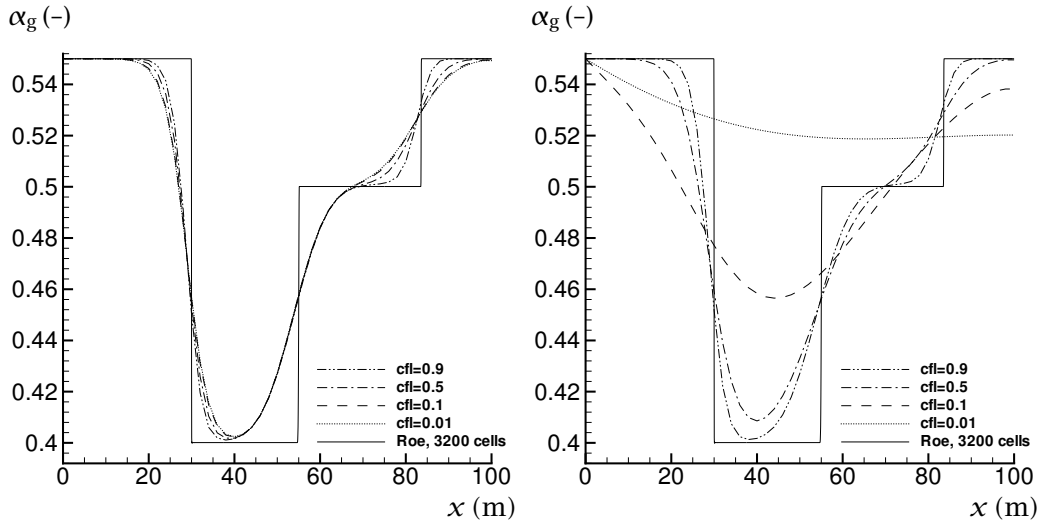

(a) MUSTA_{1-2} (b) FORCE

Figure 8.6: Gas volume fraction for the shock-tube test case. Comparison of the MUSTA_{1-2} scheme and the FORCE scheme for varying CFL number (time-step length). 50 grid cells.

CFL criterion. Furthermore, in MUSTA, when more local time-steps are taken, the neighbouring global cells do not interfere in the calculation. In FORCE, when the global grid is refined, more time steps are performed due to the CFL criterion. Therefore, more neighbouring cells are affected, since information propagates one cell per time step.

Convergence of basic scheme

Figure 8.7 on the facing page displays data obtained on various grids with the MUSTA_{4-4} scheme, that is, the four-stage MUSTA scheme with four local cells. The CFL number was $C = 0.9$. As can be seen, the results are non-oscillatory, and both the shocks and the contact discontinuity are quite sharply resolved. In fact, the results are similar to those of the first-order Roe scheme, except that the contact discontinuity is slightly more smeared.

Higher-order scheme

Figure 8.8 on page 222 shows a comparison between the first-order MUSTA_{4-4} scheme and its MUSCL extension. The employed grid had 50 cells and the CFL

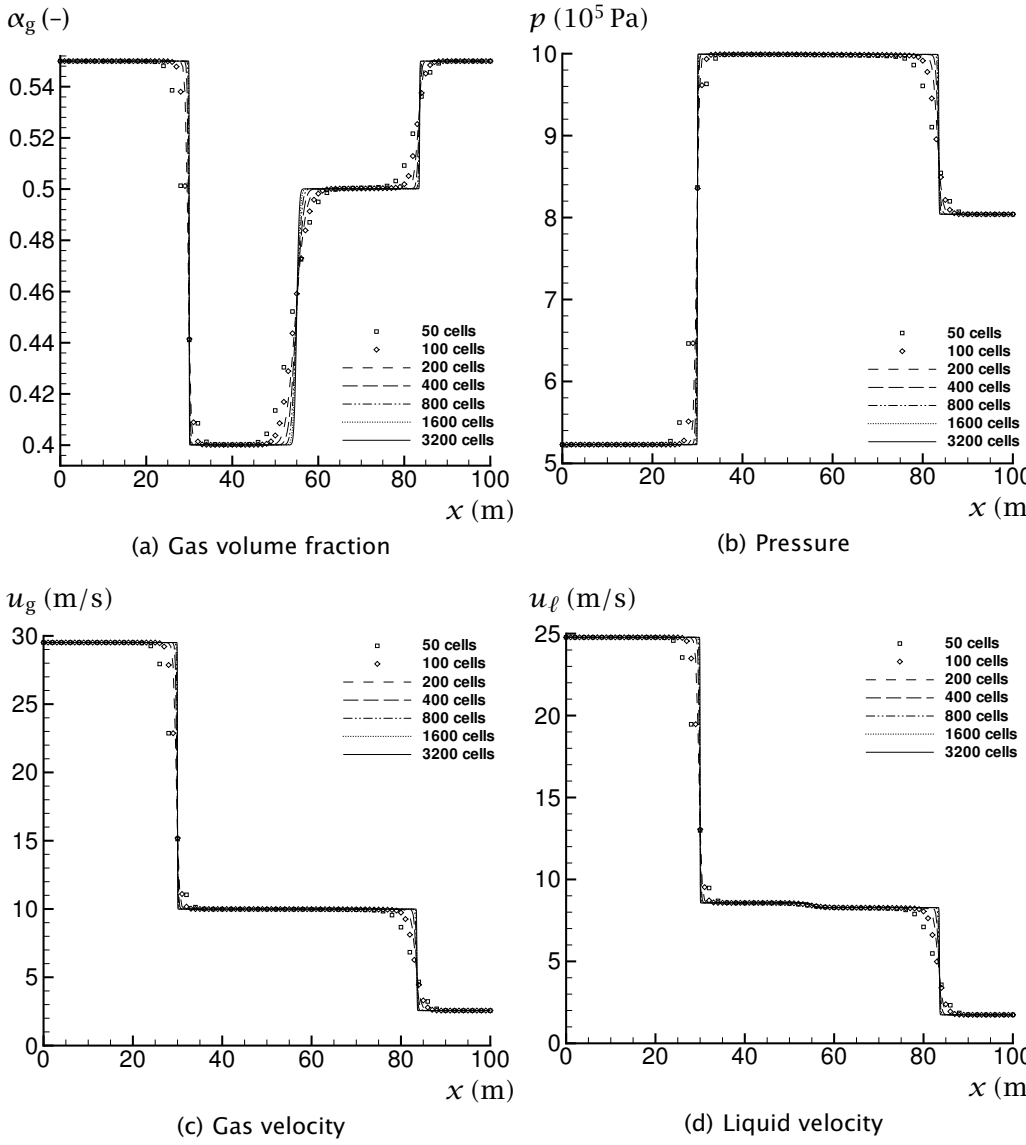

(a) Gas volume fraction

(b) Pressure

(c) Gas velocity

(d) Liquid velocity

Figure 8.7: Shock tube. Convergence of the MUSTA$_{4-4}$ scheme.

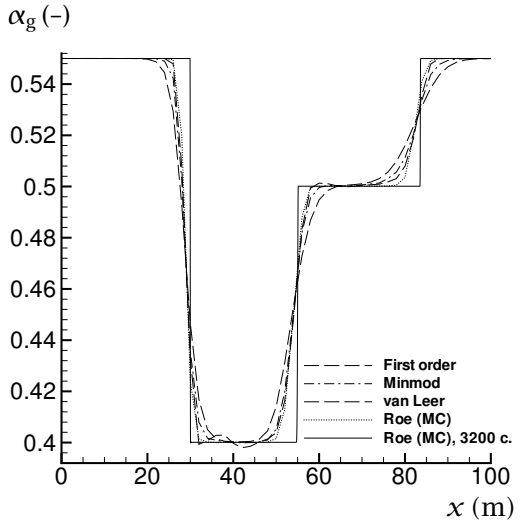

Figure 8.8: Gas volume fraction for the shock-tube test case. Comparison of the first-order and the MUSCL-MUSTA$_{4-4}$ scheme with different limiter functions on a 50-cell grid.

number was $C = 0.5$. Results obtained with the MC-limited Roe method are also shown for comparison. Employing MUSCL-MUSTA$_{4-4}$ with the minmod limiter gave a sharper resolution of both the shocks and the contact discontinuity, compared to the first-order MUSTA$_{4-4}$ scheme. However, as can be observed, the Roe-MC scheme gave a still better resolution, particularly for the right-hand-side shock. Unfortunately, using less diffusive limiters than the minmod limiter gave oscillations with the MUSCL-MUSTA$_{4-4}$ scheme. This is shown in the figure for the van Leer limiter. Henceforth we therefore only consider the minmod limiter.

The convergence for MUSCL-MUSTA$_{4-4}$ using the minmod limiter is displayed in Figure 8.9 on the facing page for $C = 0.5$. The results are non-oscillatory, and both the shocks and the discontinuity are well resolved. Nevertheless, the corresponding plots for the MC-limited Roe scheme in Figure 7.3 on page 197 show a sharper resolution.

Computational cost

A comparison of the CPU-time consumption of different MUSTA$_{M-2N}$ schemes and the Roe scheme is shown in Table 8.3 on page 224. The calculateions were run using a CFL number of 0.9. Data are only shown for a 800-cell grid, since no

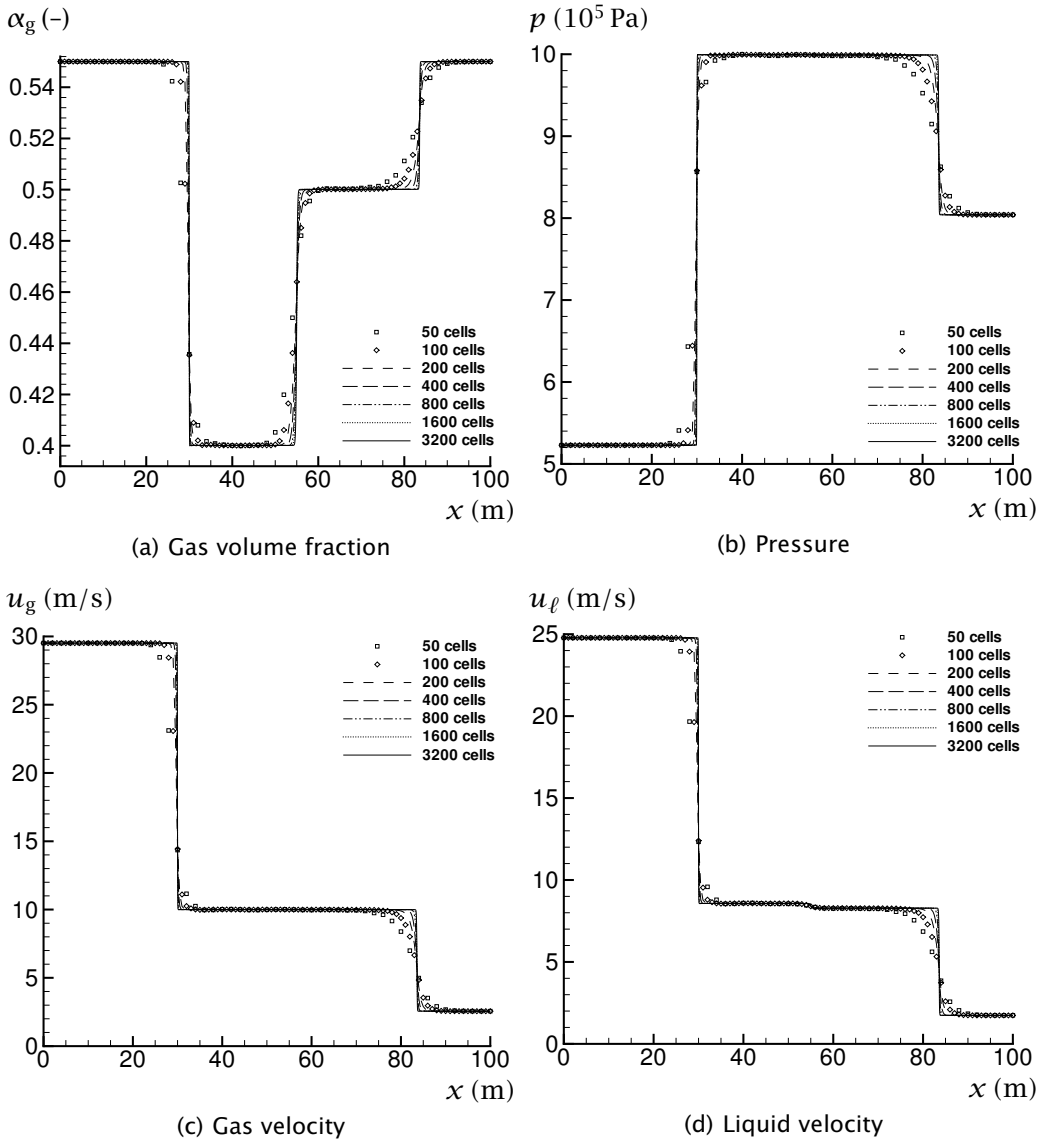

(a) Gas volume fraction

(b) Pressure

(c) Gas velocity

(d) Liquid velocity

Figure 8.9: Shock tube. Convergence of the MUSCL-MUSTA$_{4-4}$ scheme using the minmod limiter.

Table 8.3: Shock-tube test case. Comparison of CPU-time consumption.

$M-2N$	MUSTA$_{M-2N}$/Roe	M-MUSTA$_{M-2N}$/Roe-MC
$1-2$	0.19	0.40
$2-2$	0.32	0.67
$4-4$	0.78	1.58
$8-8$	2.28	4.65

grid dependency was detected. The second column shows the CPU time of the MUSTA$_{M-2N}$ schemes divided by that of the first-order Roe scheme, while the third column shows the figures for the MUSCL-MUSTA$_{M-2N}$ schemes employing the minmod limiter and the Roe scheme using the MC limiter.

The table shows that as the number of local time steps, M, and local cells, $2N$, are increased, the computational cost of the MUSTA schemes strongly grows. As noted in the previous subsections, the MUSTA scheme comes quite close to the accuracy of the Roe scheme for $M = 4$ and $2N = 4$. Therefore, it is most relevant to compare the CPU-time consumption of the (MUSCL-) MUSTA$_{4-4}$ scheme and that of the Roe method.

While care has been taken during the implementation of both types of schemes not to waste too much CPU time, optimizations are undoubtedly possible. Particularly for MUSCL-MUSTA, there are some degrees of freedom regarding the implementation. Therefore, instead of declaring a 'CPU-time winner', one may only conclude that

- The CPU-time consumption of the MUSTA$_{4-4}$ scheme and the Roe scheme are of the same order of magnitude,

- The CPU-time consumption of MUSCL-MUSTA$_{M-2N}$ is relatively larger than that of MUSTA$_{M-2N}$.

It is perhaps surprising that the centred scheme MUSTA$_{4-4}$ is not computationally much cheaper than the Roe scheme for a given grid size and time-step length. The reason is that the numerical diagonalization and matrix manipulations performed in the Roe scheme are roughly balanced by the extra computations carried out on the local MUSTA grid. This includes extra evaluations of the equation of state and the slip relation.

The second-order Roe scheme is relatively cheaper than the MUSCL-MUSTA$_{4-4}$ scheme, since in the Roe scheme, the high-resolution terms are already mostly calculated during the diagonalization of the Jacobian matrix. In MUSCL-MUSTA, on the other hand, the piecewise reconstruction of the data comes fully in addition to the calculations done in the basic scheme.

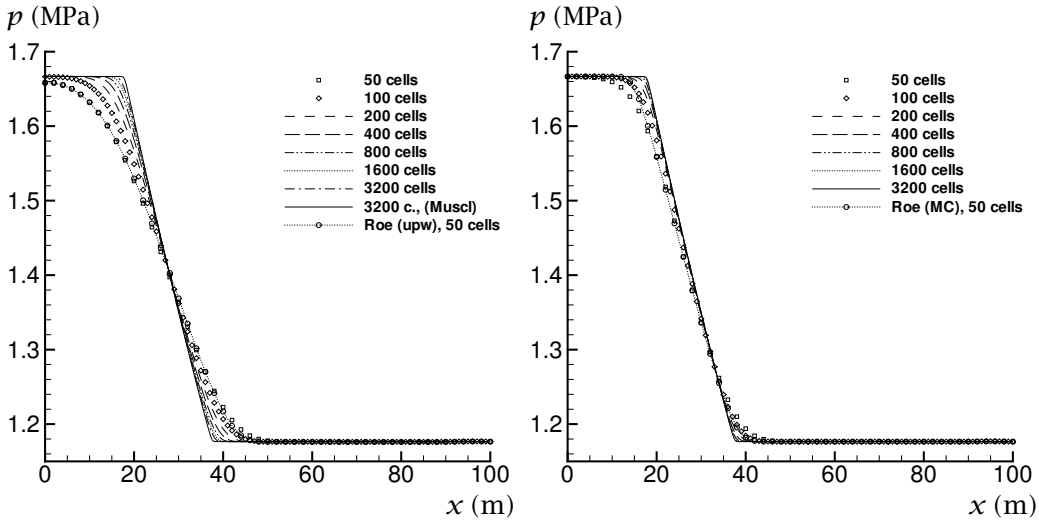

(a) Basic scheme (first-order) (b) MUSCL with minmod limiter

Figure 8.10: Pressure for the pure rarefaction test problem. Convergence of the MUSTA$_{4-4}$ scheme and its MUSCL extension.

8.3.3 Pure rarefaction

We now study the pure-rarefaction problem of Baudin *et al.* (2005a), see Section 7.5.1 on page 194. Pressure profiles for various grid sizes are presented in Figure 8.10. The employed CFL number was $C = 0.5$. Figure 8.10(a) shows the results for the basic four-stage MUSTA scheme with four local cells. Data for the first-order Roe scheme on a 50-cell grid are shown for comparison, and it can be observed that the results are very similar, see also Figure 7.1(a) on page 195. As can be seen from Figure 8.10(b), the MUSCL extension using the minmod limiter represents an improvement. However, the resolution is not quite as good as that obtained using the MC-limited Roe scheme (see also Figure 7.1(b)).

8.3.4 Transonic rarefaction

Transonic rarefactions, that is, when an eigenvalue λ^p is negative to the left of the p-wave, $\mathcal{W}^p$, and positive to the right, are not automatically handled by the Roe scheme if an entropy fix is not implemented. It is therefore interesting to compare the performance of the Roe and MUSTA schemes in such a case.

A transonic rarefaction (and some other waves) can be produced by decreasing the pressure and increasing the velocities on the right-hand side of the

Table 8.4: Initial states in the transonic-rarefaction test problem.

Quantity	symbol (unit)	left	right
Gas volume fraction	α_g (–)	0.6	0.68
Pressure	p (MPa)	1.66667	0.7
Gas velocity	u_g (m/s)	34.4233	70.0
Liquid velocity	u_ℓ (m/s)	34.4233	70.0

Table 8.5: Parameters employed in the transonic-rarefaction test problem.

	c_k (m/s)	ρ_k° (kg/m^3)
gas (g)	100	0
liquid (ℓ)	1000	998.924

pure-rarefaction test case. The initial states are listed in Table 8.4, and the equation-of-state parameters are given in Table 8.5.

The plot in Figure 8.11 on the facing page shows pressure profiles obtained after $t = 0.3$ s on a 100-cell grid, using a CFL number of $C = 0.5$. The MC-limited Roe scheme produced a rarefaction shock, something which is unphysical. As shown, this can be remedied by employing Harten's entropy fix (see Section 3.3.3 on page 55). Here we took the parameter $\delta = 20$. It can also be seen from the figure that both the MUSTA$_{4-4}$ scheme and the MUSCL-MUSTA$_{4-4}$ scheme using the minmod limiter gave physically plausible solutions.

8.3.5 Static discontinuity

We next consider a static discontinuity. This test case reveals differences between upwind and central schemes. Upwind schemes are known to preserve a static discontinuity, whereas central schemes will gradually smear it out.

This test consists of a discontinuity in the volume fraction, while the other variables are uniform. The velocities are zero. The initial states are given in Table 8.6, and Table 8.7 shows the parameters employed in the equation of state.

Figure 8.12 on page 228 shows gas-volume-fraction profiles after $t = 10$ s calculated on a 100-cell grid using $C = 0.9$. As expected, the performance of the MUSTA schemes improved as the number of stages was increased. The curve labelled M-MUSTA is for the MUSCL extension using the minmod limiter, and it shows that the MUSCL approach provided some improvement. The figure also shows that the FORCE scheme is the most diffusive, whereas the first-order Roe scheme perfectly preserves the discontinuity.

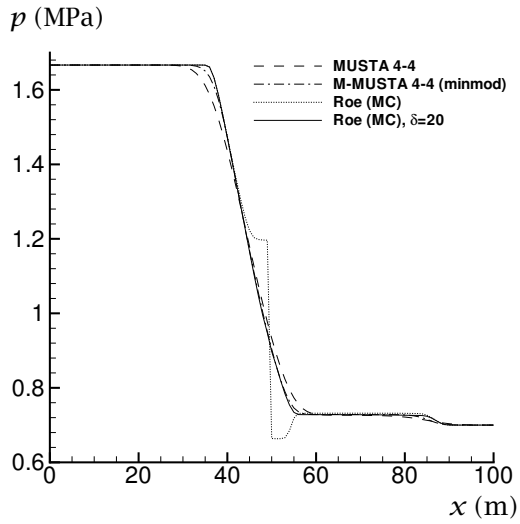

Figure 8.11: Pressure for the transonic-rarefaction problem. Comparison of the MUSTA$_{4-4}$ scheme, the MUSCL-MUSTA$_{4-4}$ scheme using the minmod limiter, the MC-Roe scheme, and the MC-Roe scheme employing Harten's entropy fix with $\delta = 20$. 100 grid cells.

Table 8.6: Initial states in the static discontinuity test problem.

Quantity	symbol (unit)	left	right
Gas volume fraction	α_g (–)	0.2	0.8
Pressure	p (kPa)	100	100
Gas velocity	u_g (m/s)	0	0
Liquid velocity	u_ℓ (m/s)	0	0

Table 8.7: Parameters employed in the static discontinuity test problem.

	c_k (m/s)	ρ_k° (kg/m^3)
gas (g)	$\sqrt{10^5}$	0
liquid (ℓ)	1000	999.9

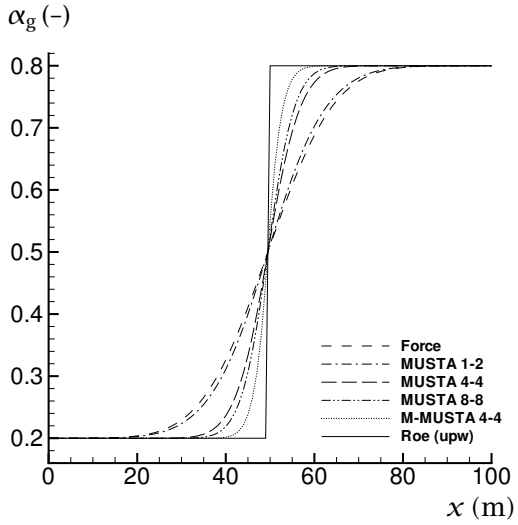

Figure 8.12: Gas volume fraction for the static discontinuity. Comparison of the FORCE scheme, various MUSTA$_{M-2N}$ schemes and the MUSCL-MUSTA$_{4-4}$ scheme with the minmod limiter. 100 grid cells.

It should be noted that the MUSTA scheme keeps smearing the discontinuity even when both the local and global CFL numbers are set equal to 1.

8.3.6 Moving discontinuity

Now we let the discontinuity move. The initial conditions are similar to those of the static-discontinuity case, except that both phases have a velocity of $u = 10\,\mathrm{m/s}$. There is no slip between the phases. Instead of a single jump in the volume fraction, there is now a 'hat'. Periodic boundary conditions are employed.

Figure 8.13 on the next page displays volume-fraction profiles after $t = 10\,\mathrm{s}$, that is, the volume fraction 'hat' has traversed the calculation domain once. As for the static-discontinuity case, the grid had 100 cells and the CFL number was $C = 0.9$. The initial profile is plotted for reference. For this case, the first-order Roe scheme (labelled 'upw') has no particular advantage compared to the MUSTA$_{4-4}$ scheme. Results for MUSTA$_{8-8}$ are not shown, since they were very similar to those of MUSTA$_{4-4}$. The Roe scheme employing the MC limiter gave the best resolution, while the MUSCL-MUSTA$_{4-4}$ scheme lay in between that and the first-order schemes. Nevertheless, the most interesting point is that the performance of the MUSTA$_{4-4}$ scheme is rather close to that of the Roe

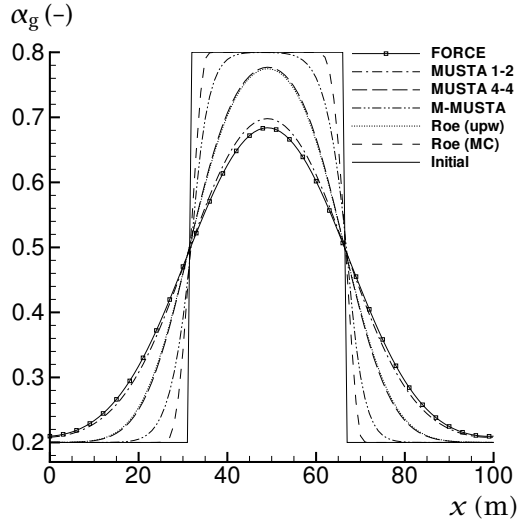

Figure 8.13: Gas volume fraction for the moving discontinuity. Comparison of the FORCE scheme, MUSTA$_{M-2N}$ schemes and the MUSCL-MUSTA$_{4-4}$ scheme with the minmod limiter. The first-order (upwind) Roe scheme and the MC-limited Roe scheme are also shown. 100 grid cells.

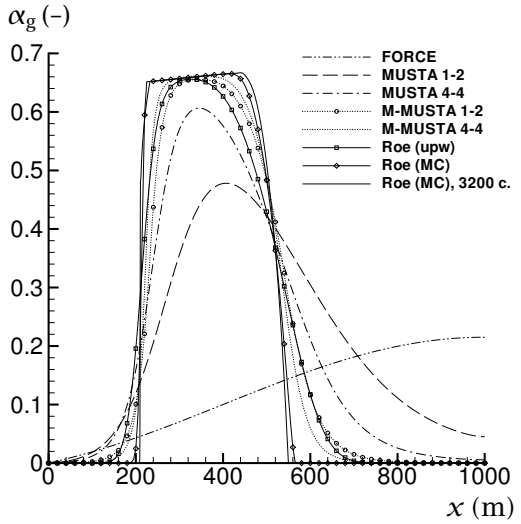

Figure 8.14: Gas volume fraction for the pipe-flow test problem. Comparison of the FORCE scheme, MUSTA$_{M-2N}$ schemes and the MUSCL-MUSTA$_{4-4}$ scheme with the minmod limiter. The first-order (upwind) Roe scheme and the MC-limited Roe scheme are also shown. 200 grid cells.

scheme.

8.3.7 Pipe-flow problem

We finally turn to the pipe-flow problem which was introduced as Example 4 by Evje and Fjelde (2003). It was described in Section 7.5.5 on page 198. This is a demanding test, particularly regarding mass transport, and it includes such challenges as a more complex, non-linear slip relation and near-single-phase flow. Moreover, the near-single-phase flow causes a large difference between the eigenvalues.

A comparison between different MUSTA variants, the FORCE scheme and the Roe scheme is given in Figure 8.14. The computations were performed on a 200-cell grid using $C = 0.5$. The solution obtained with the MC-limited Roe scheme on a fine grid is shown for reference. First, it is obvious that the FORCE scheme is useless for this kind of calculation due to its smearing of volume-fraction waves. The time-steps calculated according to (8.20) became very small because of the transition to single-phase flow, and we observe a behaviour which is similar to the one seen in Figure 8.6 on page 220. Next, it is somewhat

surprising that already MUSTA$_{1-2}$ provided a noticeable improvement, the only difference between the two schemes being that the latter employs a local CFL number of 0.9 in the calculation of the intercell fluxes. For an increasing number of stages, the MUSTA scheme gave better results, but even MUSTA$_{8-8}$ did not quite attain the volume-fraction profile of the first-order Roe scheme. Similarly to what has been seen in the previous test problems, MUSCL-MUSTA$_{4-4}$ with the minmod limiter gave quite good results, but not as sharp as those of the Roe scheme using the MC limiter.

It is interesting that the difference between the volume-fraction profile of MUSTA$_{1-2}$ and that of MUSCL-MUSTA$_{1-2}$ is significantly larger than the difference between MUSTA$_{4-4}$ and MUSCL-MUSTA$_{4-4}$. Furthermore, the volume-fraction profile of MUSCL-MUSTA$_{1-2}$ is not far from that of MUSCL-MUSTA$_{4-4}$. Hence the former scheme may be of interest for practical calculations, since it is less CPU-intensive.

Calculations performed with the MUSCL-MUSTA$_{4-4}$ scheme for various grids using $C = 0.5$ are plotted in Figure 8.15 on the next page. The results are non-oscillatory, and it can be observed that the near-single-phase flow is handled well. The results are comparable to those presented for the second-order AUSMD scheme in Evje and Fjelde (2003). Still, the resolution is not quite as good as the one obtained using the MC-limited Roe method, see also Figure 7.7 on page 203.

8.4 Summary

The multi-stage (MUSTA) centred scheme has been analysed for the drift-flux model. In this scheme, an approximate solution to the Riemann problem at the cell interfaces is found by running the first-order centred (FORCE) scheme a given number of time-steps (M) on a $2N$-cell local grid. The scheme is of special interest, since it uses no explicit information of the eigenstructure of the model, while giving a significantly improved solution compared to the FORCE scheme. Still, the scheme is dependent on an estimate of the maximum eigenvalue to be able to employ the CFL criterion.

To avoid interference from the boundaries in the local MUSTA procedure, it is necessary to choose $M < 2N$. However, in the present computations, $M = 2N$ also gave good results. Choosing $M > 2N$ may yield oscillatory solutions and should be avoided.

The four-stage MUSTA scheme with four local cells ($M = 4$ and $N = 2$) gave results quite close to those of the first-order Roe scheme. In contrast to the Roe scheme, however, MUSTA did not preserve a static discontinuity. On

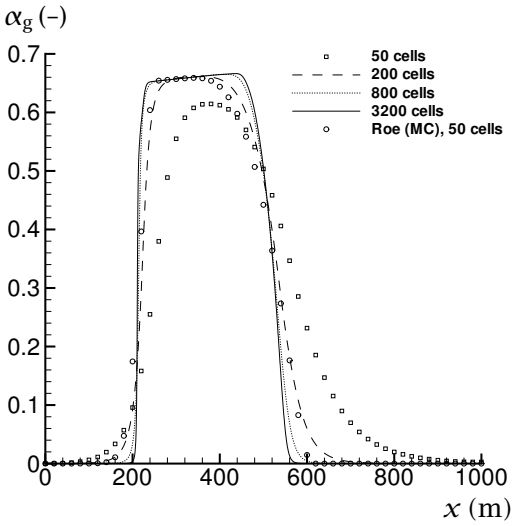

(a) Gas volume fraction

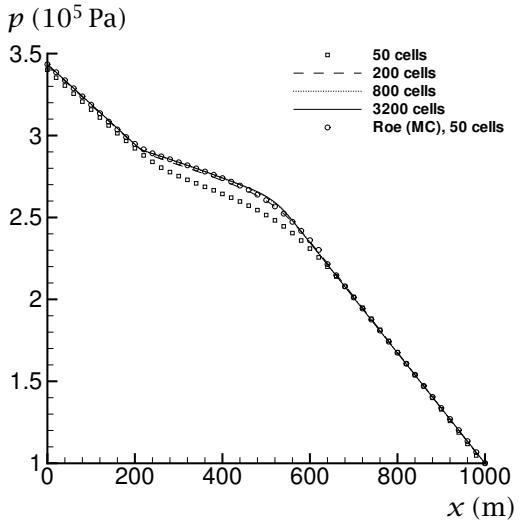

(b) Pressure

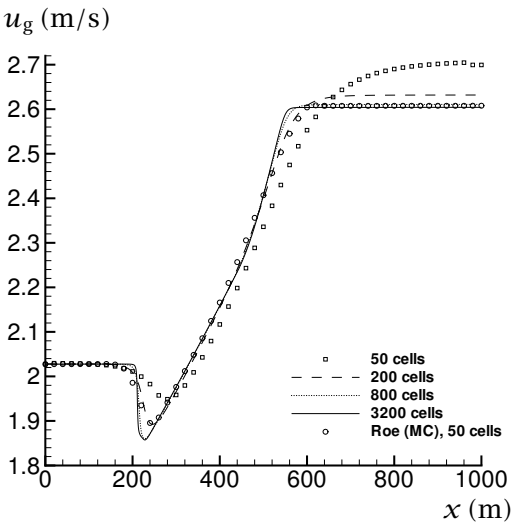

(c) Gas velocity

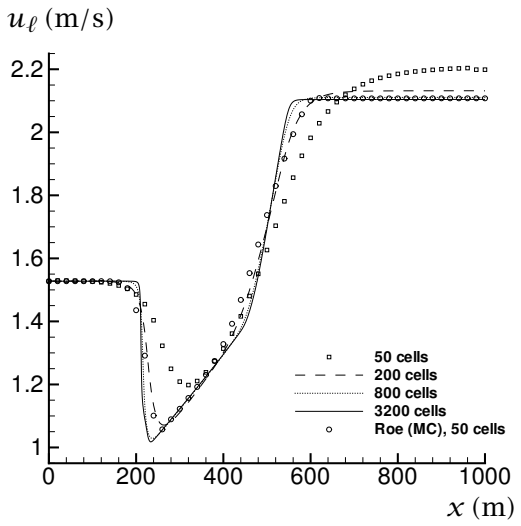

(d) Liquid velocity

Figure 8.15: Pipe-flow test problem. Convergence of the MUSCL-MUSTA$_{4-4}$ scheme using the minmod limiter.

the other hand, MUSTA handled a transonic rarefaction without producing an entropy-condition violation.

To achieve higher order in time and space, we have proposed to use the MUSTA flux in a semi-discrete MUSCL formulation. The resulting MUSCL-MUSTA scheme employing the minmod limiter produced improved and non-oscillatory results. A pipe-flow problem emphasizing volume-fraction waves and near-single-phase flow was well resolved, albeit with a less sharp resolution than the one obtained with the MC-limited Roe scheme. Unfortunately, MUSCL-MUSTA could not in general be used with less-diffusive limiters, since they produced oscillatory solutions for the tested shock tube.

Provided the number of stages is chosen within the bounds described above, the MUSTA scheme possesses robustness properties comparable to those of the Roe scheme. In particular, it generally resolves shock fronts in a non-oscillatory manner and seems to be able to handle the transition to single-phase flow while preserving positivity of volume fractions.

Since its computational cost increases quite quickly with the number of stages and local cells, the main advantage of the MUSTA scheme is its simplicity.

8.5 Conclusions

- The MUSTA scheme has been successfully applied to the drift-flux model, which is relatively complicated compared to the Euler equations. In particular, the scheme worked well for a test problem with a large gap between the eigenvalues.
- The results of the basic MUSTA scheme approached those of the first-order Roe scheme. However, the MUSCL-MUSTA scheme did not quite attain the results of the second-order Roe scheme based on wave decomposition. This is mainly since it was necessary to employ a more diffusive limiter function in MUSCL-MUSTA.
- The computational cost of the MUSTA scheme is comparable to that of the Roe scheme.
- MUSTA seems to be an appropriate choice of numerical scheme if
  1. It is desired to employ closure laws for which the Roe scheme is not valid,
  2. One wishes to avoid programming the numerical diagonalization performed in the Roe scheme,
  3. One wants to avoid possible problems due to transonic rarefactions.

9 Conclusions and recommendations

> The farther one travels, the less one knows.
>
> George Harrison

9.1 Conclusions

There is a need for well-understood models for multiphase flow, as well as robust and accurate numerical methods to solve them. This topic has been analysed in the present work, and the main conclusions are given below.

9.1.1 Modelling

The volume-averaging and the ensemble-averaging approaches for deriving the basic equations of multiphase flow have been reviewed. The form of the equations was seen to be the same, albeit with a different interpretation of the terms.

It was seen that the assumed model for the interfacial pressure difference influences the eigenstructure of the two-fluid model. The interfacial pressure difference also had a significant effect on the solution of two-phase shock-tube problems.

9.1.2 Roe-type methods

The locally linearized, approximate Riemann solver of Roe gives an upwind resolution of all waves in the flow model under consideration. It is therefore known to be accurate. Roe-type methods have been employed to solve three different two-phase flow models. The *Roe4* scheme was employed to solve the four-equation isentropic two-fluid model, and the *Roe5* scheme was proposed to solve the five-equation isentropic two-fluid model with pressure relaxation. Furthermore, a Roe scheme was constructed for the drift-flux model.

The Roe4 and the Roe5 schemes were analysed by numerical experiments, which yielded the following main conclusions:

- The Roe5 scheme with instantaneous pressure relaxation can be regarded as a numerical method to solve the four-equation system. It is significantly

more diffusive than the Roe4 scheme, whether high-resolution limiters are used or not.

– As the pressure-relaxation parameter in the Roe5 scheme is increased, the results converge towards those obtained using instantaneous relaxation. Instantaneous pressure relaxation annihilates the fastest waves, so that the solution approaches that of the four-equation system.

– It does not seem that the problem of complex eigenvalues in the four-equation system can be easily solved by the approach of two pressures and instantaneous pressure relaxation.

Regarding the derivation of the Roe scheme for the drift-flux model, the complicated structure of the model with its closure relations made it unfeasible to employ the parameter-vector method originally proposed by Roe. Instead, alternative strategies were demonstrated, and they allowed

– splitting the problem into independently solvable parts;

– handling general formulations of the closure relations within a single framework.

The proposed Roe scheme for the drift-flux model was, even for the most general case, constructed from arithmetic averages. Hence it is relatively efficient.

9.1.3 Discrete-equation multiphase model

A five-equation isentropic version of the discrete seven-equation two-phase model of Abgrall and Saurel has been presented. In the discrete-equation model, Riemann problems are solved between pure fluids. Hence, the difficulty of non-conservative products is avoided while solving the Riemann problem. Another characteristic of the discrete-equation model is that the properties of the Riemann solver influence the phasic interaction.

It has been shown how different interfacial-pressure expressions can be incorporated into the discrete-equation model.

The correspondence between the discrete-equation model and the 'conventional' continuous model has been discussed. Continuous-limit expressions for the interfacial pressure and velocity were given for the discrete model. These expressions were employed in the Roe5 scheme. Very good agreement between the discrete-equation model and the Roe5 scheme was obtained.

9.1.4 Centred schemes

Since upwind schemes explicitly make use of the mathematical structure of the model, they are often complicated. Centred schemes, on the other hand, are simple, but do normally not provide the same accuracy. The flux-limiter centred (FLIC) scheme has been tried for the four-equation two-fluid model. More work is required to obtain good results. The first-order version of the scheme (FORCE) was found to be robust, but diffusive.

The intention with the multi-stage (MUSTA) method is to come close to the accuracy of upwind schemes while keeping the simplicity of centred schemes. Here it has been successfully applied to the drift-flux model. As the number of stages was increased, the results of the MUSTA scheme approached those of the Roe method. To obtain good results, one must use the MUSTA scheme with a sufficiently large local grid. Therefore, the main advantage of the MUSTA scheme is its simplicity, rather than a speed-up of the calculations.

The second-order version based on the MUSCL technique did not quite attain the results of the second-order Roe scheme based on wave decomposition. The main reason for this is that it was necessary to employ a more diffusive limiter function in MUSCL-MUSTA.

Choosing the MUSTA scheme appears to be suitable if

1. It is desired to employ closure laws for which the Roe scheme is not valid,

2. One wishes to avoid programming the numerical diagonalization performed in the Roe scheme,

3. One wants to avoid possible problems due to transonic rarefactions.

9.1.5 Characteristic-based boundary treatment

The multiphase characteristic-based boundary condition (MPCBC) method of Olsen was discussed. The method uses PID controllers at the boundaries to avoid drifting values, while keeping the solution close to the desired set-point values.

It has been aimed to demonstrate that the MPCBC method is applicable to transient cases. Furthermore, it has been illustrated how the PID-controller parameters can be estimated. With the water-faucet case as an example, it has been shown that MPCBC can yield a reasonable approximation to physically 'open' boundary conditions.

9.2 Recommendations for further work

- An extension to two and three spatial dimensions should be considered.
- For the two-fluid model, the effect of the closure terms, such as the interfacial pressure, should be more thoroughly investigated. Comparisons with data from physical experiments should also be carried out.
- An investigation might be executed to analyse why the Roe4 method fails on the water-air separation case.
- A comparison between the two-fluid and the drift-flux model might be performed.
- It may be worthwhile to analyse the MUSTA scheme for the two-fluid model. The discretization of the non-conservative terms then needs attention.
- Methods for obtaining a semi-discrete formulation might be examined in more detail, since it is convenient to have a method where the temporal and the spatial accuracy are decoupled.
- Implicit or semi-implicit schemes may be studied if it is desired to speed up calculations where detailed knowledge of sonic waves is not required.

Bibliography

Abgrall, R. and Saurel, R. Discrete equations for physical and numerical compressible multiphase mixtures. *Journal of Computational Physics*, volume 186, no. 2: pages 361–396, April 2003.

Andrianov, N. and Warnecke, G. The Riemann problem for the Baer–Nunziato two-phase flow model. *Journal of Computational Physics*, volume 195, no. 2: pages 434–464, April 2004.

Arai, M. Characteristics and stability analyses for two-phase flow equation systems with viscous terms. *Nuclear Science and Engineering*, volume 74, no. 2: pages 77–83, 1980.

Aris, R. *Vectors, tensors, and the basic equations of fluid mechanics*. Prentice-Hall, Englewood Cliffs, New Jersey, USA, 1962. ISBN 0-486-66110-5. Republished by Dover, Mineola, New York, USA, 1989.

Baer, M. R. and Nunziato, J. W. A two-phase mixture theory for the deflagration-to-detonation transition (DDT) in reactive granular materials. *International Journal of Multiphase Flow*, volume 12, no. 6: pages 861–889, 1986.

Barre, F. and Bernard, M. The CATHARE code strategy and assessment. *Nuclear Engineering and Design*, volume 124, no. 3: pages 257–284, December 1990.

Baudin, M., Berthon, C., Coquel, F., Masson, R. and Tran, Q. H. A relaxation method for two-phase flow models with hydrodynamic closure law. *Numerische Mathematik*, volume 99, no. 3: pages 411–440, January 2005a.

Baudin, M., Coquel, F. and Tran, Q.-H. A semi-implicit relaxation scheme for modeling two-phase flow in a pipeline. *SIAM Journal on Scientific Computing*, volume 27, no. 3: pages 914–936, 2005b.

Bendiksen, K. H. An experimental investigation of the motion of long bubbles in inclined tubes. *International Journal of Multiphase Flow*, volume 10, no. 4: pages 467–483, August 1984.

Bendiksen, K. H., Malnes, D., Moe, R. and Nuland, S. The dynamic two-fluid model OLGA: Theory and application. *SPE Production Engineering*, pages 171–179, May 1991.

Benzoni-Gavage, S. *Analyse numérique des modèles hydrodynamiques d'écoulements diphasiques instationnaires dans les réseaux de production pétrolière*. Thèse, ENS Lyon, France, 1991.

Bestion, D. The physical closure laws in the CATHARE code. *Nuclear Engineering and Design*, volume 124, no. 3: pages 229–245, December 1990.

Bouré, J. A. Wave phenomena and one-dimensional two-phase flow models – Part I: Kinematic waves; experimental results; theory. *Multiphase Science and Technology*, volume 9, no. 1: pages 1–35, 1997.

Brown, G. J. Erosion prediction in slurry pipeline tee-junctions. *Applied Mathematical Modelling*, volume 26, no. 2: pages 155–170, February 2002.

Carpenter, M. H. and Kennedy, C. A. Fourth-order 2N-storage Runge-Kutta schemes. Technical Report NASA TM-109112, NASA Langley Research Center, Hampton, VA, USA, June 1994.

Chen, G.-Q. and Toro, E. F. Centered difference schemes for nonlinear hyperbolic equations. *Journal of Hyperbolic Differential Equations*, volume 1, no. 3: pages 531–566, 2004.

Chung, M.-S., Chang, K.-S. and Lee, S.-J. Numerical solution of hyperbolic two-fluid two-phase flow model with non-reflecting boundary conditions. *International Journal of Engineering Science*, volume 40, no. 7: pages 789–803, 2002.

Cleary, P. W., Prakash, M., Ha, J., Stokes, N. and Scott, C. Smooth particle hydrodynamics: Status and future potential. In: S. T. Johansen and I. G. Page, editors, *Proceedings of CFD2005 – Fourth International Conference on Computational Fluid Dynamics in the Oil and Gas, Metallurgical & Process Industries*. SINTEF, NTNU, CSIRO, Trondheim, Norway, June 2005. ISBN 82-14-03751-4. Keynote lecture.

Coquel, F., El Amine, K., Godlewski, E., Perthame, B. and Rascle, P. A numerical method using upwind schemes for the resolution of two-phase flows. *Journal of Computational Physics*, volume 136, no. 2: pages 272–288, 1997.

Cortes, J., Debussche, A. and Toumi, I. A density perturbation method to study the eigenstructure of two-phase flow equation systems. *Journal of Computational Physics*, volume 147, no. 2: pages 463–484, 1998.

Drew, D. A. Mathematical modeling of two-phase flow. *Annual Review of Fluid Mechanics*, volume 15: pages 261–291, 1983.

Drew, D. A. and Passman, S. L. *Theory of Multicomponent Fluids*, volume 135 of *Applied Mathematical Sciences*. Springer-Verlag, New York, 1999. ISBN 0-387-98380-5.

Ertesvåg, I. S. *Turbulent strøyming og forbrenning*. Tapir akademisk forlag, Trondheim, Norway, 2000. ISBN 82-519-1568-6.

Evje, S. and Fjelde, K. K. Hybrid flux-splitting schemes for a two-phase flow model. *Journal of Computational Physics*, volume 175, no. 2: pages 674–701, January 2002.

Evje, S. and Fjelde, K. K. On a rough AUSM scheme for a one-dimensional two-phase model. *Computers & Fluids*, volume 32, no. 10: pages 1497–1530, December 2003.

Evje, S. and Flåtten, T. Hybrid flux-splitting schemes for a common two-fluid model. *Journal of Computational Physics*, volume 192, no. 1: pages 175–210, November 2003.

Evje, S. and Flåtten, T. Hybrid central-upwind schemes for numerical resolution of two-phase flows. *ESAIM: Mathematical Modelling and Numerical Analysis*, volume 29, no. 2: pages 253–273, March–April 2005a.

Evje, S. and Flåtten, T. On the wave structure of two-phase flow models. *Submitted*, 2005b. Preprint available from `http://www.rf.no/Internet/petroleum.nsf/p/205`.

Faille, I. and Heintzé, E. A rough finite volume scheme for modeling two-phase flow in a pipeline. *Computers & Fluids*, volume 28, no. 2: pages 213–241, February 1999.

Fjelde, K. K. and Karlsen, K. H. High-resolution hybrid primitive–conservative upwind schemes for the drift flux model. *Computers & Fluids*, volume 31, no. 3: pages 335–367, March 2002.

Flåtten, T. *Hybrid flux splitting schemes for numerical resolution of two-phase flows*. Dr. ing. thesis, Norwegian University of Science and Technology, Department of Energy and Process Engineering, Trondheim, 2003. ISBN 82-471-5670-9.

Flåtten, T. and Munkejord, S. T. The approximate Riemann solver of Roe applied to a drift-flux two-phase flow model. *Submitted to ESAIM: Mathematical Modelling and Numerical Analysis*, 2006.

França, F. and Lahey, Jr., R. T. The use of drift-flux techniques for the analysis of horizontal two-phase flows. *International Journal of Multiphase Flow*, volume 18, no. 6: pages 787–801, November 1992.

Hansen, E. B. *Numerical Simulation of Droplet Dynamics in the Presence of an Electric Field*. Doctoral thesis, Norwegian University of Science and Technology, Department of Energy and Process Engineering, Trondheim, November 2005. ISBN 82-471-7318-2.

Harten, A. High resolution schemes for hyperbolic conservation laws. *Journal of Computational Physics*, volume 49, no. 3: pages 357–393, March 1983.

Harten, A., Lax, P. D. and van Leer, B. High resolution schemes for hyperbolic conservation laws. *SIAM Review*, volume 25, no. 1: pages 35–61, January 1983.

Haugen, F. *Regulering av dynamiske systemer*. Tapir Forlag, Trondheim, Norway, 1994. ISBN 82-519-1433-7.

Hibiki, T. and Ishii, M. Distribution parameter and drift velocity of drift-flux model in bubbly flow. *International Journal of Heat and Mass Transfer*, volume 45, no. 4: pages 707–721, February 2002.

Ishii, M. *Thermo-fluid dynamic theory of two-phase flow*. Collection de la Direction des Etudes et Recherches d'Electricité de France, Eyrolles, Paris, 1975.

Ishii, M. Drift flux model and derivation of kinematic consitutive laws. In: S. Kakaç and F. Mayinger, editors, *Proceedings of NATO Advanced Study Institute*, pages 187–208. Hemisphere, August 1977.

Jin, S. and Xin, Z. The relaxation schemes for systems of conservation-laws in arbitrary space dimensions. *Communications on Pure and Applied Mathematics*, volume 48, no. 3: pages 235–276, March 1995.

Karni, S., Kirr, E., Kurganov, A. and Petrova, G. Compressible two-phase flows by central and upwind schemes. *ESAIM: Mathematical Modelling and Numerical Analysis*, volume 38, no. 3: pages 477–493, May–June 2004.

Kataoka, I. Local instant formulation of two-phase flow. *International Journal of Multiphase Flow*, volume 12, no. 5: pages 745–758, 1986.

Ketcheson, D. I. and Robinson, A. C. On the practical importance of the SSP property for Runge-Kutta time integrators for some common Godunov-type

schemes. *International Journal for Numerical Methods in Fluids*, volume 48, no. 3: pages 271–303, January 2005.

Kraaijevanger, J. F. B. M. Contractivity of Runge-Kutta methods. *BIT*, volume 31, no. 3: pages 482–528, 1991.

Lahey, Jr., R. T., Cheng, L. Y., Drew, D. A. and Flaherty, J. E. The effect of virtual mass on the numerical stability of accelerating two-phase flows. *International Journal of Multiphase Flow*, volume 6, no. 4: pages 281–294, August 1980.

Lallemand, M.-H., Chinnayya, A. and Le Metayer, O. Pressure relaxation procedures for multiphase compressible flows. *International Journal for Numerical Methods in Fluids*, volume 49, no. 1: pages 1–56, May 2005.

Larsen, M., Hustvedt, E., Hedne, P. and Straume, T. PeTra: A novel computer code for simulation of slug flow. In: *Proceedings – 1997 SPE Annual Technical Conference and Exhibition*, pages 965–976. Society of Petroleum Engineers, San Antonio, Texas, USA, October 1997. SPE 38841.

Le Métayer, O., Massoni, J. and Saurel, R. Modelling evaporation fronts with reactive Riemann solvers. *Journal of Computational Physics*, volume 205, no. 2: pages 567–610, May 2005.

LeVeque, R. J. *Numerical Methods for Conservation Laws*. Lectures in Mathematics, ETH Zürich, Birkhäuser Verlag, Basel, Switzerland, 1990. ISBN 3-7643-2464-3.

LeVeque, R. J. *Finite Volume Methods for Hyperbolic Problems*. Cambridge University Press, Cambridge, UK, 2002. ISBN 0-521-00924-3.

Loth, E. Numerical approaches for motion of dispersed particles, droplets and bubbles. *Progress in Energy and Combustion Science*, volume 26, no. 3: pages 161–223, 2000.

Mahaffy, J. H. Numerics of codes – stability, diffusion, and convergence. *Nuclear Engineering and Design*, volume 145, no. 1–2: pages 131–145, November 1993.

Melheim, J. A. *Computer simulation of turbulent electrocoalescence*. Doctoral thesis, Norwegian University of Science and Technology, Department of Energy and Process Engineering, Trondheim, 2005. In progress.

Moran, M. J. and Shapiro, H. N. *Fundamentals of Engineering Thermodynamics*. John Wiley & Sons, New York, second edition, 1993. ISBN 0-471-59275-7.

Munkejord, S. T. Comparison of a four-equation and a five-equation Roe-type method for solving the two-fluid model. *Submitted to Computers & Fluids*, 2005a.

Munkejord, S. T. Partially-reflecting boundary conditions for transient two-phase flow. *Communications in Numerical Methods in Engineering*, 2005b. To appear.

Munkejord, S. T., Evje, S. and Flåtten, T. The multi-stage centred-scheme approach applied to a drift-flux two-phase flow model. *International Journal for Numerical Methods in Fluids*, 2006. Accepted for publication.

Munkejord, S. T., Mølnvik, M. J., Melheim, J. A., Gran, I. R. and Olsen, R. Prediction of two-phase pipe flows using simple closure relations in a 2D two-fluid model. In: S. T. Johansen and I. G. Page, editors, *Proceedings of CFD2005 – Fourth International Conference on Computational Fluid Dynamics in the Oil and Gas, Metallurgical & Process Industries*. SINTEF, NTNU, CSIRO, Trondheim, Norway, June 2005. ISBN 82-14-03751-4.

Munkejord, S. T., Olsen, R. and Melheim, J. A. Basic equations of multiphase flow. Technical Report F5258, SINTEF Energy Research, Division of Thermal Energy, Trondheim, Norway, December 2000. ISBN 82-594-1879-7. Unpublished.

Munkejord, S. T. and Papin, M. The effect of interfacial pressure in the discrete-equation multiphase model. *Computers & Fluids*, 2005. Accepted for publication.

Murrone, A. and Guillard, H. A five equation reduced model for compressible two phase flow problems. *Journal of Computational Physics*, volume 202, no. 2: pages 664–698, January 2005.

Niu, Y.-Y. Advection upwinding splitting method to solve a compressible two-fluid model. *International Journal for Numerical Methods in Fluids*, volume 36, no. 3: pages 351–371, June 2001.

Olsen, R. *Time-dependent boundary conditions for multiphase flow*. Doctoral thesis, Norwegian University of Science and Technology, Department of Energy and Process Engineering, Trondheim, September 2004. ISBN 82-471-6313-4.

Osher, S. Riemann solvers, the entropy condition, and difference approximations. *SIAM Journal on Numerical Analysis*, volume 21, no. 2: pages 217–235, 1984.

Osher, S. Convergence of generalized MUSCL schemes. *SIAM Journal on Numerical Analysis*, volume 22, no. 5: pages 947–961, October 1985.

Osher, S. and Fedkiw, R. P. Level set methods: An overview and some recent results. *Journal of Computational Physics*, volume 169, no. 2: pages 463–502, May 2001.

Paillère, H., Corre, C. and García Cascales, J. R. On the extension of the AUSM+ scheme to compressible two-fluid models. *Computers & Fluids*, volume 32, no. 6: pages 891–916, July 2003.

Papin, M. *Contribution à la modélisation d'écoulements hypersoniques particulaires. Étude et validation d'un modèle diphasique discret.* Thèse, Université Bordeaux 1, Mathématiques Appliquées, France, June 2005.

Pauchon, C. L., Dhulesia, H., Cirlot, G. B. and Fabre, J. TACITE: A transient tool for multiphase pipeline and well simulation. In: *Proceedings – SPE Annual Technical Conference and Exhibition*, pages 311–326. Society of Petroleum Engineers, New Orleans, Louisiana, USA, September 1994. SPE 28545.

Peskin, C. S. The immersed boundary method. *Acta Numerica*, volume 11: pages 479–517, 2002.

Ramshaw, J. D. and Trapp, J. A. Characteristics, stability, and short-wavelength phenomena in two-phase flow equation systems. *Nuclear Science and Engineering*, volume 66, no. 1: pages 93–102, 1978.

Ransom, V. H. Faucet flow. In: G. F. Hewitt, J. M. Delhaye and N. Zuber, editors, *Numerical Benchmark Tests*, volume 3 of *Multiphase Science and Technology*, pages 465–467. Hemisphere/Springer, Washington, USA, 1987. ISBN 0-89116-561-4.

Ransom, V. H. and Hicks, D. L. Hyperbolic two-pressure models for two-phase flow. *Journal of Computational Physics*, volume 53, no. 1: pages 124–151, 1984.

Roe, P. L. Approximate Riemann solvers, parameter vectors, and difference schemes. *Journal of Computational Physics*, volume 43, no. 2: pages 357–372, October 1981.

Romate, J. E. An approximate Riemann solver for a two-phase flow model with numerically given slip relation. *Computers & Fluids*, volume 27, no. 4: pages 455–477, May 1998.

Sainsaulieu, L. Finite-volume approximation of two phase-fluid flows based on an approximate Roe-type Riemann solver. *Journal of Computational Physics*, volume 121, no. 1: pages 1–28, October 1995.

Saurel, R. and Abgrall, R. A multiphase Godunov method for compressible multifluid and multiphase flow. *Journal of Computational Physics*, volume 150, no. 2: pages 425–467, April 1999.

Saurel, R. and LeMetayer, O. A multiphase model for compressible flows with interfaces, shocks, detonation waves and cavitation. *Journal of Fluid Mechanics*, volume 431: pages 239–271, March 2001.

Scardovelli, R. and Zaleski, S. Direct numerical simulation of free-surface and interfacial flow. *Annual Review of Fluid Mechanics*, volume 31, no. 1: pages 567–603, January 1999.

Sethian, J. A. Evolution, implementation, and application of level set and fast marching methods for advancing. *Journal of Computational Physics*, volume 169, no. 2: pages 503–555, May 2001.

Singh, R., Uzgoren, E., Tai, C.-F. and Shyy, W. A marker-based, adaptive/multigrid technique for interfacial fluid dynamics. In: S. T. Johansen and I. G. Page, editors, *Proceedings of CFD2005 – Fourth International Conference on Computational Fluid Dynamics in the Oil and Gas, Metallurgical & Process Industries*. SINTEF, NTNU, CSIRO, Trondheim, Norway, June 2005. ISBN 82-14-03751-4. Keynote lecture.

Slattery, J. C. Flow of viscoelastic fluids through porous media. *AIChE Journal*, volume 13, no. 6: pages 1066–1071, November 1967.

Soo, S. L. *Particulates and continuum: Multiphase fluid dynamics*. Hemisphere, New York, 1989. ISBN 0-89116-918-0.

Soo, S. L. *Multiphase fluid dynamics*. Science Press, Beijing, 1990. ISBN 0-291-39781-6, 70-300-0102.

Spiteri, R. J. and Ruuth, S. J. A new class of optimal high-order strong-stability-preserving time discretization methods. *SIAM Journal on Numerical Analysis*, volume 40, no. 2: pages 469–491, July 2002.

Stewart, H. B. Stability of two-phase flow calculation using two-fluid models. *Journal of Computational Physics*, volume 33, no. 2: pages 259–270, 1979.

Stewart, H. B. and Wendroff, B. Review article: Two-phase flow: Models and methods. *Journal of Computational Physics*, volume 56, no. 3: pages 363–409, 1984.

Stuhmiller, J. H. The influence of interfacial pressure forces on the character of two-phase flow model equations. *International Journal of Multiphase Flow*, volume 3, no. 6: pages 551–560, December 1977.

Taitel, Y. Flow pattern transistion in two phase flow. In: *9th International Heat Transfer Conference*, pages 237–254. Jerusalem, Israel, August 1990. Keynote lecture.

Thompson, K. W. Time-dependent boundary conditions for hyperbolic systems. *Journal of Computational Physics*, volume 68, no. 1: pages 1–24, January 1987.

Thompson, K. W. Time-dependent boundary conditions for hyperbolic systems, II. *Journal of Computational Physics*, volume 89, no. 2: pages 439–461, August 1990.

Tiselj, I. and Petelin, S. Modelling of two-phase flow with second-order accurate scheme. *Journal of Computational Physics*, volume 136, no. 2: pages 503–521, 1997.

Titarev, V. A. and Toro, E. F. Finite-volume WENO schemes for three-dimensional conservation laws. *Journal of Computational Physics*, volume 201, no. 1: pages 238–260, November 2004.

Titarev, V. A. and Toro, E. F. MUSTA schemes for multi-dimensional hyperbolic systems: analysis and improvements. *International Journal for Numerical Methods in Fluids*, volume 49, no. 2: pages 117–147, September 2005.

Toro, E. F. *Riemann solvers and numerical methods for fluid dynamics*. Springer-Verlag, Berlin, second edition, 1999. ISBN 3-540-65966-8.

Toro, E. F. Multi-stage predictor-corrector fluxes for hyperbolic equations. In: *Isaac Newton Institute for Mathematical Sciences Preprint Series*. University of Cambridge, UK, June 2003. NI03037-NPA, available from `http://www.newton.cam.ac.uk/preprints2003.html`.

Toro, E. F. and Billett, S. J. Centred TVD schemes for hyperbolic conservation laws. *IMA Journal of Numerical Analysis*, volume 20, no. 1: pages 47–79, November 2000.

Toumi, I. An upwind numerical method for two-fluid two-phase flow models. *Nuclear Science and Engineering*, volume 123, no. 2: pages 147–168, 1996.

Toumi, I. and Caruge, D. An implicit second-order numerical method for three-dimensional two-phase flow calculations. *Nuclear Science and Engineering*, volume 130, no. 2: pages 213–225, October 1998.

Toumi, I. and Kumbaro, A. An approximate linearized Riemann solver for a two-fluid model. *Journal of Computational Physics*, volume 124, no. 2: pages 286–300, March 1996.

Trapp, J. A. and Riemke, R. A. A nearly-implicit hydrodynamic numerical scheme for two-phase flows. *Journal of Computational Physics*, volume 66, no. 1: pages 62–82, September 1986.

Travis, J. R., Harlow, F. H. and Amsden, A. A. Numerical calculations of two-phase flows. *Nuclear Science and Engineering*, volume 61, no. 1: pages 1–10, 1976.

Tryggvason, G., Bunner, B., Esmaeli, A., Juric, D., Al-Rawahi, N., Tauber, W., Han, J., Nas, S. and Jan, Y.-J. A front-tracking method for the computations of multiphase flow. *Journal of Computational Physics*, volume 169, no. 2: pages 708–759, May 2001.

van der Hoef, M. A., van Sint Annaland, M., Deen, N. G. and Kuipers, J. A. M. Numerical simulation of dense gas-particle flows using the Euler-Lagrange approach. In: S. T. Johansen and I. G. Page, editors, *Proceedings of CFD2005 – Fourth International Conference on Computational Fluid Dynamics in the Oil and Gas, Metallurgical & Process Industries*. SINTEF, NTNU, CSIRO, Trondheim, Norway, June 2005. ISBN 82-14-03751-4. Keynote lecture.

van Leer, B. Towards the ultimate conservative difference scheme II. Monotonicity and conservation combined in a second-order scheme. *Journal of Computational Physics*, volume 14, no. 4: pages 361–370, 1974.

van Leer, B. Towards the ultimate conservative difference scheme IV. New approach to numerical convection. *Journal of Computational Physics*, volume 23, no. 3: pages 276–299, 1977.

van Leer, B. Towards the ultimate conservative difference scheme V. A second-order sequel to Godunov's method. *Journal of Computational Physics*, volume 32, no. 1: pages 101–136, July 1979.

van Leer, B. On the relation between the upwind-differencing schemes of Godunov, Engquist-Osher and Roe. *SIAM Journal on Scientific and Statistical Computing*, volume 5, no. 1: pages 1–20, March 1984.

Vefring, E. H., Wang, Z., Gaard, S. and Bach, G. F. An advanced kick simulator for high angle and horizontal wells – part I. In: *Proceedings – 1995 SPE/IADC Drilling Conference*, pages 123–134. Society of Petroleum Engineers, Amsterdam, The Netherlands, February–March 1995. SPE/IADC 29345.

Wesseling, P. *Principles of Computational Fluid Dynamics*, volume 29 of *Computational Mathematics*. Springer-Verlag, Berlin, 2001. ISBN 3-540-67853-0.

Whitaker, S. Advances in theory of fluid motion in porous media. *Industrial and Engineering Chemistry*, volume 61, no. 4: pages 14–28, December 1969.

Ziegler, J. G. and Nichols, N. B. Optimum settings for automatic controllers. *Transactions of the ASME*, volume 64: pages 759–768, 1942.

Zuber, N. and Findlay, J. A. Average volumetric concentration in two-phase flow systems. *Journal of Heat Transfer – Transactions of the ASME*, volume 87: pages 453–468, November 1965.

A Approximate eigenvalues of the two-fluid model

In this appendix, we state the approximate eigenvalues of the coefficient matrix (3.34) of the four-equation system. They were derived by Evje and Flåtten (2003), using a perturbation technique suggested by Toumi and Kumbaro (1996). Some further details may be found in Flåtten (2003).

Introduce the perturbation parameter

$$\varepsilon = \frac{u_{\mathrm{g}} - u_{\ell}}{\hat{c}_{\mathrm{m}}\left(1 + \frac{\alpha_{\ell}\rho_{\mathrm{g}}}{\alpha_{\mathrm{g}}\rho_{\ell}}\right)}, \tag{A.1}$$

where $\hat{c}_{\mathrm{m}}$ is an approximate mixture speed of sound given by

$$\hat{c}_{\mathrm{m}} = \sqrt{\frac{\alpha_{\mathrm{g}}\rho_{\ell} + \alpha_{\ell}\rho_{\mathrm{g}}}{(\partial\rho_{\mathrm{g}}/\partial p)\alpha_{\mathrm{g}}\rho_{\ell} + (\partial\rho_{\ell}/\partial p)\alpha_{\ell}\rho_{\mathrm{g}}}}. \tag{A.2}$$

It can be shown that the eigenvalues corresponding to pressure waves can be written as

$$\lambda_{\{1,2\}} = u_p \pm c_{\mathrm{m}}, \tag{A.3}$$

and that the eigenvalues corresponding to volume-fraction waves can be expressed by

$$\lambda_{\{3,4\}} = u_u \pm \upsilon. \tag{A.4}$$

Herein,

$$u_p = \frac{\alpha_{\mathrm{g}}\rho_{\ell}u_{\mathrm{g}} + \alpha_{\ell}\rho_{\mathrm{g}}u_{\ell}}{\alpha_{\mathrm{g}}\rho_{\ell} + \alpha_{\ell}\rho_{\mathrm{g}}} + \hat{c}_{\mathrm{m}}\mathcal{O}(\varepsilon^3), \tag{A.5}$$

$$u_u = \frac{\alpha_{\mathrm{g}}\rho_{\ell}u_{\ell} + \alpha_{\ell}\rho_{\mathrm{g}}u_{\mathrm{g}}}{\alpha_{\mathrm{g}}\rho_{\ell} + \alpha_{\ell}\rho_{\mathrm{g}}} + \hat{c}_{\mathrm{m}}\mathcal{O}(\varepsilon^3), \tag{A.6}$$

$$c_{\mathrm{m}} = \hat{c}_{\mathrm{m}}[1 + \mathcal{O}(\varepsilon^2)], \tag{A.7}$$

and

$$\upsilon = \sqrt{\frac{\Delta p_{\mathrm{i}}(\alpha_{\mathrm{g}}\rho_{\ell} + \alpha_{\ell}\rho_{\mathrm{g}}) - \alpha_{\mathrm{g}}\alpha_{\ell}\rho_{\mathrm{g}}\rho_{\ell}(u_{\mathrm{g}} - u_{\ell})^2}{(\alpha_{\mathrm{g}}\rho_{\ell} + \alpha_{\ell}\rho_{\mathrm{g}})^2}} + \hat{c}_{\mathrm{m}}\mathcal{O}(\varepsilon^3). \tag{A.8}$$

Note that $\Delta p_{\mathrm{i}} = 0$ renders υ imaginary and hence $\lambda_{\{3,4\}}$ complex. Furthermore, the above equation shows that when the CATHARE model (2.109) is employed, one needs to take the factor $\gamma > 1$.

B More on the drift-flux model

In this appendix, we give some further mathematical details of the drift-flux model of Chapters 7–8. First, the approximate eigenvalues derived by Evje and Flåtten (2005b) are reproduced. Then transformation matrices are presented for calculating the Jacobi matrix as a function of the primitive variables and the 'mass-flux' variables.

B.1 Approximate eigenvalues

Using a perturbation technique, Evje and Flåtten (2005b) derived approximate eigenvalues of the Jacobian matrix (7.38) of the drift-flux model under the assumption that the slip relation Φ satisfies the differential equation

$$\alpha_\ell \left(\frac{\partial \Phi}{\partial \alpha_\ell} \right)_p + \Phi = 0. \tag{B.1}$$

(For instance, this is not the case when the relation (7.161) on page 202 is employed.)

With the perturbation parameter

$$\varepsilon = \frac{u_\mathrm{g} - u_\ell}{\sqrt{\kappa \varrho (\alpha_\mathrm{g} - \zeta \alpha_\ell)}}, \tag{B.2}$$

the eigenvalue corresponding to the material wave was found to be

$$\lambda_\mathrm{m} = u_\mathrm{g} - \frac{\alpha_\mathrm{g} \alpha_\ell}{\alpha_\mathrm{g} + \zeta \alpha_\ell} \mu_\mathrm{g} \frac{(u_\mathrm{g} - u_\ell)^2}{\kappa} + \mathcal{O}(\varepsilon^3), \tag{B.3}$$

and the eigenvalues corresponding to the sonic waves were calculated as

$$\lambda_p = u_p \pm c_\mathrm{m}, \tag{B.4}$$

where

$$u_p = \frac{m_\mathrm{g} u_\mathrm{g} + \zeta m_\ell u_\ell}{m_\mathrm{g} + \zeta m_\ell} + \alpha_\ell m_\mathrm{g} \mu_\mathrm{g} \frac{\rho_\ell - \rho_\mathrm{g}}{2\varrho} + \frac{\alpha_\mathrm{g} \alpha_\ell}{\alpha_\mathrm{g} + \zeta \alpha_\ell} \mu_\mathrm{g} \frac{(u_\mathrm{g} - u_\ell)^2}{2\kappa} + \mathcal{O}(\varepsilon^3), \tag{B.5}$$

and the mixture sonic velocity is

$$c_{\mathrm{m}} = \frac{1}{2}\psi_1\psi_3 + \frac{\psi_2}{\psi_3}\frac{\rho_\ell}{\varrho}\left[2 - \zeta\alpha_\ell\left(\frac{\rho_\ell - \rho_{\mathrm{g}}}{\varrho}\right)\right](u_{\mathrm{g}} - u_\ell) + \mathcal{O}(\varepsilon^2), \tag{B.6}$$

with

$$\begin{aligned}
\psi_1 &= \sqrt{\kappa\varrho(\alpha_{\mathrm{g}} + \zeta\alpha_\ell)}, \\
\psi_2 &= \frac{\alpha_\ell m_{\mathrm{g}}}{\psi_1}\mu_{\mathrm{g}}, \\
\psi_3 &= \sqrt{\psi_2^2\left(\frac{\rho_\ell - \rho_{\mathrm{g}}}{\varrho}\right)^2 + 4\frac{\rho_\ell\rho_{\mathrm{g}}}{\varrho^2}}.
\end{aligned} \tag{B.7}$$

B.2 Jacobi matrices for different variables

For the composite variables

$$\boldsymbol{q} = \begin{bmatrix}\alpha_{\mathrm{g}}\rho_{\mathrm{g}} & \alpha_\ell\rho_\ell & \alpha_{\mathrm{g}}\rho_{\mathrm{g}}u_{\mathrm{g}} + \alpha_\ell\rho_\ell u_\ell + p\end{bmatrix}^T, \tag{B.8}$$

the Jacobi matrix $\boldsymbol{A}(\boldsymbol{q})$ of the drift-flux model is given by (7.38) on page 176. For some purposes, for instance characteristic-based boundary treatment, it is necessary to express the Jacobi matrix as a function of the primitive variables

$$\boldsymbol{v} = \begin{bmatrix}\alpha_{\mathrm{g}} & p & u_{\mathrm{g}}\end{bmatrix}^T. \tag{B.9}$$

The transformation matrix $\boldsymbol{J} = \partial\boldsymbol{q}/\partial\boldsymbol{v}$ becomes

$$\boldsymbol{J} = \begin{bmatrix}\rho_{\mathrm{g}} & \alpha_{\mathrm{g}}\frac{\partial\rho_{\mathrm{g}}}{\partial p} & 0 \\ -\rho_\ell & \alpha_\ell\frac{\partial\rho_\ell}{\partial p} & 0 \\ \rho_{\mathrm{g}}u_{\mathrm{g}} - \rho_\ell u_\ell & \alpha_{\mathrm{g}}u_{\mathrm{g}}\frac{\partial\rho_{\mathrm{g}}}{\partial p} + \alpha_\ell u_\ell\frac{\partial\rho_\ell}{\partial p} & \alpha_{\mathrm{g}}\rho_{\mathrm{g}} + \zeta\alpha_\ell\rho_\ell,\end{bmatrix} \tag{B.10}$$

so that we can calculate

$$\boldsymbol{B}(\boldsymbol{v}) = \boldsymbol{J}^{-1}\boldsymbol{A}\boldsymbol{J} \tag{B.11}$$

similarly to what was done in Section 3.2 on page 41.

The Jacobi matrix may also be written in terms of the 'mass-flux' variables

$$\boldsymbol{w} = \begin{bmatrix}p & \alpha_{\mathrm{g}}\rho_{\mathrm{g}}u_{\mathrm{g}} & \alpha_\ell\rho_\ell u_\ell\end{bmatrix}^T. \tag{B.12}$$

To this end, we use the transformation matrix

$$\tilde{\boldsymbol{J}} \equiv \frac{\partial\boldsymbol{w}}{\partial\boldsymbol{v}} = \begin{bmatrix}0 & 1 & 0 \\ \rho_{\mathrm{g}}u_{\mathrm{g}} & \alpha_{\mathrm{g}}u_{\mathrm{g}}\frac{\partial\rho_{\mathrm{g}}}{\partial p} & \alpha_{\mathrm{g}}\rho_{\mathrm{g}} \\ -\rho_\ell u_\ell & \alpha_\ell u_\ell\frac{\partial\rho_\ell}{\partial p} & \zeta\alpha_\ell\rho_\ell\end{bmatrix}. \tag{B.13}$$

Since

$$\frac{\partial \boldsymbol{w}}{\partial \boldsymbol{q}} = \frac{\partial \boldsymbol{w}}{\partial \boldsymbol{v}} \frac{\partial \boldsymbol{v}}{\partial \boldsymbol{q}} = \tilde{\boldsymbol{J}} \boldsymbol{J}^{-1}, \tag{B.14}$$

we can calculate

$$\tilde{\boldsymbol{B}}(\boldsymbol{w}) = \boldsymbol{K}^{-1} \boldsymbol{A} \boldsymbol{K}, \tag{B.15}$$

where $\boldsymbol{K} = \left(\tilde{\boldsymbol{J}} \boldsymbol{J}^{-1}\right)^{-1}$.